Topology optimization in structural dynamics : vibrations, fracture resistance and uncertainties

Yi Wu

UNIVERSITÉ PARIS-EST

HUNAN UNIVERSITY

THÈSE DE DOCTORAT DE L'UNIVERSITÉ PARIS-EST

SPÉCIALITÉ : MÉCANIQUE

Optimisation topologique en dynamique des structures: vibrations, résistance à la rupture et incertitudes

Yi WU

Soutenue le 15 Juin 2022

Jury :

Rapporteurs :	Piotr BREITKOPF	Ingénieur de Recherche Université de Technologie de Compiègne
	Liang XIA	Associate Professor Huazhong University of Science and Technology
Examinateurs :	Qi-Hong FANG	Professor Hunan University
	Eric LI	Associate Professor Teesside University
Directeur de thèse :	Julien YVONNET	Professeur des Universités Université Gustave Eiffel
Co-encadrant de thèse :	Zhi-Cheng HE	Professor Hunan University

ÉCOLE DOCTORALE UNIVERSITÉ PARIS-EST

Sciences, Ingénierie et Environnement

Acknowledgements

I wish to show my appreciation to my supervisor, Prof. Julien Yvonnet, who guided me throughout this thesis. I want to thank him for his acceptance, vision, tolerance, and encouragement.

I would like to thank my co-supervisor in China, Prof. Zhicheng He, for leading me into scientific research. I would also like to thank Prof. Eric Quan-Bing Li from Teesside University, UK. I want to thank him for his advice on my career and endless affirmation of me.

Thank you guys from the Université Paris-Est. They are Dr. Pengfei Li, Mr. Han Hu, Dr. Wenqiang Zuo, Dr. Xu Hu, Dr. Weizhi Luo, Mr. Xing Chen, and our little brother Boyang Ma. Special thanks to Mr. Di Bao from École Nationale Supérieure de Mécanique et d'Aérotechnique (ENSMA) for all the supports.

Thanks to the lab members at Hunan University. They are Dr. Xinyou Lin, Dr. Qiqi Li, Dr. Yaodong Hao, Dr. Xiao Xiao, Dr. Hailun Tan, Mr. Peiwen Chu and Mr. Hexin Jiang. I wish to extend my special thanks to Dr. Menghao Ping, Prof. Xiangyun Long, Prof. Jing Zheng, Dr. Shan Yin, Dr. Baoshou Liu, and Dr. Qiming Liu for their help and guidance to my research. Special thanks to Prof. Liang Xia from Huazhong University of Science and Technology for his support and recognition of my research work on fracture resistance design.

I wish to acknowledge my committee. The financial support from China Scholarship Council was greatly appreciated.

Finally, I would like to thank my wife, Ms. Shirui Li, for her support and companionship for more than ten years. I am grateful for my parents, Mr. Zhengbo Wu and Ms. Juan Wang, who unconditionally supported my academic career.

Abstract

The objective of this thesis is to develop density based-topology optimization methods for several challenging dynamic structural problems. First, we propose a normalization strategy for elastodynamics to obtain optimized material distributions of the structures that reduces frequency response and improves the numerical stabilities of the bi-directional evolutionary structural optimization (BESO). Then, to take into account uncertainties in practical engineering problems, a hybrid interval uncertainty model is employed to efficiently model uncertainties in dynamic structural optimization. A perturbation method is developed to implement an uncertainty-insensitive robust dynamic topology optimization in a form that greatly reduces the computational costs. In addition, we introduce a model of interval field uncertainty into dynamic topology optimization. The approach is applied to single material, composites and multi-scale structures topology optimization. Finally, we develop a topology optimization for dynamic brittle fracture structural resistance, by combining topology optimization with dynamic phase field fracture simulations. This framework is extended to design impact-resistant structures. In contrast to stress-based approaches, the whole crack propagation is taken into account into the optimization process.

Résumé

L'objectif de cette thèse est de développer des méthodes d'optimisation topologiques basées sur la densité pour plusieurs problèmes difficiles de structure en dynamique. Premièrement, nous proposons une stratégie de normalisation en élasto-dynamique en vue d'obtenir une distribution optimale de matériau dans la structure qui réduit la réponse aux excitations dynamiques en fréquence et améliore la stabilité numérique dans la méthode BESO (bi-directional evolutionary structural optimisation). Ensuite, pour décrire les incertitudes de paramètres pouvant intervenir dans des problèmes réalistes en ingénierie, un modèle d'incertitudes à intervalle hybride est développé pour prendre en compte les incertitudes dans le problème d'optimisation en dynamique. Une méthode de perturbation est développée pour une optimisation topologique robuste vis-à-vis des incertitudes et permettant des gains de temps de calculs importants. De plus, nous introduisons un modèle d'incertitude de champ d'intervalle dans ce cadre. L'approche est appliquée à l'optimisation topologique des structures mono-matériaux, composites et multi-échelles. Enfin, nous développons un cadre d'optimisation topologique pour la résistance des structures à la fissuration quasi-fragile dans un cadre dynamique, par combinaison avec la méthode de champs de phase. Ce cadre est étendu à la conception de structures résistantes à des impacts. Contrairement aux approches basées sur les contraintes, la totalité de la propagation des fissures est prise en compte dans le processus d'optimisation.

Table of contents

List of figures

List of tables

Chapter 1

Introduction and literature review

1.1 Background and motivations

Finding the optimal material distribution for a given design domain to obtain better structural performance is a fundamental and critical problem in engineering design. Traditionally, in most cases, the arrangement of material or the positioning of structural elements of a design is chosen intuitively or inspired by existing solutions [103]. However, there is a specific need for improving the quality of the products and shortening the design process by finding the optimum topology at an early stage of the design process [104].

In the past decades, topology optimization has been become one of the most important numerical approaches to solve this problem. It provides a feasible way to generate the optimal topological designs that minimize or maximize an objective function while satisfying certain design constraints in a given design domain. Fig.1.1 illustrates the typical topology optimization. Although the concept has been originated in mechanical design problems, it has been later been extended to a wide range of other physical disciplines, including fluids, acoustics, electromagnetism, optics, and their combinations [345]. One may find literature surveys from [75, 134, 457, 223], in which the recent advances and applications of topology optimization were summarized.

Although structures under real operating conditions are often subjected to dynamic loading, topology optimization in a dynamic context is much less studied than in a static context. It is clear that the dynamic topology optimization problems are more challenging than the static ones, and one of the reasons is the multiple forms of dynamic loads themselves. For example, for structures subjected to shock/impact loading, a time integration scheme should be considered and the dynamic analysis will be implemented for each time step, which is computationally costly for topology optimization and may be accompanied by strong nonlinearities and a large number of design constraints. When the structure is subjected

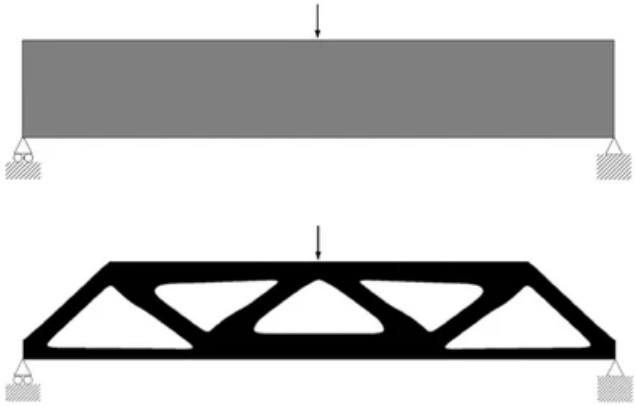

Fig. 1.1 Typical topology optimization [31]

to periodic loads or modal quantities are of interest (e.g., eigenfrequency optimization problems), calculations can be performed by steady-state analysis (i.e., in the frequency domain), which saves computational costs to a large extent, but also induces problems, such as the difficulty to obtain a clear 'solid-void' structural design [351] when the excitation frequencies are above the first resonance of the initial design.

The dynamical context makes topology optimization more complex, yet uncertainties prevalent in engineering, which could be triggered by manufacturing tolerances, loads, material properties, component tolerances and geometry [111], may exacerbate this phenomenon. On the one hand, the introduction of uncertainty implies a huge computational cost, which already exists in dynamic problems, even for steady-state analysis. For example, one might use the classical Monte Carlo Simulation (MCS) to evaluate the structural performances with uncertainties [35, 297], but the hundreds of thousands of samples of the MCS could adversely affect the speed of topology optimization iterations. On the other hand, the probabilistic model is frequently employed to describe the uncertainties in engineering (see, e.g. [298, 232]), but the probabilistic models require a large number of experimental samples to establish accurate probability distributions of uncertain parameters. Due to the difficulties and high costs of experiments, it is difficult to obtain the accurate probability distribution of the uncertain parameter. Even though alternative non-probabilistic methods exist (see e.g., the interval method [306, 266], fuzzy-set method [248] and convex method [236]) and hybrid model based methods (see [174] for literature review) for modeling the uncertainties whose complete stochastic profile cannot be confidently established, integrating practical uncertainties into topology optimization remains a challenge, especially for dynamic problems.

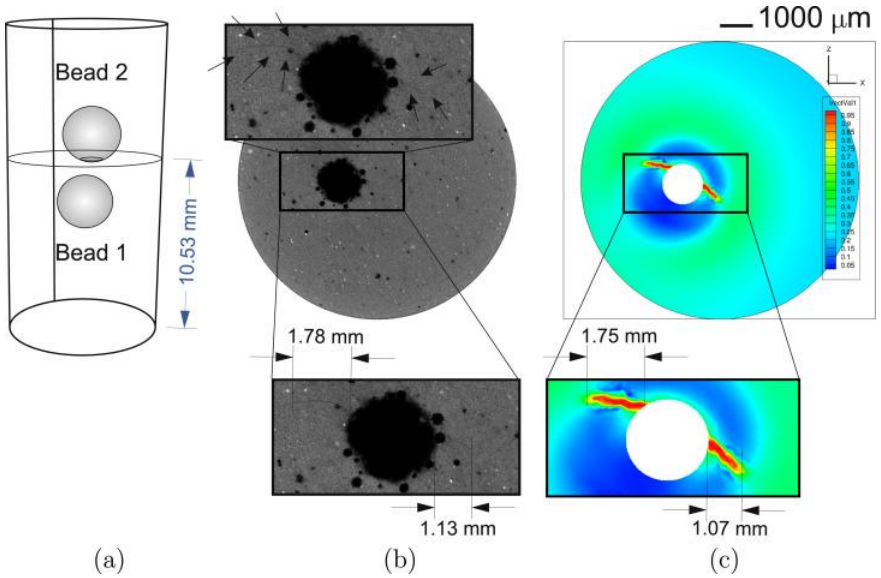

Fig. 1.2 Comparison of in situ testing-microCT experiments and phase field simulations on the cracking of a complex three-dimensional specimen made by heterogeneous quasi-brittle materials [275]: (a) position of crack; (b) experimental result and (c) simulation result.

Another issue seems to have been overlooked by the topology optimization community, namely the dynamic fracture phenomena. In contrast, crashworthiness (see [107] for a review) seems to have received more attention. One of the possible reasons for this is that traditional numerical methods for fracture propagation, such as the eXtended Finite Element Method (XFEM) [21, 267], are inherently highly complex and cannot be easily combined with topology optimization methods. In addition, the initiation and propagation of the cracks under dynamic impacts is also a very challenging topics [113]. The complex behaviors involved, such as initiation and branching, causes additional difficulties in the optimization problems, related to the huge computational cost of topology optimization superimposed with traditional numerical methods for dynamic fracture. More recently, the variational approach to fracture [112, 256] (also known as fracture phase field method, see [5] for a review) has shown to constitute a robust tool for complex fracture problems. The appropriate regularization process of the phase field method offers unique advantages to deal with initiation, propagation of multiple, complex, 3D cracks in possibly regular meshes, and also makes it easier to combine with topology optimization. Fig. 1.2 shows the direct comparison of the phase field simulation and in situ testing-microCT experiments on a complex three-dimensional specimen made by heterogeneous quasi-brittle materials, in which a fairly good agreement was observed in terms of both the length and direction of the cracks.

From the above perspectives, the motivations of this PhD thesis are listed as follows:

- Propose a normalization strategy for promoting the stability and convergence of the bi-directional evolutionary structural optimization (BESO) method and apply it to structural topology optimization for suppressing frequency response.
- Model the uncertainties by hybrid interval random method within robust topology optimization of structures, multi-scale structures and laminate plates in elastodynamics by efficient perturbation analysis.
- Introduce a non-probabilistic interval field to elastodynamics of structures subjected to periodic loading and achieve robust topology optimization.
- Develop a topology optimization framework incorporating the dynamic phase field method for designing structures with enhanced dynamic brittle fracture resistance.
- Extend the dynamic fracture involved topology optimization framework to design structures for impact work maximization.

The presented works are implemented through the bi-directional evolutionary structural optimization (BESO) method or solid isotropic material with penalization (SIMP) method, both of which are gradient-based topology optimization methods in a broad sense [345].

1.2 Literature review

1.2.1 Topology optimization frameworks

Topology optimization is often referred to as layout optimization [293, 192, 28, 327]. As early as the 19th century, Maxwell [251] performed a basic topological analysis for minimum weight truss structure with stress constraint. In 1904, Michell [255] proposed the so-called Michell's theory for analytically describing the conditions to be satisfied for the optimal truss of a loaded structure under stress constraints, which is widely regarded as a milestone in the study of structural topology optimization theory. In later times, some important developments in Michell's theory were made and several simple and practical optimal topological designs were worked out [145, 318, 326, 317, 36, 322, 319]. However, due to the difficulty of solving Michell's theory based problems, this approach has not been widely employed in practical engineering.

The landmark work done by Bendsøe and Kikuchi [33] in 1988 is recognized as the pioneer of the modern version of topology optimization research. In their work, within a

fixed grid finite element representation, the structure is composed by small individual cells and effective properties of the cells can be calculated by the homogenization method and then being optimized. This method is known as the homogenization-based method. The adoption of numerical solving procedures have allow topology optimization to solve practical engineering design problems.

1.2.1.1 SIMP approach

Shortly after the introduction of the homogenization based method, Bendsøe [26] and later others [451, 262] suggested the so-called SIMP approach to reduce the complexity of homogenization approach and improve the convergence to '0-1' solution [345]. In their work, the relation between design variables and material property is artificially interpolated by a power-law, for example, according to:

$$E(\vartheta) = \vartheta^p E_0, \tag{1.1}$$

where ϑ denotes the design variable, E_0 denotes the Young's modulus of the material composing the structure, $E(\vartheta)$ represents the design variable interpolated Young's modulus and p is the interpolation parameter. A too low or too high value of p can lead to larger gray zones or too quick convergence to local minima. In most case, the so-called "magic number" $p = 3$ is usually employed, for example, in [30], this value was confirmed to ensure the physical connection of the elements of the intermediate density, as shown in Fig. 1.3. But the value of p is non-unique and strongly depends on the physical considered problem, see e.g. [340, 42, 200]. It should be noted that there exist a few variations (e.g. [341, 459]) to the original SIMP interpolation scheme described in Eq. (1.1), and some alternative have been proposed, like the Rational Approximation of Material Properties (RAMP) model [358] and the SINH model [48].

To ensure well-posedness and mesh-independent solutions [346], as shown in Fig. 1.4, additional numerical treatments are necessary. The sensitivity filter was proposed [338] to modify element sensitivity values with the weighted averages of their neighbors within a mesh-independent radius $r_{\min}$. The filtered sensitivity value of an objective function $g(\vartheta)$ with respect to the design variable can be calculated by

$$\frac{\partial g(\vartheta)}{\partial \vartheta_e} = \frac{\sum_{i \in \mathcal{N}_e} \varpi_{ei} \frac{\partial g(\vartheta)}{\partial \vartheta_i}}{\sum_{i \in \mathcal{N}_e} \varpi_{ei}}, \tag{1.2}$$

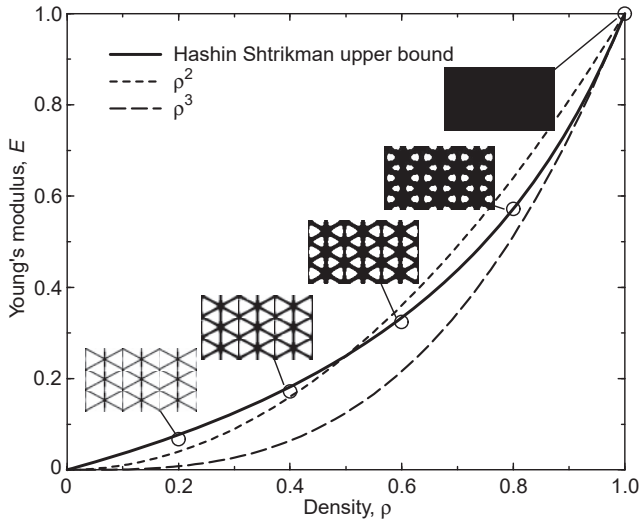

Fig. 1.3 A comparison of the SIMP model and the Hashin-Strikhman upper bound for an isotropic material with Poisson ratio 1/3 mixed with void [30].

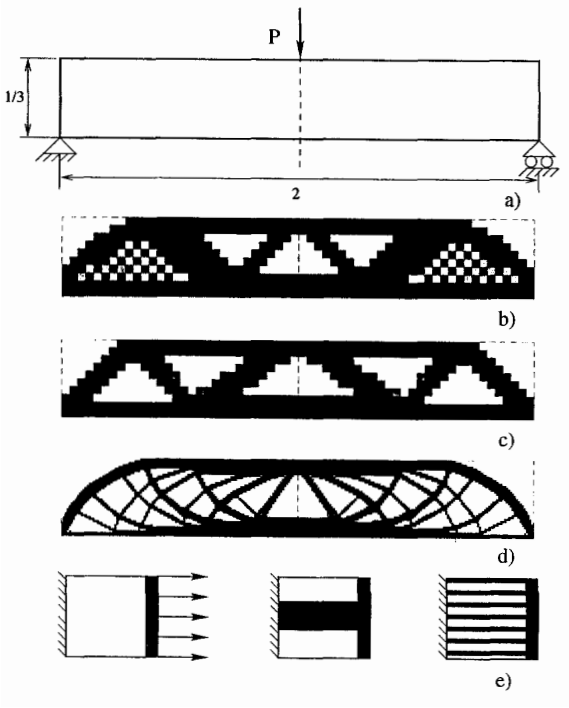

Fig. 1.4 Illustration of the mesh-dependency and checkerboard phenomenon [346]: (a) design problem; (b) checkerboard phenomenon; (c) solution for 600 element discretization; (d) solution for 5400 element discretization; (e) nonuniqueness example.

where $\mathscr{N}_e$ denotes the set of elements whose center-to-center distance r_{ei} to the e-th element is lower than the filter radius $r_{\min}$. ϖ_{ei} denotes the weighting factor, which, for example in a linear form, can be defined by $\varpi_{ei} = \max(0, r_{\min} - r_{ei})$.

Although the sensitivity filter technique seems to be heuristic, it was proved to be interpreted as an optimization problem based on a non-local elasticity approach in [344]. There have been alternative techniques proposed such as explicit constraints and penalty schemes in the form of gradient or perimeter constraints as well as regularized explicit penalization, see e.g. [138, 303, 41]. However, the sensitivity filter technique has been widely used in commercial and academic codes for a long time.

The density filter technique [49, 43] extends the idea of sensitivity filtering, with the difference that a physical density of the element is introduced and defined as a weighted average of the design variables in the neighborhood domain within radius $r_{\min}$, namely

$$\theta_e = \frac{\sum_{i \in \mathscr{N}_e} \varpi_e V_e \vartheta_e}{\sum_{i \in \mathscr{N}_e} \varpi_e V_e}, \tag{1.3}$$

where θ_e denotes the physical density and V_e denotes the elemental volume. The other symbols were defined in Eq. (1.2). The density θ_e was used here to replace the design variable in Eq. (1.1), thus in subsequent sensitivity analysis, the chain rule should be employed to build the relation between design variable and objective function.

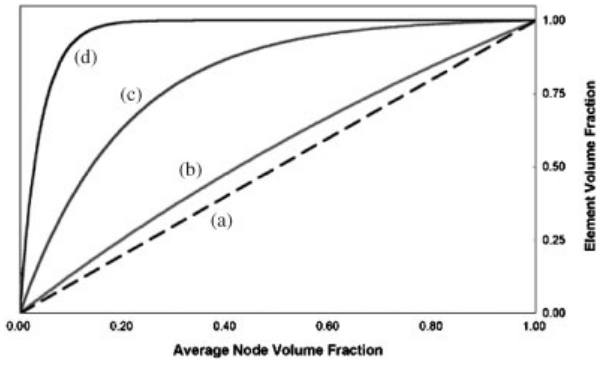

Fig. 1.5 The regularized Heaviside step function for regularization parameters: (a) $\eta = 0$ (linear); (b)$\eta = 1$; (c) $\eta = 5$; and (d) $\eta = 25$ [130].

Both sensitivity and density filters have the problem of generating grey transitions regions between solid and voids. More recently, projection schemes [130, 341, 413] were proposed for circumventing this problem. The original projection filter was proposed by Guest et al. [130] for prescribing minimum and maximum length-scales, in which a regularized Heaviside function was introduced as:

$$\varphi_e = 1 - e^{-\eta \theta_e} + \theta_e e^{-\eta}, \tag{1.4}$$

where φ_e denotes the pseudo-density of element e. η is a regularization parameter, which can be defined by 1 in the first iteration and doubled after specified time steps until it reaches a maximum value. θ_e denotes the physical density subject to the density filter definition. Fig. 1.5 depicts the regularized Heaviside step function for various regularization parameters. Similar to the use of density filter, the chain rule is also necessary for sensitivity analysis. For an objective function $g(\varphi)$ explicitly associated to the pseudo-density φ_e, its derivation to the design variable can be expressed by

$$\frac{\partial g(\varphi_e)}{\partial \vartheta_e} = \frac{\partial g}{\partial \varphi_e}\frac{\partial \varphi_e}{\partial \theta_e}\frac{\partial \theta_e}{\partial \vartheta_e}, \tag{1.5}$$

in which the derivations can be derived from the above equations.

Note that introducing power-law interpolation transforms the discretized topology optimization formulation to a continuous design variable gradient-based optimization problem. The SIMP approach can employ a very large number of optimization solvers. There are many well-proven gradient-based optimization approaches, like the Optimality Criteria (OC) methods [27, 339, 10] and the Method of Moving Asymptotes (MMA) [360].

To sum up, the SIMP approach is now mature after three decades of development, and it is almost the most widely known topology optimization method and an iconic approach [31]. In the field of mechanics, its effectiveness has been proved in many other aspects like nonlinear structural optimization [51, 301, 120, 50, 177, 425, 187, 193, 201, 238], stress-based optimization [98, 46, 200, 47, 148, 237, 377, 417] and dynamics-aimed optimization [302, 176, 90, 424, 202, 292, 439], to name a few, in addition to classical linear elastic compliance optimization problems. In multi-physics field problems, it also shows good capacities for, e.g., thermoelastic structures [348, 158, 116, 362, 76], fluid and flow problems [42, 122, 288, 1, 81, 83, 84], acoustic problems [139, 379, 95, 2, 203, 91] and optical problems [40, 371, 9, 166, 99].

1.2.1.2 BESO approach

The BESO approach is an extension of evolutionary structural optimization (ESO) method [409], which was firstly proposed by Xie and Steven [408] in the early 1990s. The main characteristic of the ESO type topology optimization is to gradually change the structural volume by removing the "low-efficiency" elements. In the original work [408], the von Mises stress of elements was compared with a prescribed critical value to determine if the element is low-efficient, and a rejection ratio was defined for determining the threshold for elemental removal. Following this proposition, other constraints such as stiffness [64], buckling load [246], frequency [407] and temperature [215] were achieved for topology optimization of

structures. However, this approach tends to yield in premature or erroneous removal of material from the structure, and leads to topologies that are not necessarily optimal, even if it is able to produce solutions that are much better than the initial guessed design in most cases [253, 213].

In [308], Querin et al. suggested an additive algorithm for ESO (AESO) and then [310] combined it with the conventional ESO method formed the early version of BESO. In their algorithm, a rejection ratio and an inclusion ratio were separately defined. Later in [309], they verified the optimality of their BESO method. From another aspect, Yang et al. [419] conducted a BESO topology optimization for stiffness optimization, in which the sensitivity number of the void elements was estimated by a linear extrapolation of the displacement. The addition and removal of elements were determined by the relative ranking of all element sensitivity numbers.

The theoretical rigor of early ESO/BESO methods was questioned [452, 323] because they were largely based on heuristic concepts. Rozvany and Querin [324, 325, 320, 321] hence proposed a sequential element rejection and admission (SERA) method to replace the void element with soft element in low Young's modulus value. Zhu et al. [455] suggested to replace the void element by an orthotropic cellular microstructure.

In [152, 155], Huang and Xie made three contributions to the modern version of the BESO method: (1) incorporating an artificial material interpolation scheme with penalization similar to SIMP approach; (2) adopting the filter scheme to make sure the existence of the solution, meanwhile avoid the checkerboard pattern; (3) proposing a sensitivity history-averaging scheme to stabilize the optimization procedure.

The penalized artificial material interpolation scheme of BESO can be expressed, for example with respect to Young's modulus, by:

$$E(\vartheta) = \vartheta^p E_0, \;\; \vartheta = \vartheta_{\min} \text{ or } 1, \tag{1.6}$$

from which, one can find common points to Eq. (1.1). However the difference of BESO's scheme is to use a total "solid-void" discrete design variable. In the above equation, $\vartheta_{\min}$ is artificially defined by a small value (e.g.,$\vartheta_{\min} = 10^{-3}$) to represent the void element.

Note that the checkerboard phenomenon and mesh-independency are also present in the BESO approach [214]. The filter scheme in the original proposition [152] was used for the evaluation of the nodal sensitivity numbers since the element sensitivity numbers were treated to be distributed on nodes. In the most cases, the sensitivity filter technique (see Eq. (1.2) is most frequently employed. In some recent literature [410, 114], it was reported that the density filter can also be adopted for dealing with the problems of strong nonlinearity, such as stress-based optimization.

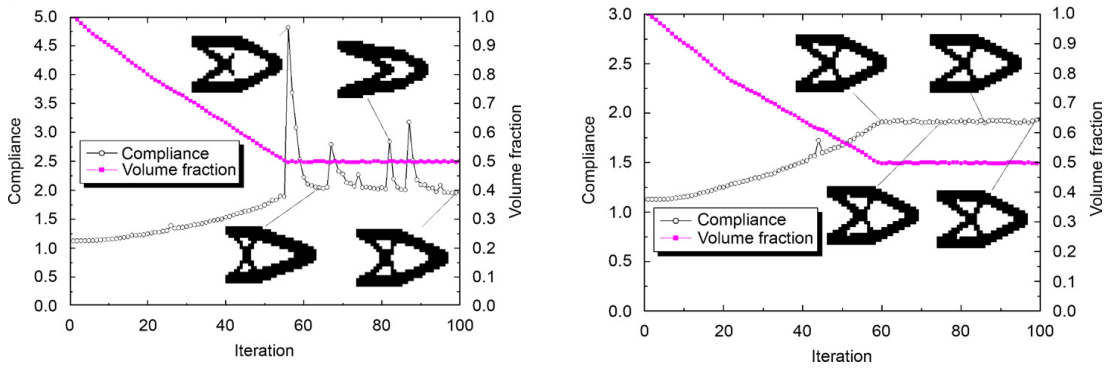

(a) (b)

Fig. 1.6 Comparison of evolutionary history: (a) without and (b) with history-averaging scheme [152].

The sensitivity history-averaging scheme modifies the sensitivity of the current iteration using the average sensitivity of the current iteration and the previous one, which can be formulated by:

$$\xi^l \leftarrow \left(\xi^l + \xi^{l-1}\right)/2, \text{ when } l \geq 2, \tag{1.7}$$

where ξ denotes the sensitivity number. The superscripts l and $l-1$ indicate the current and previous iterations, respectively. Fig. 1.6 compares the evolutionary history without and with history-averaging scheme. The history-averaging scheme efficiently stabilizes the design process and improves the convergence. It mitigates the chaotic behavior caused by the presence and absence of the sensitivity for discrete solid and void elements during the optimization procedure. In some recent studies [405, 106], this averaging scheme has been extended to the last three steps, for overcoming strong nonlinearities that existed in stress-based optimization problems.

Due to the penalized exponential interpolation of material properties by modern BESO, the sensitivity of the objective function to the design variables can be easily obtained by efficient derivation methods, e.g. the adjoint method [194, 61]. After ranking the relative value of the sensitivity number of the elements, the evolution of the structure can be conducted by the addition and removal of elements. The evolution of the volume can be expressed by:

$$V^l = \max\left\{V^*, V^{l-1}\left(1 \pm ER\right)\right\}, \tag{1.8}$$

where ER denotes the *EvolutionaryRatio* responsible for controlling the percentage of structural volume, that increases or decreases the volume of current iteration. V^* is a predefined allowable volume.

The convergence criterion for the structural evolution is defined by:

$$\delta_{err} = \frac{\left| \sum_{i=1}^{N} g(\vartheta)^{l-i+1} - \sum_{i=1}^{N} g(\vartheta)^{l-N-i+1} \right|}{\sum_{i=1}^{N} g(\vartheta)^{l-i+1}} \leq \bar{\delta}_{err}, \tag{1.9}$$

where $\bar{\delta}_{err}$ denotes the convergence threshold, N is a predefined integer, defined as 5 in most cases, used to determine the number of steps that need to be satisfied to determine convergence. The convergence usually occurs after the addition and removal of structural elements has reached the predetermined volume V^*.

The BESO approach is an important branch of topology optimization. We briefly reviewed the development of BESO from the most primitive ESO to the current generally popular version. One may refer to the monograph of BESO written by Huang and Xie [151] for more details of this approach, and refer to a comprehensive review raised by Xia et al. [404] for recent advances of the approach. We can list a series of literature in which the BESO approach has always been redefined for solving various problems, such as stiffness and natural frequency optimization [152, 156], periodic structure [153], multiple materials [155, 143], multiple constraints [154], to name a few. However, we should note that for the problems with severe variation on sensitivity numbers between the adjacent iterations, that is, the objective function and sensitivity are highly sensitive to the value of design variables, the current stabilizing scheme, such as the history averaging technique, might no longer be effective. Through lots of practice, it has been found that in this type of problem, there are often some iterative steps whose sensitivity value are much higher than other iterations. This phenomenon is caused by the sudden changes of structural response during the iterative progress. As shown in Fig. 1.7, the existence of such "dominating sensitivity" results into unreasonable topological design and unstable iterations. To our knowledge, this drawback explain why the BESO approach is still rarely applied to some particular problems with strong nonlinearity. In Chapter 2, we will address this issue and will propose a normalization scheme for overcoming such phenomenon, more specifically for the structural design of frequency response problems.

1.2.1.3 Other approaches

In addition to the three approaches mentioned above, many other types of efficient topology optimization approaches have emerged.

For example, the level-set method for topology optimization (LSM-TO) [295, 3, 389] implicitly defines the interface between material phases to describe the boundary using a

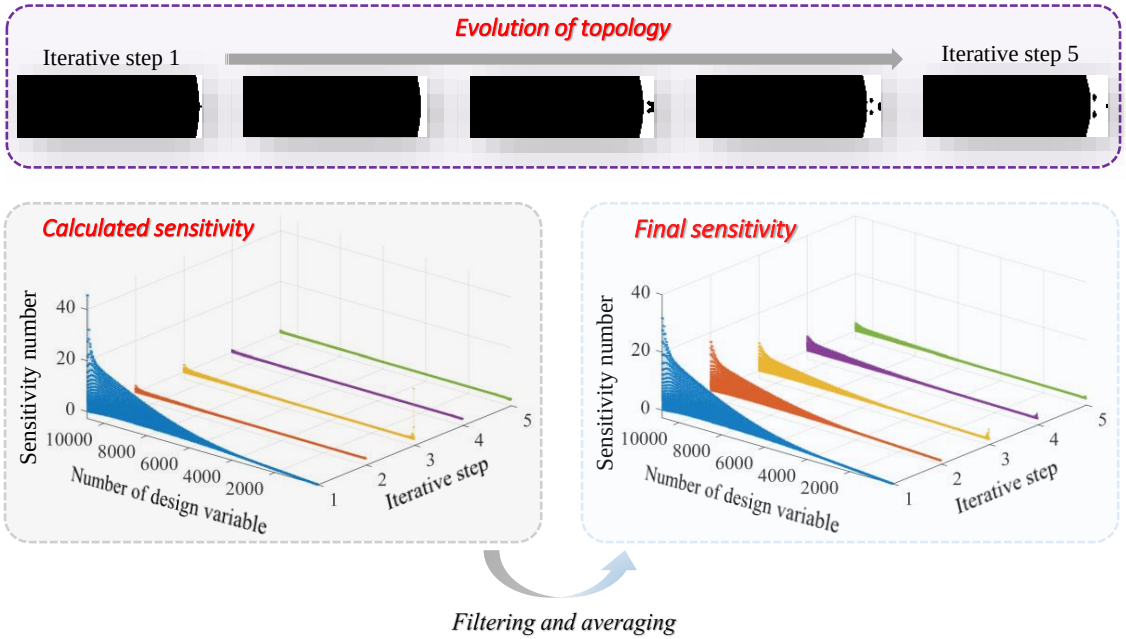

Fig. 1.7 Illustration of the "dominating sensitivity" phenomenon [449].

level-set function $\phi(\mathbf{x})$ as

$$\begin{cases} \phi(\mathbf{x}) > c, \mathbf{x} \in \Omega_s \\ \phi(\mathbf{x}) = c, \mathbf{x} \in \Gamma \\ \phi(\mathbf{x}) < c, \mathbf{x} \in \Omega_v, \end{cases} \tag{1.10}$$

where Ω denotes the design domain, which is composed by solid Ω_s and void Ω_v phases, Γ denotes the interface between the solid and void phases, c is a constant value and $\mathbf{x}$ denotes the positions situated in the design domain. The variation of the level-set function $\phi(\mathbf{x})$ determines different shape and topology of the structure. Due to its implicit boundary representation, the LSM-TO provides a natural description of geometric features and topological changes, and a series of methods have been developed, see e.g. [388, 4, 52, 393, 59, 392, 391]. However, the numerical implementation of LSM-TO is usually more complex than that of density-based methods. A literature survey on LSM-TO can be found in [374, 240].

Besides, several other explicit geometry-based topology optimization methods have been studied. In [454], a feature-driven topology optimization method with signed distance function was developed, in which the topology variation is achieved through feature layout and shape optimization and multiple engineering features of arbitrary shape are considered as the basic design primitives. In [433], freeform curves with closed B-splines were introduced as the basic design primitives to achieve topology optimization with a small number of design variables. In [285], the topology optimization of planar structures was transformed into an

optimization problem that distributes morphable bars with fixed width and semicircular ends. Guo et al. [136, 135] proposed a moving morphable component (MMC) approach to find the optimal structural topology by optimizing the shapes, lengths, thicknesses, orientations and layout (connectivity) of a set of morphable components that are used as building blocks for topology optimization. In these methods, the structural geometry is usually determined by the intersection of some geometric components and optimized by updating the parameters representing the layout and shape of these components.

Other heuristic topology optimization approaches have also been developed in the last decades. This type of methods includes Genetic Algorithms [390, 18, 460, 450], Artificial Immune Algorithms [233], Particle Swarms Algorithms [234], etc. Most of these methods are based on global search techniques and therefore feature gradient-free or only gradient-like information assisted. As a result, they are computationally expensive. Non-gradient topology optimization methods that reduce computational cost were recently reported in [131, 132]. Note that the BESO approach has also been considered a heuristic method for a long time, but its modern version is more accepted as a discrete density method due to the use of power-law parametrization and filtering techniques [345]. A critical discussion about the applicability of heuristic methodologies for topology optimization can be found in [343]. As it was pointed out in [343], heuristic methods show advantages in dealing with non-smooth, non-connected or multi-local-optima problems later, such as the design of phononic materials [87] and elastic metamaterials [88].

More recently, artificial intelligence (AI) assisted topology optimization attracted much attention [426, 287, 60, 133, 79]. In [355], a convolutional neural network (CNN) is employed to accelerate the numerical process of topology optimization by which the mapping was established from the intermediate results. Lei et al. [204] employed the supported vector regression (SVR) and K-nearest-neighbors (KNN) machine learning models to map the MMC-based topology optimization results for pursuing possible instantaneously designing. Chandrasekhar and Suresh [56] proposed a topology optimization framework that directly uses neural network (NN) activation functions and performs sensitivity analysis using a built-in backpropagation method. In [437], Zhang et al. provided a library and state-of-the-art review of the application of AI to topology optimization and conducted an in-depth exploration of the method that directly executes topology optimization using the neural network itself. It can be expected that the AI-assisted topology optimization approaches may allow significant progresses in TO approaches.

1.2.2 Topology optimization in dynamics

The operating environment of structures in engineering is often dynamic, such as wind-blown buildings and bridges, vehicles, wave-subjected dams, and operating machines. in engineering analysis or design, this dynamic behavior is usually artificially converted to static, leading to wasteful and extremely conservative solutions. In fact, this conversion is only valid if the load is slow enough to ignore inertial forces, while in other cases, direct consideration of dynamic performance is mandatory.

To account for the effects of dynamics in the topology optimization, the problems have been formulated either in the frequency domain or in the time domain.

1.2.2.1 In the frequency domain

The frequency domain based topology optimization methods has been applied to various design problems, in which the design of structures subjected to periodic loads are considered. The optimization problem is then defined as minimizing the global or local response of the structure under periodic loading (mostly based on harmonic excitation assumption). All other kinds of periodic excitation can be decomposed as a superposition of a set of harmonic excitation.

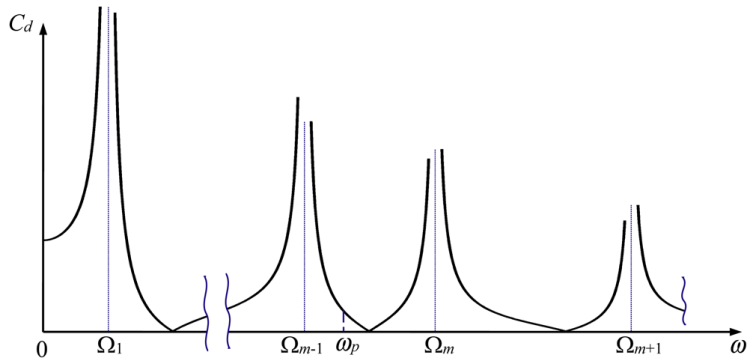

Fig. 1.8 Illustration of the *disjointed design sub-spaces* caused by complexity and non-convexity in dynamic compliance topology optimization [292].

The mean dynamic compliance is the mostly considered objective function for minimizing the structural global response, by which the structural dynamic stiffness is equivalent to be maximized. The literature on this topic is vast, see e.g. [243, 176, 290, 291, 418, 435, 220], presumably because of the similarity to the classical compliance optimization in static context. We should note that due to the presence of resonance phenomena and the multi-frequency problems in dynamic contexts, the dynamic compliance topology optimization is far more complex than the classical static one. In [292], Olhoff and Du proposed an ‘incremental

frequency technique' to overcome the *disjointed design sub-spaces*, which is illustrated by Fig. 1.8, present in dynamic compliance topological designs. As shown in Fig. 1.9, Silva et al. [351] observed that when dynamic compliance is adopted as the objective function, it is difficult to obtain a 'solid-void' design for the cases excitation frequencies higher than the first-order modal frequency of the optimized structure. In their subsequent work [352], they suggested the use of input power as an alternative objective function. Note that under the non-damping assumption, the input power is similar to dynamic compliance [176, 89, 453]. In [247], the sum of modal-compliances was suggested for efficiently treating multi-frequency topology optimization problems.

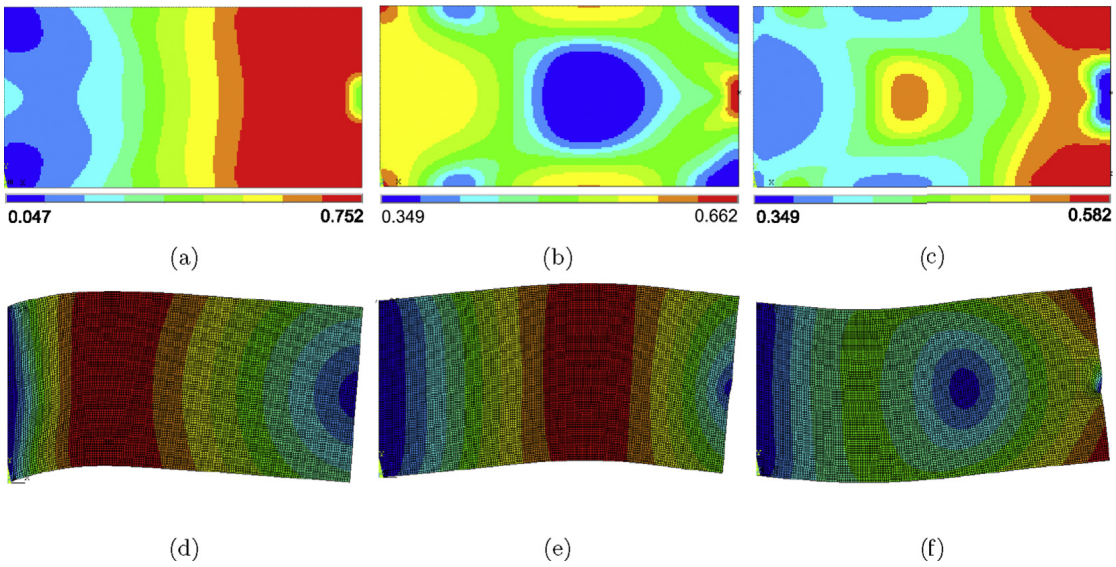

Fig. 1.9 Topological designs for minimal dynamic compliance for the cases, whose excitation frequencies are higher than the first-order modal frequency: (a) ω_f=180 Hz, (b) ω_f=600 Hz and (c) ω_f =750 Hz; (d), (e) and (f) represent the modulus of the real part of displacements for the respective layouts [351]

A relatively small number of studies [163, 423, 336, 179, 441] have focused on the topology optimization for location-specific responses reduction, in other words, local responses reduction. Tcherniak [364] maximized the steady-state frequency response at the specific point for a given excitation frequency. Liu et al. [222] made a comparative study on the dynamic analysis methods and suggested a modal acceleration method for the local dynamic responses reduction. We note that the BESO approach is rarely adopted for local frequency response problems. In [316], Rong et al. used the conventional ESO method to minimize the mass of structure with dynamic response constraints. In [378], a two-scale concurrent topology optimization approach was proposed in the BESO framework for minimizing structural local dynamic response. However, the highly localized features of the local objective

function bring difficulties for topology optimization, but is not limited to poor convergence and disjointed design sub-spaces.

Noted that the above mentioned global and local approaches in this category are much similar in solving structural dynamic response, in which there might be strong nonlinearity when the loading frequency gets close to the structural eigenfrequency. To the best of our knowledge, most studies have bypassed this problem: in their works, the excitation frequency tends to be far away from the eigenfrequency, so the optimization process generally remains linear and the topological designs stably optimized. It is foreseeable that when it comes to situations whose target frequencies are very close to the structural eigenfrequency, the existing methods may no longer be applicable [351].

For the second category, the maximization of fundamental eigenfrequency and higher order frequency have been extensively studied in topology optimization. Such topological designs are often used to improve the quality of free vibrating objects, such as increasing the fundamental frequency of buildings or bridges to reduce the chance of resonance, or changing the structure of automotive components, such as body-in-white, to improve the vibration and noise performance of automobiles. The topology optimization community has been working on this topic for three decades, see e.g. [82, 29, 196, 420, 302, 140, 244, 90, 157, 406, 305, 229, 359, 412, 216]. There are various optimization objectives in this topic, for example: maximizing the specific eigenfrequency [82, 242]; maximizing the band gap of adjacent eigenfrequencies [164]; obtaining eigenfrequencies close to desired frequencies [241]; imposed resonant peaks constraints to the resonant structure [77]. In [302, 157], alternative material interpolation schemes were studied for avoiding the artificial localized modes in low-density regions. In [191, 198], modal tracking techniques were developed for distinguishing the desired modes in varying topological structures correctly. In [11], a surrogate model was built for promoting computational efficiency, and then been extended to [108] with a strategy based on a multilevel discretization and iterative solvers. A recent comparative study on the reduced-order methods of such dynamic problems in topology optimization can be found in [212]. In [458], the forbidden frequency band was introduced as a constraint for eigenfrequencies.

In general, the implementation of topology optimization in the frequency domain focuses on the vibration and noise of the structure. Niu et al. [282] have made a comparative study on the selection of different objective functions in the frequency domain to minimize the response of vibrating structures. Besides, some studies have also focused on optimizing the damping material distribution of the structure [185, 190, 361, 230, 414, 415, 456, 349, 328, 284, 219] to achieve vibration reduction. The research on topology optimization in the frequency domain is fairly well studied, and in-depth research is still ongoing, with some results

extending to other areas, such as eigenvalue topology optimization, which formed one of the foundations for designing phononic crystals [347, 165, 421] and metamaterials [283, 217] by topology optimization.

1.2.2.2 In the time domain

The time domain method for dynamic topology optimization is formulated when the load is not cyclic. Even though the time-based scheme is more intuitive, it has been less implemented as compared to the frequency domain method. The reasons are related to computational costs, associated with time-integration schemes.

Nevertheless, a number of topology optimization methods were developed by the time domain method. Min et al. [261] minimized the time interval integrated structural dynamic compliance in the linear elastic regime. Shobeiri [335] recently extend this idea to the elastoplastic phase with material, geometric, and contact nonlinearities. Dahl et al. [71] developed a topology optimization method with time domain formulation for designing transient response of one-dimensional waveguides. Zhang and Kang [434] proposed a topology optimization method for piezoelectric structures to actively reduce the structural transient response. Nakshatrala and Tortorelli [272] developed a transient dynamic topology optimization framework and applied it to the impact mitigation. Behrou and Guest [20] presented a topology optimization framework subjected to dynamic loads, in which the total strain energy and the maximum of strain energy are respectively minimized. Zhao and Wang [439] developed an aggregation functional method for minimizing the maximal response of the structure in the time domain. Hooijkamp and Keulen [149] studied the modal reduction technique and adjoint sensitivity analysis for the topology optimization of linear transient thermomechanical structures. Zhao et al. [440] studied a two-scale concurrent topology optimization method for minimizing the dynamic response of the structure in time domain dynamic loads. Kristiansen et al. [195] extended the topology optimization to the transient impact problems with friction. In their work, the frictional impacts is taken into account to the structural optimization process. Ogawa and Yamada [286] proposed a finite deformation theory-based topology optimization method for reducing structural deformation, from which the the large deformations of the structure under arbitrary dynamic loads are allowed. More recently, a POLYTOP [363] based Matlab implementation of topology optimization subjected to dynamic loads was introduced in the educational paper by Giraldo-Londoño and Paulino [127].

An alternative scheme for solving topology optimization in the time domain is the equivalent static load method (ESLM) [63, 62]. In this method, the equivalent static load applied to the structure at each time step produces an effect equivalent to the displacement

field produced in the dynamic analysis. The equivalent static loads are then adopted for the optimization, while the rest of quantities were neglected for saving computational cost. The ESLM was firstly employed for optimizing the mean dynamic compliance in the original paper [62], and then in [161] extended to minimize the peak value in a time interval, and later to nonlinear structures [202]. Some other ingredients were also considered in the ESLM based topology optimization in time domain, such as the fatigue constrained problem [334], two-scale structures [411], dynamic reliability design [209] and crash loaded structure [17].

Most of the above-mentioned literature focuses on the optimization of the structural transient response or the resistance to external work, and the development of related techniques. Driven by the strong demand from the aircraft and vehicle industries, there is also a large part of research focusing on the topological design of structural crashworthiness [107] under time domain impact loading. The aim of this branch is to protect passengers withstanding crashes by managing and absorbing the forces when structures are subjected to severe impacts. In [252], crashworthiness was firstly introduced for topology optimization. Some methods, such as the Ground Structure Approaches (GSAs) [299, 300], the Hybrid Cellular Automata method (HCA) [270, 93, 430, 15] and the aforementioned ESLM [94, 73] were developed for crashworthiness design. The non-gradient [356, 110], heuristic [294] and surrogate model based [312] topology optimization methods were also proposed for this problem.

As a conclusion, topology optimization method in the time domain is still a challenging topic. For this reason, the dynamic fracture topology optimization design of structures under dynamic loading is still an open challenge. Even considering the stress optimization problem, only one very recent work [126] was reported.

1.2.3 Topology optimization with uncertainties

Uncertainty is widespread in practical engineering [111]. It has significant effects on the prediction of structural performance. For example, a slight disturbance of Poisson's ratio of incompressible rubber has a great influence on the band gap of ternary acoustic metamaterials [205]. Today, it is widely acknowledged that optimization methods should take into account the uncertainties of engineering systems [249].

1.2.3.1 Uncertainty modeling approaches

Uncertainties in engineering can be classified into two types according to their origins, namely the aleatory and epistemic uncertainties [146, 72].

The former type of uncertainty, also named objective or stochastic uncertainty, describes the intrinsic variability of a physical system or environment. Generally, we can use precise

probability distribution functions to describe such uncertain random variables or fields based on the probabilistic theory. Probabilistic methods were mostly adopted for addressing randomness in practical engineering (see, e.g. [12, 125, 357] for the detailed introduction). It uses probability distributions of uncertain parameters to enable the propagation analysis of uncertainties and to obtain statistical properties of the quantities of interest. However, the probabilistic methods requires a large number of measurements and high-quality experimental samples, which are fairly expensive ways, or assumed probabilistic distribution (often Gaussian), which puts demands on expert knowledge and hyperparameters estimation (such as the correlation length). For example, in uncertainty propagation analysis, material properties are often strongly assumed to be independent Gaussian distribution. These characteristics make the probabilistic methods sometimes difficult to be employed. In [162, 354], the principle of maximum entropy was employed for modeling the uncertainties. Some attempts used imprecise probability distributions for describing the uncertainties [197, 92, 19].

For uncertainties of subjective natures, that is, the epistemic uncertainty mentioned above, it is difficult to describe them in terms of probabilistic theory because of the extremely limited information about the physical system or environment. For this reason, the non-probabilistic methods were developed [265, 263], e.g. the interval model [306, 109, 167, 271], convex model [25, 168], evidence theory [429, 78] or fuzzy-set theory [428, 269], to name a few. These methods all ignore probabilistic information, and although they thus represent less information than is objectively available, such lack of information seems to be a natural fit for design problems, especially in the early stages. In [265], Moens and Vandepitte argued that to some extent, non-probabilistic methods can be considered as useful alternatives to existing probabilistic methods. In [23, 24], Ben-Haim and Elishakoff introduced a concept of non-probabilistic reliability based on the convex model, which further illustrated the importance of non-probabilistic modeling techniques.

However, we should note that the conventional non-probabilistic uncertainty models still have some limitations, namely the expensive computational cost due to dimension explosion and the difficulty in representing the spatial dependency and correlations. To this end, in [168], Jiang et al. proposed a correlation analysis technique for the non-probabilistic convex model. They later proposed a multidimensional parallelepiped model [173, 172, 279] to include the independent and dependent uncertain variables in a unified framework. In [381], Wang and Matthies extended this idea, by which the statistical characteristics of available samples can be directly employed for evaluating the marginal intervals and correlation coefficients of uncertain variables. Some other literature have focused on hybrid uncertainty models to include the probabilistic and non-probabilistic models simultaneously. The hybrid uncertainty models are twofold [174, 380]: a) parallel-type: for the multi-source uncertainty problems

that contain both probabilistic and non-probabilistic information, hybrid uncertainty models [235, 117, 386, 45, 395] were built to model uncertainty of different attributes separately; b) embedded-type: for the problems with significant probabilistic features, but the precise probability distribution is difficult to obtain, for example, the aforementioned imprecise probability problem, the hybrid uncertainty models [100, 373, 307, 169, 402, 85, 218, 382] were built to improve the ability of the probabilistic based model for coping with complex uncertainties in an unified framework.

Besides, the non-probabilistic field models were recently developed for addressing the limitations of conventional non-probabilistic models. In [264], the concept of interval field was firstly introduced to define spatial dependency by multiplying a linear combination of a series of independent interval factors with a set of deterministic basis functions. In [105], Faes and Moens proposed a explicit interval field by combining an Inverse Distance Weighting (IDW) interpolation method with a local weighting function. van Mierlo et al. [375] then extended this idea with a scaled IDW interpolation method by including an additional distance measure to emphasize the local effects. Callens et al. [53] used locally supported quartic splines to the weight function to guarantee the local effects. In [353], Sofi proposed a Karhunen-Loève (K-L) expansion based interval field model, which is analogy to the random field model, however, with some modifications. In [239, 431], Luo et al. proposed a non-probabilistic field model, in which the spatial correlation characteristic was modeled by a set of multi-ellipsoid convex model bounded non-probabilistic series expansion (NPSE) coefficients. Based on the convex model, Jiang et al. proposed interval field [280, 281] and interval process [170, 171, 206] models, in which the correlation between two spatial/temporal points were characterized by the relevant angle and ellipsoidal semi-axes of a convex model. More recently, Hu et al. [150] proposed a B-spline basis functions based interval field, by which the intuitive form of the interval properties, such as interval centre and interval radius, can be trivially obtained.

As can be seen, research on uncertainty modeling is vast and very active topic. A variety of uncertainty models are considered for topology optimization. For example, the random variable [129, 231, 97, 96, 225], random field [58, 367, 199, 438, 315, 80, 181, 16], interval model [396, 226, 448, 387], convex model [183, 184, 365], evidence theory [444, 387], fuzzy-set [422] and the hybrid model [57, 447, 445, 254, 385].

In this thesis, one objective is to combine uncertainties with topology optimization in frequency-domain dynamics applications. For the aleatory uncertainty, we will employ a hybrid interval random model to describe the probabilistic parameters with imprecise quantities, such as interval model based expectation and standard deviation. For the epistemic uncertainty, we considered the recently emerged interval field model to define the non-

probabilistic uncertainties without losing their spatial dependency. For the consideration of computational costs, efficient algorithms were prioritized, even if there is a small loss of precision.

1.2.3.2 Uncertainty, topology optimization and reliability

There are two widely accepted concepts for uncertainty related to reliability in engineering design, either making the design more reliable or more robust. This corresponds to reliability-based design optimization (RBDO) [102, 13] and robust design optimization (RDO) [370, 34, 86], respectively. The two concepts, which are also applicable to topology optimization, namely reliability-based topology optimization (RBTO) and robust topology optimization (RTO), have been extensively studied.

The RBTO was first introduced by Kharmanda and Olhoff [188], in which the failure probability was included in the topology optimization by a reliability index constraint. By adjusting the value of certain probability constraints, usually reliability index [102] or performance function [372], different topological designs can be obtained for satisfying different reliability requirements. Several methods [274, 159, 227, 38, 443, 296] were developed to evaluate the reliability of the design, among which the first-order reliability method (FORM) [250, 189, 178, 268, 350, 69, 181, 332, 254] was the most common and frequently adopted method. Note that the probability constraints, such as the failure probability, are clearly a probabilistic problem and intuitively a probabilistic modeling approach should be used to describe uncertainties. However, recently, non-probabilistic approaches have also been introduced to RBTO, named non-probabilistic reliability-based topology optimization (NRBTO) [236, 183, 384, 422, 446, 221], by mathematically defining non-probabilistic reliability index.

The RTO aims to reduce the variability of an associated output, which is often defined as the objective function with respect to uncertain parameters. Most RTO algorithms are mainly implemented in two ways, namely the worst-case approach, and the probabilistic approach. The worst-case approach focuses on optimizing the performance for the worst-case scenarios [74, 342, 8, 396, 224]. It is intuitive since the objective function can generally be evaluated by the anti-optimization problem [101]. Therefore, in some studies, this approach considered a min-max problem. While the probabilistic approach incorporated the statistical moments, for example, the expectation and variance, into the objective function. Some studies [129, 58, 97, 438] devote to optimize the expectation of the objective function (e.g. the compliance) under uncertainty, which is however, suffered some criticism with selected counter-examples [65]. An alternative is to take the variance into account as well, and thus the objective function is replaced with a linear weighting of the expectation and variance

[367, 199, 96, 57, 16]. Note that this treatment makes the problem becomes a multi-objective optimization problem, thus in [368], the physical consistency of this approach was discussed. Recently, RTO was introduced into the topology optimization of multi-scale structures [137, 55, 383, 447, 445, 175].

In [70], da Silva et al. made a comparative study of the RBTO and RTO in reliability uncertainties. It demonstrated that, when uncertainty is involved, both of RBTO and RTO resulted in reliable and/or robust designs, while the deterministic approach resulted in extremely unreliable solutions. Therefore, when implementing RBTO and RTO, more attention should be paid to efficient modeling techniques and computational cost control, which are the main challenges of topology optimization with uncertainty as mentioned by Maute in [249].

1.2.4 Topology optimization for fracture resistance

Recently, an exciting new branch of topology optimization has emerged to enhance the mechanical resistance to damage or cracks in structures and materials. The pioneering work on this topic might be traced back to Challis et al. [54], in which a LSM-TO was proposed to maximize the structural fracture resistance. In [182], Kang et al. used a J-integral approach to predict crack opening at predefined locations. In [6, 7], non-local damage field was considered for the first time in topology optimization to obtain the optimal mechanical resistance design of concrete structures and their reinforcement. Similarly, Kato and Ramm [186] investigated fiber-reinforced composites considering a damage model, in which the layout of the multi-phase materials was optimized. James and Waisman [160] developed a non-local damage topology optimization coupled algorithm for failure reduction, in which the maximal damage was constrained, similarly to what is usually done in stress-constrained problems. In [207, 208], Li et al. investigated topology optimization methods involving stored energy while constraining the elastoplastic-damage. More recently, Russ and Waisman [331] proposed a method for the structural resistance of both ductile failure and buckling in a new aggregated optimization objective with local ductile failure constraints. Liu et al. [228] investigated multi-material fracture resistance topology optimization including cohesive models.

Note that the above mentioned studies do not include a complete damage or crack evolution involving the whole loading history. In [436], Zhang et al. firstly included a full crack propagation analysis within topology optimization for fracture resistance designs, using the X-FEM [22, 267] method. However, the complexity of XFEM for dealing with initiation and complex cracks configurations strongly restricts its use within topology optimization analysis. In [403], Xia et al. combined for the first time topology optimization with fracture

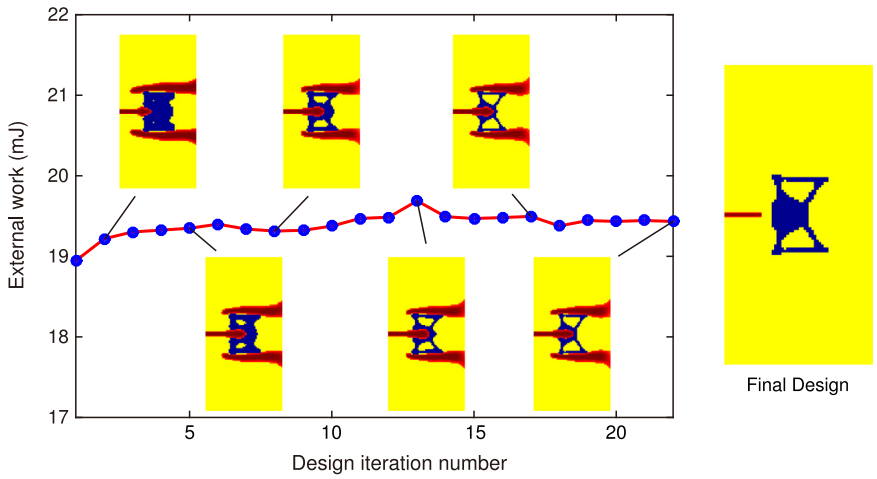

Fig. 1.10 Iterations of topology optimization for maximizing fracture resistance with corresponding final fracture pattern [403].

phase field analysis to maximize the resistance of composite structures, as shown in Fig. 1.10. The variational phase field approach to fracture [112, 44, 256, 259, 5, 277] has unique advantages to deal with initiation, propagation of multiple, complex, 3D cracks in possibly regular meshes due to an appropriate regularization process, and is highly compatible with topology optimization analysis. Da et al. [68, 67, 66] extended this work to consider fracture resistance enhancement in composite by considering both interfacial and bulk fracture. More specifically, the approaches developed in these works considered a full fracture initiation and propagation within the structure until failure and combined the phase field method with BESO. Li et al. [210] extended Xia et al.'s work to the SIMP approach and provided a comprehensive comparison of the BESO and SIMP methods for composite design to brittle fracture resistance. Russ and Waisman [329, 330] proposed two different topology optimization frameworks for the brittle fracture resistance involving one-phase structure material, combining phase field and topology optimization. In their work, the optimization problem was defined as minimizing the total volume or volume and fracture energy while ensuring fracture energy or energy dissipation constraints. Wu et al. [394] developed a LSM-TO based topology optimization for the brittle fracture resistance of two-phase composite materials.

Taking into account dynamics in the fracture process is of extreme importance for resistance of structures to impacts. When dynamics are involved, the cracks can interact with wave propagation and the final crack patterns depend on the energy of the impactor. In addition, dynamics can lead to more complex crack configurations such as crack branching or

initiation of cracks within the solid. In [260], Miller et al. analyzed the relationship between energy dissipation and crack paths instabilities in dynamic fracture of brittle materials.

The phase field method has been extended to dynamic problems in Borden et al. [39], Hofacker and Miehe [147], and many extensions and applications have been proposed (see e.g. [37, 278, 314, 121, 366, 311]).

In this thesis, topology optimization analysis for dynamic fracture resistance of structures will be investigated. As compared to available existing works, the presented framework involves the following new contributions: (a) dynamic phase field simulations to fracture is combined with topology optimization for minimizing the fracture energy or maximizing the external work of a structure; (b) semi-analytical sensitivities required in the topology optimization analysis in a dynamic fracture analysis context are provided; (c) comparisons of the obtained fracture resistance (reduction in the fracture energy or promotion in the external work) as compared to a static topology optimization designs are discussed.

1.3 Outline of the thesis

The content of this thesis is organized as follow:

In Chapter 2, we propose a normalization strategy for the BESO approach to improve numerical stability and convergence and apply it to the topology optimization of the structural frequency response problem. In Chapter 3, we incorporate uncertainties into topology optimization of structures, laminates and multi-scale structures by means of the probabilistic RTO approach. In Chapter 4, we introduce an emerging non-probabilistic interval field model for topology optimization, which is implemented using a worst-case RTO approach. In Chapter 5, we formulate a novel dynamic fracture resistance framework by combining the fracture phase-field method and topology optimization in the dynamic context, in which the fracture energy is minimized. In Chapter 6, we extend the dynamic fracture resistance framework to maximize the strength of a structure with respect to the external work. In Chapter 7, final conclusions and perspectives are drawn.

Chapter 2

A normalization strategy for BESO based structural optimization and its application to frequency response problem

The main content of this chapter has been adapted from our published paper [449].

2.1 Introduction

In this chapter, we propose a simple but efficient normalization strategy for the BESO based topology optimization. By normalizing the sensitivity of different iterations to the same order, the possible numerical instabilities caused by nonlinear iterations can be overcome. Considering that only the relative ranking of the elemental sensitivity has influence on the material adding/removal, such normalization strategy will not affect the updating of the current iteration. By employing a normalization strategy, the topology optimization for frequency response problem with respect to local frequency response is firstly implemented in the BESO framework through the normalization based-BESO (NBESO) algorithm. As an extension, the normalized weight sum (NWS) method is established for the multi-frequency problem in NBESO, by which the multi-frequency problem can be solved without interference from the frequency response amplitudes.

2.2 Topology optimization formulation

2.2.1 Equilibrium equation

The forced vibration equation without damping can be stated as

$$\boldsymbol{M}\ddot{\boldsymbol{U}}_t + \boldsymbol{K}\boldsymbol{U}_t = \boldsymbol{F}_t, \tag{2.1}$$

where $\boldsymbol{M}$ and $\boldsymbol{K}$ represent the global mass matrix and stiffness matrix, respectively; $\boldsymbol{F}_t$ denotes the loading vector of the external excitation related to time t. In a given excitation angular frequency ω_i, the loading vector can be expressed by

$$\boldsymbol{F}_t = \boldsymbol{F}e^{j\omega_i t}, \tag{2.2}$$

where $\boldsymbol{F}$ denotes the vector of the amplitude of harmonic external excitation and $j=\sqrt{-1}$. Thus, the vectors of structural displacement and acceleration responses can be expressed by

$$\boldsymbol{U}_t = \boldsymbol{U}e^{j\omega_i t}, \tag{2.3}$$

$$\ddot{\boldsymbol{U}}_t = -\omega_i^2 \boldsymbol{U}e^{j\omega_i t}, \tag{2.4}$$

where $\boldsymbol{U}$ denotes the vector of amplitude of displacement response.

Substituting Eqs. (2.2)-(2.4) to Eq. (2.1), yields

$$\left(\boldsymbol{K} - \omega_i^2 \boldsymbol{M}\right)\boldsymbol{U} \equiv \boldsymbol{K}_{\mathrm{d}}\boldsymbol{U} = \boldsymbol{F}, \tag{2.5}$$

which provides the structural equilibrium equation in the steady-state at angular frequency ω_i. It is noted that when the excitation frequency is zero, Eq. (2.5) corresponds to the equilibrium equation in static condition.

2.2.2 Material interpolation scheme

To avoid the artificial localized vibration modals in dynamic conditions, the material interpolation scheme proposed by Huang et al. [156] is adopted, which can be expressed by

$$\rho\left(x_e\right) = x_e \rho^0, \tag{2.6}$$

$$E\left(x_e\right) = \left[\frac{x_{\min} - x_{\min}^p}{1 - x_{\min}^p}\left(1 - x_e^p\right) + x_e^p\right] E^0, \tag{2.7}$$

where ρ^0 and E^0 denote the density and Young's modulus of the solid material, respectively; p denotes the penalty factor; $x_{\min}$ is a small value (e.g. 10^{-3}) of design variable to avoid singularity. By adopting the interpolation scheme, the partial derivative of elemental mass and stiffness matrices with respect to design variable can be directly obtained by

$$\frac{\partial \boldsymbol{M}_e}{\partial x_e} = \boldsymbol{M}_e^0, \tag{2.8}$$

$$\frac{\partial \boldsymbol{K}_e}{\partial x_e} = \frac{1-x_{\min}}{1-x_{\min}^p} p x_e^{p-1} \boldsymbol{K}_e^0, \tag{2.9}$$

where $\boldsymbol{M}_e^0$ and $\boldsymbol{K}_e^0$ are the solid mass and stiffness matrix, respectively.

2.2.3 Topology optimization for minimal local frequency response

2.2.3.1 Problem statement

The topology optimization formulation for minimal local frequency responses can be mathematically formulated by

$$\begin{aligned} \min_{x_e,\, e=1,\ldots,N_E} : \quad & \gamma = \sum_{n=1}^{m} U_n^2, \\ \text{s. t.} : \quad & \boldsymbol{K}_d \boldsymbol{U} = \boldsymbol{F}, \\ & \sum_{e=1}^{N_E} x_e V_e - \chi V_0 \leq 0, \\ \text{where} : \quad & x_e = x_{\min} \text{ or } 1, \end{aligned} \tag{2.10}$$

where x_e denotes the e-th design variable; N_E represents the number of the design variables; $x_{\min}$ and 1 are the value of void and solid design variables, respectively; χ, V_0 and V_e are the target volume fraction, design domain volume and elemental volume (area for 2D case); γ denotes objective function, which is the quadratic sum of structural displacement responses U_n at interested freedom-of-degrees (DOFs). The subscript n is the serial number of the target DOF and m represents the amount of the target DOFs.

2.2.3.2 Sensitivity analysis

The derivation of the objective function with respect to the design variables can be expressed by

$$\frac{\partial \gamma}{\partial x_e} = \sum_{n=1}^{m} \frac{\partial U_n^2}{\partial x_e} = 2 \sum_{n=1}^{m} U_n \frac{\partial U_n}{\partial x_e}. \tag{2.11}$$

To obtain $\frac{\partial U_n}{\partial x_e}$, we introduce a load vector $\boldsymbol{L}$ to determine the response of interest. Without loss of generality, $\boldsymbol{L}_n$ is adopted to represent the load vector for n-th target DOF, which can be expressed by

$$\boldsymbol{L}_n = \left(\underbrace{0,0,...,0,\overbrace{1}^{ns},0,...,0}_{nd} \right), \tag{2.12}$$

where nd denotes the number of DOFs, ns is the series number of the n-th target DOF. Thus, $\frac{\partial U_n}{\partial x_e}$ can be presented by

$$\frac{\partial U_n}{\partial x_e} = \boldsymbol{L}_n^T \frac{\partial \boldsymbol{U}}{\partial x_e}, \tag{2.13}$$

where $\frac{\partial \boldsymbol{U}}{\partial x_e}$ can be derived from Eq. (2.5) by the chain rule in assuming a design variable independent external load $\boldsymbol{F}$ as

$$\frac{\partial \boldsymbol{U}}{\partial x_e} = -{\boldsymbol{K}_{\mathrm{d}}}^{-1} \frac{\partial \boldsymbol{K}_{\mathrm{d}}}{\partial x_e} \boldsymbol{U}. \tag{2.14}$$

For the sake of simplicity, we introduce an adjoint vector $\boldsymbol{\Lambda}_n$ that satisfies the following equation

$$\boldsymbol{L}_n^T - \boldsymbol{\Lambda}_n^T \boldsymbol{K}_{\mathrm{d}} = 0. \tag{2.15}$$

Substituting Eqs. (2.13)-(2.15) into Eq. (2.11), yields

$$\frac{\partial \gamma}{\partial x_e} = -2 \sum_{n=1}^{m} U_n \boldsymbol{\Lambda}_n^T \left(\frac{\partial \boldsymbol{K}}{\partial x_e} - \omega_p^2 \frac{\partial \boldsymbol{M}}{\partial x_e} \right) \boldsymbol{U}, \tag{2.16}$$

where $\frac{\partial \boldsymbol{K}}{\partial x_e}$ and $\frac{\partial \boldsymbol{M}}{\partial x_e}$ can be assembled from Eqs. (2.8) and (2.9).

In the BESO framework, the derived sensitivity should be treated as follows

$$d_e^{\mathrm{f}} = -\frac{1}{p} \frac{\partial \gamma}{\partial x_e} = 2 \sum_{n=1}^{m} U_n \boldsymbol{\Lambda}_n^T \left(\frac{1 - x_{\min}}{1 - x_{\min}^p} x_e^{p-1} \boldsymbol{K}_e^0 - \frac{\omega_p^2}{p} \boldsymbol{M}_e^0 \right) \boldsymbol{U}_e, \tag{2.17}$$

where d_e^{f} denotes the elemental sensitivity number with respect to the structural local dynamic responses.

2.2.4 Topology optimization for minimal static compliance

2.2.4.1 Problem statement

In the topology optimization for frequency response problem, the structural static compliance is usually adopted as a constraint [351, 220] or part of objective [351] to avoid the possible

early convergence, which leads to failed designs in static case. In this paper, we employs the structural static compliance as one of the multi-objective. The minimum compliance design problem in the BESO framework can be formulated by

$$\begin{aligned} \min_{x_e, e=1,\ldots,N_E} : \quad & C = \boldsymbol{F}^T \boldsymbol{U}, \\ \text{s. t.} : \quad & \boldsymbol{K}\boldsymbol{U} = \boldsymbol{F}, \\ & \sum_{e=1}^{N_E} x_e V_e - \chi V_0 \leq 0, \\ \text{where} : \quad & x_e = x_{\min} \text{ or } 1, \end{aligned} \tag{2.18}$$

where C denotes the static compliance of structure. The definition of the remaining symbols in Eq. (2.18) are the same as Eq. (2.10).

2.2.4.2 Sensitivity analysis

The derivation of C in Eq. (2.18) with respect to the design variable x_e can be obtained by the adjoint method [369] as follows

$$\frac{\partial C}{\partial x_e} = -\frac{1}{2}\boldsymbol{U}^T \frac{\partial \boldsymbol{K}}{\partial x_e}\boldsymbol{U}. \tag{2.19}$$

Thus, the sensitivity number d_e^{c} of e-th element with respect to structural compliance can be derived

$$d_e^{\mathrm{c}} = -\frac{1}{p}\frac{\partial C}{\partial x_e} = \frac{1}{2}\boldsymbol{U}_e^T \left(\frac{1 - x_{\min}}{1 - x_{\min}^p} x_e^{p-1} \boldsymbol{K}_e^0 \right) \boldsymbol{U}_e. \tag{2.20}$$

2.3 The normalization strategy for BESO

2.3.1 Normalization strategy

Normalization is often adopted to process widely varying data aiming to improve the convergence. Here we introduce the Min-Max scaling method to normalize the range of independent variables as

$$\mathscr{N}(\boldsymbol{X}) = \frac{\boldsymbol{X} - X_{\min}}{X_{\max} - X_{\min}}, \tag{2.21}$$

where $\boldsymbol{X}$ denotes the vector of the initial values, and its maximum and minimum value can be presented by $X_{\max}$ and $X_{\min}$; $\mathscr{N}(\boldsymbol{X})$ denotes the normalized vector $\boldsymbol{X}$, whose values are distributed in a interval of [0, 1]. It is necessary to make a further discussion on the normalization. On the one hand, it is well known that in the BESO framework, the iteration is only related to the relative ranking of the sensitivities. Therefore, the use of

normalization strategy at each step will not affect the updating of design variables in linear situations. On the other hand, a history-averaging technique is usually adopted to deal with inaccurate assessment of sensitivity numbers [152] for stable convergence in the current BESO framework. However, when the problem is highly sensitive to the change of design variables, the history-averaging technique would be inefficient because of the great differences between the adjacent iterative steps. In this situation, doing normalization before using the history-averaging technique can reduce the possible numerical difficulties brought by the nonlinearity. It will be demonstrated to be very effective in this work for the problems whose working frequency is very close to the structural eigenfrequency so that a small variation of the topological design could cause an extreme change in the overall structural response, which is a problem that the classical BESO method cannot deal with. By introducing the normalization strategy to deal with sensitivity, this problem can be solved to a certain extent.

2.3.2 Normalized weight sum method

For the problems involving a series of similar sub-objectives, the weight sum method is the most frequently employed approach. The typical weight sum method can be formulated as follows

$$\psi = \sum_{i=1}^{k} \lambda_i f_i(\boldsymbol{x}), \tag{2.22}$$

where ψ denotes the weight summed objective function; $f_i(\boldsymbol{x})$ denotes the sub-objective with respect to variable vector $\boldsymbol{x}$; λ_i represents the corresponding weight coefficient, in which the subscript i is the serial number of sub-object.

In the topology optimization for frequency response problem, it is often used to deal with multi-frequency problems, refer to [351, 220, 144, 290, 442]. It should be noted that in the multi-frequency problems, although the optimization target is selected to minimize the quadratic sum of responses at all frequencies, the ideal optimization results usually make the whole target frequency band far away from the structural eigenfrequency. This indicates that the relative value of the sensitivity numbers of sub-object caused by changes in response with respect to design variables is not so important, high local sensitivity numbers at some frequencies should be suppressed for better overall performance. Thus the normalization strategy can be adopted again by combining with the weight sum method for integrating the multi-objectives, yielding the normalized weight sum method to estimate the sensitivity numbers for multi-objectives as

$$\boldsymbol{\Psi} = \sum_{i=1}^{k} \lambda_i \mathscr{N}(\boldsymbol{d}_i), \tag{2.23}$$

where $\boldsymbol{\Psi}$ denotes the sensitivity number column of the multi-objectives processed by the normalized weight sum method; λ_i is the weight coefficient; $\mathscr{N}(\boldsymbol{d}_i)$ denotes the normalized sensitivity, which can be obtained by Eq. (2.21).

2.3.3 NBESO method for frequency response problem

2.3.3.1 Problem statement

Here we describe the NBESO method for the structural frequency response problem with respect to single-frequency and multi-frequency problem, respectively. It should be noted that, when the target frequency (or frequencies for multi-frequency problem) is higher than the structural eigenfrequency, it is necessary to introduce a constraint or objective [351, 220] to ensure the structural static performance, in other words, to avoid the appearance of "disintegration" phenomenon [292]. In this work, we employed the structural compliance as mentioned earlier with a accompanied weighting coefficient α to control the structural static performance.

- Single-frequency

Based on the formulations shown in Eq. (2.10), this problem can be mathematically expressed by

$$\begin{aligned} \min_{x_e,\, e=1,\ldots,N_E} : \quad & \eta = \alpha C + (1-\alpha) \sum_{n=1}^{m} (U_n)^2, \\ \text{s. t.} : \quad & \left(\boldsymbol{K} - \omega^2 \boldsymbol{M}\right) \boldsymbol{U} = \boldsymbol{F}, \\ & \sum_{e=1}^{N_E} x_e V_e - \chi V_0 \leq 0, \\ \text{where} : \quad & x_e = x_{\min} \text{ or } 1, \\ & 0 \leq \alpha < 1, \end{aligned} \tag{2.24}$$

where η denotes the objective function, which is the linear combination of the structural static and dynamic performance; α denotes the weighting coefficient for adjusting the weighting of static performance. When the frequencies are lower than the structural eigenfrequency, α is unnecessary and can be defined by 0. In other cases, a reasonable definition of α affect the of the topological design of structure and guarantees its static performance. The larger value of α means weighting on the structural static performance.

The sensitivity number of η can be composed by the normalized weight sum method as

$$\boldsymbol{\xi} = \alpha \mathscr{N}(\boldsymbol{d}^{\mathrm{c}}) + (1-\alpha) \mathscr{N}\left(\boldsymbol{d}^{\mathrm{f}}\right), \tag{2.25}$$

where $\mathscr{N}\left(\boldsymbol{d}^{\mathrm{f}}\right)$ and $\mathscr{N}\left(\boldsymbol{d}^{\mathrm{c}}\right)$ can be calculated by substituting Eqs. (2.17) and (2.20) into (2.21), respectively.

- Multi-frequency

By using the proposed normalized weight sum method, this problem can be stated by

$$\begin{aligned} \min_{x_e,\, e=1,\ldots,N_E} : \quad & \eta = \alpha C + (1-\alpha) \sum_{i=1}^{k} \sum_{n=1}^{m} \lambda_i \left(U_n\right)_i^2, \\ \text{s. t. :} \quad & \left(\boldsymbol{K} - \omega_i^2 \boldsymbol{M}\right) \boldsymbol{U}_i = \boldsymbol{F}, \\ & \sum_{e=1}^{N_E} x_e V_e - \chi V_0 \leq 0, \\ \text{where :} \quad & x_e = x_{\min} \; or \; 1, \\ & \sum_{i=1}^{k} \lambda_i = 1, \\ & 0 \leq \alpha < 1, \end{aligned} \tag{2.26}$$

where λ_i denotes the weighting coefficient of the i-th ($i = 1, 2, ..., k$) discrete frequency ω_i. The superscript of U_n and $\boldsymbol{U}$ denotes the local frequency responses and overall displacement response under the i-th frequency, respectively.

The sensitivity number in this case can be expressed by

$$\boldsymbol{\xi} = \alpha \mathscr{N}\left(\boldsymbol{d}^{\mathrm{c}}\right) + (1-\alpha) \mathscr{N}\left(\sum_{i=1}^{k} \lambda_i \mathscr{N}\left(\boldsymbol{d}^{\mathrm{f}}\right)_i\right), \tag{2.27}$$

where $\mathscr{N}\left(\boldsymbol{d}^{\mathrm{f}}\right)_i$ denotes the normalized sensitivity vector in the i-th frequency, which can be derived from Eqs. (2.17) and (2.21).

2.3.3.2 Numerical implementation

The numerical implementation of the proposed NBESO method can be summarized as follows:

Step 1: Define the FE mesh, design domain and boundary conditions.

Step 2: Initialize the NBESO parameters, including the static weighting factor α, initial design variables $\boldsymbol{x}^{ini}$, target volume fraction χ, evolutionary ratio ER, filter radius $r_{\min}$, penalty parameter p, convergence tolerance τ and so on.

Step 3: Input the target frequency (single-frequency) or frequency range (multi-frequency). For the first case, the frequency can be directly input. As for the second case, the

frequency range should be discrete by frequency points ω_i and assigned corresponding weighting factors λ_i.

Step 4: Conduct the finite element analysis for calculating the structural compliance C, eigenfrequency ω_{ref} and dynamic displacement responses U_i in different frequencies ω_i.

Step 5: Calculate the sensitivity numbers of structural static compliance $\boldsymbol{d}^{\mathrm{c}}$ and local frequency response $\boldsymbol{d}^{\mathrm{f}}$ (single-frequency) or $\left(\boldsymbol{d}^{\mathrm{f}}\right)_i$ (multi-frequency) by Eqs. (2.17) and (2.20), respectively.

Step 6: Employ the normalization strategy in different conditions:

- For single-frequency case, adopt Eq. (2.25).
- For multi-frequency case, adopt Eq. (2.27).

Step 7: Use the filter scheme and history-averaging [152] to avoid numerical instabilities. The filter scheme can be expressed by

$$\overline{\xi_e} = \frac{\sum_{q=1}^{K} W\left(r_{eq}\right) \xi_q}{\sum_{q=1}^{K} W\left(r_{eq}\right)}, \tag{2.28}$$

where K denotes the total number of elements in sub-domain Ω_e. It is generated by drawing a circle of radius $r_{\min}$ from the center of element e; ξ_q denotes the sensitivity number of element q, which is calculated by the previous step; $W\left(r_{eq}\right)$ is the linear weight factor, which can be calculated by

$$W\left(r_{eq}\right) = \begin{cases} r_{\min} - r_{eq} & \text{for } r_{eq} < r_{\min}, \\ 0 & \text{for } r_{eq} \geq r_{\min}, \end{cases} \tag{2.29}$$

where r_{eq} represents the distance between the center element e and target element q. Thus, the filtered sensitivity number $\overline{\xi_e}$ can be obtained.

The history-averaging of the sensitivity number is also adopted for numerical stability, which can be expressed as below

$$\overline{\xi_e} = \frac{\overline{\xi_e^{l}} + \overline{\xi_e^{l-1}}}{2}, \ \textit{when } l \geq 2, \tag{2.30}$$

where l denotes the serial number of current iteration.

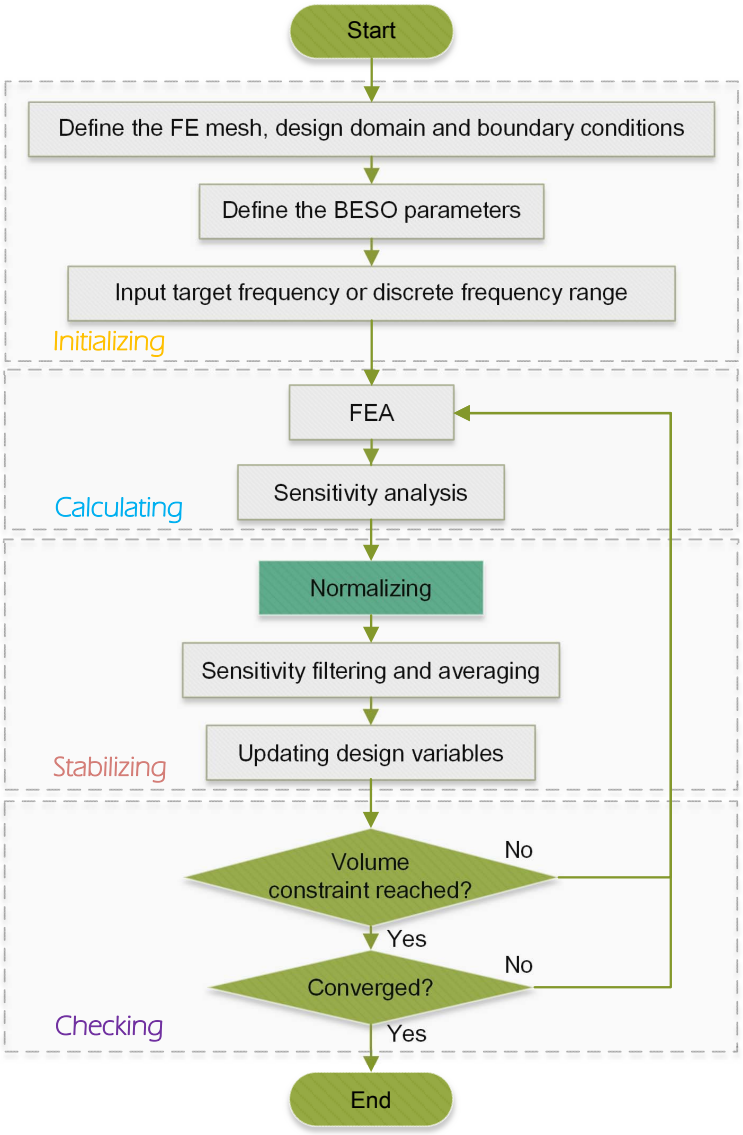

Fig. 2.1 Flowchart of the NBESO method for frequency response problem

Step 8: Update the design variables. Firstly, update the target volume (3D case) or area (2D case) fraction of current iteration step by

$$V^l = V^{l-1}(1 \pm ER), \tag{2.31}$$

where V^{l-1} can be calculated by $V^{l-1} = \sum_{e=1}^{N_E} x_e V_e$; V^0 denotes the initial total volume or area. According to the relative ranking of the sensitivity numbers, the value of design variables can be updated within the volume fraction limitation of current iteration.

Step 9: Repeat steps 4-8 until the target volume fraction is reached.

Step 10: Repeat steps 4-9 until the convergence criterion is satisfied. The convergence criterion can be expressed by

$$\delta_{err} = \frac{\left| \sum_{h=1}^{N} \eta^{l-h+1} - \sum_{h=1}^{N} \eta^{l-N-h+1} \right|}{\sum_{h=1}^{N} \eta^{l-h+1}} \leq \bar{\delta}_{err}, \tag{2.32}$$

where the superscript of η denotes the serial number of iteration; N determines the minimal iteration steps, which is usually set as 5; $\bar{\delta}_{err}$ represents the tolerance of change.

The corresponding flowchart is depicted by Fig. 2.1 to further illustrate the numerical implementation.

2.4 Numerical examples

In this section, four numerical examples are presented. The properties of the adopted material are defined as follows: Young's modulus $E = 210$GPa, Poisson's ratio $v = 0.3$ and density $\rho = 7900\text{kg/m}^3$. For the NBESO parameters, the discrete design variable x_e is either solid or void, which is defined by $x_e = 1$ or $x_{\min}$, respectively. The penalty parameter $p = 3$ is adopted. All the topology optimizations begin from the full design and gradually reduce by the evolutionary ratio $ER = 2\%$ until the target volume fraction is reached. Theoretically, the target DOFs can be every free DOFs that we are interested. In practical application, the target DOFs are mainly determined by engineering requirements and can be selected by designers. In this work, the discussion about the selection of the target DOFs is out of our mission. We just simply define the target DOFs the same as the loaded DOFs, which are marked as P in the figures of each numerical example.

2.4.1 Comparison of NBESO and BESO on a long cantilever beam

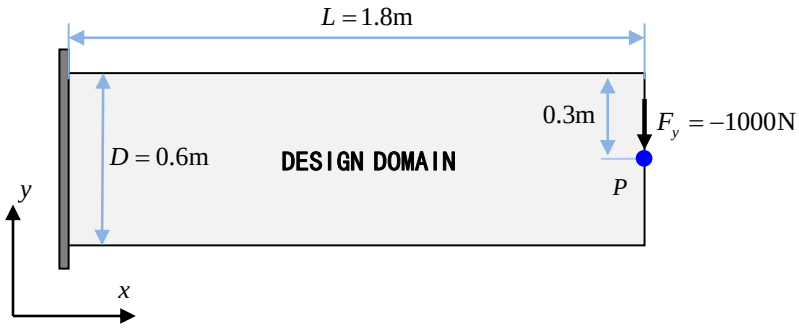

Fig. 2.2 A cantilever beam

In the first example, the NBESO method is compared to BESO method on a cantilever beam considering both single frequencies and full frequency range below the eigenfrequency. Since the target frequency range is lower than the structural eigenfrequency, the weight coefficient α in this example is 0. The design domain and boundary conditions of the cantilever beam are shown in Fig. 2.2. The design domain is discretized by 180×60 quadrilateral elements. The y-direction of position P shown in Fig. 2.2 denotes the loading and target DOF, which is located on the midpoint of the right end of the structure. The eigenfrequency of the original cantilever is 143Hz. The target volume fraction χ of this example is 50% and the filter radius $r_{\min}$ is 0.03m.

- Single-frequency

Table 2.1 Comparison of the objective function values of the topological designs shown in Fig. 2.3

Frequency(Hz)	BESO	NBESO	Gain
0	0.6455	0.6459	-0.06%
20	0.6583	0.6585	-0.03%
40	0.6964	0.6987	-0.33%
60	0.7679	0.7591	1.14%
80	0.8549	0.8495	0.63%
100	1.0104	0.9777	3.24%
120	1.4911	1.1692	21.59%
140	1.7028	1.4547	14.57%

The topological design of NBESO and BESO are firstly compared in different single-frequencies. Eq. (2.24) is adopted in this case. As shown in Fig. 2.3, The topological

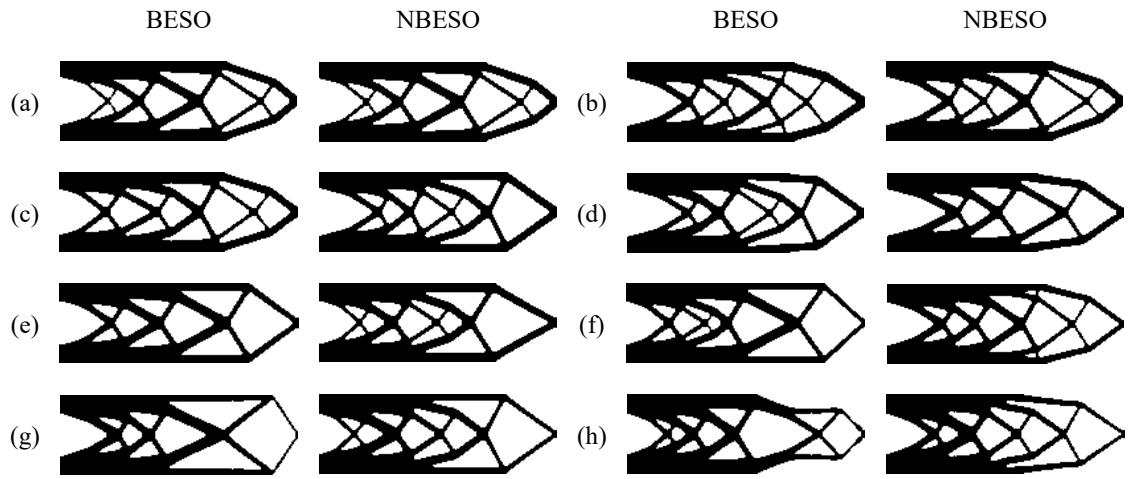

Fig. 2.3 Topological designs obtained by BESO and NBESO in different frequencies: (a) 0Hz; (b) 20Hz; (c) 40Hz; (d) 60 Hz; (e) 80Hz; (f) 100Hz; (g) 120Hz; (h) 140Hz.

designs obtained by both methods for 0Hz are almost the same, but for other frequencies are quite different. The differences trend to more and more pronounced as the frequencies get closer to the structural eigenfrequency. Table 2.1 exhibits the objective function values of the topological designs shown in Fig. 2.3 with respect to different frequencies. For the low-frequency ($0-40$Hz) designs, the differences are so small that it can be ignored. As the frequency increases, the difference becomes larger and larger, and the results of the NBESO design are significantly smaller than those of the BESO. This indicates that the proposed normalization strategy has almost no effect on topology optimization in the static situation. But for the cases whose working frequencies close to the structural eigenfrequency, the NBESO approach generates more reasonable topological designs.

To further explain the reason for this difference, the evolution of topological design and sensitivity number in the first five iterative steps of BESO and NBESO at 140Hz are depicted in Figs. 2.4 and 2.5, respectively. From Fig. 2.4, the calculated sensitivity in the first iteration is obviously a “dominating sensitivity” whose values are much higher than other steps, which causes the numerical instability during the iteration. In the BESO method, such nonlinearity is difficult to eliminate and will continually affect the sensitivity value in subsequent iterative steps. In this iteration, the calculated sensitivity of subsequent iterative steps is much lower than the "dominating sensitivity", thus the updating of the topological designs is seriously affected, resulting unreasonable broken structures. By employing the normalization strategy, as shown in Fig. 2.5, the calculated sensitivity numbers in different iterative steps are scaled to the interval of [0, 1], by which the influence of the "dominating sensitivity" can be eliminated. After filtering and averaging, the normalized sensitivities

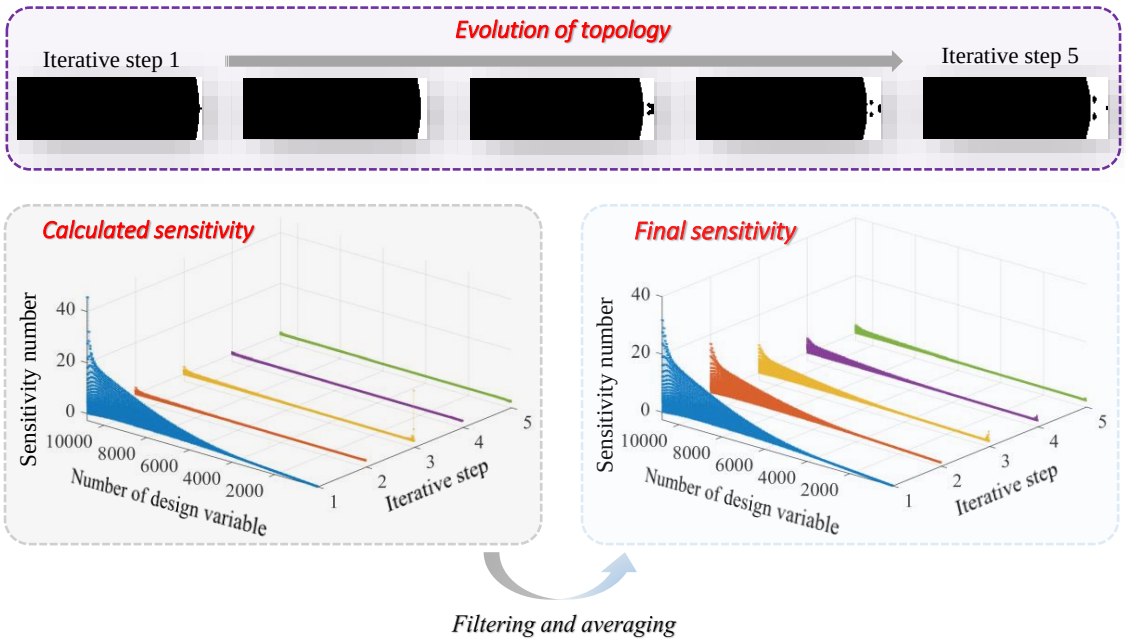

Fig. 2.4 The evolution of topological design and sensitivity number in the first five iterative steps of BESO at 140Hz

smoothly generate topological designs. It is noted that the "dominating sensitivity" would be rarely occurred at the frequencies that are insensitive to response, that is, frequencies that are far from the eigenfrequency. This is why the advantage of the normalization strategy is not obvious at low frequencies but obvious at high frequencies.

- Multi-frequency

Table 2.2 Comparison on the objective function, compliance values and the number of iterative steps of the topological designs shown in Fig. 2.6(a)

Items	BESO	NBESO
Objective function	135.7424	134.3794
Compliance	831.7838	816.8096
Number of iteration steps	146	51

The multi-frequency case considers the full frequency range below the structural eigenfrequency and Eq. (2.26) is employed. The frequency range from 0-143Hz is discretized into 144 integer frequency points, each of which has the same weighting coefficient $\lambda_i = \frac{1}{144}$. Fig. 2.6 depicts the topological designs obtained by BESO and NBESO and their frequency response functions (FRFs). Table 2.2 lists the objective function values, compliance values

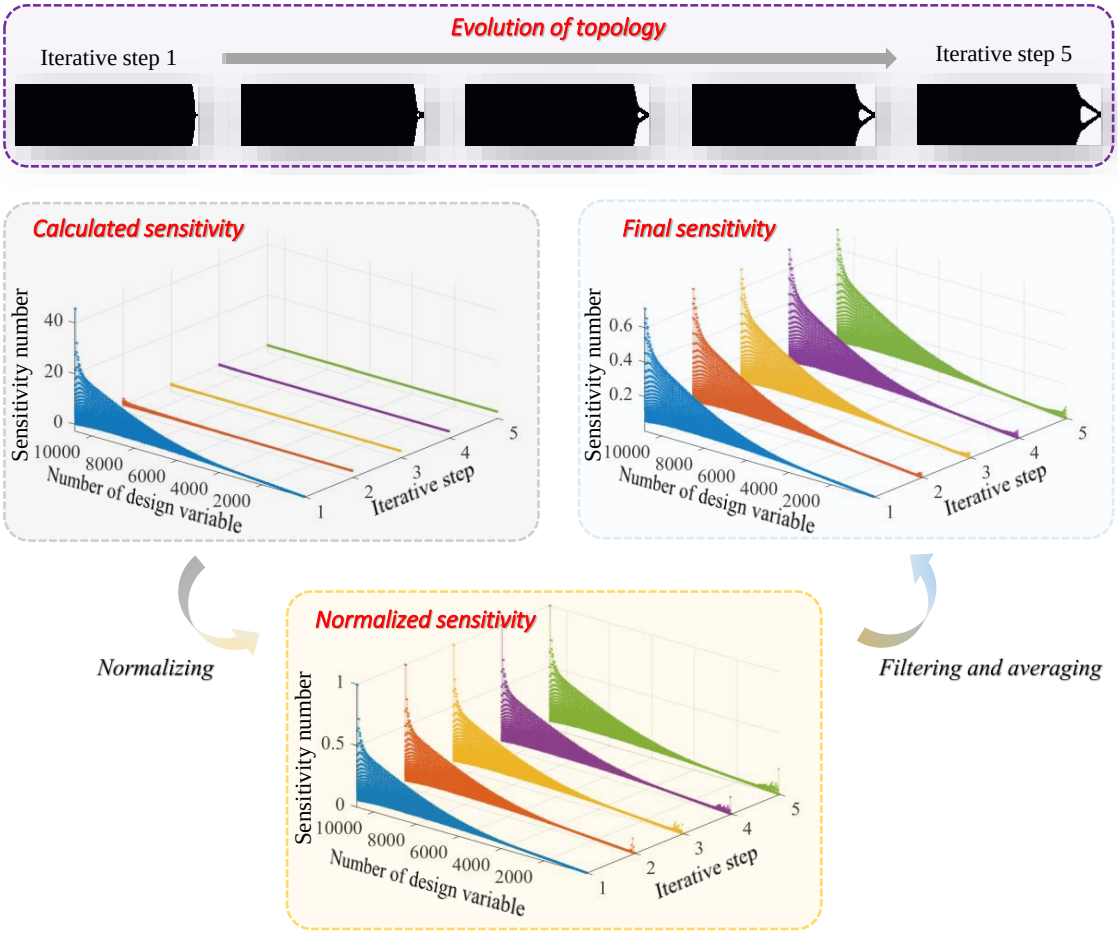

Fig. 2.5 The evolution of topological design and sensitivity number in the first five iterative steps of NBESO at 140Hz

and the number of iterative steps of the topological designs shown in Fig. 2.6(a). Obviously, NBESO generates a better design, which has lower overall frequency response, with very few iterative steps while maintaining better overall static performance (compliance). Fig. 2.7 shows the iteration process of the two methods in compliance value, volume fraction, topological design (Fig. 2.7(a-b)) and objective function (Fig. 2.7(c)). It can be seen that the NBESO method has a smoother convergence process and a faster convergence speed, which means that it has better convergence. This indicates that the normalization strategy adopted in NBESO method can deal with the problem of scattered sensitivity data. By linear weighting the normalized sensitivity, the multi-frequency involved topology optimization can be better realized.

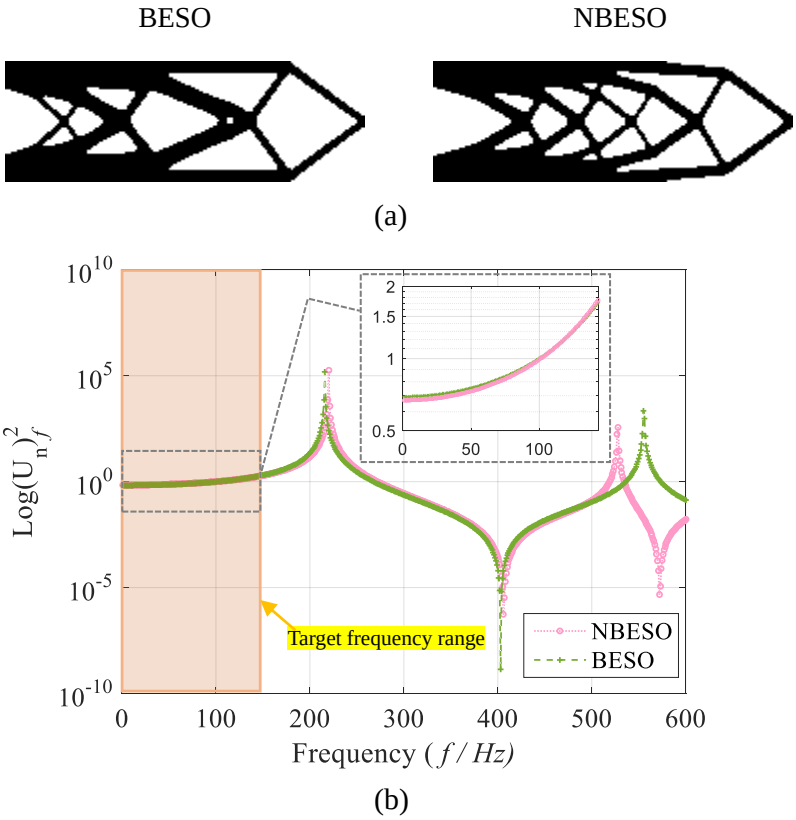

Fig. 2.6 (a) Topological designs obtained by BESO and NBESO; (b) Corresponding frequency response functions (FRFs).

2.4.2 NBESO for a clamped-clamped beam: on the frequencies above the structural eigenfrequency

This example implements the proposed NBESO method to a clamped-clamped beam considering frequency ranges above the structural eigenfrequency. Fig. 2.8 shows the design domain and boundary condition of the clamped-clamped beam. The length and width of the design domain is 1.2m and 0.3m, respectively. It is discretized by 120×30 quadrilateral elements. The top middle of the structure, which is marked as P, is loaded by an external excitation with amplitude of 1000N. It is also the target frequency response point. The structural frequency response problem is performed for four different frequency ranges above the structural eigenfrequency, which are:

- Between the eigenfrequency (421Hz) and the first antiresonance frequency (965Hz): 400-500Hz and 500-600Hz.

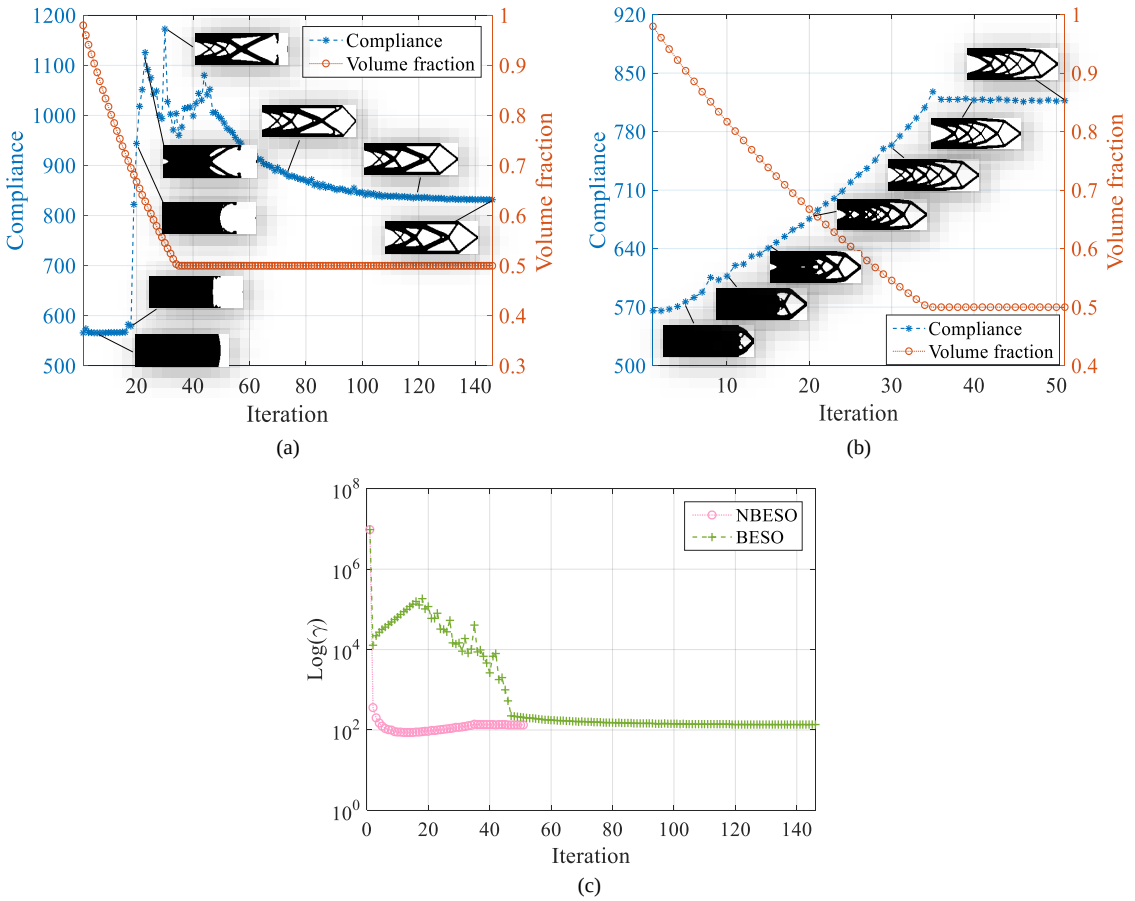

Fig. 2.7 The iteration process of topological design, volume fraction and compliance in: (a) BESO method; (b) NBESO method; (c) The iteration process of BESO and NBESO in the value of objective function.

- Between the first antiresonance frequency (965Hz) and the second resonance frequency (1707Hz): 1300-1400Hz and 1400-1500Hz.

These frequencies are discretized by integral frequencies in the topology optimization optimization for the convenience of calculation. Eq. (2.26) is employed in this example. The weighting factor α is defined by 0.5 in this example. The volume fraction χ and filter radius $r_{\min}$ are 60% and 0.03m, respectively. Fig. 2.9 shows two different design firstly for comparison, in which the 'Static design' and 'Guess design' represent the topological design obtained by the static compliance minimized topology optimization method and guessing, respectively.

Fig. 2.10 depicts the results for the first two frequency ranges, 400-500 Hz and 500-600Hz. Fig. 2.10(a) shows the topological designs obtained by the NBESO method. The topological designs are similar, because they are both at relative low frequencies and close

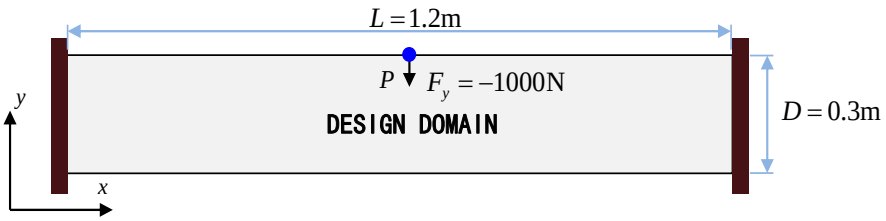

Fig. 2.8 A clamped-clamped beam.

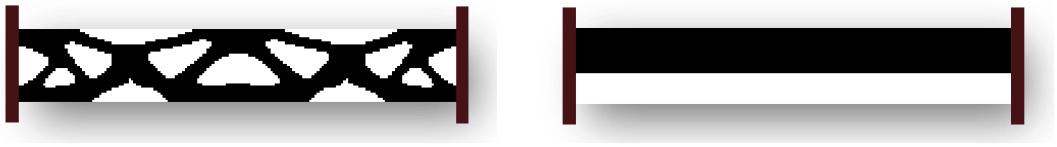

(a) (b)

Fig. 2.9 Two designs for comparison: (a) Static design; (b) Guess design.

to each other. From another aspect, both of topological designs are much different from the "Static design" shown in Fig 2.9. Since both frequency ranges are higher than the structural eigenfrequency, and the modal of the structure has changed, so the optimal design for frequency response problem has also changed a lot. Fig. 2.10(b) shows the FRFs of corresponding topological designs. For comparison, the FRFs of the original design, static design and guess design are also plotted. With similar material distribution, the FRFs of topological designs for two frequency ranges obtained by NBESO method are very similar, and have obvious advantages compared with other designs. Fig. 2.10(c) presents the iterative histories. It should be noted that there are some abrupt jumps in the optimization process , which is influenced by the strong nonlinearity of structural dynamic response when reducing the volume of the structure. Due to the use of normalization strategy, the nonlinearity is reduced to some extent. Eventually, as the iteration progresses, the topology of the structure will eventually stabilize.

Fig. 2.11 depicts the results for the frequency ranges between the first antiresonance frequency and the second resonance frequency. As shown in Fig. 2.11(a), the topological design for these two frequency ranges are much different. Compared to the static design, both designs have rich details, which can be used to resist the structural vibration at corresponding frequency ranges. Since the static response is taken into account, the two designs are somewhat similar in general to the "Static design". Fig. 2.11(b) shows their FRFs and compared with what of other designs. The FRFs indicate that the topological designs obtained by the NBESO method are much better than other designs, even better than the

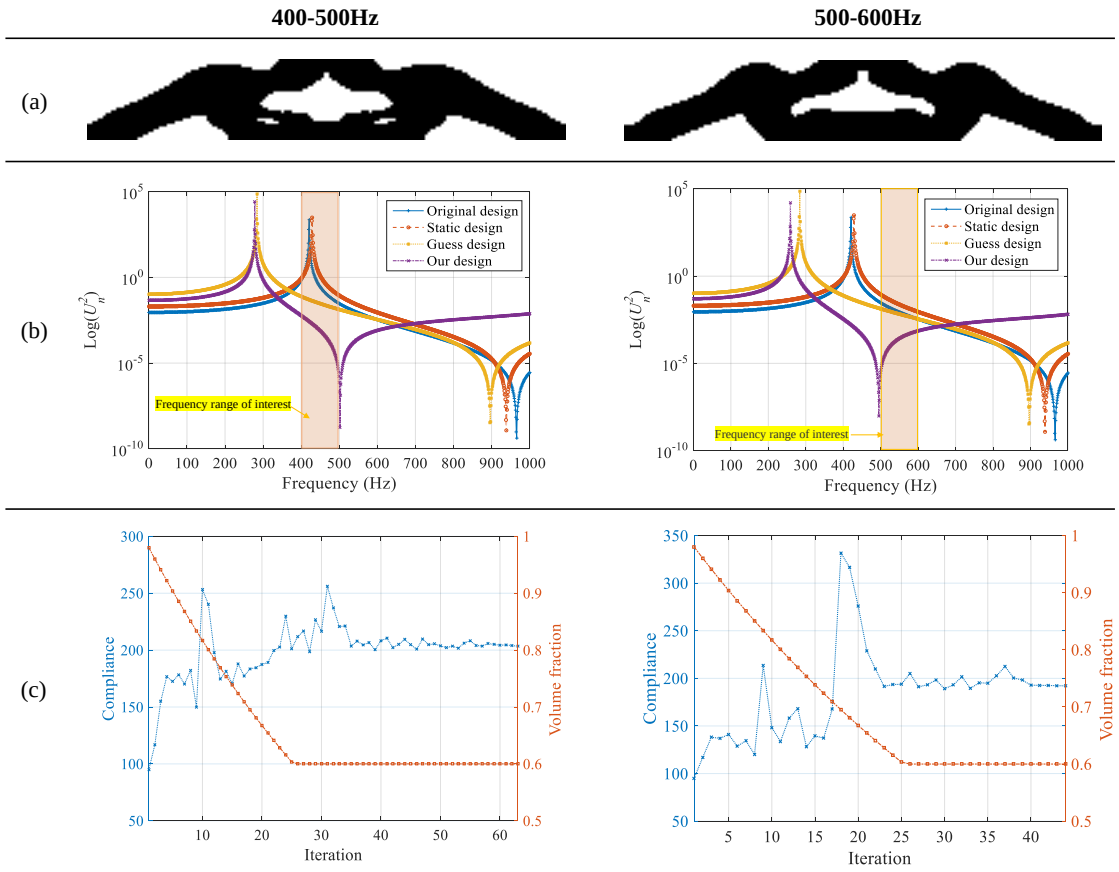

Fig. 2.10 (a) The topological designs for the first two frequency ranges; (b) Comparison on the FRFs; (c) Iteration history.

original design that uses 1.67 times more solids. It is noted that the NBESO method based designs didn't achieve anti-resonance effect within the target frequency range as done by Silva et al. [351]. It is because the static structural performance is considered to avoid the topological design with low stiffness, which is also pointed out in [351]. From the authors' point of view, such vibration reduction designs might be more practical for real engineering structures. Fig. 2.11(c) shows the iterative histories, which indicates that there is no convergence problem in the optimization process.

2.4.3 On the influence of weighting factor α

In this example, the influence of the weighting factor α for static performance is discussed. Fig. 2.12 depicts a half-MBB beam with a length of 0.6m and a width of 0.3m. The design domain is discretized by 120×60 quadrilateral elements. The point P shows the location of the loading and target position, and it is loaded and tested in the y-direction. It

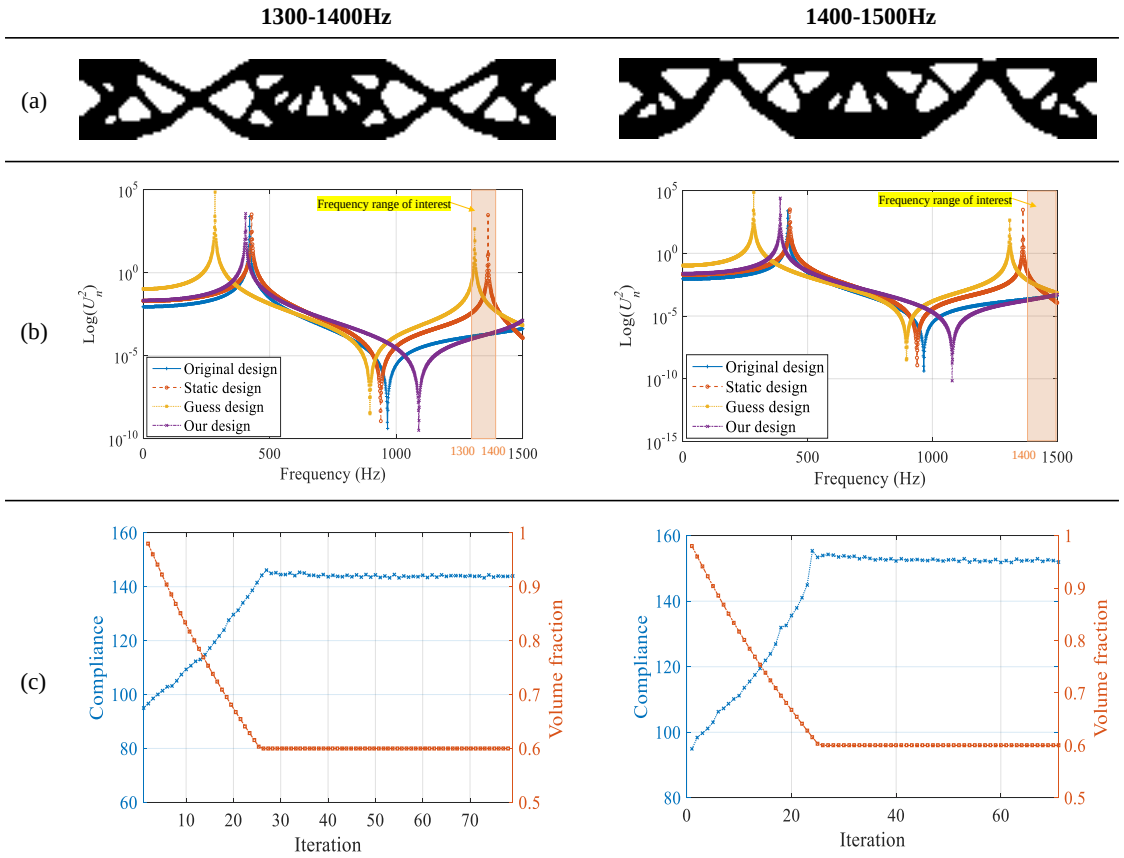

Fig. 2.11 (a) The topological designs for the last two frequency ranges; (b) Comparison on the FRFs; (c) Iteration history.

is loaded by a force with an amplitude of 1000N with various frequencies in y-direction. The eigenfrequency of the half-MBB beam is 377Hz. Two different frequency ranges [350-400Hz] and [700-750Hz] are taken into consideration to represent the frequency range near and above the eigenfrequency, respectively. For the convenience of computation, the frequency ranges are discretized by integral frequencies. The target volume fraction of this example is 50%. The filter radius $r_{\min}$ is 0.015m. Five values were taken from 0 to 1 to show the influence of different weighting factor α on topology optimization.

Fig. 2.13(a) depicts the topological designs for the first frequency range [350-400Hz] with different weighting factor α. Although this frequency range is crossed by the structural eigenfrequency, all the topological designs in this case are well generated without loss of connectivity. The use of normalization strategy increases the robustness of topology optimization in these cases. As the value of α increases, the center of gravity of topological designs moves from left to right, because the value of α affects the orientation of topology optimization. Fig. 2.13(b) shows the corresponding FRFs of the topological designs shown

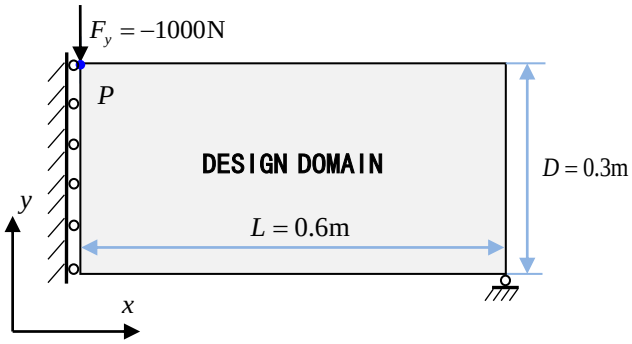

Fig. 2.12 A half-MBB beam

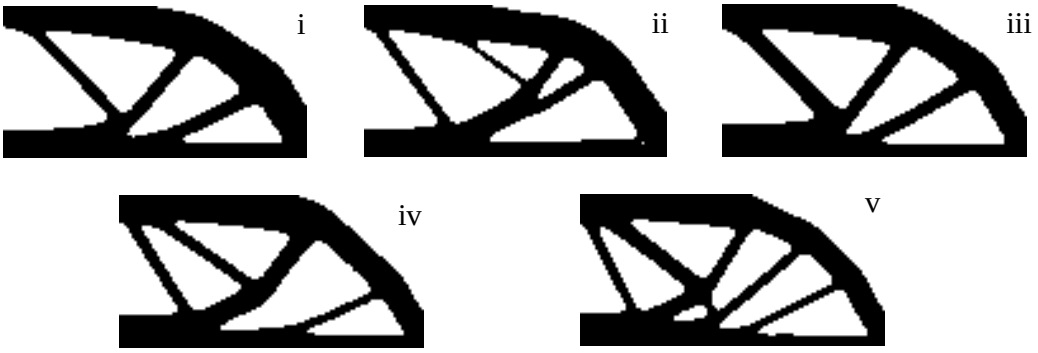

(a)

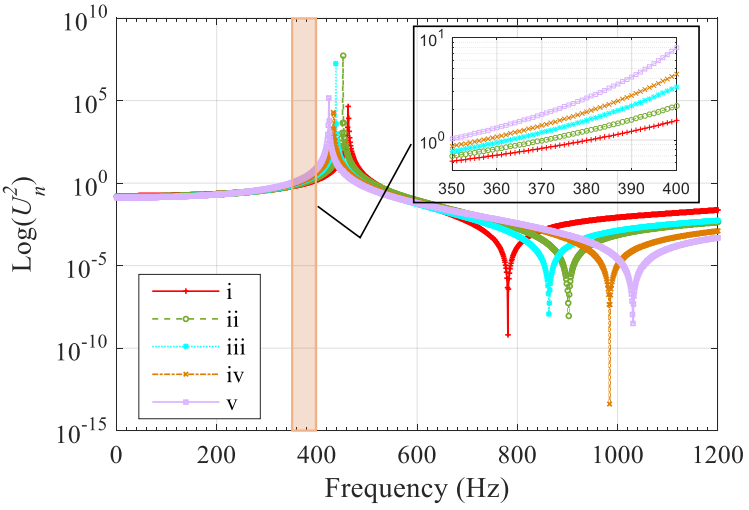

(b)

Fig. 2.13 (a) Topological designs for 350-400Hz with different weighting factors: (i) α=0.1; (ii) α=0.3; (iii) α=0.5; (iv) α=0.7; (v)α=0.9; (b) Corresponding FRFs of the topological designs.

in Fig. 2.13(a).The FRFs indicate that smaller α makes better structural dynamic response in the target frequency range. When the target frequency band is partly lower than the structural eigenfrequency, one can even let α to be 0 to pursue better structural dynamic performance. In such situation, the normalization strategy will be efficient, as demonstrated in the first example.

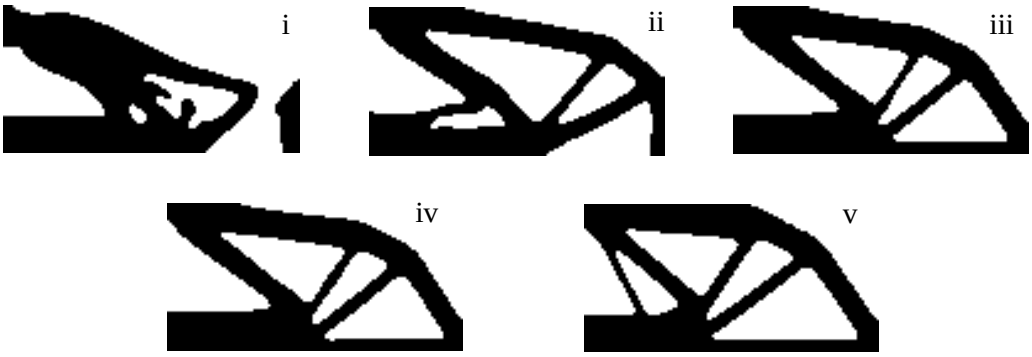

(a)

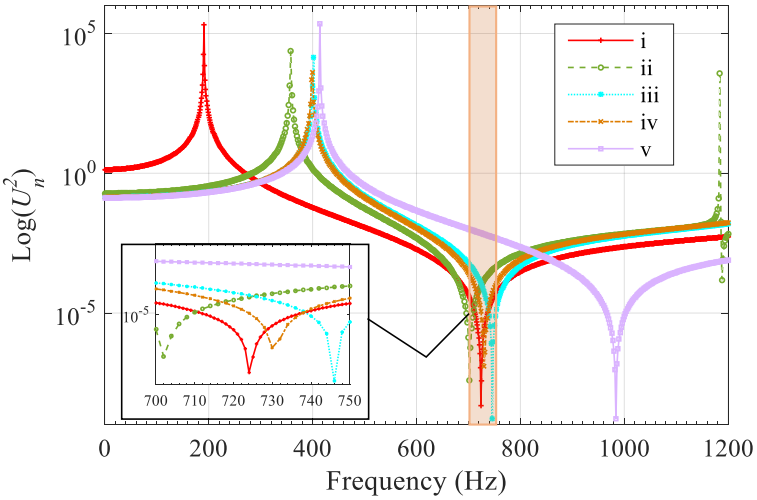

(b)

Fig. 2.14 (a) Topological designs for 700-750Hz with different weighting factors: (i) α=0.1; (ii) α=0.3; (iii) α=0.5; (iv) α=0.7; (v) α=0.9; (b) Corresponding FRFs of the topological designs.

Fig. 2.14(a) depicts the topological designs for the second frequency range [700-750Hz] with different α. It is noted that when $\alpha = 0.1$, the topological design shows discontinuity, which is the same as reported in [176, 351]. This indicates that the structural design with very weak static performance can bring better dynamic performance in this frequency range. However, in engineering structures, such design is often required to be avoided. One should do is to increase the weighting of static performance in the objective function. It can

be seen that as the value of α gradually increases, such discontinuity disappears in the topological designs. When α=0.9, the topological design is similar to that in Fig. 2.13(a), which indicates the static performance in this design might be over-weighted. Fig. 2.14(b) depicts the corresponding FRFs of the topological designs shown in Fig. 2.14(a). It shows that all the topological designs get a good dynamic frequency responses except 'design v', which puts too many weighting on static performance. The topological designs in this frequency range demonstrate that the NBESO method can be used for topology optimization of frequency ranges higher than the structural eigenfrequency while choosing a feasible weighting parameter.

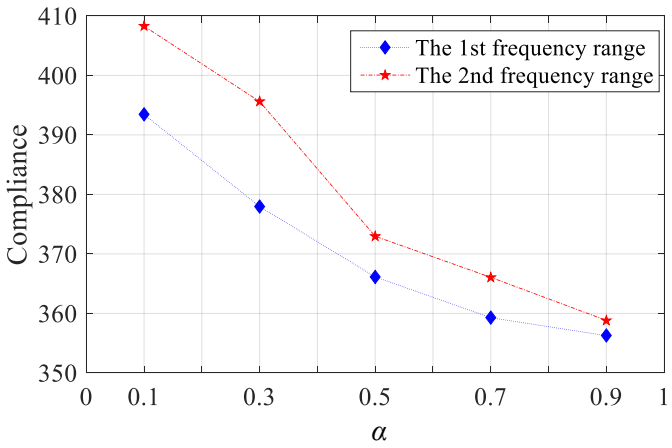

Fig. 2.15 Structural compliance of the topological designs shown in this example.

Fig. 2.15 shows the trend of the static performance (compliance) of different designs in two different frequency ranges changing with α. In both frequency ranges, the compliance of the structure decreases with the increase of α. To sum up, one can get ideal topological designs by using the proposed NBESO method, and it is feasible by setting the weighting factor to make a balance in structural static and dynamic performance.

2.4.4 Application to a 3D plate

In this example, we applied the NBESO method to reduce the frequency response of a CCCC square plate. The design domain and work condition of the plate are shown in Fig. 2.16. Based on the Mindlin-Reissner plate theory, the design domain is discretized into 80×80 quadrilateral elements on the x-y plane with one layer in the z-direction. A z-directional excitation with an amplitude of 1000N is loaded on point P, which is also defined as the response point in the same direction. The volume fraction χ is 60% and the filter radius $r_{\min}$ is 0.02m. The frequency range from 100Hz to 300Hz is evenly divided into four adjacent

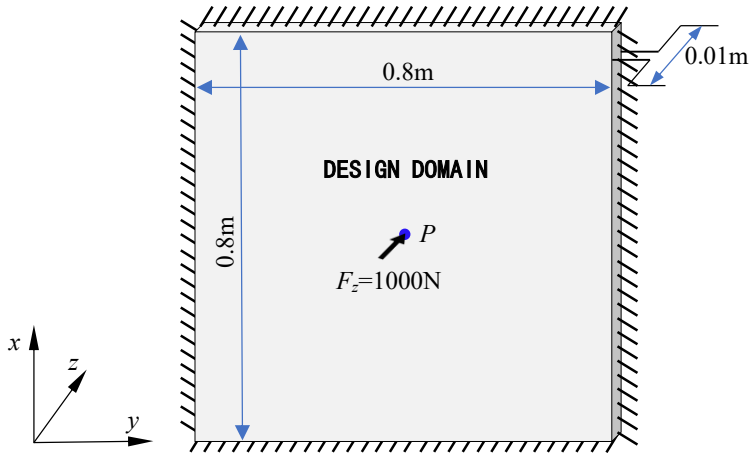

Fig. 2.16 A CCCC square plate

frequency ranges, which are set as the target intervals for the frequency response problem. Eq. (2.26) is employed in this example. For the convenience of calculation, the frequency ranges are discretized by integer frequencies, which means every frequency range involves 51 integer frequency points. It is noted that these frequency ranges are higher than the structural eigenfrequency, so the static compliance is also introduced to ensure the structural static performance. The weighting factor α in this example is 0.3.

Fig. 2.17 depicts the topological designs in the *x*-*y* plane with respect to different frequency ranges. The static design that aiming for optimal structural static performance (compliance) is also plotted for comparison. The topological designs are well generated without loss connectivity, which illustrate that the weighted sensitivity of static compliance enhanced the structural static performance. Topological designs for different target frequency ranges vary widely. It is affected by the weighted sensitivities on multi-frequency responses in different frequency ranges. To further illustrate the influences of the topological variations on the structural frequency response, Fig. 2.18 shows the FRFs of these topological designs. The colored areas in Fig. 2.18 denote the four frequency ranges of interest. In each target frequency range, the corresponding topological designs obviously have better frequency responses. This example illustrates that the proposed method is also applicable to the 3D plate structure.

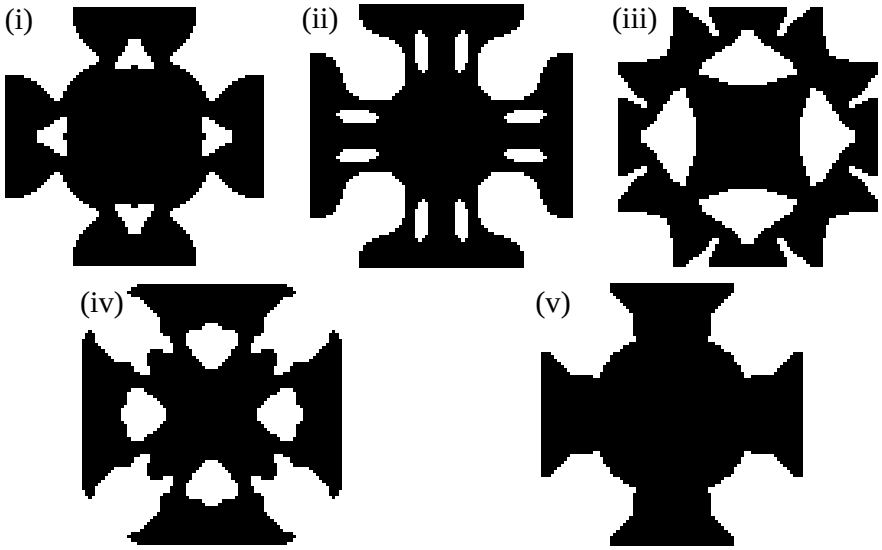

Fig. 2.17 Topological designs for different frequency ranges: (i) 0Hz (static); (ii) 100-150Hz; (iii) 150-200Hz; (iv) 200-250Hz; (v) 250-300Hz.

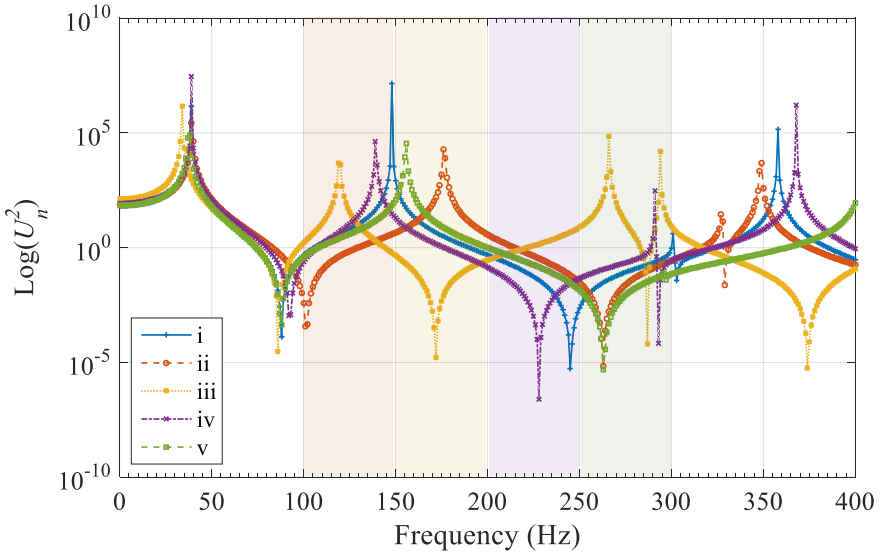

Fig. 2.18 The FRFs of the topological designs shown in Fig. 2.17.

2.5 Conclusion

In this chapter, a normalization strategy was proposed for the BESO based structural topology optimization. It is a simple but effective strategy to improve the stability and convergence of the BESO method, by which the values of sensitivity at different scales can be adjusted to a common order that overcomes the numerical difficulties in the material adding/removal process of the discrete design variables. The basis of employing the normalization strategy in BESO is that only the relative ranking of the sensitivities affects the evolution of the design variable, so the amplification and reduction on the value of the sensitivities do not affect the optimization process. Instead, when it comes to strong nonlinearity between two iterative steps, the normalization strategy can improve the convergence of the solution. Moreover, once the sensitivities are normalized to the same scale, the weight sum method, which is a basic multi-objective approach, can be easily applied.

Four numerical examples are presented to demonstrate the effectiveness and adaptability of the proposed NBESO method to the application on reducing structural frequency response. The first example illustrated that the NBESO method is not only suitable for low-frequency problem, but also efficient for the topological design near the structural eigenfrequency. The second example applied the NBESO method for two different frequency ranges higher than the structural eigenfrequency. It shows that the NBESO method generate topological designs without loss of continuity when the target frequency are above the structural eigenfrequency, which indicates its applicability in practical engineering. Example 3 discussed the influence of the weighting parameter α. The last example applied the proposed NBESO method to a 3D plate structure, in which the topological designs are also efficient. All the numerical examples gave clear solid/void material distributions, which meets the demands of practical engineering.

The main contribution of this chapter can be summarized as follows:

- A normalization strategy was proposed for BESO method to improve its convergence and numerical stability.
- A series of frequency response topology optimizations was conducted with the normalization strategy.
- The proposed NBESO method can be regarded as an extension of the current BESO method.
- More extensive applications of NBESO are foreseeable. For example, in the latest research, it has been applied to BESO-based topology optimization for stress problems [119, 118] and fracture-resistant designs [211].

Chapter 3

Robust topology optimization for the elastic dynamic structures with imprecise probabilities

The main content of this chapter is adapted from our papers [144, 398, 399].

3.1 Introduction

In this Chapter, the probabilistic uncertainty with imprecise probability distribution is considered for robust topology optimization. We employ a hybrid interval random model to describe the probabilistic parameters with imprecise quantities, such as interval model based expectation and standard deviation. Then, an improved hybrid perturbation analysis (IHPA) method is formulated to efficiently estimate the dynamic performances of the structures at a very low computational cost. Robust topological designs for conventional one material structures, multi-scale composite structures and laminated composite plates are implemented. In this Chapter, the BESO method is employed.

3.2 Modeling of imprecise probability

3.2.1 Description of imprecise probability

For the probabilistic uncertainty, the probability distribution function (PDF) can be adopted to describe the uncertain parameters. However, in practical engineering, precise PDF may sometimes hardly be obtained due to a lack or poor quality of information [174]. We assume

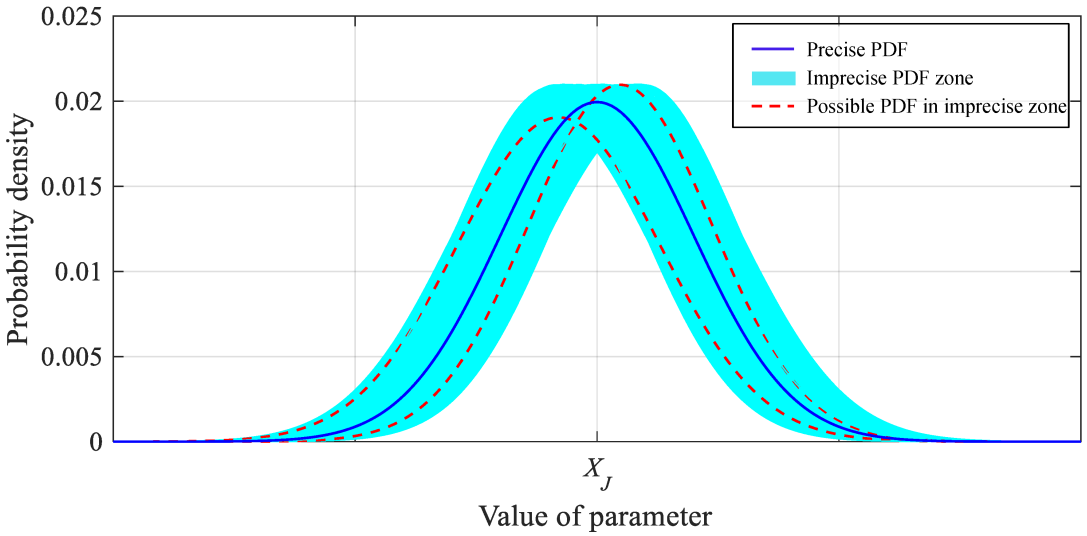

Fig. 3.1 The probability distribution functions of precise and imprecise probability with normal distribution.

that the uncertain parameter X_J obeys a normal distribution but lacks information. As shown in Fig. 3.1, the possible PDFs constitute a zone in cyan. For the sake of comparison, two of the possible PDFs are presented by red dash line and the PDF based on the exact probability density assumption is marked with a blue line. By comparison, it is clear that the precise probability distribution function has limitations and does not reflect all cases when there is insufficient information.

To further describe uncertainty with imprecise probability distribution, a p-box model [432] is plotted by adopting the information in Fig. 3.1. The corresponding cumulative distribution functions (CDF) are shown in Fig. 3.2 in green. It can be seen that the probability of imprecise uncertainty is located within a 'strip', which can be represented by an interval. By determining the upper and lower bound of the imprecise uncertainty, the probability range of the parameters are clarified. For an arbitrary parameter X_J, its probability can be expressed by $\left[\overline{\mathrm{P}_{X_J}}, \underline{\mathrm{P}_{X_J}}\right]$. Fig. 3.2 indicates that the interval model has potential to be integrated into the probabilistic-based model to describe imprecise probability.

3.2.2 Hybrid interval random model

Assume that all the uncertain parameters are independent, and X represents an uncertain probabilistic parameter with imprecise probability. By adopting the interval model to describe X, $X(\mathbf{Y})$ is obtained. Without loss of generality, we define $X_J(\mathbf{Y}_J)$ as the J-th hybrid interval random variable of the hybrid interval random vector $\mathbf{X}(\mathbf{Y})$ that composed of all independent

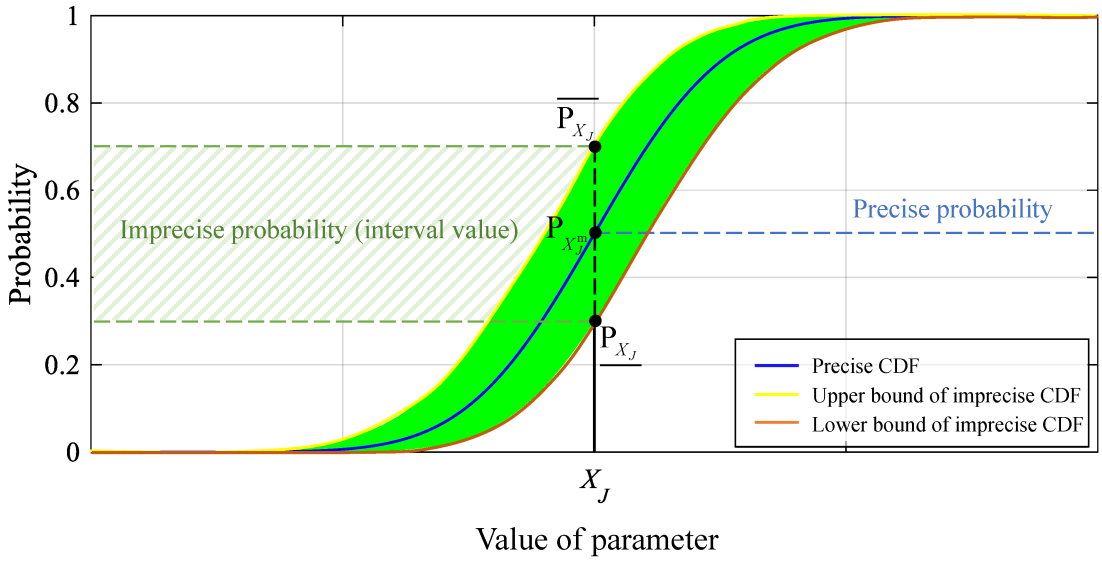

Fig. 3.2 P-box model for the description of uncertainty with imprecise probability.

hybrid interval random variables and $\mathbf{X}(\mathbf{Y})$ can be expressed by:

$$\begin{aligned} \mathbf{X}(\mathbf{Y}) &= (X_1(\mathbf{Y}_1), X_2(\mathbf{Y}_2), ..., X_J(\mathbf{Y}_J), ...), \qquad J = 1,2,...,M, \\ \mathbf{Y}_J &= \left(Y_J^1, Y_J^2, ..., Y_J^K, ...\right), \qquad K = 1,2,...,N, \end{aligned} \tag{3.1}$$

where M and N represent the number of random and interval parameters, respectively; J and K index their series number. For each interval vector, $\mathbf{Y}_J$ can be expressed by:

$$\begin{aligned} \mathbf{Y}_J &= Y_J^{\mathrm{m}} + \mathbf{Y}_J^{\mathrm{I}}, \\ Y_J^{\mathrm{m}} &= \frac{\underline{\mathbf{Y}_J} + \overline{\mathbf{Y}_J}}{2}, \\ Y_J^{\mathrm{I}} &= [-\Delta Y_J, +\Delta Y_J], \\ \Delta Y_J &= \frac{\overline{\mathbf{Y}_J} - \underline{\mathbf{Y}_J}}{2}, \end{aligned} \tag{3.2}$$

where $\underline{\mathbf{Y}_J}$ and $\overline{\mathbf{Y}_J}$ denote the lower and upper bounds of interval vector $\mathbf{Y}_J$; Y_J^{m} is the mean value of $\mathbf{Y}_J$, which can be calculated by averaging the lower and upper bounds value as shown in Eq. $(3.2)_2$; $\mathbf{Y}_J^{\mathrm{I}}$ denotes the variation interval of $\mathbf{Y}_J$, which depends on the difference of the lower and upper bound values as shown in Eq. $(3.2)_3$. The deviation ΔY_J of the symmetrical interval can be acquired by averaging the upper and lower bounds of $\mathbf{Y}_J$ as shown in Eq. $(3.2)_4$.

In the combination form, the J-th hybrid interval random parameter $X_J(\mathbf{Y}_J)$ can be expressed by:

$$\begin{aligned} X_J(\mathbf{Y}_J) =& X_J(Y_J^{\mathrm{m}}) + X_J\left(\mathbf{Y}_J^{\mathrm{I}}\right), \\ X_J(Y_J^{\mathrm{m}}) =& \frac{X_J\left(\underline{\mathbf{Y}_J}\right) + X_J\left(\overline{\mathbf{Y}_J}\right)}{2}, \\ X_J\left(\mathbf{Y}_J^{\mathrm{I}}\right) =& \left[-\Delta X_J(\mathbf{Y}_J), +\Delta X_J(\mathbf{Y}_J)\right], \\ \Delta X_J(\mathbf{Y}_J) =& \frac{X_J\left(\overline{\mathbf{Y}_J}\right) - X_J\left(\underline{\mathbf{Y}_J}\right)}{2}. \end{aligned} \tag{3.3}$$

The expectation and standard deviation of the J-th hybrid interval random parameter $X_J(\mathbf{Y}_J)$ can be expressed as $\mu(X_J(\mathbf{Y}_J))$ and $\sigma(X_J(\mathbf{Y}_J))$, respectively. By adopting Eq. (3.3), the interval expression of $\mu(X_J(\mathbf{Y}_J))$ and $\sigma(X_J(\mathbf{Y}_J))$ can be represented.

3.3 An improved hybrid perturbation analysis (IHPA) method

We consider a steady-state equilibrium equation of the continuum in the frequency domain, which has been described in Chapter 2. It can be expressed by the following formulation with considering the imprecise probability, which is:

$$\boldsymbol{K}_d(\mathbf{X}(\mathbf{Y}))\boldsymbol{U}(\mathbf{X}(\mathbf{Y})) = \boldsymbol{F}, \tag{3.4}$$

where $\boldsymbol{K}_d(\mathbf{X}(\mathbf{Y}))$ denotes the dynamic stiffness matrix with uncertainty; $\boldsymbol{F}$ is the force vector with deterministic assumption; $\boldsymbol{U}(\mathbf{X}(\mathbf{Y}))$ denotes the uncertain displacement vector.

In the IHPA method, we first assume that the interval variables related to $\mathbf{X}(\mathbf{Y})$ are deterministic. The first-order Taylor series expansion of $\boldsymbol{U}(\mathbf{X}(\mathbf{Y}))$ at the expectation of the interval random parameter vector $\mathbf{X}(\mathbf{Y})$ can be expressed by:

$$\begin{aligned} \boldsymbol{U}(\mathbf{X}(\mathbf{Y})) =& \boldsymbol{U}(\mu(\mathbf{X}(\mathbf{Y}))) + \sum_{J=1}^{M} \left.\frac{\partial \boldsymbol{U}(\mathbf{X}(\mathbf{Y}))}{\partial X_J(\mathbf{Y}_J)}\right|_{X_J(\mathbf{Y}_J)=\mu(X_J(\mathbf{Y}_J))} (X_J(\mathbf{Y}_J) - \mu(X_J(\mathbf{Y}_J))) \\ &+ \mathrm{o}(X_J(\mathbf{Y}_J)), \end{aligned} \tag{3.5}$$

where $\mathrm{o}(X_J(\mathbf{Y}_J))$ denotes the remainder of the first-order Taylor series expansion. When the variation of the parameter is relatively small, this remainder can be ignored. According to

the random moment method [117], the above equation can be expressed by two parts as:

$$\begin{aligned} E(\boldsymbol{U}) =& \boldsymbol{U}(\mu(\mathbf{X}(\mathbf{Y}))), \\ SD(\boldsymbol{U}) =& \sum_{J=1}^{M} \left.\frac{\partial \boldsymbol{U}(\mathbf{X}(\mathbf{Y}))}{\partial X_J(\mathbf{Y}_J)}\right|_{X_J(\mathbf{Y}_J)=\mu(X_J(\mathbf{Y}_J))} \sigma(X_J(\mathbf{Y}_J)), \end{aligned} \tag{3.6}$$

where $E(\boldsymbol{U})$ and $SD(\boldsymbol{U})$ denote the expectation and standard deviation, respectively; $\sigma(X_J(\mathbf{Y}_J))$ is equal to $X_J(\mathbf{Y}_J) - \mu(X_J(\mathbf{Y}_J))$ in Eq. (3.5).

As the interval variables are considered, both of $E(\boldsymbol{U})$ and $SD(\boldsymbol{U})$ are the interval vectors. Performing the first-order Taylor series expansion again, yields:

$$\begin{aligned} E^I(\boldsymbol{U}) =& \boldsymbol{U}(\mu(\mathbf{X}(\mathbf{Y}^{\mathrm{m}}))) \\ & \pm \sum_{J=1}^{M}\sum_{K=1}^{N} \left.\frac{\partial \boldsymbol{U}(\mu(X_J(\mathbf{Y}_J)))}{\partial \mu\left(X_J\left(\mathbf{Y}_J^{\mathrm{I}}\right)\right)}\right|_{\mu\left(X_J\left(\mathbf{Y}_J^{\mathrm{I}}\right)\right)=\mu\left(X_J\left(Y_J^{\mathrm{m}}\right)\right)} \left(\mu\left(X_J\left(Y_J^K\right)\right) - \mu\left(X_J\left(Y_J^{\mathrm{m}}\right)\right)\right) \\ & + \mathrm{o}\left(\mu\left(X_J\left(\mathbf{Y}_J^{\mathrm{I}}\right)\right)\right), \\ SD^I(\boldsymbol{U}) =& \sum_{J=1}^{M} \left\{ \left.\frac{\partial \boldsymbol{U}(X_J(\mathbf{Y}_J))}{\partial X_J(\mathbf{Y}_J)}\right|_{X_J(\mathbf{Y}_J)=\mu(X_J(\mathbf{Y}_J))} \sigma(X_J(Y_J^{\mathrm{m}})) \right. \\ & \pm \sum_{K=1}^{N} \left[\left.\frac{\partial^2 \boldsymbol{U}(X_J(\mathbf{Y}_J))}{\partial X_J(\mathbf{Y}_J)\partial X_J\left(\mathbf{Y}_J^{\mathrm{I}}\right)}\right|_{\substack{X_J(\mathbf{Y}_J)=\mu(X_J(\mathbf{Y}_J)) \\ X_J\left(\mathbf{Y}_J^{\mathrm{I}}\right)=X_J\left(Y_J^{\mathrm{m}}\right)}} \left(\mu(X_J(Y_J^{\mathrm{m}})) - \mu\left(X_J\left(Y_J^{\mathrm{K}}\right)\right)\right)\sigma(X_J(Y_J^{\mathrm{m}})) \right. \\ & \left. \left. + \left.\frac{\partial \boldsymbol{U}(X_J(\mathbf{Y}_J))}{\partial X_J(\mathbf{Y}_J)}\right|_{X_J(\mathbf{Y}_J)=\mu(X_J(\mathbf{Y}_J))} \frac{\partial \sigma(X_J(Y_J^{\mathrm{m}}))}{\partial X_J\left(\mathbf{Y}_J^{\mathrm{I}}\right)} \left(\mu\left(X_J\left(Y_J^{\mathrm{K}}\right)\right) - \mu\left(X_J\left(Y_J^{\mathrm{m}}\right)\right)\right) \right] \right. \\ & \left. + \mathrm{o}\left(X_J\left(\mathbf{Y}_J^{\mathrm{I}}\right)\right) \right\}, \end{aligned} \tag{3.7}$$

where E^I and SD^I indicate both of the upper and lower bounds of the expectation and standard deviation. The quantities $\mathrm{o}\left(\mu\left(X_J\left(\mathbf{Y}_J^{\mathrm{I}}\right)\right)\right)$ and $\mathrm{o}\left(X_J\left(\mathbf{Y}_J^{\mathrm{I}}\right)\right)$ can be ignored as the variation of parameter is relatively small. For simplicity, the above equation can be rewritten as:

$$\begin{aligned} E^I(\boldsymbol{U}) \approx& \boldsymbol{U}_0 \pm \sum_{J=1}^{M}\sum_{K=1}^{N} \boldsymbol{U}_{1,J}\Delta\mu\left(X_J\left(Y_J^K\right)\right), \\ SD^I(\boldsymbol{U}) \approx& \sum_{J=1}^{M} \left(\boldsymbol{U}_{2,J}\sigma(X_J(Y_J^{\mathrm{m}})) \pm \sum_{K=1}^{N} \left(\boldsymbol{U}_{3,JK}\sigma(X_J(Y_J^{\mathrm{m}}))\Delta\mu\left(X_J\left(Y_J^K\right)\right) + \boldsymbol{U}_{2,J}\Delta\sigma\left(X_J\left(Y_J^K\right)\right)\right) \right), \end{aligned} \tag{3.8}$$

where

$$\begin{aligned}
\boldsymbol{U}_0 =& \boldsymbol{U}\left(\mu\left(\mathbf{X}\left(\mathbf{Y}^{\mathrm{m}}\right)\right)\right), \\
\boldsymbol{U}_{1,J} =& \left.\frac{\partial \boldsymbol{U}\left(\mu\left(X_J\left(\mathbf{Y}_J\right)\right)\right)}{\partial \mu\left(X_J\left(\mathbf{Y}_J^{\mathrm{I}}\right)\right)}\right|_{\mu\left(X_J\left(\mathbf{Y}_J^{\mathrm{I}}\right)\right)=\mu\left(X_J\left(Y_J^{\mathrm{m}}\right)\right)}, \\
\boldsymbol{U}_{2,J} =& \left.\frac{\partial \boldsymbol{U}\left(X_J\left(\mathbf{Y}_J\right)\right)}{\partial X_J\left(\mathbf{Y}_J\right)}\right|_{X_J(\mathbf{Y}_J)=\mu(X_J(\mathbf{Y}_J))}, \\
\boldsymbol{U}_{3,JK} =& \left.\frac{\partial^2 \boldsymbol{U}\left(X_J\left(\mathbf{Y}_J\right)\right)}{\partial X_J\left(\mathbf{Y}_J\right)\partial X_J\left(\mathbf{Y}_J^{\mathrm{I}}\right)}\right|_{\substack{X_J(\mathbf{Y}_J)=\mu(X_J(\mathbf{Y}_J)) \\ X_J\left(\mathbf{Y}_J^{\mathrm{I}}\right)=X_J\left(Y_J^{\mathrm{m}}\right)}},
\end{aligned} \tag{3.9}$$

and

$$\begin{aligned}
\Delta\mu\left(X_J\left(Y_J^K\right)\right) =& \frac{\partial X_J\left(\mathbf{Y}_J^{\mathrm{I}}\right)}{\partial \mu\left(X_J\left(\mathbf{Y}_J^{\mathrm{I}}\right)\right)}\left(\mu\left(X_J\left(Y_J^{\mathrm{m}}\right)\right)-\mu\left(X_J\left(Y_J^K\right)\right)\right), \\
\Delta\sigma\left(X_J\left(Y_J^K\right)\right) =& \frac{\partial \sigma\left(X_J\left(Y_J^{\mathrm{m}}\right)\right)}{\partial X_J\left(Y_J^K\right)}\left(\mu\left(X_J\left(Y_J^{\mathrm{m}}\right)\right)-\mu\left(X_J\left(Y_J^{\mathrm{K}}\right)\right)\right),
\end{aligned} \tag{3.10}$$

where $\boldsymbol{U}_0$ and its derivations $\boldsymbol{U}_{1,J}$, $\boldsymbol{U}_{2,J}$ and $\boldsymbol{U}_{3,JK}$ can be calculated by substituting the mean value of expectation of the imprecise probability $\mu\left(\mathbf{X}\left(\mathbf{Y}^{\mathrm{m}}\right)\right)$ into Eq. (3.4) as:

$$\begin{aligned}
\boldsymbol{U}_0 =& \boldsymbol{K}_d^{-1}\left(\mu\left(\mathbf{X}\left(\mathbf{Y}^{\mathrm{m}}\right)\right)\right)\boldsymbol{F}, \\
\boldsymbol{U}_{1,J} =& -\boldsymbol{K}_d^{-1}\left(\mu\left(\mathbf{X}\left(\mathbf{Y}^{\mathrm{m}}\right)\right)\right)\frac{\partial \boldsymbol{K}_d\left(\mu\left(X_J\left(\mathbf{Y}_J\right)\right)\right)}{\partial \mu\left(X_J\left(\mathbf{Y}_J^{\mathrm{I}}\right)\right)}\boldsymbol{U}_0, \\
\boldsymbol{U}_{2,J} =& -\boldsymbol{K}_d^{-1}\left(\mu\left(\mathbf{X}\left(\mathbf{Y}^{\mathrm{m}}\right)\right)\right)\frac{\partial \boldsymbol{K}_d\left(X_J\left(\mathbf{Y}_J\right)\right)}{\partial X_J\left(\mathbf{Y}_J\right)}\boldsymbol{U}_0, \\
\boldsymbol{U}_{3,JK} =& -\boldsymbol{K}_d^{-1}\left(\mu\left(\mathbf{X}\left(\mathbf{Y}^{\mathrm{m}}\right)\right)\right)\left[2\frac{\partial \boldsymbol{K}_d\left(\mu\left(X_J\left(\mathbf{Y}_J\right)\right)\right)}{\partial X_J\left(\mathbf{Y}_J\right)}\boldsymbol{U}_{2,J}+\frac{\partial^2 \boldsymbol{K}_d\left(\mu\left(X_J\left(\mathbf{Y}_J\right)\right)\right)}{\partial X_J\left(\mathbf{Y}_J\right)\partial X_J\left(\mathbf{Y}_J^{\mathrm{I}}\right)}\boldsymbol{U}_0\right].
\end{aligned} \tag{3.11}$$

By adopting the IHPA method, the variation of the displacement response can be quickly estimated, and the structural performance can be evaluated. It is necessary to make a further discussion on the IHPA method. On the one hand, due to the high efficiency of the first-order Taylor series expansion, the number of finite element analysis (FEA) required for the uncertain objective function calculated by IHPA is greatly reduced. For a problem with n hybrid interval random variables, the total number of FEA calls is:

$$N_{calls} = 1 + 3n, \tag{3.12}$$

where N_{calls} denotes the total number of FEA calls. The amount of FEA calls increases linearly with the increase of the variable. At the same amount of FEA calls, its accuracy is much higher than that of the Monte Carlo simulation (MCS) based method. In view of the high

computational cost of topology optimization, it is very suitable for the uncertainty involved problems. On the other hand, the first-order Taylor series expansion based-perturbation method has been approved to be accurate for linear uncertainty with small variation ranges [401, 57]. Generally speaking, the IHPA method allows topology optimization to handle imprecise probabilistic parameters, and at the same time, to ensure the accuracy for evaluating uncertainties with small variation at low computational cost. The computational efficiency of this method will be demonstrated in the numerical examples, in which IHPA is compared with the MCS.

3.4 Robust structural topology optimization

In this section, we employ the IHPA to solve robust topology optimization problems for one-material structures. Two typical dynamic performance indicators in the frequency domain of the structure: dynamic compliance and eigenvalue are considered, respectively.

3.4.1 Robust dynamic-compliance topology optimization

3.4.1.1 Problem statement

In this section, we optimize the overall response level of the structure. Unlike the optimization of the local steady-state response that we described earlier in Chapter 2, this method extends the well-known compliance to the dynamic context, by which the overall vibration of the structure can be reduced. Taking uncertainty into account, the structural dynamic compliance can be expressed by:

$$C_d\left(\mathbf{X}\left(\mathbf{Y}\right)\right) = \boldsymbol{F}^T \boldsymbol{U}\left(\mathbf{X}\left(\mathbf{Y}\right)\right). \tag{3.13}$$

The robust topology optimization for this problem can be expressed by:

$$\begin{aligned} \min_{\boldsymbol{x}}: \quad & \mathscr{G} = \overline{E}\left(C_d\right) + \kappa \cdot \overline{SD}\left(C_d\right), \\ \text{s.t.}: \quad & \sum_{e=1}^{N_E} x_e V_e - \chi V_0 \leq 0, \end{aligned} \tag{3.14}$$

where $\mathscr{G}$ denotes the robust objective function, which is the linear weighted combination of the maximal expectation and standard deviation of dynamic-compliance; κ is a predefined robust parameter. The rest of symbols have been introduced in the previous chapter. Adopting the IHPA method, according to Eqs. (3.13) and (3.8), the maximal value of expectation and

standard deviation of the dynamic-compliance can be expressed by:

$$\begin{aligned}
\overline{E}\left(C_d\right) =& \boldsymbol{F}^T \left\{ \boldsymbol{U}_0 + \sum_{J=1}^{M} \sum_{K=1}^{N} \boldsymbol{U}_{1,J} \Delta\mu \left(X_J \left(Y_J^K \right) \right) S_{1,JK} \right\}, \\
\overline{SD}\left(C_d\right) =& \boldsymbol{F}^T \left\{ \sum_{J=1}^{M} \left(\boldsymbol{U}_{2,J} \boldsymbol{\sigma} \left(X_J \left(Y_J^{\mathrm{m}} \right) \right) S_{2,J} \right) + \right. \\
& \left. \sum_{K=1}^{N} \left(\boldsymbol{U}_{3,JK} \boldsymbol{\sigma} \left(X_J \left(Y_J^{\mathrm{m}} \right) \right) \Delta\mu \left(X_J \left(Y_J^K \right) \right) + \boldsymbol{U}_{2,J} \Delta\boldsymbol{\sigma} \left(X_J \left(Y_J^K \right) \right) S_{3,JK} \right) \right\},
\end{aligned} \tag{3.15}$$

where $S_{1,JK}$, $S_{2,J}$ and $S_{3,JK}$ denote the sign of relative parts respectively, namely:

$$\begin{aligned}
S_{1,JK} =& \operatorname{sign}\left(\boldsymbol{U}_{1,J} \Delta\mu \left(X_J \left(Y_J^K \right) \right) \right), \\
S_{2,J} =& \operatorname{sign}\left(\boldsymbol{U}_{2,J} \boldsymbol{\sigma} \left(X_J \left(Y_J^{\mathrm{m}} \right) \right) \right), \\
S_{3,JK} =& \operatorname{sign}\left(\boldsymbol{U}_{3,JK} \boldsymbol{\sigma} \left(X_J \left(Y_J^{\mathrm{m}} \right) \right) \Delta\mu \left(X_J \left(Y_J^K \right) \right) + \boldsymbol{U}_{2,J} \Delta\boldsymbol{\sigma} \left(X_J \left(Y_J^K \right) \right) \right).
\end{aligned} \tag{3.16}$$

Above, we should note that $S_{1,JK}$, $S_{2,J}$ and $S_{3,JK}$ are not continuous. Following [395], we propose a continuous version of the sign function by employing a regularized Heaviside step function as:

$$S\left(f\left(x_e\right)\right) = \tanh\left(\zeta \cdot f\left(x_e\right)\right), \tag{3.17}$$

where ζ is a regularization parameter. The derivation of $S\left(f\left(x_e\right)\right)$ with respect to the design variable can be expressed by:

$$\frac{\partial S\left(f\left(x_e\right)\right)}{\partial x_e} = \left(1 - \tanh^2\left(\zeta\, f\left(x_e\right)\right)\right) \left(\zeta \frac{\partial f\left(x_e\right)}{\partial x_e} \right). \tag{3.18}$$

3.4.1.2 Sensitivity analysis

The sensitivity number d_e can be obtained by processing the derivation of robust objective function with respect to the design variable x_e, as:

$$d_e = -\frac{1}{p} \frac{\partial \mathscr{G}}{\partial x_e} = -\frac{1}{p} \left(\frac{\partial \overline{E}\left(C_d\right)}{\partial x_e} + \kappa \frac{\partial \overline{SD}\left(C_d\right)}{\partial x_e} \right). \tag{3.19}$$

Using the property that the load is independent to the design variable, $\frac{\partial \overline{E}(C_d)}{\partial x_e}$ and $\frac{\partial \overline{SD}(C_d)}{\partial x_e}$ shown in (3.19) can be derived from Eqs. (3.15), (3.11) and (3.13), as:

$$
\begin{aligned}
\frac{\partial \overline{E}(C)}{\partial x_e} =& \boldsymbol{F}^T \left(\frac{\partial \boldsymbol{U}_0}{\partial x_e} + \sum_{J=1}^{M} \sum_{K=1}^{N} \left(\frac{\partial \boldsymbol{U}_{1,J}}{\partial x_e} \Delta\mu \left(X_J \left(Y_J^K \right) \right) S_{JK}^1 + \boldsymbol{U}_{1,J} \Delta\mu \left(X_J \left(Y_J^K \right) \right) \frac{\partial S_{1,JK}}{\partial x_e} \right) \right), \\
\frac{\partial \overline{SD}(C)}{\partial x_e} =& \boldsymbol{F}^T \left\{ \sum_{J=1}^{M} \left\{ \left(\frac{\partial \boldsymbol{U}_{2,J}}{\partial x_e} \sigma \left(X_J \left(Y_J^{\mathrm{m}} \right) \right) S_{2,J} + \boldsymbol{U}_{2,J} \sigma \left(X_J \left(Y_J^{\mathrm{m}} \right) \right) \frac{\partial S_{2,J}}{\partial x_e} \right) \right. \right. \\
& + \sum_{K=1}^{N} \left[\left(\frac{\partial \boldsymbol{U}_{3,JK}}{\partial x_e} \sigma \left(X_J \left(Y_J^{\mathrm{m}} \right) \right) \Delta\mu \left(X_J \left(Y_J^K \right) \right) + \frac{\partial \boldsymbol{U}_{2,J}}{\partial x_e} \Delta\sigma \left(X_J \left(Y_J^K \right) \right) \right) S_{3,JK} \right. \\
& \left. \left. \left. + \left(\boldsymbol{U}_{3,JK} \sigma \left(X_J \left(Y_J^{\mathrm{m}} \right) \right) \Delta\mu \left(X_J \left(Y_J^K \right) \right) + \boldsymbol{U}_{2,J} \Delta\sigma \left(X_J \left(Y_J^K \right) \right) \right) \frac{\partial S_{3,JK}}{\partial x_e} \right] \right\},
\end{aligned}
\tag{3.20}
$$

with

$$
\begin{aligned}
\frac{\partial \boldsymbol{U}_0}{\partial x_e} =& -\frac{\partial \boldsymbol{K}_d^{-1} \left(\mu \left(\mathbf{X} \left(\mathbf{Y}^{\mathrm{m}} \right) \right) \right)}{\partial x_e} \boldsymbol{F}, \\
\frac{\partial \boldsymbol{U}_{1,J}}{\partial x_e} =& -\frac{\partial \boldsymbol{K}_d^{-1} \left(\mu \left(\mathbf{X} \left(\mathbf{Y}^{\mathrm{m}} \right) \right) \right)}{\partial x_e} \frac{\partial \boldsymbol{K}_d \left(\mu \left(X_J \left(\mathbf{Y}_J \right) \right) \right)}{\partial \mu \left(X_J \left(\mathbf{Y}_J^{\mathrm{I}} \right) \right)} \boldsymbol{U}_0 - \boldsymbol{K}_d^{-1} \left(\mu \left(\mathbf{X} \left(\mathbf{Y}^{\mathrm{m}} \right) \right) \right) \\
& \left(\frac{\partial^2 \boldsymbol{K}_d \left(\mu \left(X_J \left(\mathbf{Y}_J \right) \right) \right)}{\partial \mu \left(X_J \left(\mathbf{Y}_J^{\mathrm{I}} \right) \right) \partial x_e} \boldsymbol{U}_0 + \frac{\partial \boldsymbol{K}_d \left(\mu \left(X_J \left(\mathbf{Y}_J \right) \right) \right)}{\partial \mu \left(X_J \left(\mathbf{Y}_J^{\mathrm{I}} \right) \right)} \frac{\partial \boldsymbol{K}_d^{-1} \left(\mu \left(\mathbf{X} \left(\mathbf{Y}^{\mathrm{m}} \right) \right) \right)}{\partial x_e} \boldsymbol{F} \right), \\
\frac{\partial \boldsymbol{U}_{2,J}}{\partial x_e} =& -\frac{\partial \boldsymbol{K}_d^{-1} \left(\mu \left(\mathbf{X} \left(\mathbf{Y}^{\mathrm{m}} \right) \right) \right)}{\partial x_e} \frac{\partial \boldsymbol{K}_d \left(X_J \left(\mathbf{Y}_J \right) \right)}{\partial X_J \left(\mathbf{Y}_J \right)} \boldsymbol{U}_0 - \boldsymbol{K}_d^{-1} \left(\mu \left(\mathbf{X} \left(\mathbf{Y}^{\mathrm{m}} \right) \right) \right) \\
& \left(\frac{\partial^2 \boldsymbol{K}_d \left(\partial X_J \left(\mathbf{Y}_J \right) \right)}{\partial X_J \left(\mathbf{Y}_J \right) \partial x_e} \boldsymbol{U}_0 + \frac{\partial \boldsymbol{K}_d \left(X_J \left(\mathbf{Y}_J \right) \right)}{\partial X_J \left(\mathbf{Y}_J \right)} \frac{\partial \boldsymbol{K}_d^{-1} \left(\mu \left(\mathbf{X} \left(\mathbf{Y}^{\mathrm{m}} \right) \right) \right)}{\partial x_e} \boldsymbol{F} \right), \\
\frac{\partial \boldsymbol{U}_{3,JK}}{\partial x_e} =& -\frac{\partial \boldsymbol{K}_d^{-1} \left(\mu \left(\mathbf{X} \left(\mathbf{Y}^{\mathrm{m}} \right) \right) \right)}{\partial x_e} \left(2 \frac{\partial \boldsymbol{K}_d \left(\mu \left(X_J \left(\mathbf{Y}_J \right) \right) \right)}{\partial X_J \left(\mathbf{Y}_J \right)} \boldsymbol{U}_{2,J} + \frac{\partial^2 \boldsymbol{K}_d \left(\mu \left(X_J \left(\mathbf{Y}_J \right) \right) \right)}{\partial X_J \left(\mathbf{Y}_J \right) \partial X_J \left(\mathbf{Y}_J^{\mathrm{I}} \right)} \boldsymbol{U}_0 \right) \\
& - \boldsymbol{K}_d^{-1} \left(\mu \left(\mathbf{X} \left(\mathbf{Y}^{\mathrm{m}} \right) \right) \right) \left\{ 2 \left[\frac{\partial^2 \boldsymbol{K}_d \left(\mu \left(X_J \left(\mathbf{Y}_J \right) \right) \right)}{\partial X_J \left(\mathbf{Y}_J \right) \partial x_e} \boldsymbol{U}_{2,J} - \frac{\partial \boldsymbol{K}_d \left(\mu \left(X_J \left(\mathbf{Y}_J \right) \right) \right)}{\partial X_J \left(\mathbf{Y}_J \right)} \right. \right. \\
& \left(\frac{\partial \boldsymbol{K}_d^{-1} \left(\mu \left(\mathbf{X} \left(\mathbf{Y}^{\mathrm{m}} \right) \right) \right)}{\partial x_e} \frac{\partial \boldsymbol{K}_d \left(X_J \left(\mathbf{Y}_J \right) \right)}{\partial X_J \left(\mathbf{Y}_J \right)} \boldsymbol{U}_0 + \boldsymbol{K}_d^{-1} \left(\mu \left(\mathbf{X} \left(\mathbf{Y}^{\mathrm{m}} \right) \right) \right) \left(\frac{\partial^2 \boldsymbol{K}_d \left(\mu \left(X_J \left(\mathbf{Y}_J \right) \right) \right)}{\partial X_J \left(\mathbf{Y}_J \right) \partial x_e} \boldsymbol{U}_0 \right. \right. \\
& \left. \left. \left. + \frac{\partial \boldsymbol{K}_d \left(\mu \left(X_J \left(\mathbf{Y}_J \right) \right) \right)}{\partial X_J \left(\mathbf{Y}_J \right)} \frac{\partial \boldsymbol{K}_d^{-1} \left(\mu \left(\mathbf{X} \left(\mathbf{Y}^{\mathrm{m}} \right) \right) \right)}{\partial x_e} \boldsymbol{F} \right) \right) \right] + \frac{\partial^3 \boldsymbol{K}_d \left(\mu \left(X_J \left(\mathbf{Y}_J \right) \right) \right)}{\partial X_J \left(\mathbf{Y}_J \right) \partial X_J \left(\mathbf{Y}_J^{\mathrm{I}} \right) \partial x_e} \boldsymbol{U}_0 \\
& \left. + \frac{\partial^2 \boldsymbol{K}_d \left(\mu \left(X_J \left(\mathbf{Y}_J \right) \right) \right)}{\partial X_J \left(\mathbf{Y}_J \right) \partial X_J \left(\mathbf{Y}_J^{\mathrm{I}} \right)} \frac{\partial \boldsymbol{K}_d^{-1} \left(\mu \left(\mathbf{X} \left(\mathbf{Y}^{\mathrm{m}} \right) \right) \right)}{\partial x_e} \boldsymbol{F} \right\},
\end{aligned}
\tag{3.21}
$$

where for a non-singular matrix $\boldsymbol{K}_d^{-1}(\mu(\mathbf{X}(\mathbf{Y}^{\mathrm{m}})))$, we have:

$$\boldsymbol{K}_d(\mu(\mathbf{X}(\mathbf{Y}^{\mathrm{m}})))\boldsymbol{K}_d^{-1}(\mu(\mathbf{X}(\mathbf{Y}^{\mathrm{m}}))) = \mathbf{I}. \tag{3.22}$$

Taking derivation of above equation, we have:

$$\frac{\partial \boldsymbol{K}_d^{-1}(\mu(\mathbf{X}(\mathbf{Y}^{\mathrm{m}})))}{\partial x_e} = -\boldsymbol{K}_d^{-1}(\mu(\mathbf{X}(\mathbf{Y}^{\mathrm{m}})))\frac{\partial \boldsymbol{K}_d(\mu(\mathbf{X}(\mathbf{Y}^{\mathrm{m}})))}{\partial x_e}\boldsymbol{K}_d^{-1}(\mu(\mathbf{X}(\mathbf{Y}^{\mathrm{m}}))). \tag{3.23}$$

3.4.2 Robust eigenvalue topology optimization

In this section, we consider an eigenvalue topology optimization. The problem can be expressed by:

$$\begin{aligned} \min_{\boldsymbol{x}}: \quad & \mathscr{G} = -\left(\overline{E}(\lambda_i) + \kappa \cdot \overline{SD}(\lambda_i)\right), \\ \text{s.t.}: \quad & \sum_{e=1}^{N_E} x_e V_e - \chi V_0 \leq 0, \end{aligned} \tag{3.24}$$

where $\mathscr{G}$ denotes the robust objective function; λ_i denotes the eigenvalue of the structure, in which the subscript i indexes its order. Here we minimize the opposite number of the linear weighted combination of the maximal expectation and standard deviation of the i-th eigenvalue. The eigenvalue without uncertainties in the free vibration problem can be solved by:

$$(\boldsymbol{K} - \lambda_i \boldsymbol{M})\varphi_i = 0, \tag{3.25}$$

where φ_i represents the eigenvector corresponding to λ_i. Based on the Rayleigh quotient, the i-th eigenvalue can be expressed by:

$$\lambda_i = \frac{\varphi_i^T \boldsymbol{K} \varphi_i}{\varphi_i^T \boldsymbol{M} \varphi_i}. \tag{3.26}$$

By adopting the IHPA method again, the robust objective function and its sensitivity can be similarly obtained, and is not repeated here.

3.4.3 Numerical examples

In this section, two numerical examples are presented. The first example considers the robust compliance topology optimization, and the last example is for robust eigenvalue topology optimization. The Young's modulus, density and Poisson's ratio of the material and the thickness of the 2D structures are assumed uncertain and follow the normal distribution.

Table 3.1 lists the hybrid interval random model based uncertain material properties with imprecise probability.

Table 3.1 Uncertain material properties and thickness with imprecise probability.

Parameters	Expectation	Standard deviation
Young's modulus, E (GPa)	[189, 231]	[18.9, 23.1]
Poisson's ratio, ν	[0.285, 0.315]	$[1.425, 1.575]\times10^{-3}$
Density, ρ (g/mm^3)	[7505, 8205]	[750, 820.5]
Thickness, t (mm)	[0.95, 1.05]	[0.0475, 0.0525]

Four-node quadrilateral finite element is adopted. The robust parameter $\kappa = 1$ is defined for these examples. For the BESO parameters, the evolutionary ratio is set to 2%, and the filter radius is 20mm. The penalty exponent p =3.0 is used. The design variable is discretely defined as x_e =1 and 0.01 to represent the solid and void elements, respectively. The volume fraction constraint is $\chi = 0.5$.

3.4.3.1 A cantilever beam for robust compliance topology optimization

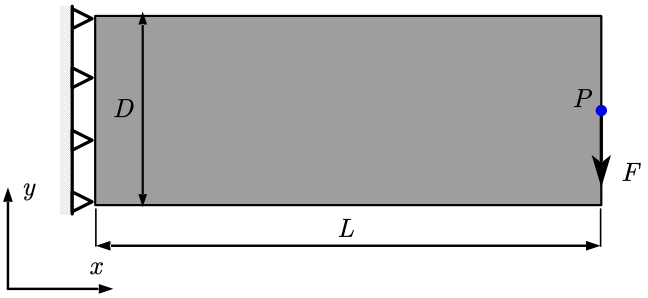

Fig. 3.3 Illustration of the cantilever beam.

In this example, a cantilever beam is considered. Fig. 3.3 illustrates the design domain, boundary conditions and external load of the cantilever beam. The length and width of this cantilever beam are $L = 900$mm and $D = 300$mm, respectively. The left end of the cantilever is fixed, and an external excitation with frequency is loaded on the middle of the right end which is marked by P. The structure is discretized by a 90×30 finite element mesh.

We first consider three different loading frequencies, namely 0Hz, 50Hz and 100Hz. Fig. 3.4 depicts the results, in which Fig. 3.4(a) and (b) are the robust topological designs for uncertain material properties and uncertain thickness, respectively, and Fig. 3.4(c) is the topology optimization based on deterministic assumption. It can be seen that the topology

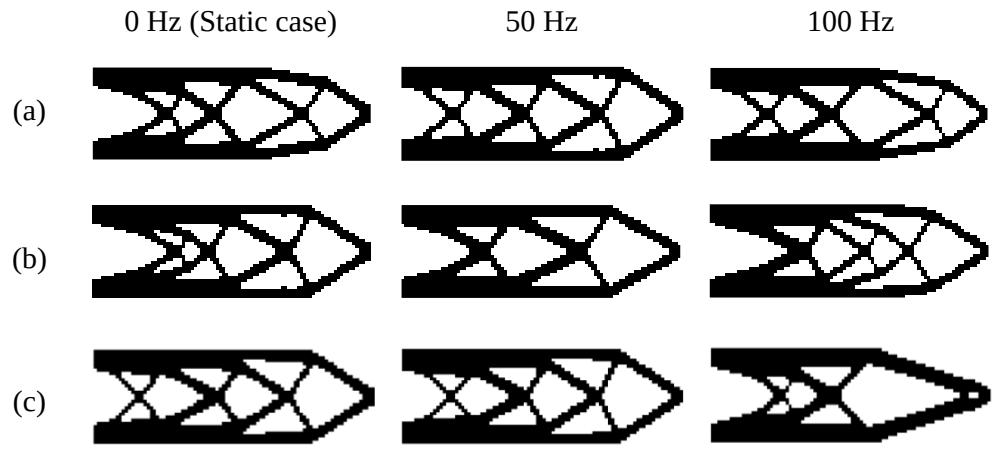

Fig. 3.4 Robust topological designs for different loading frequencies: (a) with uncertain material properties; (b) with uncertain thickness; (c) with deterministic assumption.

optimization results considering uncertainty at different excitation frequencies are not the same than those based on deterministic assumptions.

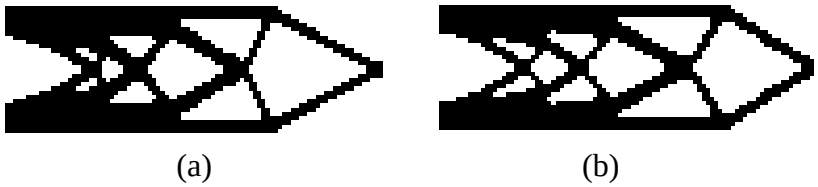

Fig. 3.5 Robust topological designs for frequency-band excitation: (a) with uncertain material properties; (b) with uncertain thickness;

Next, we consider the robust topology optimization for frequency-band excitation. The frequency-bands are discretized into integer frequencies for the sake of computational costs. Fig. 3.5 depicts the topological designs, in which Fig. 3.5(a) is the robust design for uncertain material properties and Fig. 3.5(b) shows the result for uncertain thickness. For the first case, the frequency band 10Hz-350Hz is considered. As for the second case, a frequency band 10Hz-200Hz is considered. We can observe that these designs present different topological layouts.

3.4.3.2 A Simply supported beam for robust eigenvalue topology optimization

Following [156], in this example, we consider a simply supported beam to maximize its first-order bending eigenvalue. Fig. 3.6 shows the geometry and boundary condition of the simply supported beam, in which the length and width are $L = 1600$mm and 200mm, respectively. The structure is discretized by a 160×20 finite element mesh.

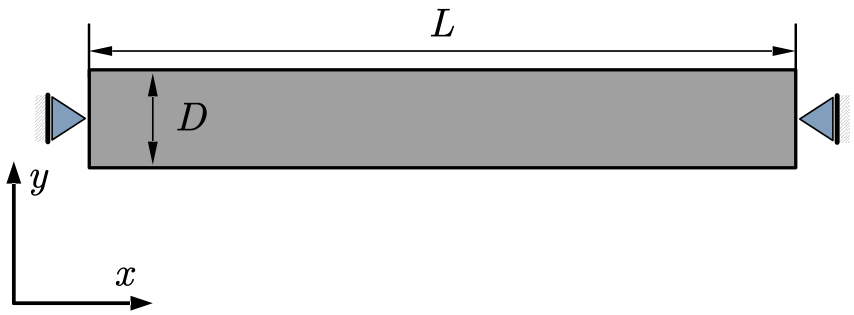

Fig. 3.6 Illustration of the simply supported beam

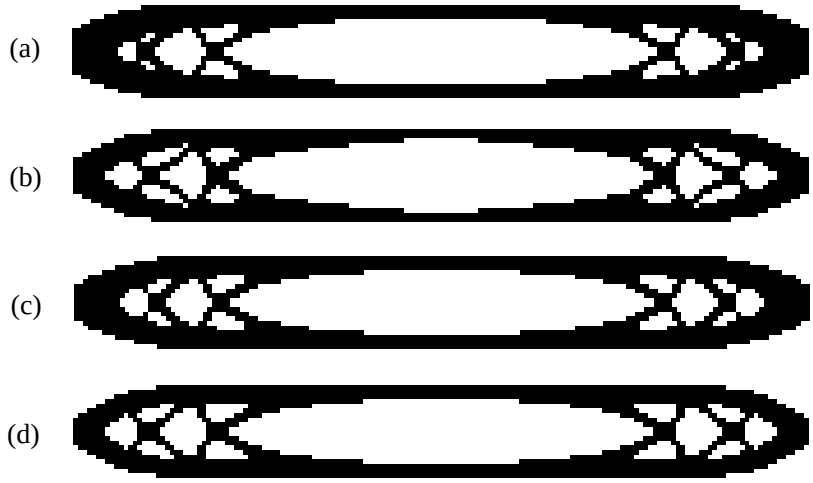

Fig. 3.7 Topological designs for maximal first-order bending eigenvalue: (a) with both uncertain material properties and uncertain thickness; (b) with uncertain material properties; (c) with uncertain thickness; (d) with deterministic assumption.

Fig. 3.7 depicts the topological designs of the simply supported beam for the maximal first-order bending eigenvalue, in which Fig. 3.7(a) simultaneously considers the uncertain material properties and thickness; Fig. 3.7 (b) and (c) involve the individual uncertain material properties and thickness, respectively; Fig. 3.7(d) is the result for deterministic assumption. It is observed that the uncertainties of material properties and geometry play an important role to the final layouts. The slight variance of material properties and geometry may result in an obvious difference between the deterministic and robust designs. This example illustrates how uncertainty affects the final design.

3.5 Application to the laminated plates

In this section, we extend the robust topology optimization to the design of laminated plates.

3.5.1 FEM modeling of the laminated plate

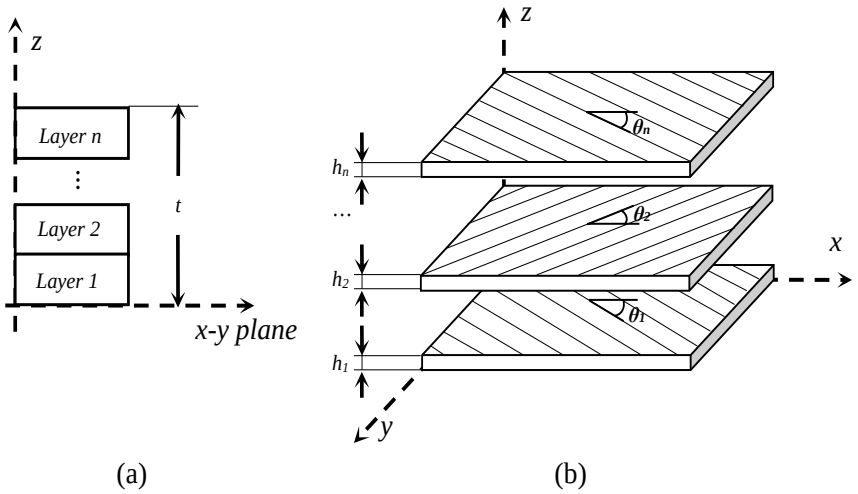

Fig. 3.8 Layered composite orthotropic plate: (a) Illustration of the layers in the thickness direction; (b) Exploded view.

For a multi-layer laminated plate, the stiffness matrix can be derived by the first-order shear deformation theory (FSDT) based on the linear elastic and orthotropic assumption [313]. As shown in Fig. 3.8, the laminate consists of n plies with the individual thickness h_k and the layer orientations θ_k. The thickness of the laminate t is equal to the sum of h_k. By assuming a null transverse normal stress σ_z, the stress-strain relation in layer k with respect to the local coordinate can be expressed by:

$$\boldsymbol{\sigma}^k_{1-2} = \begin{Bmatrix} \sigma^k_1 \\ \sigma^k_2 \\ \tau^k_{12} \\ \tau^k_{13} \\ \tau^k_{23} \end{Bmatrix} = \begin{bmatrix} Q^k_{11} & Q^k_{12} & & & \\ Q^k_{21} & Q^k_{22} & & & \\ & & Q^k_{33} & & \\ & & & Q^k_{44} & \\ & & & & Q^k_{55} \end{bmatrix} \begin{Bmatrix} \varepsilon^k_1 \\ \varepsilon^k_1 \\ \gamma^k_{12} \\ \gamma^k_{13} \\ \gamma^k_{23} \end{Bmatrix} = \mathbf{Q}^k \boldsymbol{\varepsilon}^k_{1-2}, \tag{3.27}$$

where $\mathbf{Q}^k$ denotes the plane-stress reduced elastic constant matrices of the k-th layer; Q_{ij}^k can be substituted by the material parameters as:

$$\begin{gathered} Q_{11}^k = E_1^k / \left(1 - \nu_{12}^k \nu_{21}^k\right), Q_{12}^k = \nu_{12}^k E_2^k / \left(1 - \nu_{12}^k \nu_{21}^k\right), Q_{22}^k = E_2^k / \left(1 - \nu_{12}^k \nu_{21}^k\right), \\ Q_{33}^k = G_{12}^k, Q_{44}^k = G_{23}^k, Q_{55}^k = G_{13}^k, \end{gathered} \tag{3.28}$$

where the symbols E, ν and G denote the Young's modules, Poisson's ratio and shearing modulus, respectively. The subscripts denote the directions, in which 1 denotes the principal direction and 2 means the other direction.

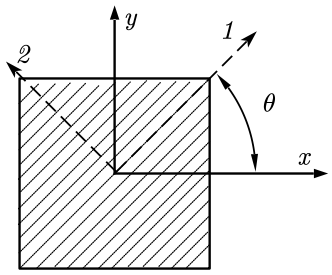

Fig. 3.9 Illustration of the relationship between 1-2 coordinate and *x*-*y* coordinate.

Fig. 3.9 illustrates the relationship between the 1-2 coordinate and *x*-*y* coordinate, which can be converted by:

$$\mathbf{T}^k = \begin{bmatrix} \cos^2\theta^k & \sin^2\theta^k & 2\sin\theta^k\cos\theta^k & & \\ \sin^2\theta^k & \cos^2\theta^k & -2\sin\theta^k\cos\theta^k & & \\ -\sin\theta^k\cos\theta^k & \sin\theta^k\cos\theta^k & \cos^2\theta^k - \sin^2\theta^k & & \\ & & & \cos\theta^k & \sin\theta^k \\ & & & \sin\theta^k & \cos\theta^k \end{bmatrix}, \tag{3.29}$$

by which, the stress-strain relations of the *k*-layer in geometrical *x*-*y* coordinate can be expressed by:

$$\begin{aligned} \sigma_{x-y}^k &= \left(\mathbf{T}^k\right)^{-1} \sigma_{1-2}^k \\ &= \left(\mathbf{T}^k\right)^{-1} \mathbf{Q}^k \left(\mathbf{T}^k \varepsilon_{x-y}^k\right) \\ &= \mathbf{D}^k \varepsilon_{x-y}^k, \end{aligned} \tag{3.30}$$

where

$$\begin{aligned} \varepsilon_{x-y}^k &= \left\{ \begin{array}{ccccc} \varepsilon_{xy}^k & \varepsilon_{yy}^k & \gamma_{xy}^k & \gamma_{xz}^k & \gamma_{yz}^k \end{array} \right\}^{\mathrm{T}}, \\ \sigma_{x-y}^k &= \left\{ \begin{array}{ccccc} \sigma_{xy}^k & \sigma_{yy}^k & \tau_{xy}^k & \tau_{xz}^k & \tau_{yz}^k \end{array} \right\}^{\mathrm{T}}, \end{aligned} \tag{3.31}$$

and $\mathbf{D}^k$ denote the elastic matrix of the *k* layer in *x*-*y* coordinate.

In the FEM framework, the elemental stiffness matrix of the composite plate can be composed by two parts as:

$$\boldsymbol{K}_e^0 = \boldsymbol{K}_e^b + \boldsymbol{K}_e^s, \tag{3.32}$$

where $\boldsymbol{K}_e^b$ and $\boldsymbol{K}_e^s$ denote the bending and shear parts, respectively, which can be represented by

$$\boldsymbol{K}_e^b = \sum_{k=1}^{n} \int_A \frac{1}{3} \left(z_{k+1} - z_k\right)^3 \left(\mathbf{B}_e^b\right)^{\mathrm{T}} \mathbf{D}_b^k \mathbf{B}_e^b dA, \tag{3.33}$$

and

$$\boldsymbol{K}_e^s = \sum_{k=1}^{n} \int_A \left(z_{k+1} - z_k\right) \left(\mathbf{B}_e^s\right)^{\mathrm{T}} \mathbf{D}_s^k \mathbf{B}_e^s dA, \tag{3.34}$$

in which n denotes the number of layers across the thickness direction, z_k is the underside coordinate of layer k in thickness direction; A denotes the area of e-th element; $\mathbf{B}_e^b$ and $\mathbf{B}_e^s$ represent the strain-displacement matrix of the bending and shear part, respectively.

The elemental mass matrix $\mathbf{M}_e^0$ does not associate to the ply orientations, whose matrix form can be directly assembled as

$$\mathbf{M}_e^0 = \int_A \rho_e \mathbf{N}^{\mathrm{T}} \mathbf{N} dA. \tag{3.35}$$

3.5.2 Numerical examples

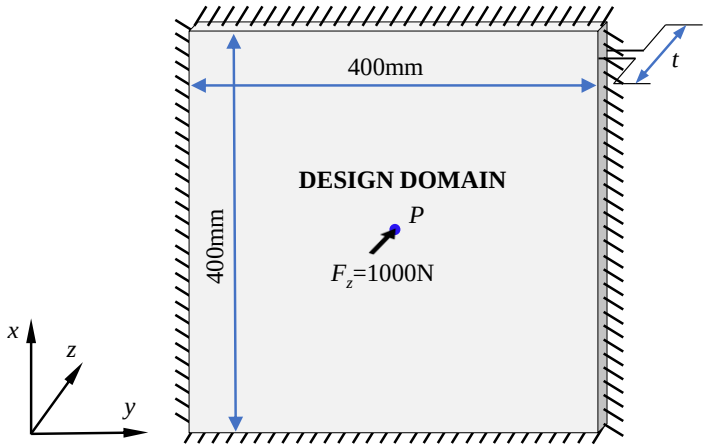

Fig. 3.10 Geometry and boundary conditions of the CCCC square plate.

In this section, we implement robust topology optimization for the laminated plates. Fig. 3.10 depicts the geometry and boundary conditions of the plate, in which the CCCC plate is clamped around, and an excitation is loaded on the center of the sandwich square plate in

z-direction. The thickness of the plate is $t = 50$mm.The design domain is discretized into a 80×80 mesh with quadratic elements in x-y plane. The BESO parameters are defined as follows: the initial design variable x_e is set to 1, and the void element $x_{\min}$ is defined as 0.001. The target volume fraction χ is 50%. The evolutionary ratio is set to 0.02, and the filter radius is 20mm. The penalty parameter p is 3, and the robust parameter is $\kappa = 1$. It is assumed that the plate is a multi-layered composite, in which each ply is composed with the same orthotropic material but in different orientations. The material properties of the orthotropic material with deterministic assumption are given in Table 3.2.

Table 3.2 The material properties of the orthotropic material with deterministic assumption.

Parameter	Unit	Value
E_{12}	GPa	135
E_{21}	GPa	13.5
G_{12}	GPa	6
G_{13}	GPa	6
G_{23}	GPa	5
ν_{12}	-	0.27
ρ	g/cm^3	1780

In the following, some of the properties are considered to be uncertain due to the realistic situations. The uncertain parameters are assumed to be independent and follow normal distribution but has imprecise probabilistic distribution. For each example, three different loading frequencies are considered. The optimal topologies of several types of laminated composite plates with different combinations of uncertainties are eventually obtained.

3.5.2.1 A symmetric 3-layer laminated composite plate with uncertain material properties

In this example, we consider an asymmetric 3-layer laminate with material uncertainty. As shown in Fig. 3.11, the plate is composed by 3 layers with ply orientation $-60^\circ/0^\circ/60^\circ$. Each layer has the same thickness h. The material has uncertain Young's modulus, Poisson's ratio and density, whose imprecise expectation and standard deviation is given in Table 3.3. The other parameters of the material are the same as Table 3.2. The structural mean-compliance in three different frequencies, 0Hz, 750Hz and 1500Hz, are optimized. The eigenfrequency of the initial design is 1938Hz.

Fig. 3.12 depicts the topological designs obtained by RTO and deterministic topology optimization (DTO) for different loading frequencies of the asymmetric 3-layer laminated plate. It can be seen that the differences of topological designs obtained by the two methods

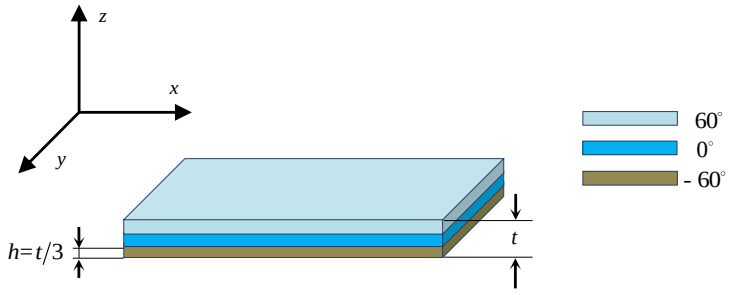

Fig. 3.11 Symmetric 3-layer laminated composite plate

Table 3.3 Uncertain material properties.

Parameter	Unit	Expectation	Standard deviation
E_{21}	GPa	[12.15, 14.85]	[1.215, 1.485]
ν_{21}	-	[0.243, 0.297]	[0.0243, 0.0297]
ρ	g/cm^3	[1701, 2079]	[170.1,207.9]

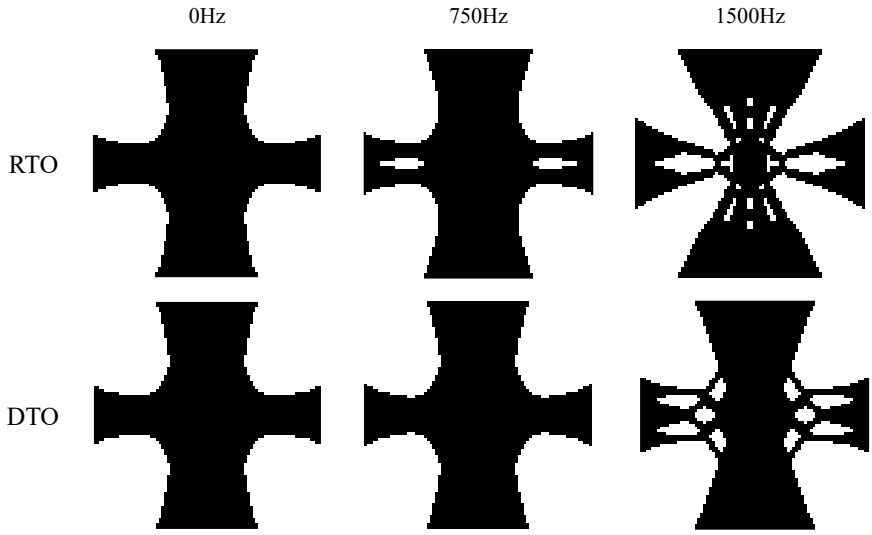

Fig. 3.12 Topological designs obtained by RTO and DTO in different loading frequencies.

becomes apparent as the excitation frequency gets closer to the eigenfrequency. This indicates that under static load, the uncertainty of the bending stiffness of the structure does not have a significant influence on the design. When it comes to dynamic situation, such uncertainty can be amplified due to its influence on the structural eigenfrequency, which has a further impact on the structure design. In addition, when the excitation frequency is close to the structural eigenfrequency, the impact of uncertainty on the structure design appears to be more obvious. Table 3.4 shows the values of robust objective function and its expectation and standard deviation of the topological designs shown in Fig. 3.12 under uncertainties. Besides, the structural eigenfrequencies in deterministic assumption are also presented. It is clear that the RTO based designs have better performance than that of DTO when it comes to uncertainties. In addition, the eigenfrequency of RTO based designs are always higher than that of DTO to prevent the structural eigenfrequency from getting too close to the excitation frequency in case of uncertainty.

Table 3.4 The objective function values of compliance and their expectation and standard deviation under uncertain material properties and structural eigenfrequency of the topologies shown in Fig. 3.12.

Loading frequency	Method	$\overline{E}(C_d)$	$\overline{SD}(C_d)$	$\mathscr{G}$	Eigenfrequency
0Hz	RTO	10.6867	0.2248	10.9115	1632
	DTO	10.6886	0.2249	10.9134	1631
750Hz	RTO	11.7430	0.4559	12.1989	1645
	DTO	11.8709	0.4595	12.3304	1637
1500Hz	RTO	31.6268	10.8266	42.4534	1838
	DTO	56.0681	35.8288	91.8969	1708

Fig. 3.13 presents the iterative histories for each loading frequency. We note that there might be abrupt jumps in the process, but the overall convergence is good.

3.5.2.2 An unequal thickness asymmetric 8-layer composite plate with simultaneous uncertainty

In this example, we consider an unequal thickness asymmetric 8-layer composite plate structure with both uncertainties of material and angle. The unequal thickness asymmetry 8-layer composite plate is shown in Fig. 3.14, which can be described as $0°h/90°2h/-45°h/45°h/-45°h/45°h/90°2h/0°h$. All the parameters are indicated in Table 3.5, and the rest of the parameters are assumed to be deterministic as shown in Table 3.2 and Fig. 3.14. The eigenfrequency of the initial design is 2042Hz.

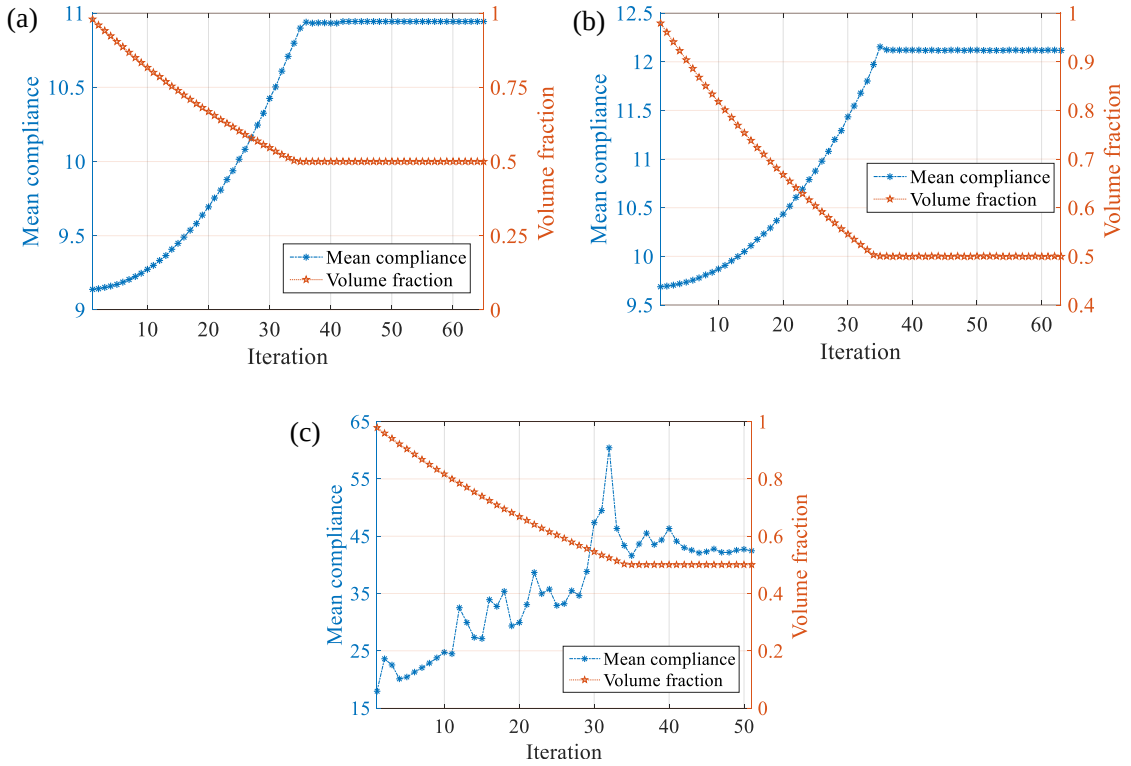

Fig. 3.13 Iteration histories of the RTO in different loading frequencies: (a) 0Hz; (b) 750Hz; (c) 1500Hz.

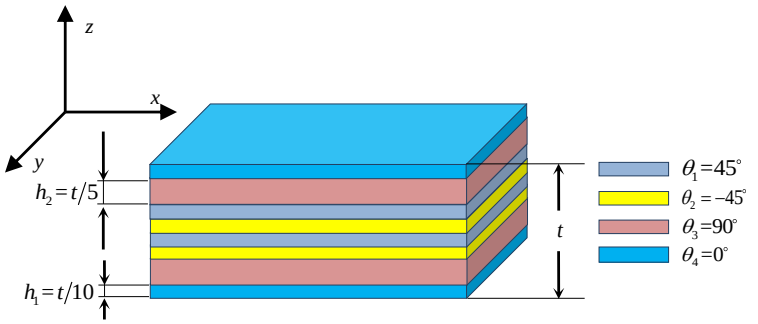

Fig. 3.14 Illustration of the unequal thickness asymmetry 8-layer composite plate

Table 3.5 Uncertain material properties.

Parameter	Unit	Expectation	standard deviation
E_{21}	GPa	[12.15, 14.85]	[1.215, 1.485]
ν_{21}	-	[0.243, 0.297]	[0.0243, 0.0297]
ρ	g/cm^3	[1701, 2079]	[170.1,207.9]
θ_1	°	[44,46]	[0.9,1.1]
θ_2	°	[-44,-46]	[0.9,1.1]

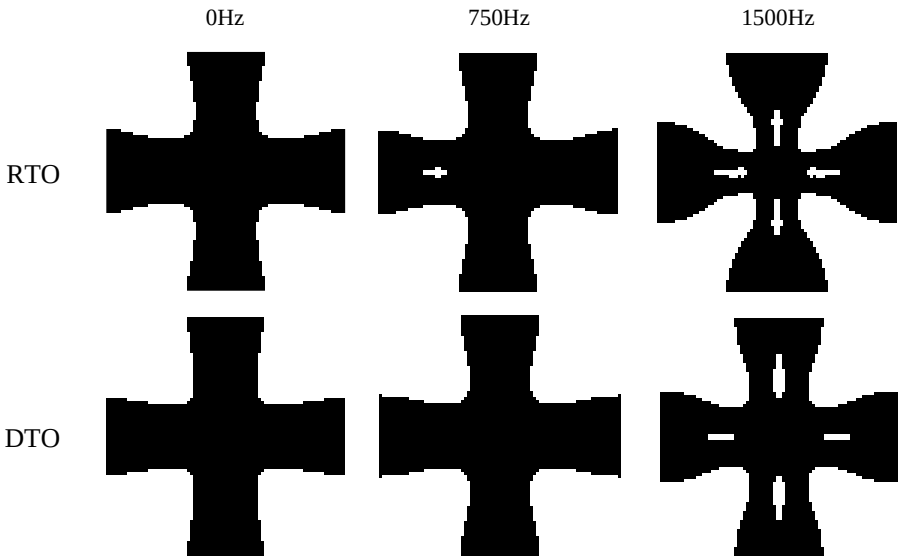

Fig. 3.15 Topological designs obtained by RTO and DTO in different loading frequencies.

Fig. 3.15 depicts the top view of the optimized unequal thickness asymmetry 8-layer composite plate obtained by the RTO and DTO. For various loading frequencies, the topological designs of RTO are different from that of DTO. Table 3.6 shows the value of the robust objective function and their expectation and standard deviation under uncertainties and the eigenfrequency in deterministic assumption. By comparison, the RTO designs are better than the DTO designs, especially for the case with high-frequency load. Fig. 3.16 presents the evolutionary histories of the RTO in each frequency, which shows that there is no convergence difficulty in the optimization process.

Table 3.6 The objective function values of compliance and their expectation and standard deviation under uncertain material properties and structural eigenfrequency of the topologies shown in Fig. 3.15.

Loading frequency	Method	$\overline{E}(C_d)$	$\overline{SD}(C_d)$	$\mathscr{G}$	Eigenfrequency
0Hz	RTO	10.5007	0.4215	10.9222	1769
	DTO	10.5211	0.4234	10.9445	1763
750Hz	RTO	11.4654	0.6508	12.1162	1780
	DTO	11.4868	0.6578	12.1446	1774
1500Hz	RTO	21.4951	5.4772	26.9723	1965
	DTO	25.5157	9.4077	34.9234	1845

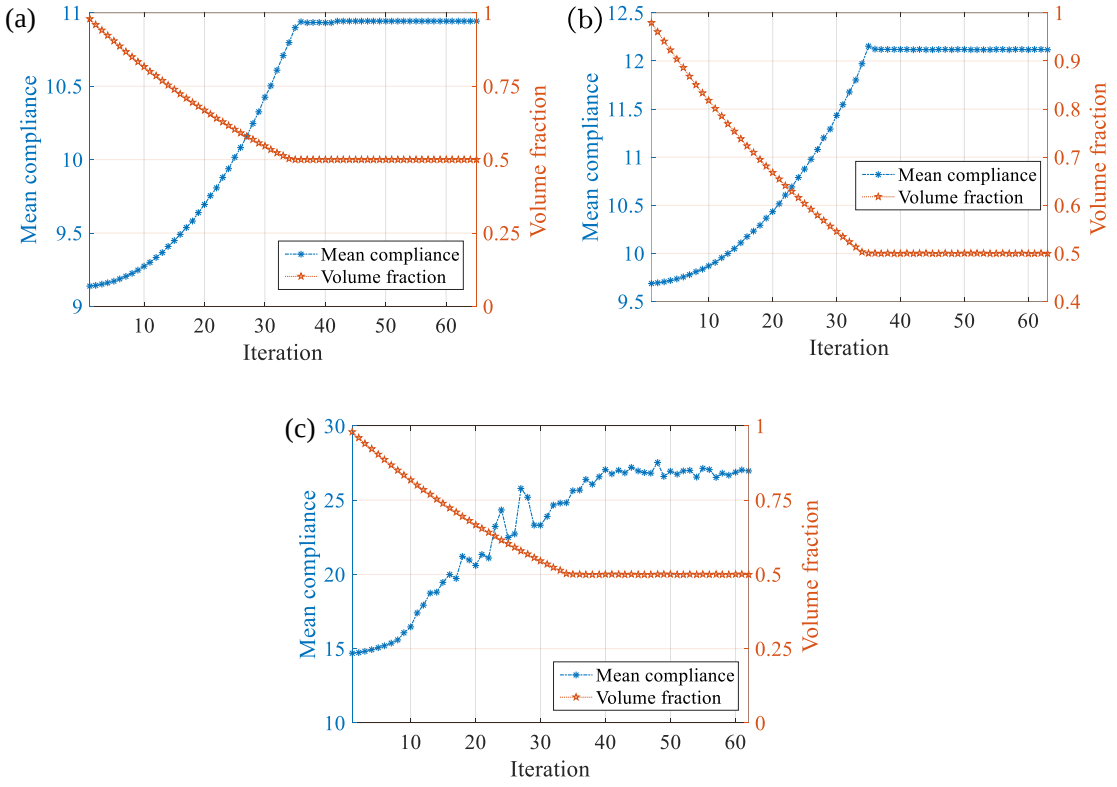

Fig. 3.16 Iteration histories of the RTO in different loading frequencies: (a) 0Hz; (b) 750Hz; (c) 1500Hz.

3.6 Robust concurrent topology optimization of structure and its composite material

In this section, we extend the proposed method to the concurrent design of two-scale composite structures.

3.6.1 Concurrent topology optimization

Consider a two-scale structure as shown in Fig. 3.17, it is assumed that the boundary condition and external excitation of the macro-structure are already known. Fig. 3.17(b) represents the micro-structure of composite material that constructs the macro-structure. The micro-structure is composed of two basic materials: phase 1 in blue and phase 2 in pink. Assume that the composite material is constituted by periodic unit cell (PUC), which can be represented by Fig. 3.17(c). We use x_a and x_i to express the design variable at macro- and micro-scales, respectively, and NE and Ne denote their amount. For the convenience of

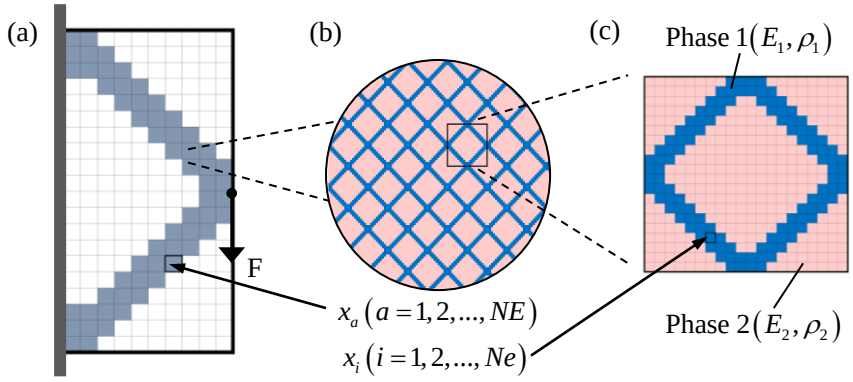

Fig. 3.17 Composite material composed two-scale structure: (a) macro-structure; (b) micro-structure of composite material; (c) periodic unit cell (PUC).

distinction, we use subscripts 1 and 2 to index the density and elasticity modulus of phase 1 and phase 2, respectively.

The concurrent topology optimization (CTO) for minimal dynamic-compliance of the two-scale structure can be expressed by:

$$\begin{aligned} \min_{x_a,x_i}: \quad & C_d, \\ \text{s.t.}: \quad & C_d = \boldsymbol{F}^T \boldsymbol{U}, \\ & m(x_a,x_i) - \chi m_0 \leq 0, \end{aligned} \tag{3.36}$$

where the objective function C_d is the structural compliance. At the micro-scale, $x_i = x_{\min}$ or 1 identifies the distribution of the two-phase composite, in which $x_i = 1$ defines the i-th element as phase 1, otherwise it is filled by phase 2. By adopting the solid isotropic material with penalization (SIMP) scheme, the density and elasticity matrix of the i-th element can be associated with design variable, namely:

$$\begin{aligned} \rho_i(x_i) =& x_i\rho_1 + (1-x_i)\rho_2, \\ \mathbf{C}_i(x_i) =& x_i^p \mathbf{C}_1 + \left(1-x_i^p\right)\mathbf{C}_2, \end{aligned} \tag{3.37}$$

where p denotes the penalization index. For each PUC, their effective density and elasticity matrix $\rho^H(x_i)$ and $\mathbf{C}^H(x_i)$ can be obtained from the numerical homogenization theory [142, 427] when the base cell is very small compared to the size of the structure. The

effective properties of the PUC with material interpolation scheme is directly given by

$$\begin{aligned}\rho^H(x_i) =& \frac{1}{|Y|}\sum_{i=1}^{Ne} V_i\left[x_i\rho_1 + (1-x_i)\rho_2\right],\\ \mathbf{C}^H(x_i) =& \frac{1}{|Y|}\sum_{i=1}^{Ne}\int_Y (\varepsilon_0-\varepsilon)^T\left[x_i^p\mathbf{C}_1 + \left(1-x_i^p\right)\mathbf{C}_2\right](\varepsilon_0-\varepsilon)\,dY,\end{aligned} \tag{3.38}$$

where V_i is the volume of the i-th element on micro-scale; $|Y|$ denotes the total volume (area for 2D cases) of the PUC; ε_0 is the unit test strains, e.g. $[1,0,0]^T$, $[0,1,0]^T$, $[0,0,1]^T$, for 2D cases. The strain fields ε are induced by these test strains with the periodical boundary conditions. We denote that the effective density and elasticity matrix depend on the distribution of design variables on the micro-scale. For more details on this formulation, one may refer to e.g. [337, 141].

At the macro-scale, $x_a = x_{\min}$ or 1 determines whether the element is void or solid, respectively, in which the solid elements are constructed by two-phase composite. Following [156], an alternative interpolation scheme is adopted to avoid the so-called *artificial modal* [302] phenomenon. This interpolation can be expressed by:

$$\begin{aligned}\rho_a(x_a,x_i) =& x_a\rho^H(x_i),\\ \mathbf{C}_a(x_a,x_i) =& \left[\frac{x_{\min}-x_{\min}^p}{1-x_{\min}^p}\left(1-x_a^p\right)+x_a^p\right]\mathbf{C}^H(x_i).\end{aligned} \tag{3.39}$$

In Eq. (3.36), χ denotes the target mass fraction and $m_0 = \sum_{a=1}^{NE} V_a\rho_1$ is the mass of the full filled design. The mass of the topological design $m(x_a,x_i)$ can be expressed by:

$$m(x_a,x_i) = \sum_{a=1}^{NE} x_a V_a \rho^H(x_i). \tag{3.40}$$

Here, we note that there are many kinds of multi-scale topology optimization methods (see e.g. [115] for a review), in most of which the volume fractions on each scale were arbitrarily appointed separately. This artificial volume distribution would limit the final structural performance. In this work, we perform the topology optimization of macro- and micro- structures under a uniform weight constraint [416]. To this end, the sensitivity on both scales is treated as follows:

$$\begin{aligned}\xi_a =& d_a \Big/ \frac{\partial m}{\partial x_a},\\ \xi_i =& d_i \Big/ \frac{\partial m}{\partial x_i},\end{aligned} \tag{3.41}$$

where ξ_a and ξ_i denote the finalized sensitivity number on the macro-scale and micro-scale, respectively; $\frac{\partial m}{\partial x_a}$ and $\frac{\partial m}{\partial x_i}$ are the variations of the total weight m to the design variables on macro- and micro- scales. From Eqs. (3.37)-(3.39), we obtained:

$$\begin{aligned} \frac{\partial m}{\partial x_a} &= V_a \rho^H (x_i), \\ \frac{\partial m}{\partial x_i} &= \frac{V_i}{|Y|} (\rho_1 - \rho_2) \sum_{a=1}^{NE} x_a V_a. \end{aligned} \tag{3.42}$$

3.6.2 Robust concurrent topology optimization

Based on the IHPA method, the robust concurrent topology optimization (RCTO) for the dynamic-compliance minimizing can be mathematically stated by:

$$\begin{aligned} \min_{x_a, x_i} : \quad & \mathscr{G} = \overline{E}(C_d) + \kappa \overline{SD}(C_d), \\ \text{s.t.} : \quad & m(x_a, x_i) - \chi m_0 \leq 0. \end{aligned} \tag{3.43}$$

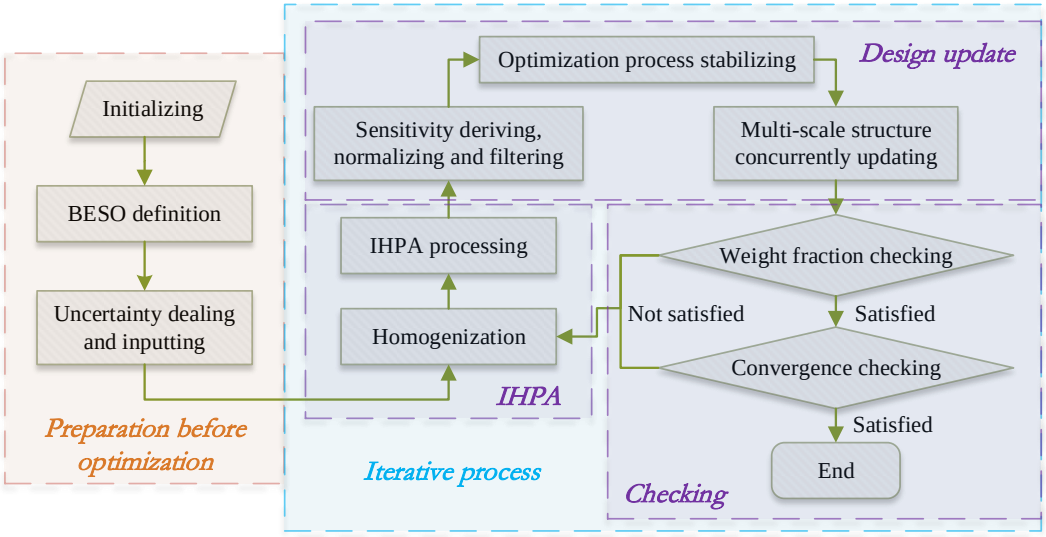

Fig. 3.18 Flow chart of the RCTO procedure.

Fig. 3.18 shows the flowchart of the RCTO procedure, and its detailed explanation is outlined as follows:

Step 1: Initializing: Carry out the finite element mesh. Initialize the original design of the macro-structure and the micro-structure by defining x_a and x_i.

Step 2: BESO definition: Define the BESO parameters such as the target weight fraction χ, the evolutionary ratio ER and the filter radius for macro-scale $r_{\min}^{\mathrm{mac}}$ and micro-scale $r_{\min}^{\mathrm{mic}}$.

Step 3: Uncertainty modeling: Use the hybrid interval random model to describe the uncertain parameters with imprecise probability. Input some important distribution parameters, for instance, the expectation and standard deviation.

Step 4: Homogenization: Calculate the effective property of PUC. Meanwhile, derive the partial derivatives of the effective elastic matrix and the effective density matrix with respect to the related uncertain parameter.

Step 5: IHPA processing: Perform IHPA as shown in Section 3.3. Carry out the maximal expectation $\overline{E}$ and standard deviation $\overline{SD}$ of the robust objective function.

Step 6: Sensitivity deriving, normalizing and filtering: Calculate the sensitivity of the objective function to design variables at each scales; Process the sensitivity by Eq. (3.41) to for the concurrent design; Perform sensitivity filtering as shown in Eq. (2.28).

Step 7: Optimization process stabilizing: For the l-th iteration ($l > 1$), average the sensitivity with its history value as shown in Eq. (2.30).

Step 8: Multi-scale structure concurrently updating: Reconstruct the macro-structure and composite material according to the ranking of the elemental sensitivity numbers at both scales. With the limitation of weight fraction χ, the design variables of the element of high sensitivity are assigned to 1, the others are assigned to 10^{-6}. As a result, the topologies of both scales are updated concurrently.

Step 9: Weight fraction checking: Repeat Steps 4-8 when the weight fraction of current iteration does not meet the target weight fraction. And then determine the target weight fraction of the two-scale system for the next iteration as follows

$$\chi^{l+1} = \chi^{l}\left(1 \pm ER\right), \tag{3.44}$$

in which, the weight fraction is reduced when the current weight fraction χ^{l} is larger than χ; otherwise the weight fraction is increased.

Step 10: Convergence checking: Repeat Step 4-9 until the objective function is convergent. The convergence criterion has been presented in Eq. (2.32).

Step 11: End: Output the final robust design of structure and its composite material.

3.6.3 Numerical examples

In this section, both of 2D and 3D numerical examples are presented. For the 2D cases, the design domain is discretized by four nodes quadrilateral elements at both scales. The size of PUCs is 1mm×1mm, which is divided into a 50×50 finite element mesh. For the 3D case, the design domain is meshed by 1mm×1mm×1mm hexahedral elements, which is divided into a 14×14×14 finite element mesh. Fig. 3.19 shows the initial design of PUC, where the elements in blue denote phase 1 and the green ones represent phase 2. Based on the BESO framework, the initial design of macro-structure is a full design with initial design variable $x_a = 1$ and $x_{\min} = 10^{-6}$ is adopted in this work. The penalty parameters p at both scales are 3 and the evolutionary ratio ER is 0.02. The filter radius is 3 times of the elemental side length at each scale.

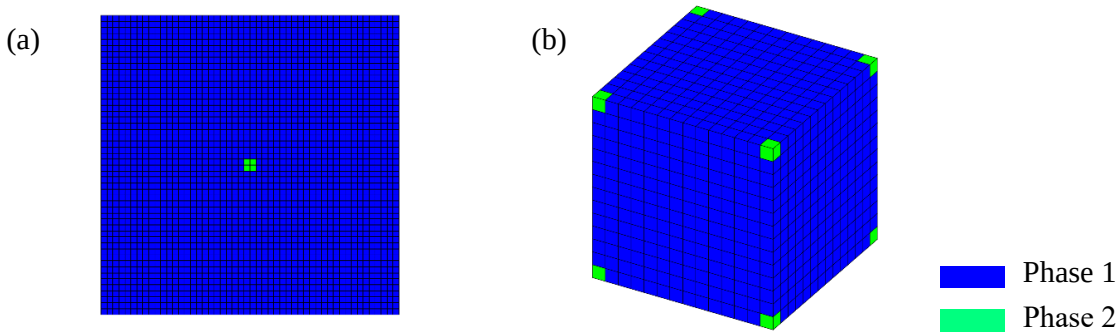

Fig. 3.19 Initial designs of PUC: (a) for 2D case; (b) for 3D case.

Table 3.7 Material properties adopted in this section.

Material	Properties	Expectation	Standard deviation
Phase 1	Young's modulus (GPa)	[190, 210]	[19, 21]
	Poisson's ratio	[0.285, 0.315]	$[1.425, 1.575]\times10^{-3}$
	Density (g/mm^3)	[7900, 8100]	[790, 810]
Phase 2	Young's modulus (GPa)	[140, 160]	[14, 16]
	Poisson's ratio	[0.285, 0.315]	$[1.425, 1.575]\times10^{-3}$
	Density (g/mm^3)	[790, 810]	[79, 81]

Table 3.7 shows the uncertain material properties adopted in this section, in which the parameters are assumed to follow normal distribution and the expectation and standard deviation are interval value. We should note that the normal distribution is not bounded, by which there might be some extreme conditions, where the Young's modulus or density has negative value. To solve such rare phenomena, one may refer to [397].

3.6.3.1 Cantilever beam with different robust optimization parameter κ

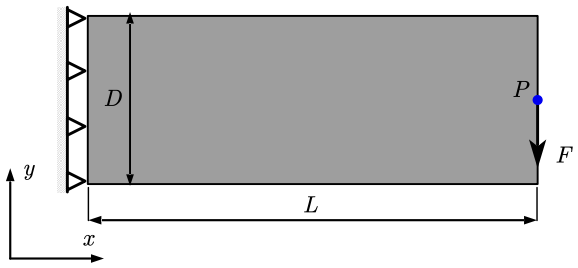

Fig. 3.20 Illustration of the cantilever beam.

In this example, various robust optimization parameters κ are considered. The geometry and boundary condition of the 2D cantilever beam are shown in Fig. 3.20. The length and height of the design domain are 120mm and 40mm respectively. The force is assumed to be periodic, with an amplitude of 1000N and a frequency of 500Hz. The total weight constraint is 50%. Three different robust optimization parameters $\kappa = 1$, 3 and 5 are employed.

Fig. 3.21 shows the results of DCTO and RCTO. It is observed that there are differences in both layouts of macro-structure and PUC. With different robust parameter κ, the topological designs are also changed. These results show that RCTO can figure out topological designs different from DCTO. Corresponding comparison on objective function value of the designs shown in Fig. 3.21 are provided in Table 3.8, in which the values are predicted by the proposed IHPA method. It can be seen that the compliance of the RCTO designs are lower than the DCTO-based design, which means that the proposed RCTO performs better than the DCTO when it comes uncertainty. The value of compliance decreases gradually with increasing κ.

Table 3.8 Objective function values of results shown in Fig. 3.21 with uncertainties.

Method	Value of objective function	Difference
DCTO	842.3289	-
RCTO,$\kappa = 1$	830.5541	-11.7748
RCTO,$\kappa = 3$	824.9767	-17.3522
RCTO,$\kappa = 5$	824.5547	-17.7742

Table 3.9 compares the results simulated by IHPA and MCS to confirm the accuracy of IHPA. In the implementation of the MCS, we adopt a sample size of 10^6, in which the sample size of the random variable and interval values are both 10^3. The FEA calls for IHPA and MCS are 16 and 10^6, respectively. Two conclusions can be drawn from the comparison:

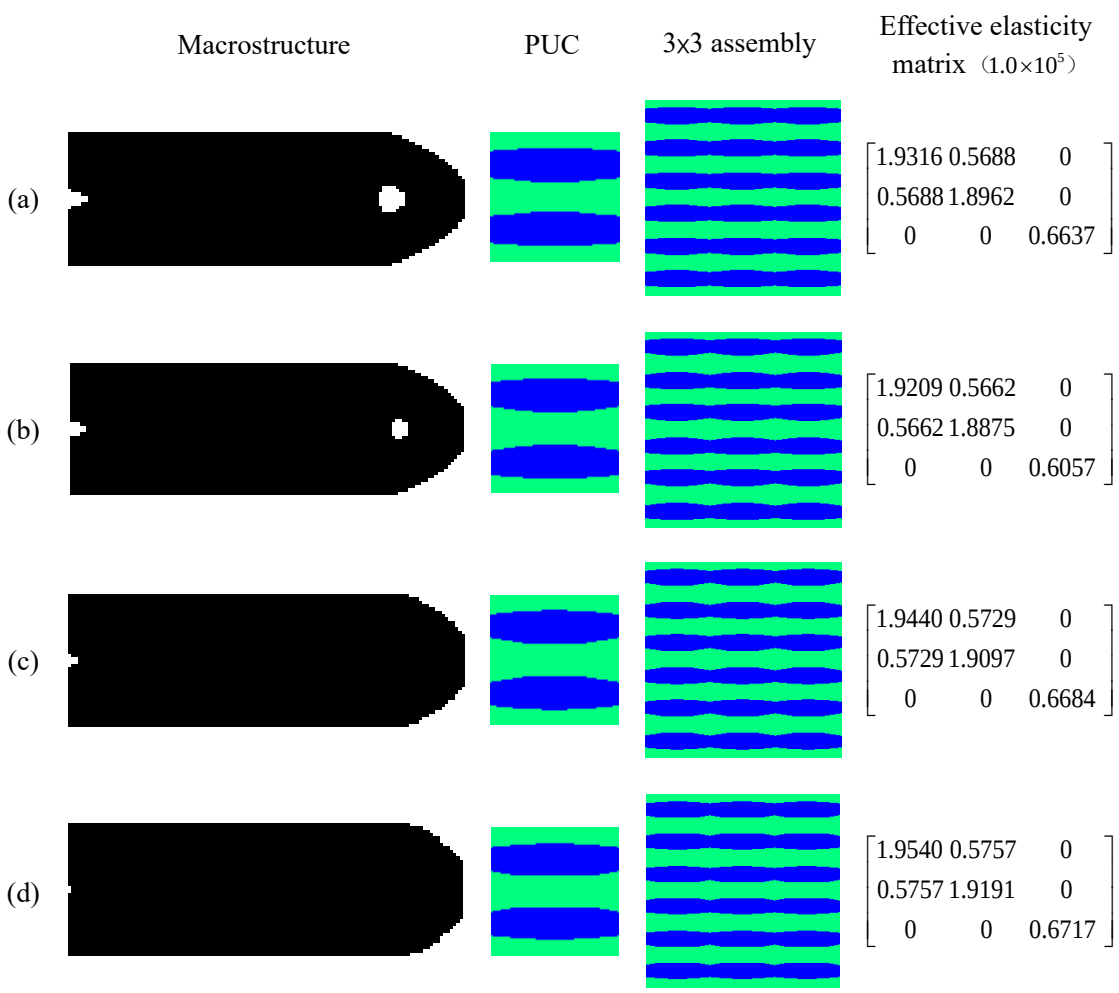

Fig. 3.21 Topological designs of the macro-structure, PUC, 3x3 assembled PUC and the effective elasticity matrix: (a) DCTO; (b) $\kappa = 1$; (c) $\kappa = 3$; (d) $\kappa = 5$.

On the one hand, there are some errors of the IHPA results compared to the MCS, which are within acceptable limits. On the other hand, the IHPA calculates the worst-case objective function with only 16 FEA calls, which is a great improvement over the MCS that requires 10^6 times of FEA calls.

3.6.3.2 Michell-type structure with different weight constraint

In this example, we consider a Michell-type structure. Fig. 3.22 depicts the Michell-type structure, in which the length and height of the structure are 90mm and 40mm, respectively. The force is is applied at the bottom center of the structure, with an amplitude of 1000N and a frequency of 2000Hz. Three different weight constraints: 75%, 40% and 5% are employed. The robust parameter is $\kappa = 1$. Fig. 3.23 depicts the topological designs of RCTO and DCTO

Table 3.9 Accuracy confirmation of IHPA and by comparing with MCS on the objective function value.

Topological design	IHPA	MCS	Relative errors
DCTO	842.3289	855.6219	1.55%
RCTO,$\kappa = 1$	830.5541	844.7816	1.68%
RCTO,$\kappa = 3$	824.9767	838.1235	1.57%
RCTO,$\kappa = 5$	824.5547	836.6609	1.45%

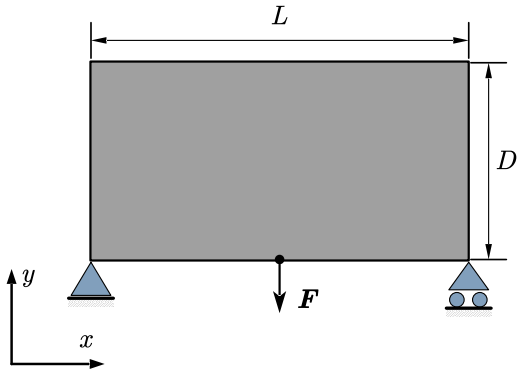

Fig. 3.22 Geometry and boundary condition of the Michell-type structure

with different weight constraints. The optimal distributions of macro-structure and PUC have different forms under different target weight fraction. By comparing the robust and deterministic design under different volumes, the topological distributions of the two designs are also significantly different. Table 3.10 compares the objective function value of these designs and all the values are calculated by IHPA. The comparison shows that under the same weight fraction, the result obtained by RCTO is smaller than that obtained by DCTO. It illustrates that the proposed RCTO method performs better when it comes to uncertainties.

Table 3.10 Objective function values of the designs shown in Fig. 3.23.

Weight constraint	RCTO	DCTO
75%	73.0651	74.9310
40%	78.8372	79.6482
5%	277.1851	282.0695

Fig. 3.24 shows the iteration history of RCTO with different weight fraction constraints, where Fig. 3.24(a), (b) and (c) represent the case of χ =75%, χ =40% and χ =5% re-

spectively and some intermediate topology designs are also provided. It illustrates that the proposed RCTO method has no convergence difficulties.

3.6.3.3 3D prismatic structure

Fig. 3.25 depicts a 3D prismatic structure with fixed left side. The length, width and height of the structure are 24mm, 8mm and 8mm, respectively. The design domain is discretized into $24 \times 8 \times 8$ eight-node hexahedral elements. A periodic force F with a magnitude of 1000N is loaded on the right bottom of the structure. The weight constraint is defined as 70% in this example. Two different excitation frequencies, 1000Hz and 2000Hz are considered. The robust optimization weight parameter is set to $\kappa = 1$.

Fig. 3.26 shows the topological designs of the two-scale 3D prismatic structure, in which the volume fraction of solid and phase 1 on the corresponding scale are all shown. The RCTO and DCTO designs are compared directly. It can be observed that both approaches work well. The corresponding topological layouts of the macro-structures and composite micro-structures are figured out. The results that the final designs of the structure are different due to the loading frequency, which indicates that it is necessary to optimize separately for different frequencies. By comparing the optimization results under different excitation frequencies, it can be found that the topology configurations obtained by RCTO and DCTO are also quite different for the existence of uncertainty. Such differences in design will lead to performance changes under uncertain conditions.

Table 3.11 Objective function values of the designs shown in Fig. 3.26

Frequency (Hz)	RCTO	DCTO
1000	59.6613	59.7918
2000	63.3583	64.1979

Table 3.11 shows the objective function value of different topological designs shown in Fig. 3.26. All the results are calculated by the IHPA method. By comparison, it is found that the results of RCTO are smaller than that of DCTO. That means that the proposed method can better realize concurrent topology optimization under imprecise uncertainty. This proves the robustness of the proposed RCTO method, which performs better than the traditional DCTO method under the hybrid interval random modeled imprecise uncertainty, again.

3.7 Conclusion

In this Chapter, we investigated the robust topology optimization method for the uncertainties with imprecise quantities in frequency-domain dynamic structures. A hybrid interval random model was employed to describe the probabilistic parameters. An improved hybrid perturbation analysis method was developed for efficiently estimating the dynamic performances of the structures at very low computational costs. We have applied this approach to several structures, including conventional one material structures, laminated composite plates and multi-scale composite structures. The numerical examples have illustrated the efficiency of the proposed method.

In general, the proposed method has potential to deal with the uncertainties that may be encountered in topology optimization for practical engineering. However, we should also note that the this method might not be applicable if the problem is of high nonlinearity or the uncertainty is of strong correlation and spatial dependency.

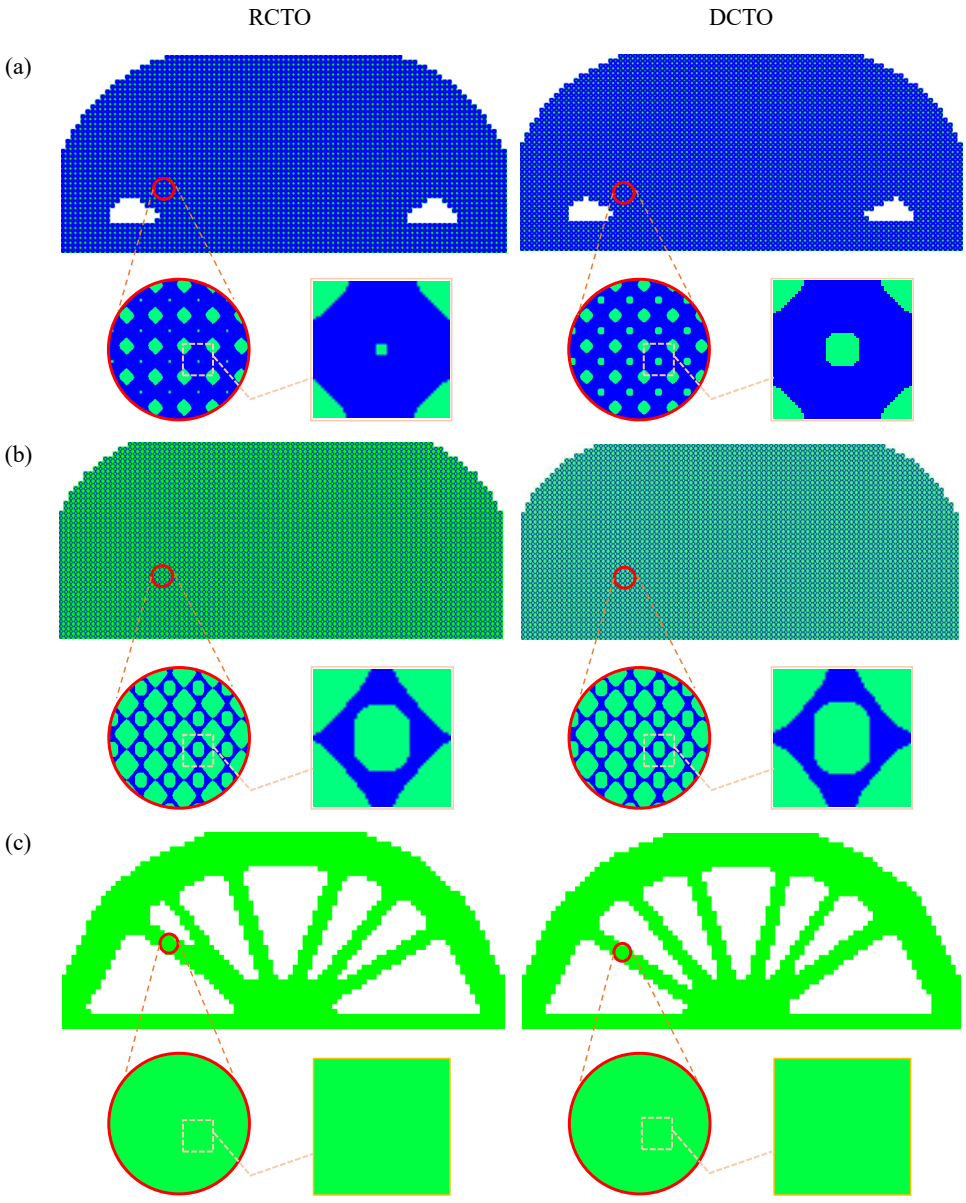

Fig. 3.23 Topological designs of the 2D Michell-type structure acquired by RCTO (left) and DCTO (right) with different weight fraction constraints: (a) χ =75%; (b) χ =40%; (c)χ =5%.

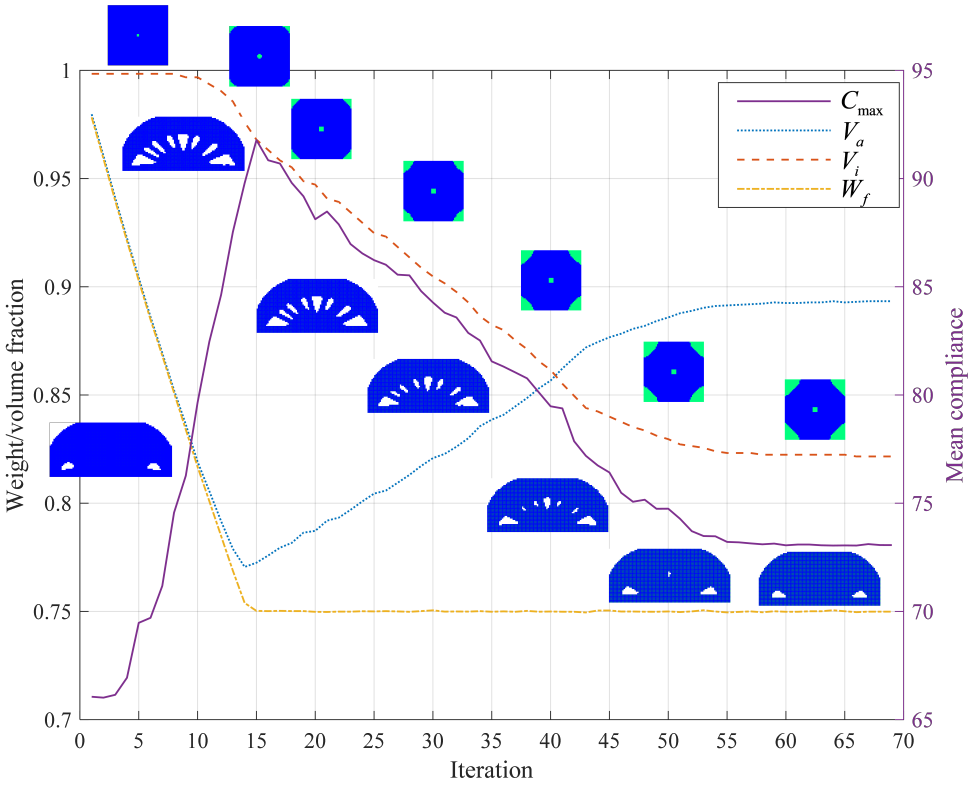
Weight/volume fraction
Mean compliance
Iteration
$C_{\max}$
V_a
V_i
W_f

(a)

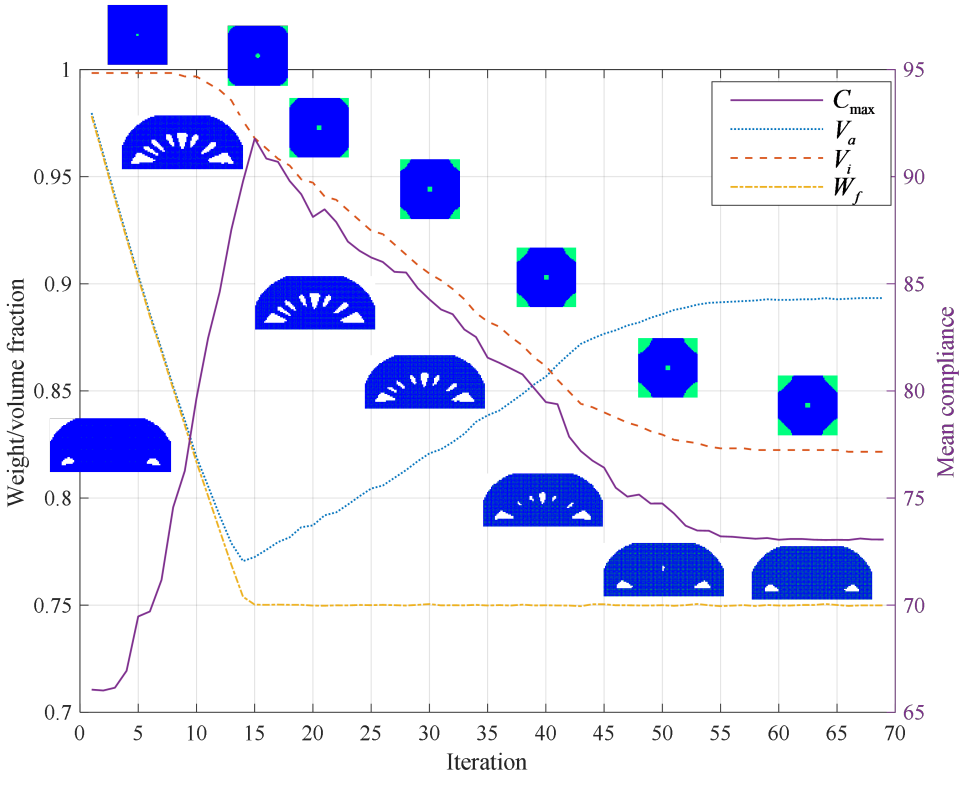
Weight/volume fraction
Mean compliance
Iteration
$C_{\max}$
V_a
V_i
W_f

(b)

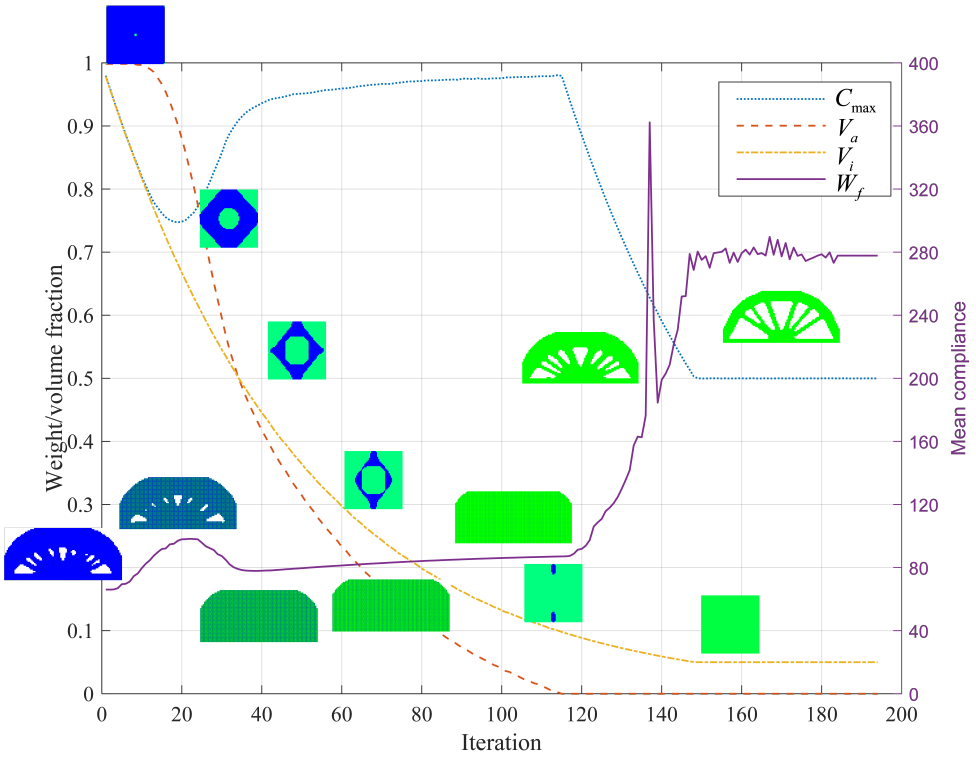

(c)

Fig. 3.24 Iteration history of the Michel-type structure with different weight fraction constraints: (a) χ =75%; (b) χ =40%; (c)χ =5%.

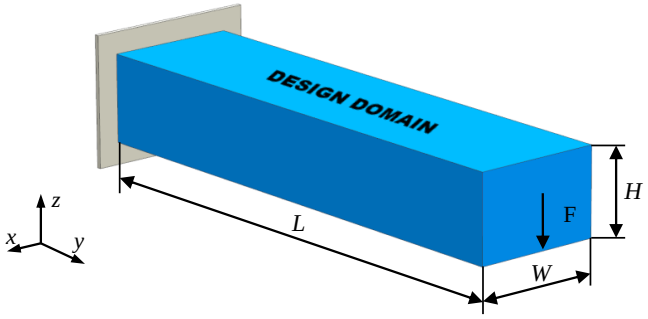

Fig. 3.25 Illustration of the 3D prismatic structure.

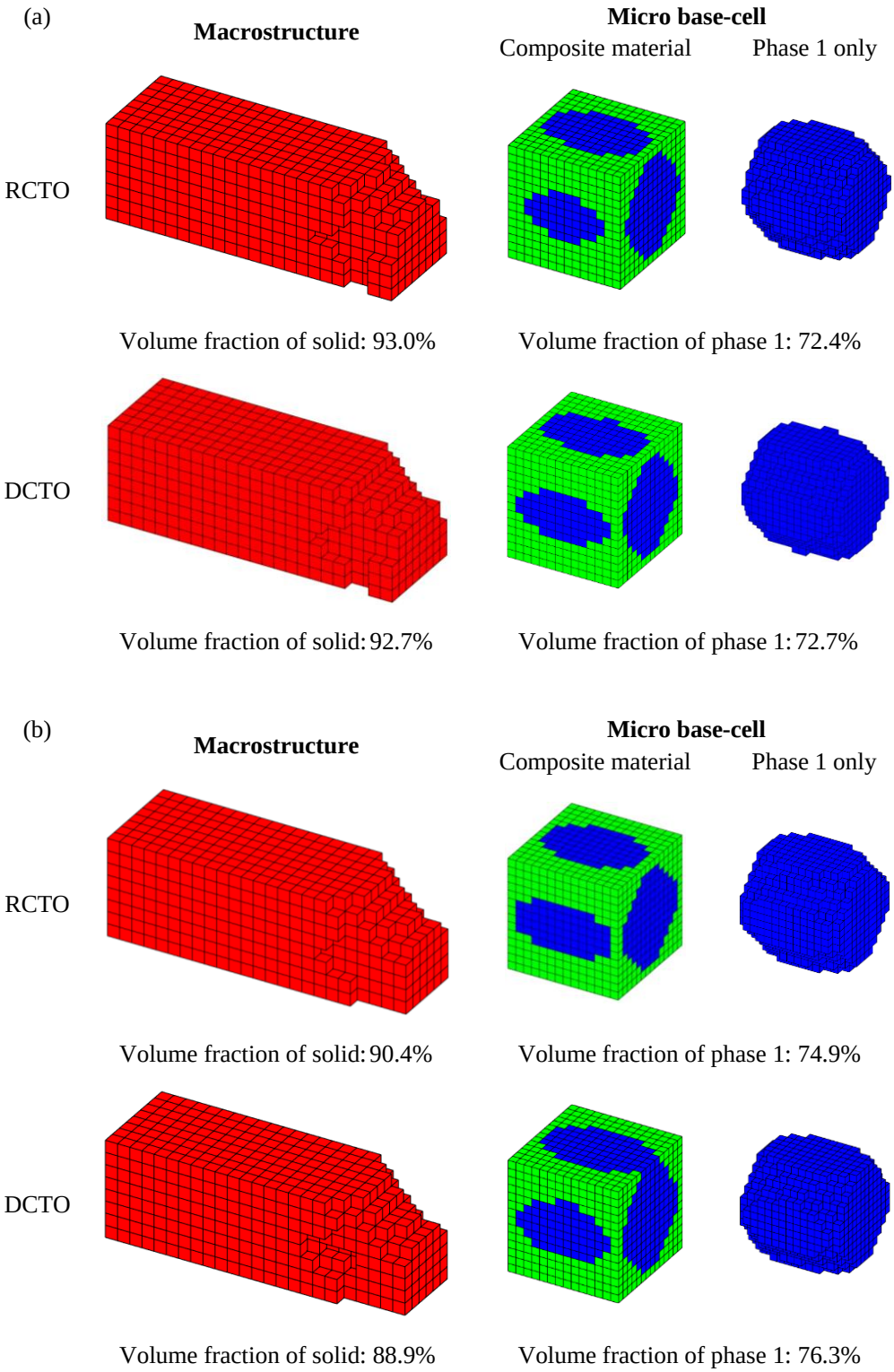

Fig. 3.26 Topological designs of the two-scale 3D prismatic structure under different loading frequencies: (a) 1000Hz; (b) 2000Hz.

Chapter 4

Introducing interval-field uncertainties in topology optimization

4.1 Introduction

In this Chapter, we propose to introduce non-probabilistic uncertainty with spatial dependence into topology optimization. A recently emerged interval field model [280] is employed for modeling the spatially varied non-probabilistic uncertainties. The uncertain material properties and loading are considered. Based on the robust topology optimization framework, we investigate an interval-field based perturbation analysis (IFPA) method to predict the median and radius of structural compliance under uncertainties, and derive the corresponding expressions of sensitivity analysis. We illustrate the accuracy and efficiency of the IFPA in predicting the structural compliance by compared with the Monte-Carlo Simulations. The numerical examples illustrate the potential of employing such spatially-varied interval uncertainties in topology optimization.

4.2 Brief review of interval field model

In this section, we briefly review the interval field model and interval Karhunen-Loève (K-L) expansion method proposed by Ni and Jiang [280].

4.2.1 Definition of interval field

A spatially varied uncertain-but-bounded quantity can be denoted by $\mathscr{Z}(\mathbf{x}) \in \mathscr{Z}^I(\mathbf{x})$, in which $\mathscr{Z}$ denotes the uncertain parameter. It is a scalar related to its spatial location $\mathbf{x}$; $\mathscr{Z}^I$ represents the interval of this uncertainty. For a given spatial point $\mathbf{x}_k$, the interval of the

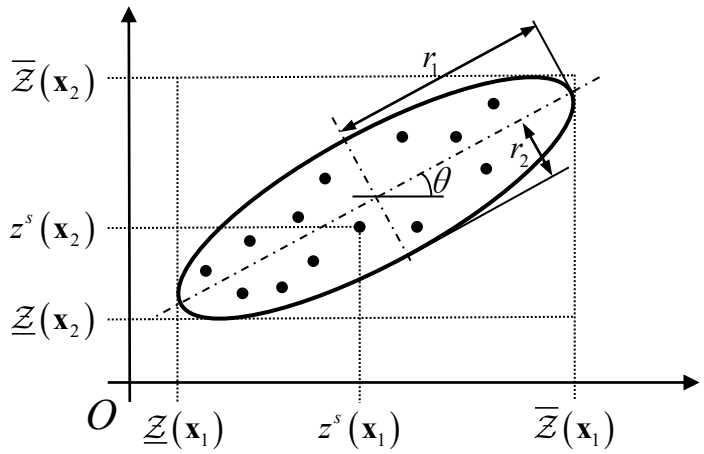

Fig. 4.1 Correlation of two interval variables.

quantity can be represented by $\mathscr{Z}^I(\mathbf{x}_k) = \left[\underline{\mathscr{Z}}(\mathbf{x}_k), \overline{\mathscr{Z}}(\mathbf{x}_k)\right]$, in which $\underline{\mathscr{Z}}(\mathbf{x}_k)$ and $\overline{\mathscr{Z}}(\mathbf{x}_k)$ are the lower and upper bound of the quantity at this location. The dimension of the interval field is determined by the dimension of $\mathbf{x}$. The midpoint $\mathscr{Z}^m(\mathbf{x})$ and radius $\mathscr{Z}^r(\mathbf{x})$ of the interval field can be expressed by:

$$\mathscr{Z}^m(\mathbf{x}) = \frac{\overline{\mathscr{Z}}(\mathbf{x}) + \underline{\mathscr{Z}}(\mathbf{x})}{2} \quad \text{and} \quad \mathscr{Z}^r(\mathbf{x}) = \frac{\overline{\mathscr{Z}}(\mathbf{x}) - \underline{\mathscr{Z}}(\mathbf{x})}{2}. \tag{4.1}$$

By employing the ellipsoid convex model [168, 173], the covariance function of the uncertainty can be expressed by:

$$\mathscr{C}_{\mathscr{Z}^I}(\mathbf{x}_1, \mathbf{x}_2) = Cov\left(\mathscr{Z}^I(\mathbf{x}_1), \mathscr{Z}^I(\mathbf{x}_2)\right) = \sin\theta\cos\theta\left(r_1^2 - r_2^2\right), \tag{4.2}$$

where $\mathscr{C}_{\mathscr{Z}^I}(\mathbf{x}_1, \mathbf{x}_2)$ denotes the covariance function of the uncertainty between different locations; θ, r_1 and r_2 denotes the relevant angle, major length and minor length, respectively. They are quantified through the ellipse enclosing all their bivariate samples. Fig. 4.1 depicts the correlation of two interval variables, in which the symbols θ, r_1 and r_2 are expressed.

Accordingly, the correlation coefficient function can be presented by:

$$\mathscr{R}_{\mathscr{Z}}(\mathbf{x}_1, \mathbf{x}_2) = R\left(\mathscr{Z}^I(\mathbf{x}_1), \mathscr{Z}^I(\mathbf{x}_2)\right) = \frac{\mathscr{C}_{\mathscr{Z}}(\mathbf{x}_1, \mathbf{x}_2)}{\mathscr{Z}^r(\mathbf{x}_1)\,\mathscr{Z}^r(\mathbf{x}_2)}. \tag{4.3}$$

4.2.2 Truncated interval K-L expansion

An interval field in the K-L expansion form can be expressed by:

$$\mathscr{Z}(\mathbf{x}) = \mathscr{Z}^m(\mathbf{x}) + \sum_{i=1}^{\infty} \mathscr{Z}^r(\mathbf{x}) \sqrt{\lambda_i} \phi_i(\mathbf{x}) \gamma_i, \quad \gamma_i \in [-1,1], \tag{4.4}$$

where $\mathscr{Z}^m$ and $\mathscr{Z}^r$ are the midpoint function and the radius function of the interval field, respectively, as previously stated; λ_i and $\varphi_i(\mathbf{x})$ denotes the eigenvalues and eigenfunctions of the correlation coefficient function $\mathscr{R}_{\mathscr{Z}}(\mathbf{x}_1, \mathbf{x}_2)$, in which $\lambda_i \in [0, \infty)$; γ_i denote a series of dimensionless uncorrelated interval variables that satisfy $\sum_{i=1}^{\infty} \gamma_i^2 \leq 1$. From Mercer's Theorem [376], the eigenvalues and eigenfunctions satisfies the following spectral decomposition with respect to the correlation coefficient function, which is:

$$\mathscr{R}_{\mathscr{Z}}(\mathbf{x}_1, \mathbf{x}_2) = \sum_{i=1}^{\infty} \lambda_i \phi_i(\mathbf{x}_1) \phi_i(\mathbf{x}_2), \tag{4.5}$$

in which the eigenvalues and eigenfunctions can be obtained by solving the following homogeneous Fredholm integral equation of the second kind [14]:

$$\int_{\mathscr{D}} \mathscr{R}_{\mathscr{Z}}(\mathbf{x}_1, \mathbf{x}_2) \phi_i(\mathbf{x}_1) \, \mathrm{d}\mathbf{x}_1 = \lambda_i \phi_i(\mathbf{x}_2), \tag{4.6}$$

where the orthogonal eigenfunctions are normalized. It is noted that the Fredholm integral equation can be hardly analytically solved for many problems [125]. Following [280, 281], we employ the Nyström method [14] in this work. The eigenvalue problem shown in Eq. (4.6) can be approximated by:

$$\sum_{i=1}^{N} w_i \mathscr{R}_{\mathscr{Z}}(\mathbf{x}_i, \mathbf{x}) \hat{\phi}_j(\mathbf{x}_i) = \hat{\lambda}_j \hat{\phi}_j(\mathbf{x}), \tag{4.7}$$

where $\hat{\lambda}_j$ and $\hat{\phi}_j$ denote the approximated value of the true eigenvalues λ_j and eigenfunctions ϕ_j; i denotes the integration points; w is the integration weight coefficient. For more details of the Nyström method in this interval K-L expansion, one may refer to [280, 281]. Besides, this problem can also be solved by the collocation method [123], the Galerkin method [124], to name a few.

For practical considerations, such interval K-L expansion with infinite terms can be approximated by truncating with only finite principle terms. From Eq. (4.5), we have:

$$\sum_{i=1}^{\infty} \lambda_i = |\mathscr{D}|, \tag{4.8}$$

where $|\mathscr{D}|$ denotes the area of the spatial domain $\mathscr{D}$. Taking only the first M terms, we have following approximation:

$$\sum_{i=1}^{M} \lambda_i \leq |\mathscr{D}|, \tag{4.9}$$

in which $M \ll \infty$. The approximating index of such truncating to the original interval field can be denoted by:

$$\tau = \frac{1}{|\mathscr{D}|} \sum_{i=1}^{M} \lambda_i, \tag{4.10}$$

where if the value of M is sufficient, the precision of such approximating can be guaranteed. The interval K-L expansion can be approximated by the truncated M terms, namely:

$$\mathscr{Z}(\mathbf{x}) \approx \mathscr{Z}^m(\mathbf{x}) + \sum_{i=1}^{M} \mathscr{Z}^r(\mathbf{x}) \sqrt{\lambda_i} \phi_i(\mathbf{x}) \gamma_i, \quad \gamma_i \in [-1, 1]. \tag{4.11}$$

4.3 Estimation of structural compliance

4.3.1 Interval field-based perturbation analysis (IFPA)

We consider a non-damping steady-state system, whose equilibrium equation has been described in Chapter 2. Combining the spatially varied uncertainties, the equation can be expressed by:

$$\boldsymbol{K}_d(\mathscr{Z})\boldsymbol{u}^I = \boldsymbol{F}(\mathscr{Z}), \tag{4.12}$$

where $\boldsymbol{K}_d(\mathscr{Z})$ contains the material and geometry uncertainties, and $\boldsymbol{F}(\mathscr{Z})$ expresses the loading uncertainty and $\boldsymbol{u}^I$ represents the interval of uncertain displacement response caused by the uncertainties.

Referring to the truncated interval K-L expansion shown in Eq. (4.11), we can use the first-order Taylor series expansion at the midpoints and ignoring the higher-order items to

approximate the uncertain dynamic stiffness matrix and force vector, given by:

$$\begin{aligned}\boldsymbol{K}_d(\mathscr{Z}) &\approx \boldsymbol{K}_{d,0} + \sum_{i=1}^{M} \left.\frac{\partial \boldsymbol{K}_d(\mathscr{Z})}{\partial \gamma_i^K}\right|_{\boldsymbol{\gamma}^K=0} \gamma_i^K, \\ \boldsymbol{F}(\mathscr{Z}) &\approx \boldsymbol{F}_0 + \sum_{i=1}^{M} \left.\frac{\partial \boldsymbol{F}(\mathscr{Z})}{\partial \gamma_i^F}\right|_{\boldsymbol{\gamma}^F=0} \gamma_i^F,\end{aligned} \tag{4.13}$$

where $\boldsymbol{K}_{d,0}$ and $\boldsymbol{F}_0$ are the deterministic term; M denotes the truncating number of the interval K-L expansion as previously stated. The superscript of the standard uncorrelated interval variable γ_i indicates its affiliation. The partial derivation of the mean stiffness matrix and force vector with respect to γ_i can be obtained by using the chain rule as:

$$\begin{aligned}\frac{\partial \boldsymbol{K}_d(\mathscr{Z})}{\partial \gamma_i^K} &= \frac{\partial \boldsymbol{K}_d(\mathscr{Z})}{\partial \mathscr{Z}} \frac{\partial \mathscr{Z}(\mathbf{x})}{\partial \gamma_i^K}, \\ \frac{\partial \boldsymbol{F}(\mathscr{Z})}{\partial \gamma_i^F} &= \frac{\partial \boldsymbol{F}(\mathscr{Z})}{\partial \mathscr{Z}} \frac{\partial \mathscr{Z}(\mathbf{x})}{\partial \gamma_i^F},\end{aligned} \tag{4.14}$$

where $\frac{\partial \boldsymbol{K}_d(\mathscr{Z})}{\partial \mathscr{Z}}$ and $\frac{\partial \boldsymbol{F}(\mathscr{Z})}{\partial \mathscr{Z}}$ denotes partial derivation of the dynamic stiffness matrix and loading vector with respect to the uncertain parameter $\mathscr{Z}$. For instance, $\mathscr{Z}$ can be Young's modules, Poisson's ratio, density, thickness and loading amplitude. For example, in the FEM framework, they can be uniformly written as:

$$\begin{aligned}\frac{\partial \boldsymbol{K}_d(\mathscr{Z})}{\partial \mathscr{Z}} &= \int_\Omega \left(\boldsymbol{B}^T \frac{\partial \boldsymbol{D}}{\partial \mathscr{Z}} \boldsymbol{B} + 2\boldsymbol{B}^T \boldsymbol{D} \frac{\partial \boldsymbol{B}}{\partial \mathscr{Z}} \right) - \omega_p^2 \left(\frac{\partial \rho}{\partial \mathscr{Z}} \boldsymbol{N}^T \boldsymbol{N} + 2\rho \boldsymbol{N}^T \frac{\partial \boldsymbol{N}}{\partial \mathscr{Z}} \right) d\Omega, \\ \frac{\partial \boldsymbol{F}(\mathscr{Z})}{\partial \mathscr{Z}} &= \int_\Gamma \boldsymbol{N}^T \frac{\partial \bar{\boldsymbol{t}}}{\partial \mathscr{Z}} d\Gamma.\end{aligned} \tag{4.15}$$

Another partial derivation shown in Eq. (4.14), $\frac{\partial \mathscr{Z}(\mathbf{x})}{\partial \gamma_i^K}$, can be directly derived from the truncated interval K-L expansion, which is:

$$\frac{\partial \mathscr{Z}(\mathbf{x})}{\partial \gamma_i} = \mathscr{Z}^r(\mathbf{x}) \sqrt{\lambda_i} \varphi_i(\mathbf{x}). \tag{4.16}$$

The uncertain displacement response $\boldsymbol{u}^I$ can be denoted by the sum of deterministic value $\boldsymbol{u}_0$ and perturbation value $\boldsymbol{u}'$, namely:

$$\boldsymbol{u}^I = \boldsymbol{u}_0 + \boldsymbol{u}'. \tag{4.17}$$

Substituting Eqs. (4.13) and (4.17) into Eq. (4.12), yields:

$$\left(\boldsymbol{K}_{d,0}+\sum_{i=1}^{M}\frac{\partial \boldsymbol{K}_d(\mathscr{Z})}{\partial \gamma_i^K}\bigg|_{\boldsymbol{\gamma}^K=0}\gamma_i^K\right)\left(\boldsymbol{u}_0+\boldsymbol{u}'\right)=\boldsymbol{F}_0+\sum_{i=1}^{M}\frac{\partial \boldsymbol{F}(\mathscr{Z})}{\partial \gamma_i^F}\bigg|_{\boldsymbol{\gamma}^F=0}\gamma_i^F. \tag{4.18}$$

Taking the property that $\boldsymbol{K}_{d,0}\boldsymbol{u}_0=\boldsymbol{F}_0$ and neglecting the second-order item, Eq. (4.18) has the following approximating:

$$\left(\sum_{i=1}^{M}\frac{\partial \boldsymbol{K}_d(\mathscr{Z})}{\partial \gamma_i^K}\bigg|_{\boldsymbol{\gamma}^K=0}\gamma_i^K\right)\boldsymbol{u}_0+\boldsymbol{K}_0\boldsymbol{u}'\approx\sum_{i=1}^{M}\frac{\partial \boldsymbol{F}(\mathscr{Z})}{\partial \gamma_i^F}\bigg|_{\boldsymbol{\gamma}^F=0}\gamma_i^F, \tag{4.19}$$

namely,

$$\boldsymbol{u}'\approx\boldsymbol{K}_0^{-1}\left(\sum_{i=1}^{M}\frac{\partial \boldsymbol{F}(\mathscr{Z})}{\partial \gamma_i^F}\bigg|_{\boldsymbol{\gamma}^F=0}\gamma_i^F-\left(\sum_{i=1}^{M}\frac{\partial \boldsymbol{K}_d(\mathscr{Z})}{\partial \gamma_i^K}\bigg|_{\boldsymbol{\gamma}^K=0}\gamma_i^K\right)\boldsymbol{u}_0\right), \tag{4.20}$$

by which, the uncertainty of the displacement response can be efficiently approximated.

4.3.2 Structural compliance with uncertainty

In this section, we consider the structural compliance in dynamics. Note that other dynamic performance indices can be defined in a similar way, such as eigenvalues. The structural compliance with uncertainty can be stated by:

$$C_d(\mathscr{Z})=\boldsymbol{F}^T(\mathscr{Z})\boldsymbol{u}^I, \tag{4.21}$$

where the uncertain structural compliance $C_d(\mathscr{Z})$ expresses the product of uncertain loading and displacement response. Substituting Eqs. (4.13), (4.17) and (4.20) into Eq. (4.21) and neglecting the high-order terms, yields:

$$C_d(\mathscr{Z})\approx\boldsymbol{F}_0^T\boldsymbol{u}_0+P_i(\mathscr{Z})\gamma_i^F+Q_i(\mathscr{Z})\gamma_i^K, \tag{4.22}$$

in which, for convenience, we denote:

$$\begin{aligned}P_i(\mathscr{Z})&=2\boldsymbol{u}_0^T\frac{\partial \boldsymbol{F}(\mathscr{Z})}{\partial \gamma_i^F}\bigg|_{\boldsymbol{\gamma}^F=0},\\ Q_i(\mathscr{Z})&=-\boldsymbol{u}_0^T\frac{\partial \boldsymbol{K}_d(\mathscr{Z})}{\partial \gamma_i^K}\bigg|_{\boldsymbol{\gamma}^K=0}\boldsymbol{u}_0.\end{aligned} \tag{4.23}$$

Many approaches were developed to minimize the influence of uncertainty in topology optimization. In this work, we employ the robust optimization approach to minimize the *worst case* of the structural performance. Specifically, the upper bound of the compliance should be determined, which can be obtained by solving the following set of a convex optimization problem:

$$\begin{cases} \overline{C_d}(\mathscr{Z}) = \max\limits_{\boldsymbol{\gamma}^F,\boldsymbol{\gamma}^K} : \boldsymbol{F}_0^T\boldsymbol{u}_0 + \sum\limits_{i=1}^{M} P_i(\mathscr{Z})\gamma_i^F + \sum\limits_{i=1}^{M} Q_i(\mathscr{Z})\,\gamma_i^K, \\ \quad s.t. \quad \boldsymbol{\gamma}^F, \boldsymbol{\gamma}^K \in \Omega^M, \end{cases} \tag{4.24}$$

where $\overline{C_d}(\mathscr{Z})$ denotes the upper bound of the structural compliance with uncertainty $\mathscr{Z}$. The above convex optimization problem can be solved by adopting the Lagrange multiplier as

$$\overline{C}_d(\mathscr{Z}) = \boldsymbol{F}_0^T\boldsymbol{u}_0 + \|\boldsymbol{P}(\mathscr{Z})\|_2 + \|\boldsymbol{Q}(\mathscr{Z})\|_2\,, \tag{4.25}$$

where $\|\boldsymbol{.}\|_2$ denotes the Euclidean norm operator; $\boldsymbol{P}(\mathscr{Z})$ and $\boldsymbol{Q}(\mathscr{Z})$ are the vectors that contain $P_i(\mathscr{Z})$ and $Q_i(\mathscr{Z})$, respectively. For clarity, we denote

$$C_d^m = \boldsymbol{F}_0^T\boldsymbol{u}_0 \quad \text{and} \quad C_d^r(\mathscr{Z}) = \|\boldsymbol{P}(\mathscr{Z})\|_2 + \|\boldsymbol{Q}(\mathscr{Z})\|_2\,, \tag{4.26}$$

in which C_d^m denotes the median of the structural compliance, and $C_d^r(\mathscr{Z})$ denotes the radius from the maximum to the median of the structural compliance.

4.4 Topology optimization formulations

4.4.1 Material interpolation scheme

Considering the well-known Solid Isotropic Material with Penalization (SIMP) model [30], the elemental pseudo-density can be associated to the material properties, which enables the optimization algorithm making topological designs. The interpolation scheme can be uniformly expressed by:

$$\begin{aligned} E(\varphi) &= [\beta + (1-\beta)\,\varphi^p]\,E_0, \\ \rho(\varphi) &= [\beta + (1-\beta)\,\varphi^q]\,\rho_0, \end{aligned} \tag{4.27}$$

where E_0 and ρ_0 denotes the Young's modulus and density of the material; φ denotes the pseudo-density for the topology optimization problem, in which $\varphi \in [0,1]$; $E(\varphi)$ and $\rho(\varphi)$ are the pseudo-density interpolated Young's modulus and density; β is a small value to avoid singularity when a zero pseudo-density is taken. In this work, we choose $\beta = 10^{-6}$; p and q

are the penalty factors for Young's modulus and density, respectively. Typically, $p = 3$ for the Young's modulus and $p = 1$ for the density.

Following [291], we adopt an alternative interpolation scheme of the SIMP model to avoid the artificial localized modes in the low density area [273] of the vibration problem, in which the penalty factor of density are modified to:

$$q = \begin{cases} 9, & \text{if} \quad \varphi \leq \varphi_{threshold}, \\ 1, & \text{otherwise}, \end{cases} \tag{4.28}$$

in which, $\varphi_{threshold}$ is a value to determine whether the element is of "low-density". In this paper, $\varphi_{threshold} = 0.1$. As reported by [351], the discontinuity of Eq. (4.28) doesn't affect the topology optimization procedure in this work.

4.4.2 Robust topology optimization

Based on the robust topology optimization framework, the topology optimization formulation considering the spatially varied uncertainty $\mathscr{Z}$ with interval field model can be stated by:

$$\begin{aligned} \min_{\varphi \in [0,1]} : \quad & \mathscr{G} = C_d^m + \kappa \cdot C_d^r(\mathscr{Z}), \\ \text{s. t.} : \quad & C_d(\mathscr{Z}) = \boldsymbol{F}^T(\mathscr{Z})\boldsymbol{u}^I, \\ & V - \chi V_0 \leq 0, \end{aligned} \tag{4.29}$$

where $\mathscr{G}$ denotes the objective function, which is the linear combination of the median and radius of the structural compliance in the *worst case*; κ is a robust parameter that governs the impact of the uncertainties on the objective function. A larger value of κ implies the stronger need for the robustness; V denotes the structural volume (area in 2D), which can be computed by $V = \sum_{e=1}^{N_e} \varphi_e V_e$, in which N_e is the number of the design variables and V_e is the elemental volume; $V_0 = \sum_{e=1}^{N_e} V_e$ is the total volume of the design domain; χ denotes the target volume fraction constraints.

4.4.3 Sensitivity analysis

In this section, the sensitivities of the two components of objective function are separately derived. The adjoint method [194] is employed.

$$\frac{\partial \mathscr{G}}{\partial \varphi_e} = \frac{\partial C_d^m}{\partial \varphi_e} + \kappa \cdot \frac{\partial C_d^r(\mathscr{Z})}{\partial \varphi_e}. \tag{4.30}$$

By introducing a Lagrange multiplier vector $\boldsymbol{\Phi}$, which has the same dimension to $\boldsymbol{u}_0$, the first term of the objective function can be expanded to:

$$\hat{C}_d^m = \boldsymbol{F}_0^T \boldsymbol{u}_0 + \boldsymbol{\Phi}^T \left(\boldsymbol{K}_{d,0} \boldsymbol{u}_0 - \boldsymbol{F}_0 \right), \tag{4.31}$$

in which $\boldsymbol{K}_0 \boldsymbol{u}_0 - \boldsymbol{F}_0 = 0$, thus for arbitrary value of $\boldsymbol{\Phi}$ we have $\hat{C}_d^m = C_d^m$. Taking the derivation of Eq. (4.31) with respect to the pseudo-density, yields:

$$\begin{aligned} \frac{\partial C_d^m}{\partial \varphi_e} &= \frac{\partial \boldsymbol{F}_0^T}{\partial \varphi_e} \boldsymbol{u}_0 + \boldsymbol{F}_0^T \frac{\partial \boldsymbol{u}_0}{\partial \varphi_e} + \boldsymbol{\Phi}^T \left(\frac{\partial \boldsymbol{K}_{d,0}}{\partial \varphi_e} \boldsymbol{u}_0 + \boldsymbol{K}_{d,0} \frac{\partial \boldsymbol{u}_0}{\partial \varphi_e} - \frac{\partial \boldsymbol{F}_0}{\partial \varphi_e} \right) \\ &= \boldsymbol{\Phi}^T \frac{\partial \boldsymbol{K}_{d,0}}{\partial \varphi_e} \boldsymbol{u}_0 + \left(\boldsymbol{F}_0^T + \boldsymbol{\Phi}^T \boldsymbol{K}_{d,0} \right) \frac{\partial \boldsymbol{u}_0}{\partial \varphi_e} + \frac{\partial \boldsymbol{F}_0^T}{\partial \varphi_e} \left(\boldsymbol{u}_0 - \boldsymbol{\Phi}^T \right), \end{aligned} \tag{4.32}$$

where the load is assumed to be pseudo-density independent in this work, which means $\frac{\partial \boldsymbol{F}_0^T}{\partial \varphi_e} = 0$. To vanish the part with unknown derivation $\frac{\partial \boldsymbol{u}_0}{\partial \varphi_e}$, let $\boldsymbol{\Phi}^T$ take the following value:

$$\boldsymbol{\Phi}^T = -\boldsymbol{K}_{d,0}^{-1} \boldsymbol{F}_0^T = -\boldsymbol{u}_0{}^T, \tag{4.33}$$

by which the sensitivity of C_d^m can be expressed by:

$$\frac{\partial C_d^m}{\partial \varphi_e} = -\boldsymbol{u}_0{}^T \frac{\partial \boldsymbol{K}_{d,0}}{\partial \varphi_e} \boldsymbol{u}_0. \tag{4.34}$$

Similarly, the radius shown in Eq. $(4.26)_2$ can be expanded to:

$$\hat{C}_d^r(\mathscr{Z}) = \sqrt{\sum_{i=1}^{M} P_i^2 + \boldsymbol{\mu}_i^T \left(\boldsymbol{K}_{d,0} \boldsymbol{u}_0 - \boldsymbol{F}_0 \right)} + \sqrt{\sum_{i=1}^{M} Q_i^2 + \boldsymbol{\theta}_i^T \left(\boldsymbol{K}_{d,0} \boldsymbol{u}_0 - \boldsymbol{F}_0 \right)}, \tag{4.35}$$

where $\boldsymbol{\mu}$ and $\boldsymbol{\theta}$ are both a series of arbitrary vectors that have the same dimension to $\boldsymbol{u}_0$. The subscript of $\boldsymbol{\mu}$ and $\boldsymbol{\theta}$ denote truncated interval K-L expansion terms they belong to. Taking

the partial derivation of Eq. (4.35) with respect to φ_e, we have:

$$\begin{aligned}\frac{\partial C_d^r(\mathscr{Z})}{\partial \varphi_e} =& \frac{\sum_{i=1}^{M}\left[2P_i\left(2\frac{\partial^2 \boldsymbol{F}^T(\mathscr{Z})}{\partial \gamma_i^F \partial \varphi_e}\Big|_{\gamma^F=0}\boldsymbol{u}_0 + 2\frac{\partial \boldsymbol{F}^T(\mathscr{Z})}{\partial \gamma_i^F}\Big|_{\gamma^F=0}\frac{\partial \boldsymbol{u}_0}{\partial \varphi_e}\right) + \boldsymbol{\mu}_i^T\left(\boldsymbol{K}_{d,0}\frac{\partial \boldsymbol{u}_0}{\partial \varphi_e} + \frac{\partial \boldsymbol{K}_{d,0}}{\partial \varphi_e}\boldsymbol{u}_0 - \frac{\partial \boldsymbol{F}_0}{\partial \varphi_e}\right)\right]}{2\sqrt{\sum_{i=1}^{M} P_i^2 + \boldsymbol{\mu}_i^T\left(\boldsymbol{K}_{d,0}\boldsymbol{u}_0 - \boldsymbol{F}_0\right)}} \\ &+ \frac{\sum_{i=1}^{M}\left[2Q_i\left(\boldsymbol{u}_0^T\frac{\partial^2 \boldsymbol{K}(\mathscr{Z})}{\partial \gamma_i^K \partial \varphi_e}\Big|_{\gamma^K=0}\boldsymbol{u}_0 + 2\boldsymbol{u}_0^T\frac{\partial \boldsymbol{K}(\mathscr{Z})}{\partial \gamma_i^K}\Big|_{\gamma^K=0}\frac{\partial \boldsymbol{u}_0}{\partial \varphi_e}\right) + \boldsymbol{\theta}_i^T\left(\boldsymbol{K}_{d,0}\frac{\partial \boldsymbol{u}_0}{\partial \varphi_e} + \frac{\partial \boldsymbol{K}_{d,0}}{\partial \varphi_e}\boldsymbol{u}_0 - \frac{\partial \boldsymbol{F}_0}{\partial \varphi_e}\right)\right]}{2\sqrt{\sum_{i=1}^{M} Q_i^2 + \boldsymbol{\theta}_i^T\left(\boldsymbol{K}_{d,0}\boldsymbol{u}_0 - \boldsymbol{F}_0\right)}},\end{aligned} \tag{4.36}$$

in which, as previously stated, we use the property that:

$$\frac{\partial^2 \boldsymbol{F}^T(\mathscr{Z})}{\partial \gamma_i^F \partial \varphi_e}\Big|_{\gamma^F=0} = \boldsymbol{0} \quad \text{and} \quad \frac{\partial \boldsymbol{F}_0}{\partial \varphi_e} = \boldsymbol{0}, \tag{4.37}$$

and Eq. (4.36) can be simplified to:

$$\begin{aligned}\frac{\partial C_d^r(\mathscr{Z})}{\partial \varphi_e} =& \frac{1}{2\|\boldsymbol{P}(\mathscr{Z})\|_2}\sum_{i=1}^{M}\left[\boldsymbol{\mu}_i^T\frac{\partial \boldsymbol{K}_{d,0}}{\partial \varphi_e}\boldsymbol{u}_0 + \left(4P_i\frac{\partial \boldsymbol{F}^T(\mathscr{Z})}{\partial \gamma_i^F}\Big|_{\gamma^F=0} + \boldsymbol{\mu}_i^T\boldsymbol{K}_{d,0}\right)\frac{\partial \boldsymbol{u}_0}{\partial \varphi_e}\right] \\ &+ \frac{1}{2\|\boldsymbol{Q}(\mathscr{Z})\|_2}\sum_{i=1}^{M}\left[2Q_i\boldsymbol{u}_0^T\frac{\partial^2 \boldsymbol{K}(\mathscr{Z})}{\partial \gamma_i^K \partial \varphi_e}\Big|_{\gamma^K=0}\boldsymbol{u}_0 + \boldsymbol{\theta}_i^T\frac{\partial \boldsymbol{K}_{d,0}}{\partial \varphi_e}\boldsymbol{u}_0\right. \\ &\left. + \left(\boldsymbol{\theta}_i^T\boldsymbol{K}_{d,0} + 4Q_i\boldsymbol{u}_0^T\frac{\partial \boldsymbol{K}(\mathscr{Z})}{\partial \gamma_i^K}\Big|_{\gamma^K=0}\right)\frac{\partial \boldsymbol{u}_0}{\partial \varphi_e}\right].\end{aligned} \tag{4.38}$$

To vanish the items with $\frac{\partial \boldsymbol{u}_0}{\partial \varphi_e}$, we take the following values for the Lagrange multipliers $\boldsymbol{\mu}$ and $\boldsymbol{\theta}$:

$$\boldsymbol{\mu}_i^T = -\boldsymbol{K}_{d,0}^{-1}\left(4P_i\frac{\partial \boldsymbol{F}^T(\mathscr{Z})}{\partial \gamma_i^F}\Big|_{\gamma^F=0}\right) \quad \text{and} \quad \boldsymbol{\theta}_i^T = -\boldsymbol{K}_{d,0}^{-1}\left(4Q_i\boldsymbol{u}_0^T\frac{\partial \boldsymbol{K}(\mathscr{Z})}{\partial \gamma_i^K}\Big|_{\gamma^K=0}\right), \tag{4.39}$$

by which the sensitivity of the radius can be finally expressed by:

$$\begin{aligned}\frac{\partial C_d^r(\mathscr{Z})}{\partial \varphi_e} =& \frac{1}{2\|\boldsymbol{P}(\mathscr{Z})\|_2}\sum_{i=1}^{M}\boldsymbol{\mu}_i^T\frac{\partial \boldsymbol{K}_{d,0}}{\partial \varphi_e}\boldsymbol{u}_0 \\ &+ \frac{1}{2\|\boldsymbol{Q}(\mathscr{Z})\|_2}\sum_{i=1}^{M}\left(2Q_i\boldsymbol{u}_0^T\frac{\partial^2 \boldsymbol{K}(\mathscr{Z})}{\partial \gamma_i^K \partial \varphi_e}\Big|_{\gamma^K=0}\boldsymbol{u}_0 + \boldsymbol{\theta}_i^T\frac{\partial \boldsymbol{K}_{d,0}}{\partial \varphi_e}\boldsymbol{u}_0\right).\end{aligned} \tag{4.40}$$

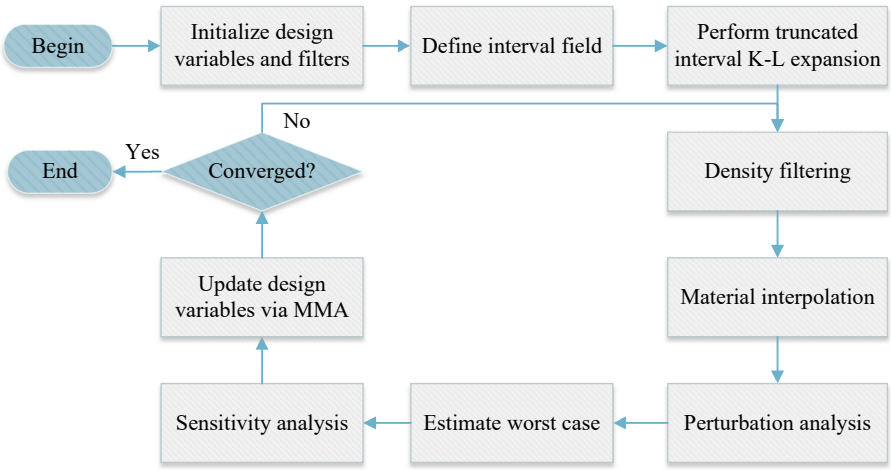

Fig. 4.2 Topology optimization flow chart.

4.4.4 Optimization techniques

The density filter technique [49] is adopted for the numerical stability, by which the problems like mesh dependence and checkerboard issue in topology optimization can be solved. The filtered density regarded as the pseudo-density can be expressed by:

$$\varphi_e = \frac{\sum_{i\in\mathcal{N}_e} \varpi_e V_e \vartheta_e}{\sum_{i\in\mathcal{N}_e} \varpi_e V_e}, \tag{4.41}$$

where ϑ denotes the design variable; $\mathcal{N}_e$ is the set of elements with $r_{ei} \leq r_{\min}$, in which r_{ei} denotes the center-to-center distance between elements e and i. ϖ_{ei} is the corresponding weighting coefficient that is determined by $\varpi_{ei} = \max(0, r_{\min} - r_{ei})$.

Using the chain rule, the sensitivities of objective functions and optimization constraints with respect to the design variables can be derived by:

$$\frac{\partial f(\varphi_e)}{\partial \vartheta_e} = \frac{\partial f}{\partial \varphi_e}\frac{\partial \varphi_e}{\partial \vartheta_e}. \tag{4.42}$$

The distribution of the design variables ϑ can then be optimized by the method of moving asymptotes (MMA) proposed by Svanberg [360]. The topology optimization is terminated when the maximal iteration $L_{\max}$ is reached, or the convergence criterion is satisfied, which is:

$$ch = \max_j |[\boldsymbol{\vartheta}^n]_j - \left[\boldsymbol{\vartheta}^{n-1}\right]_j| \leq \tau, \tag{4.43}$$

where *ch* denotes the absolute value of the maximal change of the design variables of the adjacent iterations; τ is the threshold value, which is defined by $\tau = 10^{-2}$ in this paper. Fig. 4.2 summarizes the flow chart of the proposed method.

4.5 Numerical examples

In this section, two numerical examples are presented, in which the uncertainty of material property and loading are respectively considered. Table 4.1 provides the adopted material properties based on deterministic assumption.

Table 4.1 Material parameters.

Material properties	Symbol	Value	Unit
Young's modulus	E_0	2.1×10^5	MPa
Poisson's ratio	ν	0.3	-
Density	ρ_0	8×10^{-9}	ton/mm^3

Referring to [125], we take the following exponential kernel type correlation coefficient function for two arbitrary positions with coordinates $\mathbf{x}_1\,(u_1, v_1)$ and $\mathbf{x}_2\,(u_2, v_2)$ in a 2D plane:

$$\mathscr{R}\left(\mathbf{x}_1, \mathbf{x}_2\right) = \exp\left(-\frac{|u_1 - u_2|}{l_x} - \frac{|v_1 - v_2|}{l_y}\right), \tag{4.44}$$

in which l_x and l_y denote the correlation lengths at x and y directions, respectively. Note that for 1D problem, only one direction need to be considered.

4.5.1 Cantilever beam with material uncertainty

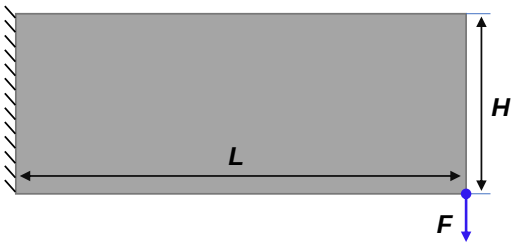

Fig. 4.3 Geometry and boundary condition of the cantilever beam

In this example, we investigate a cantilever beam with spatially varied material uncertainty. We consider four different robust parameters $\kappa = 0$, 1, 3 and 9, respectively, the effectiveness of the proposed method for promoting the robustness of topology optimization is illustrated.

It is noted that for $\kappa = 0$, the deterministic design is recovered. Fig. 4.3 depicts the cantilever beam, in which the length and height are $L = 90$mm and $H = 30$mm, respectively. The left end of the beam is clamped, and the lower right corner is loaded by a harmonic external citation with an amplitude $F = 1000$N and loading frequency $\omega_p = 3500$Hz. The cantilever beam is discretized by a 180×60 four-node quadrilateral finite element mesh. The target volume fraction is $\chi = 0.5$. The filter radius is chosen as $r_{\min} = 1.5$mm. The maximal iteration is limited to 1000 steps.

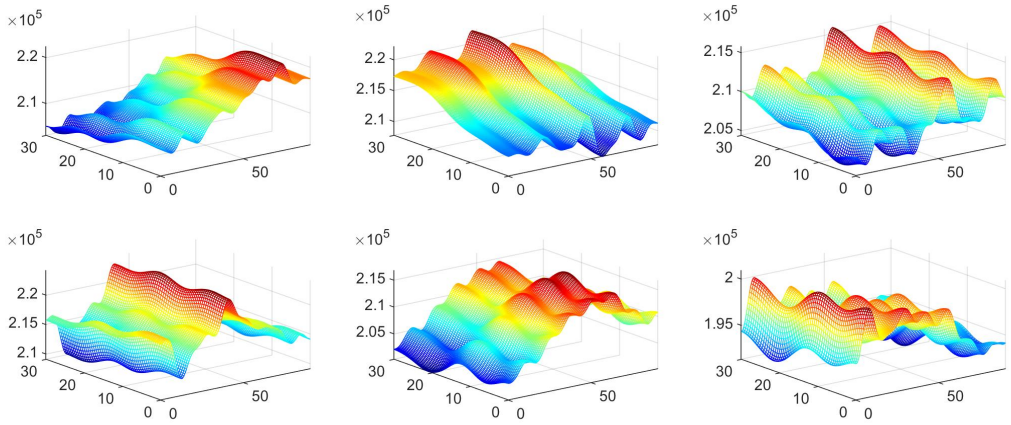

Fig. 4.4 The spatially varied Young's modulus in this example: for 6 samples

Uncertain Young's modulus is assumed with a constant midpoint function $E^m(\mathbf{x}) = 2.1 \times 10^5$Mpa and radius function $E^r(\mathbf{x}) = 0.2E^m(\mathbf{x})$. The correlation lengths are defined by $l_u = 120$mm and $l_v = 360$mm. Fig.4.4 depicts 6 different distribution samples of the Young's modulus that follow the above assumption. The truncating number of the interval K-L expansion in this example is $M = 24$, by which the approximating index reaches $\tau = 98.54\%$.

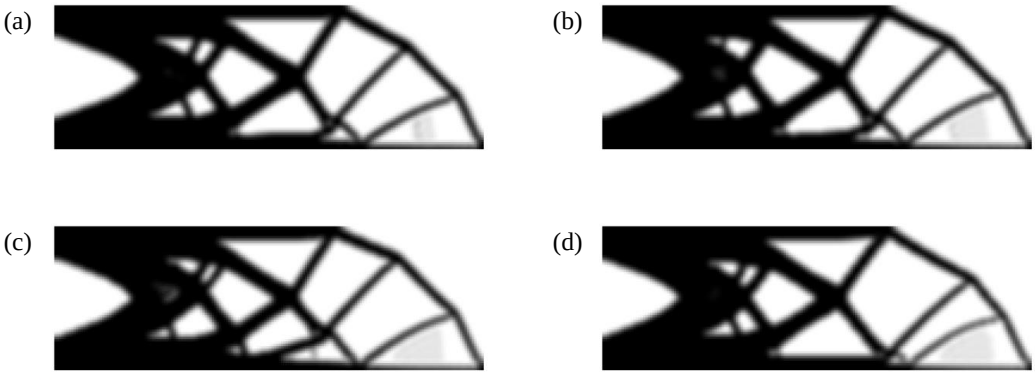

Fig. 4.5 Topological designs with different robust parameters: (a) $\kappa = 0$ (deterministic design); (b) $\kappa = 1$; (c) $\kappa = 3$; (d) $\kappa = 9$.

Table 4.2 Comparison of the decomposed dynamic compliance.

Robust parameter	C_d^m	$C_d^r(\mathscr{Z})$	$\overline{C}_d(\mathscr{Z})$	$\frac{C_d^r(\mathscr{Z})}{C_d^m}$
$\kappa = 0$	2308.79	834.05	3142.84	36.13%
$\kappa = 1$	2317.92	776.66	3094.58	33.51%
$\kappa = 3$	2370.06	749.07	3119.13	31.61%
$\kappa = 9$	2432.42	730.59	3163.01	30.04%

Fig. 4.5 depicts the topological designs obtained by employing different values of robust parameter κ. Compared to the deterministic design (Fig. 4.5a), it can be seen that the proposed method gives different topological designs with respect to the spatially varied Young's modulus. The influence of changing the robust parameter can be observed on the topological designs. Table 4.2 shows the comparison of the decomposed performances on the dynamic compliance of the designs shown in Fig. 4.5. The results are predicted by the proposed IFPA. It is obvious that as the robust parameter increases, the radius of dynamic compliance of the corresponding topology designs in dealing with uncertainty is reduced. The ratios of the radius to the median are also decreased. This means that the robustness of the structural design has been improved. It should be noted, however, that increasing the robust parameter does not necessarily lead to an improvement in the overall performance of the structure. For more discussion on this problem, one may refer to [368].

Fig. 4.6 depicts the iteration process of the corresponding topological designs shown in Fig. 4.5, in which the iterative values of both the objective function and the ratio of radius to median are plotted. Fig. 4.6 illustrates the good convergence of the proposed topology optimization method.

Next, we perform the Monte-Carlo Simulation (MCS) on the final topological designs to validate the prediction of the IFPA to the sampling results under the same uncertainty. The population of the MCS is defined by 10^6, in which the Young's modulus is distributed in the prescribed interval and remains consistency with the spatial correlation coefficient function defined by Eq. (4.44). Fig. 4.7 shows the results of IFPA and MCS, where (a-b) corresponds to the topological designs of Fig. 4.5(a-d), respectively. The results of MCS sampling are marked with blue crosses, from which we can see that the distribution of the topological designs with larger robust parameter is more tight. The red line and black dash line are the results of $\overline{C}_d(\mathscr{Z})$ and C_d^m predicted by the IFPA. We can see that only a very small number of samples are outside the predicted range of extreme values, which demonstrates the accuracy of the IFPA in the topology optimization problem. In terms of computational cost, IFPA requires only 25 FEA calls while MCS requires 10^6 FEAcalls. Such advantage makes IFPA more suitable for topology optimization.

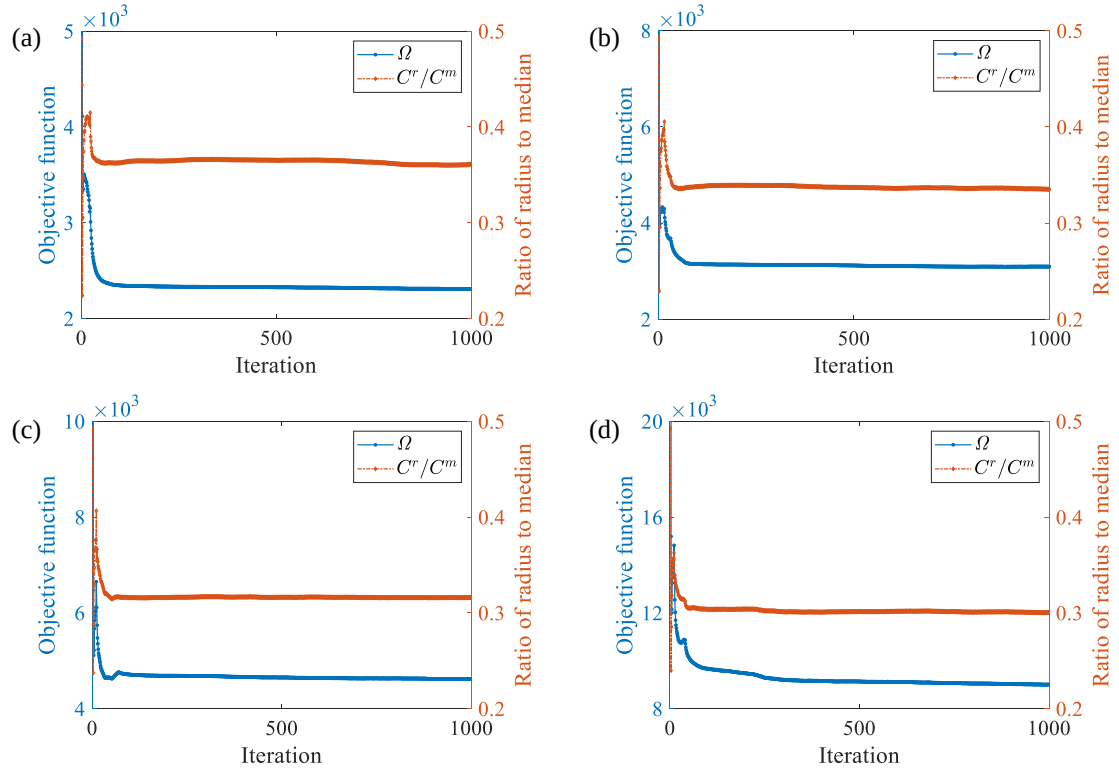

Fig. 4.6 Iteration process of the objective function and ratio of radius to median for the topological designs shown in 4.5: (a) $\kappa = 0$ (deterministic design); (b) $\kappa = 1$; (c) $\kappa = 3$; (d) $\kappa = 9$.

4.5.2 Michell-type structure with loading uncertainty

In this example, a Michell-type structure with spatially varied loading uncertainty is considered. Fig. 4.8 shows the Michell-type structure. The length and width of the structure is $L = 90$mm and $H = 45$mm, respectively. It is discretized by a 180×90 four-node quadrilateral finite element mesh. The left lower corner of the structure is fixed and the right lower corner is supported. The middle third of the boundary below the structure is subjected to spatially varying uncertain loads, which will be described in detail later. The topology optimization parameters are defined as follows: the target volume fraction is $\chi = 0.3$, the radius of the density filter is $r_{\min} = 1$mm, the number of iterations is limited to 1000. The robust parameter is $\kappa = 3$ in this example.

The spatially varied loading uncertainty is expressed by the interval field model. We assume that the direction of the force is constant and there is uncertainty only in the magnitude of the force. The magnitude of these loading have a constant midpoint function $F_y^m(\mathbf{x}) = -10$N, in which the minus sign denotes the direction of the force. The radius function of this

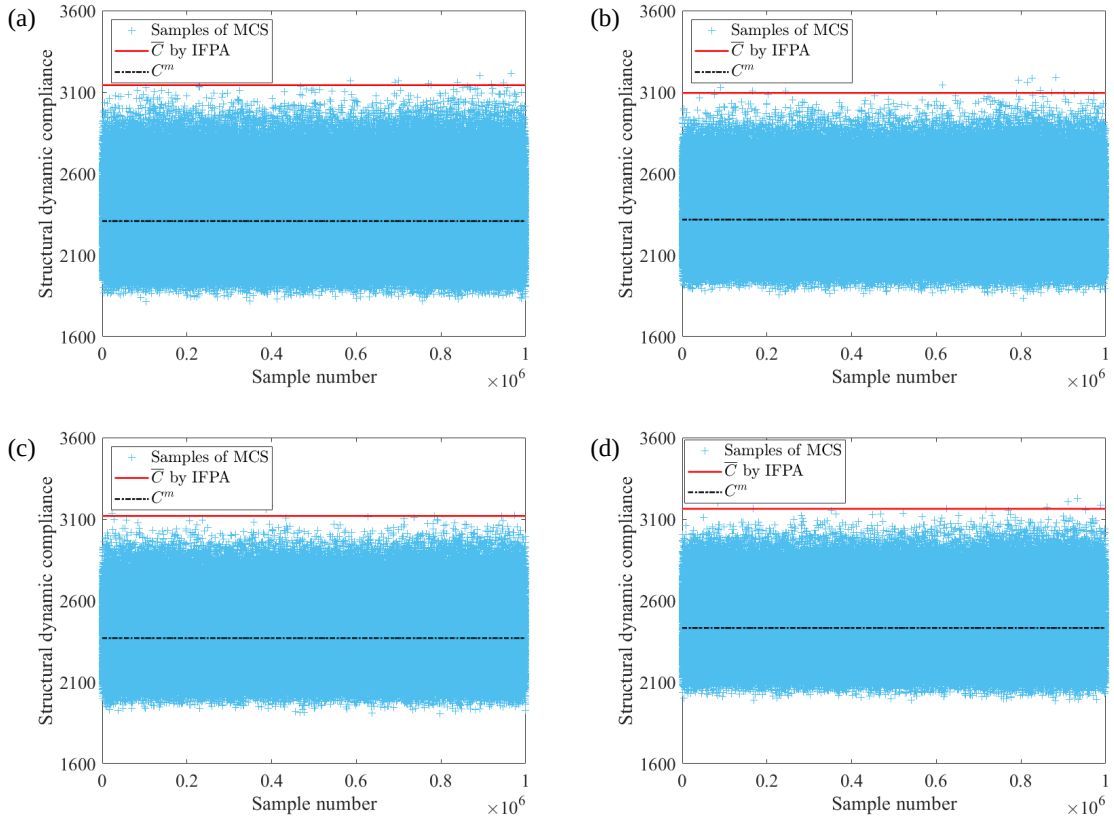

Fig. 4.7 Comparison of the results obtained by IFPA and MCS: (a) $\kappa = 0$ (deterministic design); (b) $\kappa = 1$; (c) $\kappa = 3$; (d) $\kappa = 9$.

uncertainty is $F_y^r(\mathbf{x}) = 0.2F_y^m(\mathbf{x})$. Since the load exists only at the boundary, we only need to define the correlation length at the x-direction. In this example, we employed two different correlation lengths $l_x = 30$ and 120, with corresponding truncating numbers $M = 8$ and 6. Fig. 4.9 (a-b) provide 100 samples of the spatially varied loading uncertainty corresponding to the two different correlation lengths. The horizontal coordinates in the figure indicate the coordinates corresponding to the loading force, and the vertical coordinates indicate the absolute value of the loading force. The colored lines indicate different samples. We can see that the larger value of correlation length makes a more flat distribution of uncertain values. Fig. 4.9 (c) depicts another 100 samples for correlation length $l_x = 10^6$, in which there is almost no spatial variation in the amplitude of the force for each sample. In this way, the interval field model can be regarded as a conventional interval model.

We should note that topology optimization is more sensitive to the loading directions than to the magnitudes [97], which implies that only a small improvement of the objective function values could be observed. In this work, our objective is to introduce the interval field model into topology optimization and explore the influence of the spatial correlation on the

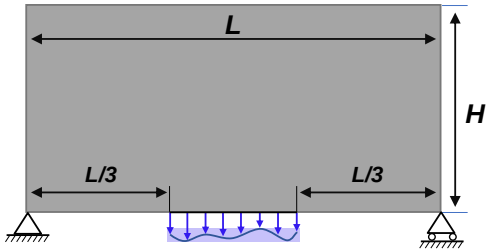

Fig. 4.8 Geometry and boundary condition of the Michell-type structure

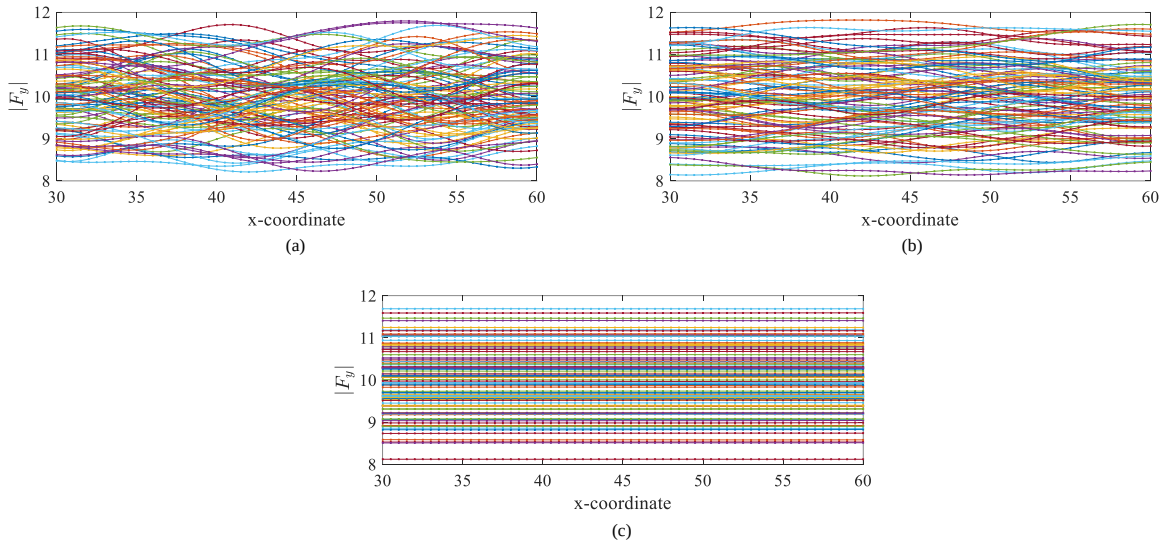

Fig. 4.9 Samples of the spatially varied external force with different correlation lengths: (a) $l_x = 30$; (b) $l_x = 120$; (c) $l_x = 10^5$.

final topological designs, since only the uncertain amplitude of loading in the conventional interval model based uncertainties has no effect on the final topology layout.

Fig. 4.10 depicts the topological designs. Fig. 4.10 (a) is the deterministic deign and also the robust design for interval model based uncertainty. Fig. 4.10 (b-c) depict the robust design respect to the interval field uncertainty, in which (b) and (c) correspond to $l_x = 30$ and 120, respectively. We can see that the spatially varied loading uncertainty has obvious influence on the topological design, which indicates the advantage of employing the interval

Table 4.3 Comparison of structural compliance predicted by IFPA: $l_x = 30$.

Methods	C_d^m	$C_d^r(\mathscr{Z})$	$\overline{C}_d(\mathscr{Z})$
DTO	34.06	11.69	45.75
RTO	33.72	11.57	45.29

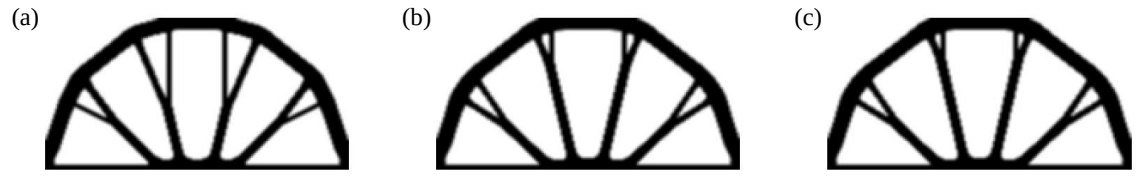

Fig. 4.10 Topological designs for uncertain loads with different spatial correlation lengths: (a) Deterministic design ($l_x = \infty$, for comparison); (b) Robust design ($l_x = 30$); (c) Robust design ($l_x = 120$).

Table 4.4 Comparison of structural compliance predicted by IFPA: $l_x = 120$.

Methods	C_d^m	$C_d^r(\mathscr{Z})$	$\overline{C}_d(\mathscr{Z})$
DTO	34.06	13.08	47.14
RTO	33.67	12.93	46.60

field model as compared with the conventional interval model. Besides, although quite similar, there remains small difference between the designs for different correlation lengths, which illustrates the necessity of employing the interval field model in topology optimization. Tables 4.3 and 4.4 show the comparison of structural compliance predicted by IFPA under correlation lengths $l_x = 30$ and 120, respectively. We can see slight improvements of the RTO designs. Fig. 4.11 depicts the iteration process of the topological designs shown in Fig. 4.10. We can see that there is no convergent difficulty of these designs.

Fig. 4.12 depicts the MCS results for the topological designs obtained by the robust topology optimization, of which the population of MCS is 10^5, marked by blue crosses. The worst case structural compliance predicted by IFPA is plotted by the red line. We can see that IFPA is able to predict the performance of the structure under the uncertain loading modeled by interval field. Regarding to the computational costs, IFPA requires only 7 FEA calls, which is far more efficient than MCS, especially for the topology optimization problem.

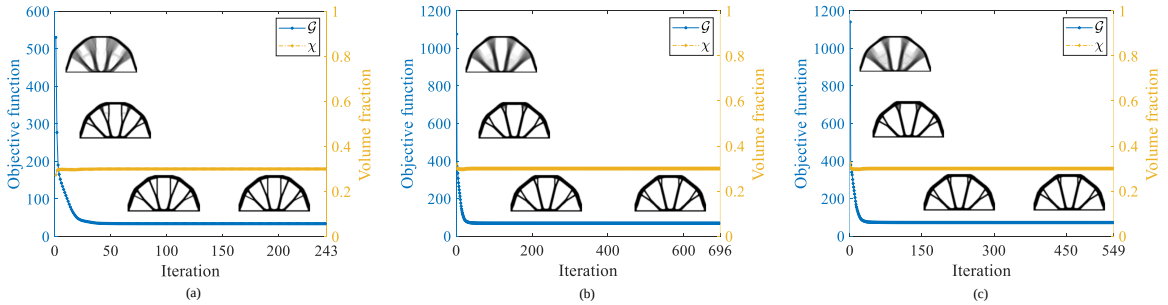

Fig. 4.11 Iteration process of the topological designs shown in Fig. 4.10: (a) Deterministic design ($l_x = \infty$, for comparison); (b) Robust design ($l_x = 30$); (c) Robust design ($l_x = 120$).

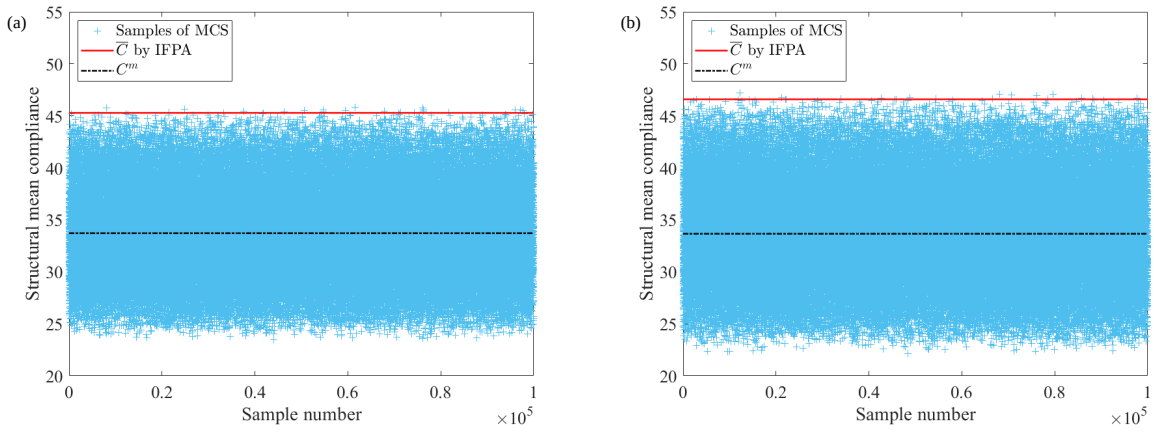

Fig. 4.12 Comparison of the results obtained by IFPA and MCS: (a) $l_x = 30$; (b) $l_x = 120$.

4.6 Conclusions

In this Chapter, we have introduced spatially varied non-probabilistic uncertainty into topology optimization. By employing an interval field model, the spatial dependence of the non-probabilistic uncertainty was considered. Based on the robust topology optimization framework, uncertainties are incorporated in topology optimization and the worst case of the structural compliance under uncertainty was optimized. An efficient IFPA method was proposed, and sensitivity analysis of the robustness objective function was derived accordingly. We considered two sources of uncertainty in the numerical examples, namely material uncertainty and load uncertainty, separately. The results showed the merits of incorporating spatial dependent uncertainty into topology optimization. The efficiency and accuracy of the proposed IFPA were also illustrated.

Chapter 5

Topology optimization for enhanced dynamic fracture resistance of structures

The main content of this chapter is adapted from our paper [400].

5.1 Introduction

In this Chapter, a topology optimization framework for improving the dynamic fracture resistance of structures is proposed. The phase field method for fracture is combined with SIMP topology optimization. The topology optimization problem is defined as minimizing the fracture energy during the whole dynamic loading process, from initiation of cracks to full failure of the structure, under volume and compliance constraints. Semi analytical expressions of sensitivities in a dynamic context are provided to solve the topology optimization problem efficiently. Numerical examples involving structures subjected to impact loading are investigated. It is shown that the present framework allows a significant reduction of the fracture energy as compared to designs obtained by static optimization.

5.2 Dynamic phase field fracture model

In this section, the dynamic phase field method for crack propagation in quasi-brittle solids is briefly reviewed. A structure defined in a domain $\Omega \subset \mathbb{R}^D$ is considered, with D the space dimension, with external boundary $\partial\Omega \subset \mathbb{R}^{D-1}$. In the context of the phase field method, as shown in Fig. 5.1, the crack surfaces collectively denoted by Γ are described by a continuous damage field $d \in [0,1]$, which takes 0 value when the material is undamaged and 1 when the material is cracked. The portions of $\partial\Omega$, $\partial\Omega_u$ and $\partial\Omega_t$ denote the Dirichlet and Neumann

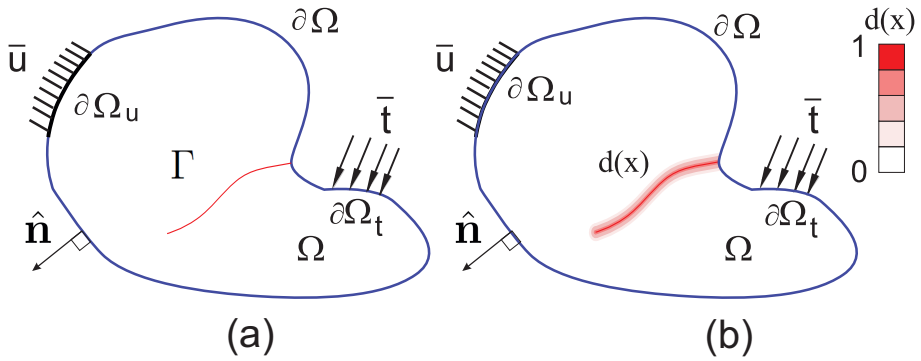

Fig. 5.1 Cracked solid: (a) representation of cracks by surfaces; (b) continuous approximation of cracks by a damage field $d(\boldsymbol{x})$.

boundaries, respectively (see Fig. 5.1). We define $\boldsymbol{u}$, $\dot{\boldsymbol{u}} = \frac{d\boldsymbol{u}}{dt}$ and $\ddot{\boldsymbol{u}} = \frac{d^2\boldsymbol{u}}{dt^2}$ as the displacement, velocity and acceleration vectors, respectively.

In this context, the elastic strain energy E^s is defined by

$$E^s(\boldsymbol{u},d) = \int_\Omega \psi_e(\boldsymbol{\varepsilon}(\boldsymbol{u}),d)\,\mathrm{d}\Omega, \tag{5.1}$$

where ψ_e is a strain density function, whose form will be specified later, and $\boldsymbol{\varepsilon} = \frac{1}{2}\left(\nabla\boldsymbol{u} + \nabla^T\boldsymbol{u}\right)$ is the linearized second-order strain tensor, with $\nabla(\cdot)$ the gradient operator. The kinetic energy of the solid is defined by:

$$E^k(\dot{\boldsymbol{u}}) = \int_\Omega \frac{1}{2}\rho\dot{\boldsymbol{u}}\cdot\dot{\boldsymbol{u}}\,\mathrm{d}\Omega, \tag{5.2}$$

where ρ is the material density. In the phase field method, a non-local fracture energy is defined according to

$$E^f(d) = \int_\Omega c_1\mathscr{G}_c\left(\omega(d) + \ell^2\nabla d\cdot\nabla d\right)\mathrm{d}\Omega, \tag{5.3}$$

where c_1 is a constant, $\mathscr{G}_c$ is the Griffith-type critical energy release rate, $\omega(d)$ is a local damage density function, and ℓ is a length regularization parameter, which defines the width of the regularized crack. Finally the work of external forces is defined by

$$W^{ext}(\boldsymbol{u}) = \int_{\partial\Omega_t}\bar{\boldsymbol{t}}\cdot\boldsymbol{u}\,\mathrm{d}S + \int_\Omega \boldsymbol{f}\cdot\boldsymbol{u}\,\mathrm{d}\Omega, \tag{5.4}$$

where $\bar{\boldsymbol{t}}$ denotes prescribed traction over the portion of the boundary $\partial\Omega_t$ (see Fig. 5.1), and $\boldsymbol{f}$ denotes body forces. The action-integral over the time interval $[t_1,t_2]$ is defined by:

$$\mathscr{A} = \int_{t_1}^{t_2}\left[E^s(\boldsymbol{u},d) + E^f(d) - E^k(\dot{\boldsymbol{u}}) - W^{ext}(\boldsymbol{u})\right]\mathrm{d}t. \tag{5.5}$$

In the dynamic context, the variational principle of nonlocal damage at the core of the phase field method implies minimization of the action-integral under the constraint of irreversibility of the damage field, i.e.

$$\dot{d} \geq 0, \tag{5.6}$$

where $\dot{d} = \mathrm{d}(d)/\mathrm{d}t$ denotes the rate of the damage field.

In the following, the different equations of the model in the case of an assumed isotropic quasi-brittle solid are specified. We follow Miehe et al. [256] and express the strain density function such that damage is induced by traction only as:

$$\psi_e = \Big((1-d)^2 + b\Big)\, \psi_e^+ + \psi_e^-, \tag{5.7}$$

where ψ_e^+ and ψ_e^- denote the positive and negative components of the strain density function, respectively, which can be computed from the strain tensor as

$$\psi_e^\pm = \frac{\lambda}{2} \langle \mathrm{Tr}\,[\boldsymbol{\varepsilon}] \rangle_\pm^2 + \mu\, \boldsymbol{\varepsilon}^\pm : \boldsymbol{\varepsilon}^\pm, \tag{5.8}$$

where λ and μ are the Lamé coefficients, which can be related to the Young's modulus E and Poisson's ratio ν by

$$\lambda = \frac{E\nu}{(1+\nu)(1-2\nu)} \quad \text{and} \quad \mu = \frac{E}{2(1+\nu)}. \tag{5.9}$$

Note that other decompositions exist (see a comparison and discussion e.g. in [276]). Above, $\langle\cdot\rangle_\pm$ can be expressed by $\langle a \rangle_\pm = \frac{1}{2}(a \pm |a|)$ and $\mathrm{Tr}\,[\cdot]$ denotes the trace operator. The positive and negative parts $\boldsymbol{\varepsilon}^\pm$ can be expressed by:

$$\boldsymbol{\varepsilon}^\pm = \sum_{p=1}^{D} \langle \varepsilon^p \rangle_\pm\, \mathbf{Q}^p, \qquad \mathbf{Q}^p = \mathbf{v}^p \otimes \mathbf{v}^p, \tag{5.10}$$

where D denotes the space dimension and ε^p and $\mathbf{v}^p$ are the eigenvalues and eigenvectors of $\boldsymbol{\varepsilon}$, respectively. The following definitions are used: $\omega(d) = d^2$ and $c_1 = \frac{1}{2\ell}$ [44]. Other choices are possible, e.g. using $\omega(d) = d$ and $c_1 = \frac{3}{8\ell}$ [304]. The first choice induces damage for any loading (even though very low at the beginning) while the second choice leads to a linear elastic stage before damage. Due to its simplicity, the first choice is adopted here. A more in-depth comparison of the different available models and applications in a dynamic context can be found in [245].

With these models at hand, stationary variation of (5.5) leads to the following Euler-Lagrange equations:

$$\begin{cases} \nabla \cdot \boldsymbol{\sigma} + \boldsymbol{f} = \rho \ddot{\boldsymbol{u}}, \\ \dfrac{\mathscr{G}_c}{\ell} \left(d - \ell^2 \Delta d \right) = 2 \left(1 - d \right) \psi_e^+, \end{cases} \tag{5.11}$$

where $\nabla \cdot (\cdot)$ and $\Delta (\cdot)$ denote the divergence and Laplacian operators, respectively, and where $\boldsymbol{\sigma}$ is the Cauchy stress tensor $\boldsymbol{\sigma} = \frac{\partial \psi_e}{\partial \boldsymbol{\varepsilon}}$, which is expressed under the above assumptions by:

$$\begin{aligned} \boldsymbol{\sigma} &= \left((1-d)^2 + b \right) \frac{\partial \psi_e^+}{\partial \boldsymbol{\varepsilon}} + \frac{\partial \psi_e^-}{\partial \boldsymbol{\varepsilon}} \\ &= \left((1-d)^2 + b \right) \left(\lambda \langle \mathrm{Tr} \left[\boldsymbol{\varepsilon} \right] \rangle_+ \mathbf{1} + 2\mu \boldsymbol{\varepsilon}^+ \right) + \left(\lambda \langle \mathrm{Tr} \left[\boldsymbol{\varepsilon} \right] \rangle_- \mathbf{1} + 2\mu \boldsymbol{\varepsilon}^- \right), \end{aligned} \tag{5.12}$$

where $\mathbf{1}$ is the second-order identity tensor and $b << 1$ a small numerical parameter used to maintain stability in the case of fully broken elements. Above, $\boldsymbol{\varepsilon}^\pm$ and $\langle \mathrm{Tr} (\boldsymbol{\varepsilon}) \rangle_\pm$ can be related to $\boldsymbol{\varepsilon}$ through the following operators:

$$\boldsymbol{\varepsilon}^\pm = \mathbb{P}^\pm : \boldsymbol{\varepsilon}, \tag{5.13}$$

$$\langle \mathrm{Tr} \left[\boldsymbol{\varepsilon} \right] \rangle_\pm = R^\pm \, \mathrm{Tr} \left[\boldsymbol{\varepsilon} \right], \tag{5.14}$$

in which the components of $\mathbb{P}^\pm$ are given in closed form as [257]:

$$\mathbb{P}^\pm_{ijkl} := \frac{\partial \boldsymbol{\varepsilon}^\pm}{\partial \boldsymbol{\varepsilon}} = \sum_p^D H \left(\pm \varepsilon^p \right) \left(\mathbf{Q}^p \right)_{ij} \left(\mathbf{Q}^p \right)_{kl} + \frac{1}{2} \sum_p^D \sum_{q \neq p}^D \phi_{pq} \left(\left(\mathbf{Q}^p \right)_{ik} \left(\mathbf{Q}^q \right)_{jl} + \left(\mathbf{Q}^p \right)_{il} \left(\mathbf{Q}^q \right)_{jk} \right), \tag{5.15}$$

with

$$\phi_{pq} = \begin{cases} \dfrac{\langle \varepsilon^p \rangle_\pm - \langle \varepsilon^q \rangle_\pm}{\varepsilon^p - \varepsilon^q}, & \text{if} \quad \varepsilon^p \neq \varepsilon^q \\ H \left(\pm \varepsilon^p \right), & \text{if} \quad \varepsilon^p = \varepsilon^q \end{cases} \tag{5.16}$$

where $H (\cdot)$ denotes the Heaviside step function. The operator $R^\pm$ is expressed by

$$R^\pm = \frac{1}{2} \left(sign \left(\pm \mathrm{Tr} \left[\boldsymbol{\varepsilon} \right] \right) + 1 \right). \tag{5.17}$$

To achieve non-reversible evolution of cracks, a strain history functional introduced by Miehe et al. [256, 147, 258] is adopted to replace ψ_e^+ in Eq. (5.11), as

$$\mathscr{H}(\boldsymbol{x},t) = \max_{s\in(0,t]} \left\{ \psi_e^+(\boldsymbol{x},s) \right\}. \tag{5.18}$$

Then, the equations (5.11) are substituted by

$$\begin{cases} \nabla\cdot\boldsymbol{\sigma} + \boldsymbol{f} = \rho\ddot{\boldsymbol{u}}, \\ \dfrac{\mathscr{G}_c}{\ell}\left(d - \ell^2\Delta d\right) = 2\left(1-d\right)\mathscr{H}. \end{cases} \tag{5.19}$$

The above equations are completed with boundary conditions as

$$\begin{cases} \boldsymbol{u} = \bar{\boldsymbol{u}} & \text{on } \partial\Omega_u, \\ \boldsymbol{\sigma}\cdot\hat{\mathbf{n}} = \bar{\boldsymbol{t}} & \text{on } \partial\Omega_t, \\ \nabla d\cdot\hat{\mathbf{n}} = 0 & \text{on } \partial\Omega, \end{cases} \tag{5.20}$$

where $\hat{\mathbf{n}}$ denotes the outward unitary normal vector to $\partial\Omega$ (see Fig. 5.1).

Multiplying Eqs. (5.19) by two different test functions, $\delta\boldsymbol{u}$ for the displacement problem and δd for the phase field problem, respectively, integrating the resulting expression over the domain Ω, and using the divergence theorem together with boundary conditions yields the associated weak forms: find $d \in H^1(\Omega)$ and find $\boldsymbol{u} \in \mathscr{D} = \left\{\boldsymbol{v} | \boldsymbol{v} = \bar{\boldsymbol{u}} \text{ on } \partial\Omega_u, \boldsymbol{v} \in H^1(\Omega)\right\}$ such that:

$$\int_\Omega \left(2\mathscr{H}(\boldsymbol{u}) + \frac{\mathscr{G}_c}{\ell}\right) d\ \delta d + \mathscr{G}_c\ell\nabla d\cdot\nabla d\ \mathrm{d}\Omega = \int_\Omega 2\mathscr{H}(\boldsymbol{u})\delta d\ \mathrm{d}\Omega, \tag{5.21}$$

$$\int_\Omega \left\{\rho\ddot{\boldsymbol{u}}\cdot\delta\boldsymbol{u} + \boldsymbol{\sigma}(\boldsymbol{u},d) : \boldsymbol{\varepsilon}(\delta\boldsymbol{u})\right\}\mathrm{d}\Omega - \int_{\partial\Omega_t} \bar{\boldsymbol{t}}\cdot\delta\boldsymbol{u}\ \mathrm{d}S - \int_\Omega \boldsymbol{f}\cdot\delta\boldsymbol{u}\ \mathrm{d}\Omega = 0, \tag{5.22}$$

for all $\delta d \in H^1(\Omega)$ and $\delta\boldsymbol{u} \in H_0^1(\Omega) = \left\{\boldsymbol{v} | \boldsymbol{v} = 0 \text{ on } \partial\Omega_u, \boldsymbol{v} \in H^1(\Omega)\right\}$, H^1 is the usual Sobolev space of square-integrable derivative functions.

5.3 Numerical solving procedure

Displacement field $\boldsymbol{u}$, phase field d and their gradients $\boldsymbol{\varepsilon}(\boldsymbol{u})$ and ∇d are approximated by classical FEM interpolation in the elements of the FEM mesh according to:

$$\begin{aligned} \boldsymbol{u}(\boldsymbol{x}) &= \boldsymbol{N}_u(\boldsymbol{x})\boldsymbol{u}^e, \qquad \boldsymbol{\varepsilon}(\boldsymbol{x}) = \boldsymbol{B}_u(\boldsymbol{x})\boldsymbol{u}^e, \\ d(\boldsymbol{x}) &= \boldsymbol{N}_d(\boldsymbol{x})\boldsymbol{d}^e, \quad \nabla d(\boldsymbol{x}) = \boldsymbol{B}_d(\boldsymbol{x})\boldsymbol{d}^e, \end{aligned} \tag{5.23}$$

where $\boldsymbol{u}^e$ and $\boldsymbol{d}^e$ denote the nodal displacement and phase field in an element e, $\boldsymbol{N}$ and $\boldsymbol{B}$ denote the matrices of the shape functions and their derivatives, respectively. The indices (u and d) of $\boldsymbol{N}$ and $\boldsymbol{B}$ refer to displacement and phase field variables, respectively.

A staggered scheme is adopted. At one time step t^n , the phase field problem (5.21) is solved, assuming the displacement field $\boldsymbol{u}$ given. Then, the mechanical problem (5.22) is solved assuming the phase field d given. These problems are solved alternatively before solving the problems at the next time step. Note that the mechanical problem (5.22) is nonlinear due to the separated description of the strain field in (5.10). Here, we transform this problem into a linear one by expressing the projectors $\mathbb{P}^{\pm}$ with with respect to the displacements know from the previous time step $n-1$, i.e. $\mathbb{P}^{\pm}(\boldsymbol{\varepsilon}^n) \simeq \mathbb{P}^{\pm}(\boldsymbol{\varepsilon}^{n-1})$, $\mathscr{R}^{\pm}(\boldsymbol{\varepsilon}^n) \simeq \mathscr{R}^{\pm}(\boldsymbol{\varepsilon}^{n-1})$.

At time t^n, the strain history functional described in Eq. (5.18) can be calculated using

$$\mathscr{H}^n = \begin{cases} \left(\psi_e^+\right)^n & \text{if } \left(\psi_e^+\right)^n - \mathscr{H}^{n-1} > 0, \\ \mathscr{H}^{n-1} & \text{otherwise,} \end{cases} \tag{5.24}$$

Note that $\mathscr{H}^n$ is discontinuous, which brings difficulties to the subsequent sensitivity derivations presented in section 5.4. To alleviate this issue, we introduce a continuous version of the history function as:

$$\tilde{\mathscr{H}}^n \simeq \mathscr{H}^{n-1} + \left[\left(\psi_e^+\right)^n - \mathscr{H}^{n-1}\right] g\left(\left(\psi_e^+\right)^n - \mathscr{H}^{n-1}\right), \tag{5.25}$$

where g is a regularized Heaviside function, defined by

$$g(x) = \frac{1}{2}\left(1 + \frac{2}{\pi}\arctan\left(\frac{x}{\zeta}\right)\right), \tag{5.26}$$

and ζ is regularization parameter. When ζ decreases, the approximation is closer to a sharp jump (see Fig. 5.2). In this paper, $\zeta = 10^{-6}$ is adopted.

More specifically, expressing the strain and stress tensors in vector forms in 2D , i.e. $[\boldsymbol{\varepsilon}] = [\varepsilon_{11}, \varepsilon_{22}, 2\varepsilon_{12}]$, $[\boldsymbol{\sigma}] = [\sigma_{11}, \sigma_{22}, \sigma_{12}]$, the constitutive law (5.12) can be expressed at time t^n as:

$$\begin{aligned} [\boldsymbol{\sigma}_n] = \left((1-d^n)^2 + b\right) \left\{\lambda \mathscr{R}^+_{n-1}\left([\boldsymbol{\varepsilon}^n]\cdot[\mathbf{1}]\right)[\mathbf{1}] + 2\mu \boldsymbol{P}^+_{n-1}[\boldsymbol{\varepsilon}^n]\right\} \\ + \lambda \mathscr{R}^-_{n-1}\left([\boldsymbol{\varepsilon}^n]\cdot[\mathbf{1}]\right)[\mathbf{1}] + 2\mu \boldsymbol{P}^-_{n-1}[\boldsymbol{\varepsilon}^n], \end{aligned} \tag{5.27}$$

where $\mathscr{R}^{\pm}_{n-1} = \mathscr{R}^{\pm}\left(\boldsymbol{\varepsilon}^{n-1}\right)$ and $\boldsymbol{P}^{\pm}_{n-1} = \boldsymbol{P}^{\pm}\left(\boldsymbol{\varepsilon}^{n-1}\right)$, and $\boldsymbol{P}^{\pm}$ are the matrix forms associated with the fourth-order tensors $\mathbb{P}^{\pm}$.

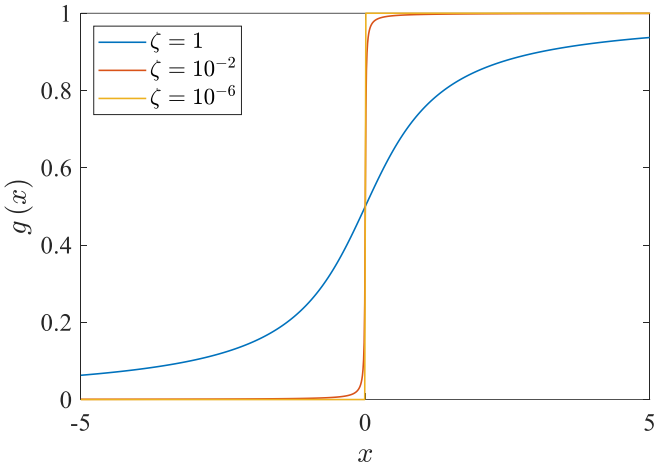

Fig. 5.2 Regularized Heaviside function.

Introducing (5.23) and (5.27) in (5.21)-(5.22) we obtain a linear system of equations in the form

$$\boldsymbol{K}_d^n \boldsymbol{d}^n = \boldsymbol{F}_d^n, \quad \text{(phase field problem)}, \tag{5.28}$$

$$\boldsymbol{M}\ddot{\boldsymbol{u}}^n + \boldsymbol{K}_u^n \boldsymbol{u}^n = \boldsymbol{F}_u^n, \quad \text{(displacement problem)}, \tag{5.29}$$

with

$$\boldsymbol{M} = \int_\Omega \rho \boldsymbol{N}_u{}^T \boldsymbol{N}_u \mathrm{d}\Omega \quad \text{and} \quad \boldsymbol{F}_u^n = \int_{\partial\Omega_{\bar{t}}} \boldsymbol{N}_u \bar{\boldsymbol{t}}^n \, \mathrm{d}S. \tag{5.30}$$

$$\begin{aligned} \boldsymbol{K}_u^n = \int_\Omega \boldsymbol{B}_u^T \left\{ \left((1-d^n)^2 + b\right) \left(\lambda \mathscr{R}_{n-1}^+ [\mathbf{1}]^T [\mathbf{1}] + 2\mu \boldsymbol{P}_{n-1}^+\right) \right\} \boldsymbol{B}_u \mathrm{d}\Omega, \\ + \int_\Omega \boldsymbol{B}_u^T \left\{ \lambda \mathscr{R}_n^- [\mathbf{1}]^T [\mathbf{1}] + 2\mu \boldsymbol{P}_n^- \right\} \boldsymbol{B}_u \mathrm{d}\Omega, \end{aligned} \tag{5.31}$$

$$\boldsymbol{K}_d^n = \int_\Omega \{ (\frac{\mathscr{G}_c}{\ell} + 2\mathscr{H}^n) \boldsymbol{N}_d^T \boldsymbol{N}_d + \mathscr{G}_c \ell \boldsymbol{B}_d^T \boldsymbol{B}_d \} \mathrm{d}\Omega, \tag{5.32}$$

and

$$\boldsymbol{F}_d^n = \int_\Omega 2\boldsymbol{N}_d^T \mathscr{H}^n \mathrm{d}\Omega. \tag{5.33}$$

Then, a time-stepping $\mathscr{I} = [t^0, t^1, t^2, ..., t^M]$ is introduced, where $t^n - t^{n-1} = \Delta t$ is a time step, assumed to be constant. An unconditionally stable implicit Newmark scheme is used to solve (5.29) according to:

$$\dot{\boldsymbol{u}}^n = \dot{\boldsymbol{u}}^{n-1} + \frac{\Delta t}{2}\left(\ddot{\boldsymbol{u}}^{n-1} + \ddot{\boldsymbol{u}}^n\right), \tag{5.34}$$

with

$$\boldsymbol{u}^n = \boldsymbol{u}^{n-1} + \Delta t\,\dot{\boldsymbol{u}}^{n-1} + \left(\frac{\Delta t^2}{4}\right)\left(\ddot{\boldsymbol{u}}^{n-1} + \ddot{\boldsymbol{u}}^n\right), \tag{5.35}$$

$$\ddot{\boldsymbol{u}}^n = \left(\frac{4}{\Delta t^2}\right)\left(\boldsymbol{u}^n - \hat{\boldsymbol{u}}^n\right) \quad , \tag{5.36}$$

$$\hat{\boldsymbol{u}}^n = \boldsymbol{u}^{n-1} + \Delta t\,\dot{\boldsymbol{u}}^{n-1} + \left(\frac{\Delta t^2}{4}\right)\ddot{\boldsymbol{u}}^{n-1}. \tag{5.37}$$

Introducing (5.36) into (5.29), we finally obtain at one iteration k and at one time step t^n the linear problem to be solved:

$$\tilde{\boldsymbol{K}}_u \boldsymbol{u}^n = \tilde{\boldsymbol{F}}_u^n, \tag{5.38}$$

with

$$\tilde{\boldsymbol{K}}_u = \left(\frac{4}{\Delta t^2}\right)\boldsymbol{M} + \boldsymbol{K}_u^n, \tag{5.39}$$

$$\tilde{\boldsymbol{F}}_u^n = \boldsymbol{F}_u^n + \boldsymbol{M}\left(\frac{4}{\Delta t^2}\right)\left[\boldsymbol{u}^{n-1} + \Delta t\,\dot{\boldsymbol{u}}^{n-1} + \left(\frac{\Delta t}{2}\right)^2 \ddot{\boldsymbol{u}}^{n-1}\right]. \tag{5.40}$$

Note that in the present work iterations are used within the staggered scheme, i.e the mechanical and phase field problems are solved alternatively during one time step t^n until a convergence criterion is reached. In this work, the convergence criterion is reached when the maximum value of the nodal phase field variation between two iterations is lower than a threshold. This algorithm allows larger time steps in the present implicit Newmark's scheme. In addition, such staggered scheme is a key ingredient to simplify the sensitivity analysis developed in section 5.4.3.

The general algorithm is summarized in Algorithm 1, where quantities at one time step t^n and at one iteration k are denoted by $(.)_k^n$.

Algorithm 1: Staggered dynamic Phase Field algorithm solving procedure.

Initialize: $\boldsymbol{u}^0$, $\dot{\boldsymbol{u}}^0$, $\ddot{\boldsymbol{u}}^0$, $\boldsymbol{d}^0$, $\mathscr{H}^0 = \boldsymbol{0}$;
for $n = 1 : M$ *(Loop over all time steps)* **do**
  Input: $\boldsymbol{u}^{n-1}$
  Initialize $\boldsymbol{u}_0^n = \boldsymbol{u}^{n-1}$
  $k = k+1$
  while $Err > tol$ *(Convergence loop)* **do**
    $k = k+1$;
    Input: $\boldsymbol{u}_{k-1}^n$
    Solve $\boldsymbol{K}_d(\boldsymbol{u}_{k-1}^n)\boldsymbol{d}_k^n = \boldsymbol{F}_d(\boldsymbol{u}_{k-1}^n)$
    Output: $\boldsymbol{d}_k^n$
    Input: $\boldsymbol{d}_k^n, \boldsymbol{u}_{k-1}^n$
    Solve $\boldsymbol{K}_u(\boldsymbol{u}_{k-1}^n, \boldsymbol{d}_k^n)\boldsymbol{u}_k^n = \boldsymbol{F}_u(\boldsymbol{u}_{k-1}^n)$
    Output: $\boldsymbol{u}_k^n$
    Compute $Err = \max_j |\left[\boldsymbol{d}_k^n\right]_j - \left[\boldsymbol{d}_{k-1}^n\right]_j|$
    $\boldsymbol{u}_{k-1}^n = \boldsymbol{u}_k^n$
  end
  $\boldsymbol{u}^n = \boldsymbol{u}_k^n$
end

5.4 Topology optimization formulations

5.4.1 Material interpolation scheme

In the present paper, the SIMP topology optimization method (Solid Isotropic Material with Penalization (SIMP) method [30, 26]) is adopted. This method belongs to the so-called density-based topology optimization (TO) methods (see a review and classification of TO in [345]). In this framework, the geometry of the structural domain is defined by a pseudo-density parameter $\varphi \in [0,1]$. Then, a continuous description of the material properties is defined according to:

$$\begin{aligned} E(\varphi) &= [E_{\min} + (1 - E_{\min})\,\varphi^{p_E}]\,E_0, \\ \rho(\varphi) &= [\rho_{\min} + (1 - \rho_{\min})\,\varphi^{p_\rho}]\,\rho_0, \\ \mathscr{G}_c(\varphi) &= \left[\mathscr{G}_{c,\min} + \left(1 - \mathscr{G}_{c,\min}\right)\varphi^{p_{\mathscr{G}}}\right]\mathscr{G}_{c,0}, \end{aligned} \tag{5.41}$$

where E_0, ρ_0 and $\mathscr{G}_{c,0}$ denote the material properties of the solid for $\varphi = 1$, and $E_{\min}$, $\rho_{\min}$ and $\mathscr{G}_{c,\min}$ are artificial lower values to avoid numerical singularity in zero-pseudo density zones. Above, p_E, p_ρ and $p_{\mathscr{G}}$ are penalty parameters. These parameters are chosen so as to avoid intermediate values of φ. Here, we choose $p_E = 3$, $p_\rho = 1$ and $p_{\mathscr{G}} = 1$. The

values of $E_{\min}$, $\rho_{\min}$ and $\mathscr{G}_{c,\min}$ are defined as $E_{\min} = 10^{-6}$, $\rho_{\min} = 10^{-6}$ and $\mathscr{G}_{c,\min} = 10^{-2}$, respectively. Note that alternative approaches, e.g. the BESO method [152] could be used (see [210] for a comparison between SIMP and BESO in the context of fracture resistance maximization).

5.4.2 Optimization problem

In this section, we define the topology optimization problem related to minimizing the dynamic fracture of a structure. Following previous works on fracture resistance maximization using topology optimization [403, 210], the phase field method described in section 5.3 is used to describe the full fracture process of the structure, from initiation until full failure, while here the dynamic effects are taken into account. The problem can be formulated as follows:

$$\begin{aligned} &\min_{\varphi\in[0,1]} : G_{\mathrm{f}}(\varphi), \\ &\text{s. t.} : \boldsymbol{K}_d^n \boldsymbol{d}^n = \boldsymbol{F}_d^n, \;\; n = 1,2,...,M \\ &\qquad \boldsymbol{M}\ddot{\boldsymbol{u}}^n + \boldsymbol{K}_u^n \boldsymbol{u}^n = \boldsymbol{F}_u^n, \;\; n = 1,2,...,M \\ &\qquad C - C_0 \leq 0, \\ &\qquad V - \chi V_0 \leq 0, \end{aligned} \tag{5.42}$$

where $G_{\mathrm{f}}(\varphi)$ denotes the fracture energy, and $C = \boldsymbol{F}^s \cdot \boldsymbol{u}^s$ denotes a structural static compliance.

Here, the compliance constraint is only used to ensure connectivity of the material within the structure. Without this constraint, unrealistic topologies with disconnected parts could be obtained in this dynamic context, as cracks may occur in the middle of the structure. The compliance C is evaluated by a separated static test with an external force F^s = -100 N. Note that such compliance constraint has been used by several other authors in a dynamic topology optimization context, even though in a linear vibration regime (see e.g. [351, 449]). Above, $\boldsymbol{u}^s$ is the static displacement response of the undamaged structure under a test static external load $\boldsymbol{F}^s$ and C_0 is the prescribed compliance upper bound; V is the target structural volume (area in 2D), which can be computed as $V = \sum_{e=1}^{N_e} V_e \varphi_e$, and $V_0 = \sum_{e=1}^{N_e} V_e$ is the total volume of the design domain, and χ denotes the target volume fraction constraint. We define the fracture energy over the whole loading history as:

$$G_{\mathrm{f}} = \int_0^T \int_\Omega \left(\frac{1}{\ell} d \cdot \dot{d} + \ell \nabla d \cdot \nabla \dot{d} \right) \mathscr{G}_c \, \mathrm{d}\Omega \, \mathrm{d}t. \tag{5.43}$$

Using the trapezoidal rule, G_{f} can be numerically approximated as

$$G_{\mathrm{f}} = \sum_{n=1}^{M} \frac{1}{2} \left[(\boldsymbol{d}^n)^T \boldsymbol{K}_g \dot{\boldsymbol{d}}^n + \left(\boldsymbol{d}^{n-1}\right)^T \boldsymbol{K}_g \dot{\boldsymbol{d}}^{n-1} \right] \Delta t, \tag{5.44}$$

where $\boldsymbol{K}_g$ is defined by

$$\boldsymbol{K}_g = \int_\Omega \mathscr{G}_c \left(\frac{1}{\ell} (\boldsymbol{N}_d)^T \boldsymbol{N}_d + \ell (\boldsymbol{B}_d)^T \boldsymbol{B}_d \right) \mathrm{d}\Omega. \tag{5.45}$$

Above, $\boldsymbol{K}_g$ is a matrix which depends neither on damage nor on displacement fields.

5.4.3 Sensitivity of fracture energy

In this section, the sensitivity of fracture energy is derived in a dynamic context. The derivations require the use of the adjoint method [194, 61, 51]. For the widely known derivations related to the compliance and volume fraction, one may refer to [32, 10] for details.

The sensitivity of G_{f} with respect to a change in the pseudo-density is given by

$$\frac{\partial G_{\mathrm{f}}}{\partial \varphi_e} = \sum_{n=1}^{M} \frac{1}{2} \frac{\partial}{\partial \varphi_e} \left[(\boldsymbol{d}^n)^T \boldsymbol{K}_g \dot{\boldsymbol{d}}^n + \left(\boldsymbol{d}^{n-1}\right)^T \boldsymbol{K}_g \dot{\boldsymbol{d}}^{n-1} \right] \Delta t, \tag{5.46}$$

and involves evaluating $\frac{\partial \boldsymbol{d}^n}{\partial \varphi^e}$ and $\frac{\partial \dot{\boldsymbol{d}}^n}{\partial \varphi^e}$. Using the chain rule, we have

$$\frac{\partial \dot{\boldsymbol{d}}^n}{\partial \varphi^e} = \frac{\partial \dot{\boldsymbol{d}}^n}{\partial \boldsymbol{d}^n} \frac{\partial \boldsymbol{d}^n}{\partial \varphi^e}, \tag{5.47}$$

where $\frac{\partial \dot{\boldsymbol{d}}^n}{\partial \boldsymbol{d}^n}$ can be obtained by the Newmark scheme (5.34)-(5.36)(5.37) as the simple expression:

$$\frac{\partial \dot{\boldsymbol{d}}^n}{\partial \boldsymbol{d}^n} = \frac{2}{\Delta t}. \tag{5.48}$$

To express $\frac{\partial \boldsymbol{d}^n}{\partial \varphi_e}$ the adjoint method [51] is employed. Introducing two vectors of Lagrange multipliers (adjoint vectors) $\boldsymbol{\lambda}^n$ and $\boldsymbol{\lambda}^{n-1}$, and assuming that the problems

$$\boldsymbol{R}_d^n = \boldsymbol{K}_d^n \boldsymbol{d}^n - \boldsymbol{F}_d^n = \boldsymbol{0}, \tag{5.49}$$

$$\boldsymbol{R}_d^{n-1} = \boldsymbol{K}_d^n \boldsymbol{d}^{n-1} - \boldsymbol{F}_d^{n-1} = \boldsymbol{0}, \tag{5.50}$$

have been solved, then the terms $\left(\boldsymbol{\lambda}^n\right)^T \boldsymbol{R}_d^n$ and $\left(\boldsymbol{\lambda}^{n-1}\right)^T \boldsymbol{R}_d^{n-1}$ can be added to the objective function without change as:

$$G_{\mathrm{f}} = \sum_{n=1}^{N_{\mathrm{s}}} \left\{ \frac{1}{2} \left[\left(\boldsymbol{d}^n\right)^T \boldsymbol{K}_g \dot{\boldsymbol{d}}^n + \left(\boldsymbol{d}^{n-1}\right)^T \boldsymbol{K}_g \dot{\boldsymbol{d}}^{n-1} \right] \Delta t + \left(\boldsymbol{\lambda}^n\right)^T \boldsymbol{R}_d^n + \left(\boldsymbol{\lambda}^{n-1}\right)^T \boldsymbol{R}_d^{n-1} \right\}. \quad (5.51)$$

In addition, using (5.8), $\left(\psi_e^+\right)^n$ can be expressed using the discrete (vector) forms of strain tensor as:

$$\left(\psi_e^+\right)^n = \frac{1}{2} \boldsymbol{\varepsilon}^n \left(\lambda \mathscr{R}_{n-1}^+ \left[\mathbf{1}\right]^T \left[\mathbf{1}\right] + 2\mu \boldsymbol{P}_{n-1}^+ \right) \boldsymbol{\varepsilon}^n. \quad (5.52)$$

In (5.52), it is worth noting that ε obviously depends on φ_e. However, for the sake of simplicity, we assume that the term involving $\frac{\partial \boldsymbol{\varepsilon}}{\partial \varphi_e}$ has small influence as compared to the other terms and neglect it. Then, the following approximation is made:

$$\frac{\partial \left(\psi_e^+\right)^n}{\partial \varphi_e} \simeq \frac{1}{2} \boldsymbol{\varepsilon}^n \left(\frac{\partial \lambda}{\partial \varphi_e} \mathscr{R}_{n-1}^+ \left[\mathbf{1}\right]^T \left[\mathbf{1}\right] + 2 \frac{\partial \mu}{\partial \varphi_e} \boldsymbol{P}_{n-1}^+ \right) \boldsymbol{\varepsilon}^n. \quad (5.53)$$

Taking the derivation of G_{f} with respect to the pseudo-density, using (5.48) and combining similar terms, the following expression is obtained, after some calculations:

$$\begin{aligned} \frac{\partial \hat{G}_{\mathrm{f}}}{\partial \varphi_e} = \sum_{n=1}^{N_{\mathrm{s}}} \Bigg\{ & \frac{1}{2} \left[\left(\boldsymbol{d}^n\right)^T \frac{\partial \boldsymbol{K}_g}{\partial \varphi_e} \dot{\boldsymbol{d}}^n + \left(\boldsymbol{d}^{n-1}\right)^T \frac{\partial \boldsymbol{K}_g}{\partial \varphi_e} \dot{\boldsymbol{d}}^{n-1} \right] \Delta t \\ & + \left(\boldsymbol{\lambda}^n\right)^T \left(\frac{\partial \boldsymbol{K}_d^n}{\partial \varphi_e} \boldsymbol{d}^n - \frac{\partial \boldsymbol{F}_d^n}{\partial \varphi_e} \right) + \left(\boldsymbol{\lambda}^{n-1}\right)^T \left(\frac{\partial \boldsymbol{K}_d^{n-1}}{\partial \varphi_e} \boldsymbol{d}^{n-1} - \frac{\partial \boldsymbol{F}_d^{n-1}}{\partial \varphi_e} \right) \\ & + \left[\frac{1}{2} \left(\left(\dot{\boldsymbol{d}}^n\right)^T \boldsymbol{K}_g + \left(\boldsymbol{d}^n\right)^T \boldsymbol{K}_g \frac{\partial \dot{\boldsymbol{d}}^n}{\partial \boldsymbol{d}^n} \right) \Delta t + \left(\boldsymbol{\lambda}^n\right)^T \boldsymbol{K}_d^n \right] \frac{\partial \boldsymbol{d}^n}{\partial \varphi_e} \\ & + \left[\frac{1}{2} \left(\left(\dot{\boldsymbol{d}}^{n-1}\right)^T \boldsymbol{K}_g + \left(\boldsymbol{d}^{n-1}\right)^T \boldsymbol{K}_g \frac{\partial \dot{\boldsymbol{d}}^{n-1}}{\partial \boldsymbol{d}^{n-1}} \right) \Delta t + \left(\boldsymbol{\lambda}^{n-1}\right)^T \boldsymbol{K}_d^{n-1} \right] \frac{\partial \boldsymbol{d}^{n-1}}{\partial \varphi_e} \Bigg\}. \end{aligned} \quad (5.54)$$

The terms $\frac{\partial \boldsymbol{d}^n}{\partial \varphi_e}$ and $\frac{\partial \boldsymbol{d}^{n-1}}{\partial \varphi_e}$ are difficult to evaluate in practice. However, as $\boldsymbol{R}_d^n = \mathbf{0}$ and $\boldsymbol{R}_d^{n-1} = \mathbf{0}$, the vectors $\boldsymbol{\lambda}^n$ and $\boldsymbol{\lambda}^{n-1}$ can be chosen arbitrarily. They are then chosen to eliminate the unknown terms $\frac{\partial \boldsymbol{d}^n}{\partial \varphi_e}$ and $\frac{\partial \boldsymbol{d}^{n-1}}{\partial \varphi_e}$ such that:

$$\left[\frac{1}{2} \left(\left(\dot{\boldsymbol{d}}^n\right)^T \boldsymbol{K}_g + \left(\boldsymbol{d}^n\right)^T \boldsymbol{K}_g \frac{\partial \dot{\boldsymbol{d}}^n}{\partial \boldsymbol{d}^n} \right) \Delta t + \left(\boldsymbol{\lambda}^n\right)^T \boldsymbol{K}_d^n \right] \frac{\partial \boldsymbol{d}^n}{\partial \varphi_e} = 0, \quad (5.55)$$

and

$$\left[\frac{1}{2}\left(\left(\dot{\boldsymbol{d}}^{n-1}\right)^T\boldsymbol{K}_g+\left(\boldsymbol{d}^{n-1}\right)^T\boldsymbol{K}_g\frac{\partial\dot{\boldsymbol{d}}^{n-1}}{\partial\boldsymbol{d}^{n-1}}\right)\Delta t+\left(\boldsymbol{\lambda}^{n-1}\right)^T\boldsymbol{K}_d^{n-1}\right]\frac{\partial\boldsymbol{d}^{n-1}}{\partial\varphi_e}=0. \tag{5.56}$$

Eqs. (5.55) and (5.56) are equal to zero if the expressions under brackets on the left-hand are equal to zero, corresponding to the following systems of equations:

$$2\boldsymbol{K}_d^n\boldsymbol{\lambda}^n=-\left(\boldsymbol{K}_g\dot{\boldsymbol{d}}^n+\boldsymbol{K}_g\frac{\partial\dot{\boldsymbol{d}}^n}{\partial\boldsymbol{d}^n}\boldsymbol{d}^n\right)\Delta t, \tag{5.57}$$

and

$$2\boldsymbol{K}_d^{n-1}\boldsymbol{\lambda}^{n-1}=-\left(\boldsymbol{K}_g\dot{\boldsymbol{d}}^{n-1}+\boldsymbol{K}_g\frac{\partial\dot{\boldsymbol{d}}^{n-1}}{\partial\boldsymbol{d}^{n-1}}\boldsymbol{d}^{n-1}\right)\Delta t. \tag{5.58}$$

Solving Eqs. (5.57) and (5.58), the Lagrange multipliers $\boldsymbol{\lambda}^n$ and $\boldsymbol{\lambda}^{n-1}$ are then available. Above, the expressions of $\dot{\boldsymbol{d}}^n$ can be computed according to (5.34). The sensitivity of the fracture energy is then finally obtained as:

$$\boxed{\begin{aligned}\frac{\partial G_{\mathrm{f}}}{\partial\varphi_e}=\sum_{n=1}^{N_{\mathrm{s}}}\Bigg\{&\frac{1}{2}\left[\left(\boldsymbol{d}^n\right)^T\frac{\partial\boldsymbol{K}_g}{\partial\varphi_e}\dot{\boldsymbol{d}}^n+\left(\boldsymbol{d}^{n-1}\right)^T\frac{\partial\boldsymbol{K}_g}{\partial\varphi_e}\dot{\boldsymbol{d}}^{n-1}\right]\Delta t\\&+\left(\boldsymbol{\lambda}^n\right)^T\left(\frac{\partial\boldsymbol{K}_d^n}{\partial\varphi_e}\boldsymbol{d}^n-\frac{\partial\boldsymbol{F}_d^n}{\partial\varphi_e}\right)+\left(\boldsymbol{\lambda}^{n-1}\right)^T\left(\frac{\partial\boldsymbol{K}_d^{n-1}}{\partial\varphi_e}\boldsymbol{d}^{n-1}-\frac{\partial\boldsymbol{F}_d^{n-1}}{\partial\varphi_e}\right)\Bigg\},\end{aligned}} \tag{5.59}$$

in which $\frac{\partial\boldsymbol{K}_g}{\partial\varphi_e}$ can be derived from Eq. (5.45), as:

$$\frac{\partial\boldsymbol{K}_g}{\partial\varphi_e}=\int_\Omega\frac{\partial\mathscr{G}_c}{\partial\varphi_e}\left(\frac{1}{\ell}\left(\boldsymbol{N}_d\right)^T\boldsymbol{N}_d+\ell\left(\boldsymbol{B}_d\right)^T\boldsymbol{B}_d\right)\mathrm{d}\Omega. \tag{5.60}$$

The terms $\frac{\partial\boldsymbol{K}_d^n}{\partial\varphi_e}$ and $\frac{\partial\boldsymbol{F}_d^n}{\partial\varphi_e}$ are given by

$$\begin{aligned}\frac{\partial\boldsymbol{K}_d^n}{\partial\varphi_e}&=\int_\Omega\left\{\left(2\frac{\partial\mathscr{H}_n}{\partial\varphi_e}+\frac{\partial\mathscr{G}_c}{\ell\partial\varphi_e}\right)\left(\boldsymbol{N}_d\right)^T\boldsymbol{N}^d+\frac{\partial\mathscr{G}_c}{\partial\varphi_e}\ell\left(\boldsymbol{B}_d\right)^T\boldsymbol{B}_d\right\}\mathrm{d}\Omega,\\\frac{\partial\boldsymbol{F}_d^n}{\partial\varphi_e}&=\int_\Omega 2\frac{\partial\mathscr{H}_n}{\partial\varphi_e}\boldsymbol{N}_d\mathrm{d}\Omega,\end{aligned} \tag{5.61}$$

where $\frac{\partial \mathscr{G}_c}{\partial \varphi_e}$ can be obtained from the material interpolation scheme (5.41), and $\frac{\partial \mathscr{H}^n}{\partial \varphi_e}$ can be derived from Eq. (5.25):

$$\frac{\partial \mathscr{H}^n}{\partial \varphi_e} = \frac{\partial \psi_e^+}{\partial \varphi_e} g\left(\psi_e^+ - \mathscr{H}^{n-1}\right) + \left[\psi_e^+ - \mathscr{H}^{n-1}\right] \frac{\partial g\left(\psi_e^+ - \mathscr{H}^{n-1}\right)}{\partial \varphi_e}, \tag{5.62}$$

with

$$\frac{\partial g\left((\psi_e^+)^n - \mathscr{H}^{n-1}\right)}{\partial \varphi_e} = \frac{\zeta \frac{\partial \left(\psi_e^+\right)^n}{\partial \varphi_e}}{\pi\left(\zeta^2 + \left(\left(\psi_e^+\right)^n - \mathscr{H}^{n-1}\right)^2\right)}, \tag{5.63}$$

and the term $\frac{\partial \left(\psi_e^+\right)^n}{\partial \varphi_e}$ have been approximated by Eq. (5.53). Note that above adjoint vectors $\boldsymbol{\lambda}^n$ and $\boldsymbol{\lambda}^{n-1}$ are here path-independent, in contrast to other formulations, see e.g. [329, 330]. This strong assumption has the advantage to gratefully simplify the formulation and the implementation. The influence of such simplification on the accuracy of the sensitivities will be tested in the numerical examples.

5.4.4 Optimization techniques

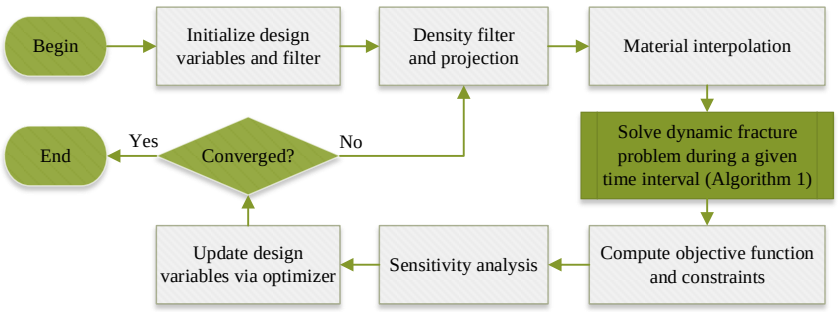

Fig. 5.3 Optimization flow chart.

To improve stability, mesh independence and to eliminate so called *checkerboard* issues [346], filtering techniques are often used in topology optimization. Following [333, 10], a filtered density variable θ_e is introduced as

$$\theta_e = \frac{\sum_{i \in \mathscr{N}_e} \varpi_e V_e \vartheta_e}{\sum_{i \in \mathscr{N}_e} \varpi_e V_e}, \tag{5.64}$$

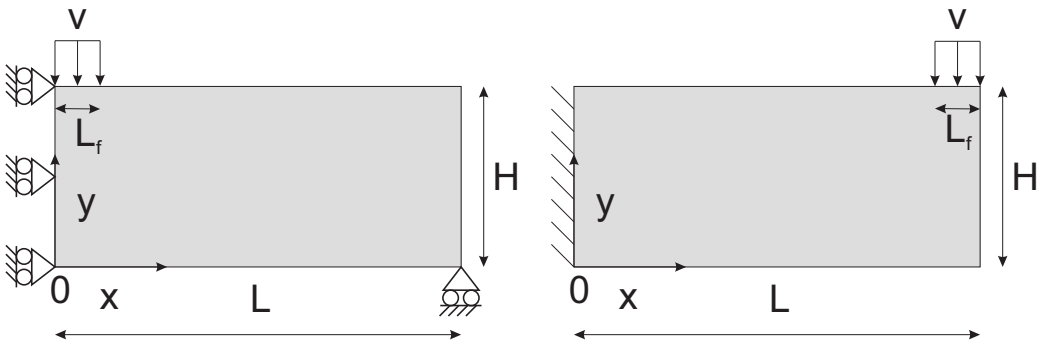

Fig. 5.4 Geometry and boundary conditions of: (a) Half MBB-beam; (b) Cantilever beam.

where ϑ denotes the design variable and $\mathscr{N}_e$ denotes the set of elements whose center-to-center distance r_{ei} to the e-th element is lower than the filter radius $r_{\min}$. The corresponding weighting factor ϖ_{ei} is defined by $\varpi_{ei} = \max(0, r_{\min} - r_{ei})$.

The projection technique proposed by Guest et al. [130] is then adopted to minimize transition regions with pseudo-density values φ between zero and one, as

$$\varphi_e = 1 - e^{-\eta\theta_e} + \theta_e e^{-\eta}, \tag{5.65}$$

where φ_e is the elemental pseudo-density, and η is a parameter defined by 1 in the first iteration and is doubled after every specified time steps until it reaches a chosen maximum value, taken here as 128 by numerical tests.

Using this procedure, the sensitivities of the objective functions and optimization constraints with respect to the design variable can be further derived by means of the chain rule as

$$\frac{\partial f(\varphi_e)}{\partial \vartheta_e} = \frac{\partial f}{\partial \varphi_e}\frac{\partial \varphi_e}{\partial \theta_e}\frac{\partial \theta_e}{\partial \vartheta_e}. \tag{5.66}$$

The method of moving asymptotes (MMA) proposed by Svanberg [360] is adopted for seeking the optimal distribution of the design variables ϑ. Following [128], the η-based modification on the asymptotes are adopted for removing spurious oscillations after doubling the projection parameter η. The convergence criterion of the topology optimization is determined by the maximal change on the design variable, which should be less than 10^{-3}. Fig. 5.3 summarizes the flow chart of the proposed topology optimization.

5.5 Numerical examples

In this section, two typical 2D structures are considered. These have been widely studied in the topology optimization community. The first one is a 3-point bending beam, also

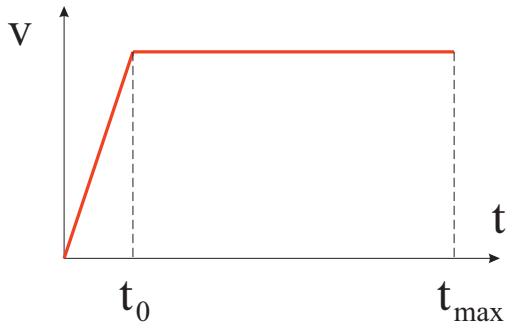

Fig. 5.5 Prescribed velocity.

Table 5.1 Material parameters.

Material properties	Symbol	Value	Unit
Young's modulus	E_0	1.9×10^5	MPa
Poisson's ratio	ν	0.3	-
Density	ρ_0	8×10^{-9}	ton/mm^3
Critical energy release rate	$\mathscr{G}_{c,0}$	22.17	N/mm

called MBB-beam in the literature [289]. For the sake of computational costs, only the right half of this axisymmetric beam is considered as shown in Fig. 5.4(a). The left end is simply supported in the x-direction and the lower right-end corner is simply supported in the y-direction. The second structure is a cantilever beam, which is shown in Fig. 5.4(b). The length and width of these two structures are the same, $L = 150$ mm and $H = 60$ mm. A velocity is prescribed on a surface of length $L_f = 4$mm. Fig. 5.5 depicts the loading velocity profile, which increases from 0 to v_0 by a time t_0, and then remains constant until the maximum time $t_{\max}$ is reached. The material properties adopted here are taken from the Kalthoff-Winkler experiment [180], and are summarized in Table 5.1. The same geometry, loading curve and parameters will be kept in all following examples. In the example of section 5.5.1, the structure is discretized into a coarse 75×30 four-node quadrilateral elements mesh for the sake of computational costs. In the examples of sections 5.5.2 and 5.5.3, a finer mesh with 150×60 four-node quadrilateral finite elements is adopted.

To evaluate the added value of the present framework, two solutions are defined:

1. A so-called "S-design" solution. This solution is obtained by static topology optimization with minimization of compliance under volume constraint with a static force chosen as $\boldsymbol{F}^s = -100$N. Then, the design is remained unchanged during the dynamic fracture simulation. The obtained design for the two problems studied in the next

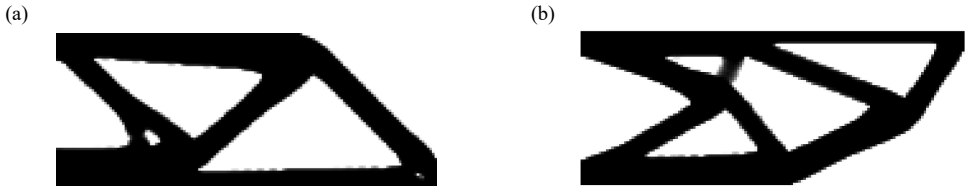

Fig. 5.6 S-designs obtained for :(a) the half MBB-beam; (b) the cantilever beam.

Table 5.2 Numerical parameters for validation of sensitivity analysis.

φ	$\Delta\varphi_e$	ℓ	v_0	Δt	t_0	$t_{\max}$	tol
0.5	10^{-6}	4 mm	40m/s	1 μs	2 μs	80 μs	10^{-5}

examples, namely the half MBB-beam and the cantilever beam are depicted in Fig. 5.6.

2. A so-called "DF-design" solution. In that case, the problem 5.42 is solved to define the topology: at each iteration of the algorithm, a static problem is firstly solved to prescribe the compliance constraint, then a full dynamic fracture simulation is performed to evaluate the fracture energy, and compute the sensitivities to update the topology.

5.5.1 Validation of sensitivity analysis

First the sensitivity analysis developed in section 5.4.3 is validated. Both half MBB-beam and cantilever beam are considered.

The central finite difference method is employed to provide a reference solution to be compared with our semi-analytical sensitivities expressions, according to:

$$\frac{\mathrm{d}f(\varphi)}{\mathrm{d}\varphi_e} \approx \frac{f(\varphi_1,...,\varphi_e+\Delta\varphi_e,...,\varphi_{N_e}) - f(\varphi_1,...,\varphi_e-\Delta\varphi_e,...,\varphi_{N_e})}{2\Delta\varphi_e}, \tag{5.67}$$

where $\Delta\varphi_e$ is a pseudo-density perturbation parameter. The value of the numerical parameters are listed on Table 5.2.

Figs. 5.7(a) and (b) depict the fracture plot of the half MBB-beam and cantilever beam at time $t_{\max} = 80$ μs, in which only $d > 0.6$ is depicted for the sake of clarity. Figs. 5.7(c) and

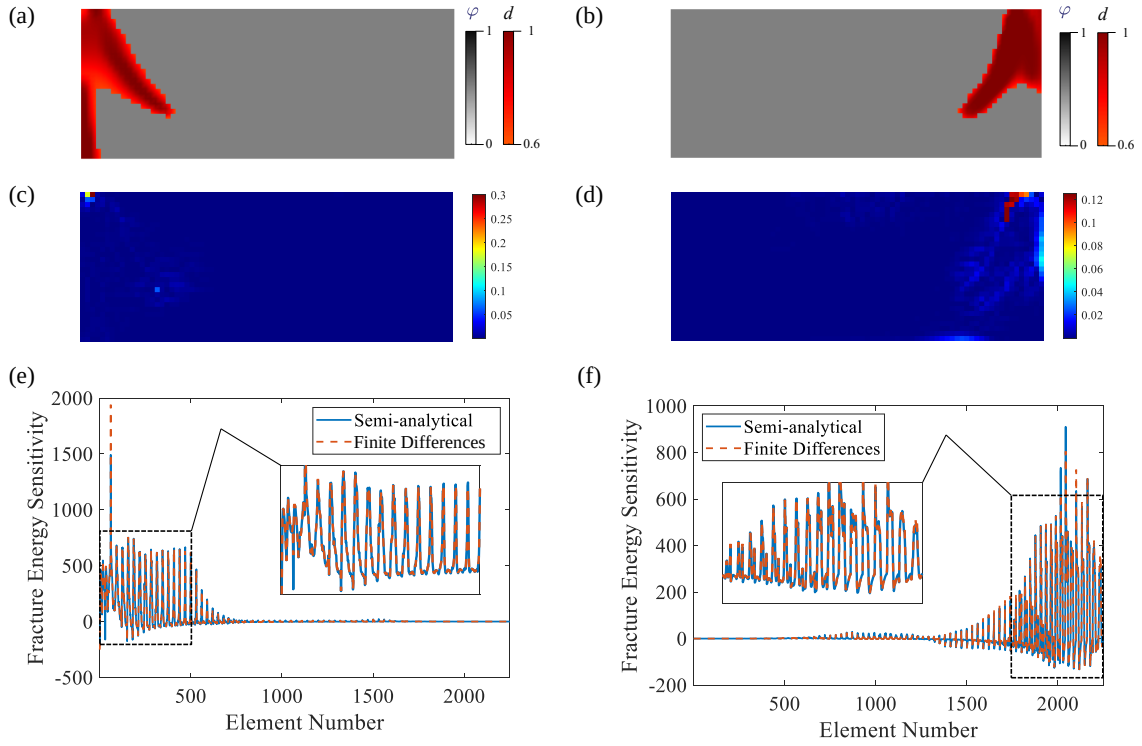

Fig. 5.7 Validation of fracture energy sensitivity analysis: fracture pattern at $t_{\max} = 80$ μs in (a) the half MBB-beam; (b) the cantilever beam; error of normalized sensitivity values (c) the half MBB-beam; (d) the cantilever beam; sensitivity values in elements at $t_{\max} = 80$ in (e) the half MBB-beam and (f) the cantilever beam.

Table 5.3 Comparison of fracture energy using DF-design for $t_{\max} = 40$ μs and S-design at final simulation time for different loading rates.

Loading rate (m/s)	S-design	DF-design	Fracture energy reduction
20	258.23	91.51	64.5%
40	2213.33	347.92	84.3%
60	4133.94	627.92	84.8%

(d) show the normalized error map of the sensitivity values, which is defined by:

$$error = \frac{\left| \boldsymbol{\xi}^{dif} - \boldsymbol{\xi}^{ana} \right|}{\left| \overline{\xi^{ana}} \right|}, \tag{5.68}$$

where $\boldsymbol{\xi}$ denotes the vector of element sensitivity values. The superscripts dif and ana indicate the finite difference method and semi-analytical method, respectively, and $\overline{\xi^{ana}}$ denotes the maximum element sensitivity obtained by the semi-analytical method. Figs. 5.7(e) and (f) show a comparison between elemental sensitivities associated with the fracture energy of these two structures. A good agreement between our analytical expressions of sensitivities and the reference finite difference solution is noticed.

Fig. 5.8 depicts the sensitivity validation on a structure with random distribution of densities $\varphi_e \in [0,1]$ in the elements. After generating the densities using a uniform probability of distributions, a filter is then applied. The other parameters are provided in Table 5.2.

We can note that even though the absolute values of sensistivities are good, the relative errors might locally be high, even though localized, associated with the approximation made in Eq. (5.53). However, these errors remain acceptable. In addition, it will be shown in the next examples that the made approximation allows a large simplification of the whole methodology, while keeping important dynamic fracture reduction results.

5.5.2 Half-MBB beam

In this example, the presented methodology is applied to the Half-MBB beam (see Fig. 5.4(a)) to minimize the fracture energy with respect to the topology of the structure. Three different values of loading rates are investigated, $v_0 = 20$ m/s, $v_0 = 40$ m/s and $v_0 = 60$ m/s, respectively. Two maximal loading times, $t_{\max} = 40$ μs and $t_{\max} = 100$ μs, are separately considered. The compliance constraints are defined by $C_0 = 200$ N.mm and $C_0 = 300$ N.mm for both loading times. The volume fraction constraint is $\chi = 0.5$. The filter radius is chosen as $r_{\min} = 4.5$ and $\ell = 2$ mm, $\Delta t = 1$ μs, $t_0 = 2$ μs and $tol = 10^{-5}$.

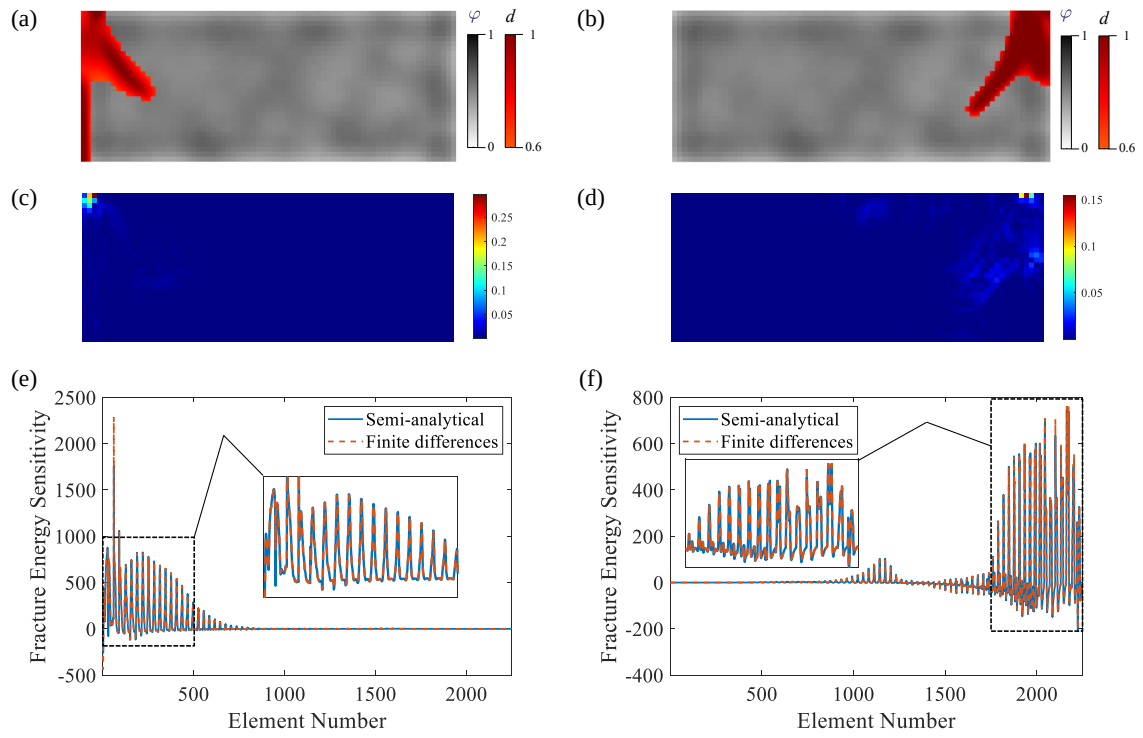

Fig. 5.8 Validation of fracture energy sensitivity analysis on a design-variable-random-distributed structure: fracture pattern at $t_{\max} = 80$ μs in (a) the half MBB-beam; (b) the cantilever beam; error of normalized sensitivity values (c) the half MBB-beam; (d) the cantilever beam; sensitivity values in elements at $t_{\max} = 80$ in (e) the half MBB-beam and (f) the cantilever beam.

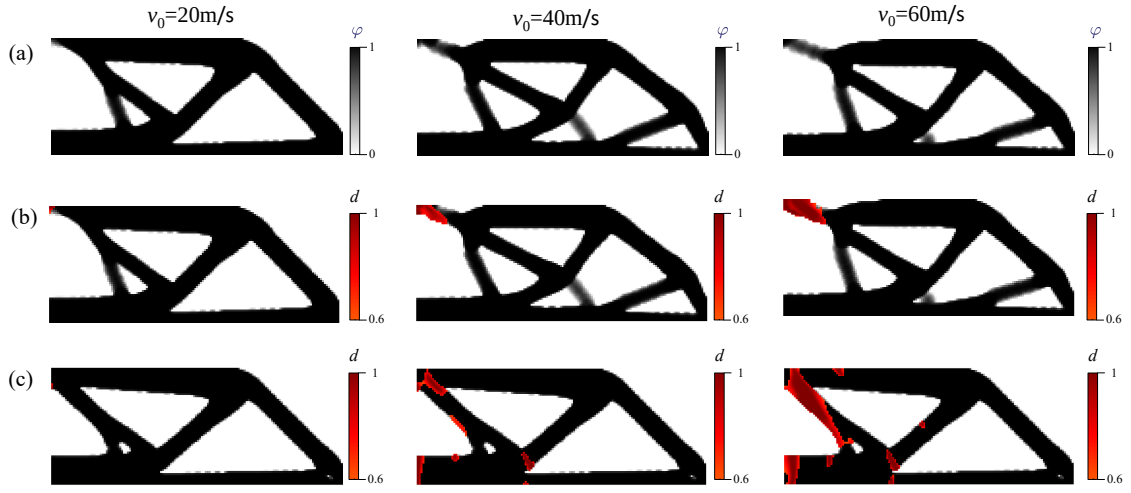

Fig. 5.9 Obtained topological designs for $t_{\max} = 40\mu s$ and corresponding final fracture patterns for different loading rates: (a) DF-design: final topology; (b) DF-design: final crack pattern; (c) S-design: final crack patterns.

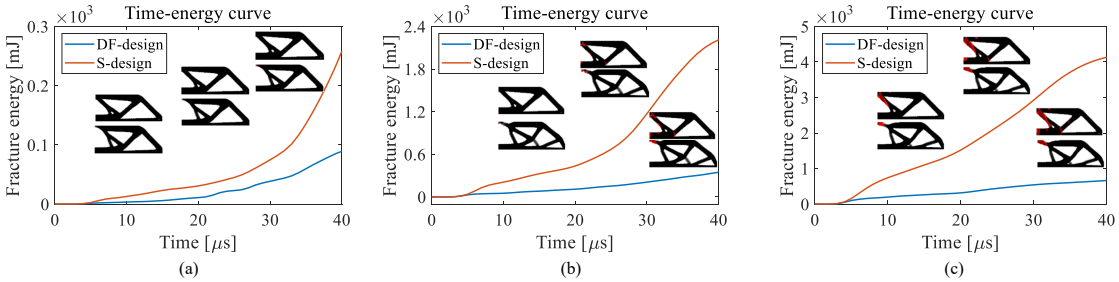

Fig. 5.10 Comparison of time-energy curves for S-and DF-designs for $t_{\max} = 40$ μs at different loading rates: (a) $v_0 = 20$ m/s; (b) $v_0 = 40$ m/s; $v_0 = 60$ m/s

Table 5.4 Comparison on the fracture energy for DF-designs for $t_{\max} = 100$ μs and S-design at the final time for different loading rates.

Loading rate (m/s)	S-design	DF-design	Fracture energy reduction
20	2312.37	313.97	86.4%
40	5396.64	1007.77	81.2%
60	8127.18	2530.02	68.9%

Fig. 5.9(a) shows the topological designs for $t_{\max} = 40$ μs for the different loading rates. Material on the right side of the loading area is removed because it is the location of cracks initiation under high-speed impact. Fig. 5.9(b) shows the crack patterns at $t_{\max} = 40$ μs. For comparison, the crack patterns of the reference S-design (static case) are shown accordingly in Fig. 5.9(c) . Fig. 5.10 compares the fracture energy evolution in time for the present Dynamic Fracture DF- and S- optimized designs, in a period of time [0-40μs]. An important decrease of the fracture energy using the DF-design for all loading rates is appreciated, which shows the importance of including the dynamics in the topology optimization analysis as compared to the designs obtained by simple static analysis. Corresponding comparisons and fracture energy reduction at $t = 40$ μs are presented in Table 5.3. When the loading rate increases, and thus the related dynamic effects, the reduction of the fracture energy as compared to the one obtained by static analysis is even larger.

Fig. 5.11 depicts the iterative process plots of the above topology optimizations. Regardless of the jumps caused by the variation of the projection parameter η, a good convergence is appreciated. All the optimization constraints are verified, except the compliance constraint for $v_0 = 60$ m/s, which might be too strict to be reached in this case. The competition between minimizing the fracture energy and satisfying the compliance constraint might be one possible reason for the observed oscillations. For the case $v_0 = 20$m/s, 647 iterations were necessary, for a total of 8.7 h on a single processor for the whole optimization process.

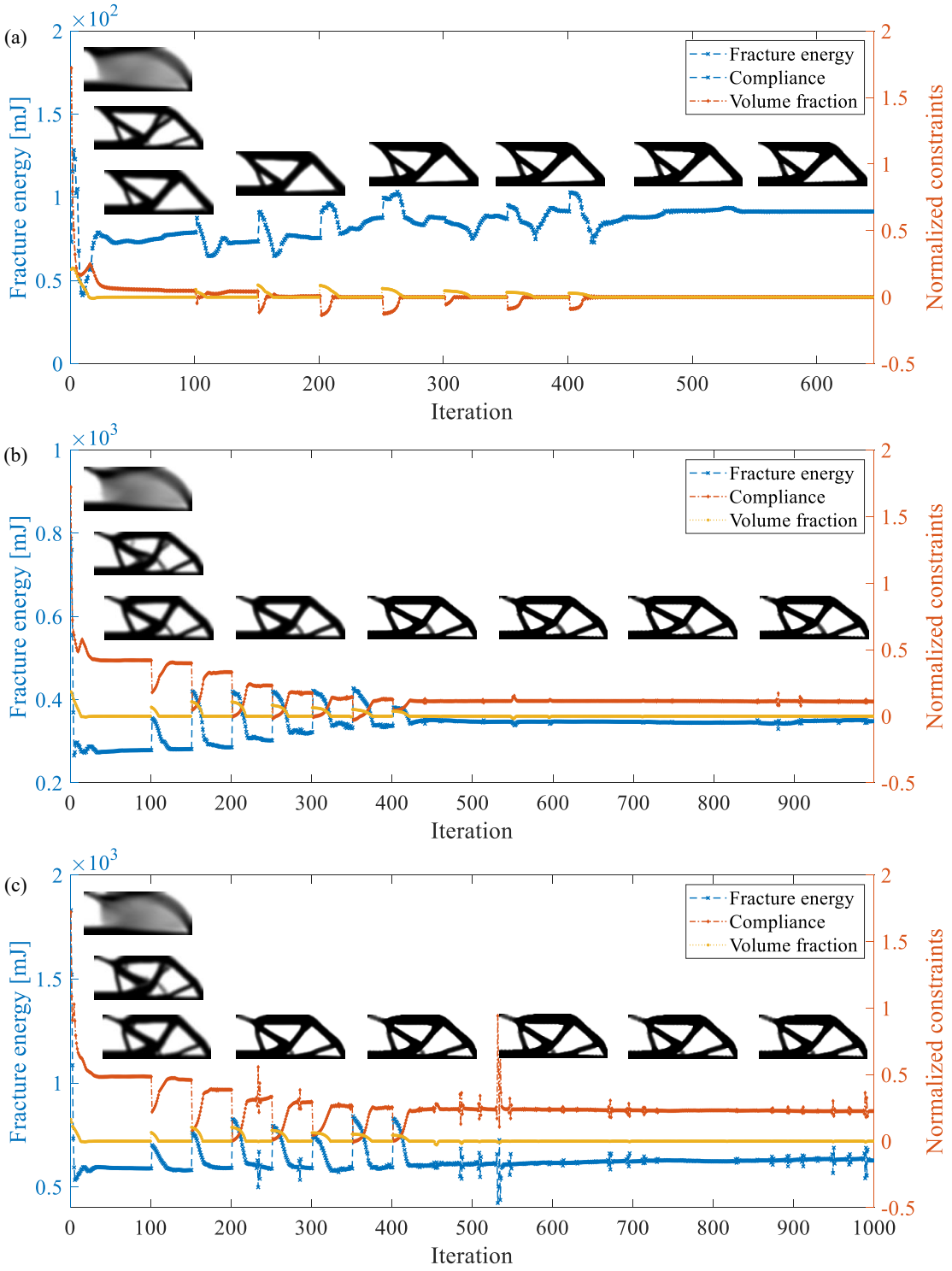

Fig. 5.11 Iterative topology optimization process for $t_{\max} = 40\ \mu s$ under different lading rates: (a) $v_0 = 20$ m/s; (b) $v_0 = 40$ m/s; (c) $v_0 = 60$ m/s.

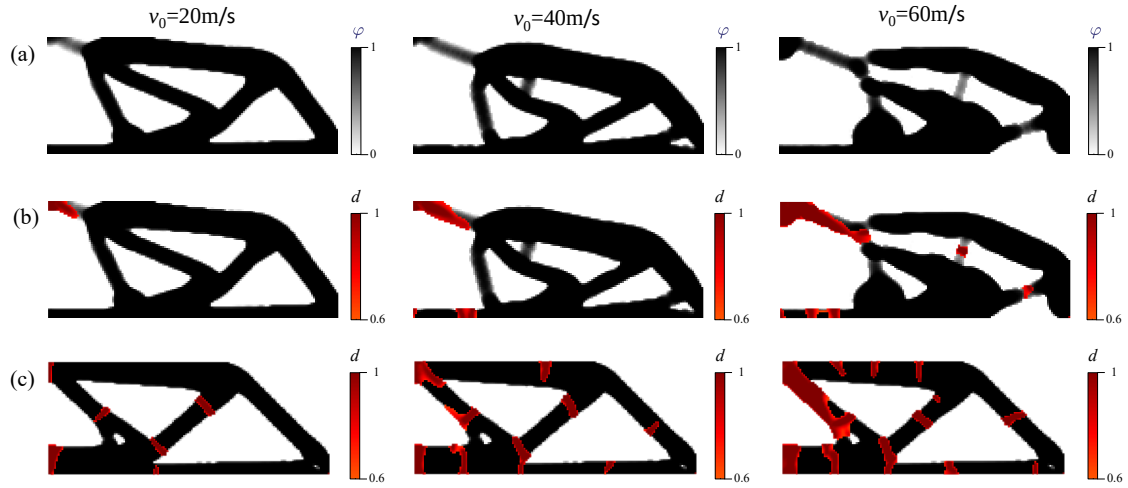

Fig. 5.12 Topological designs for $t_{\max} = 100\ \mu s$ and corresponding final fracture patterns for different loading rates: (a) DF-design: final topology; (b) DF-design: final crack pattern; (c) S-design: final crack patterns.

Next, a longer loading period is investigated, with $t_{\max} = 100\ \mu$s. Fig. 5.12 depicts the topological designs and their final fracture patterns under different loading rates. Compared to the designs for $t_{\max} = 40\ \mu s$ shown in Fig. 5.9, the obtained designs show an obvious difference, and the final fracture patterns also change accordingly. Fig. 5.13 depicts the iterative processes of these topological designs. In this case, although the objective function remains oscillatory, these oscillations remain small and around a stable value. The computational time for the case $v_0 = 20$m/s is 23 h for 672 iterations. The computational times are here proportional to the chosen loading period. Fig. 5.14 compares the fracture energy evolution in a period of time [0-100 μs] obtained by the present DF-designs for $t_{\max} = 100\ \mu s$ and the S-designs. Once again, an important decrease of the fracture energy using the DF-design for all loading rates is appreciated. Corresponding comparisons and fracture energy reductions at $t = 100\ \mu$s are indicated in Table 5.4.

5.5.3 Cantilever beam

In this section, the cantilever cantilever beam shown in Fig. 5.4(b) is investigated. Similarly, three different values of loading rates, $v_0 = 20$ m/s, $v_0 = 40$ m/s and $v_0 = 60$ m/s are studied. The maximal loading time in this example is defined by $t_{\max} = 60\ \mu$s. The compliance constraint is defined by $C_0 = 200$ N ·mm. The volume fraction constraint is $\chi = 0.5$. The filter radius is chosen as $r_{\min} = 4.5$ and $\ell = 2$ mm, $\Delta t = 1\ \mu$s, $t_0 = 2\ \mu$s and $tol = 10^{-5}$.

Fig. 5.15(a) shows the topological designs of the cantilever beam for different loading rates. Here, the proposed method gives different topology designs for different loading rates.

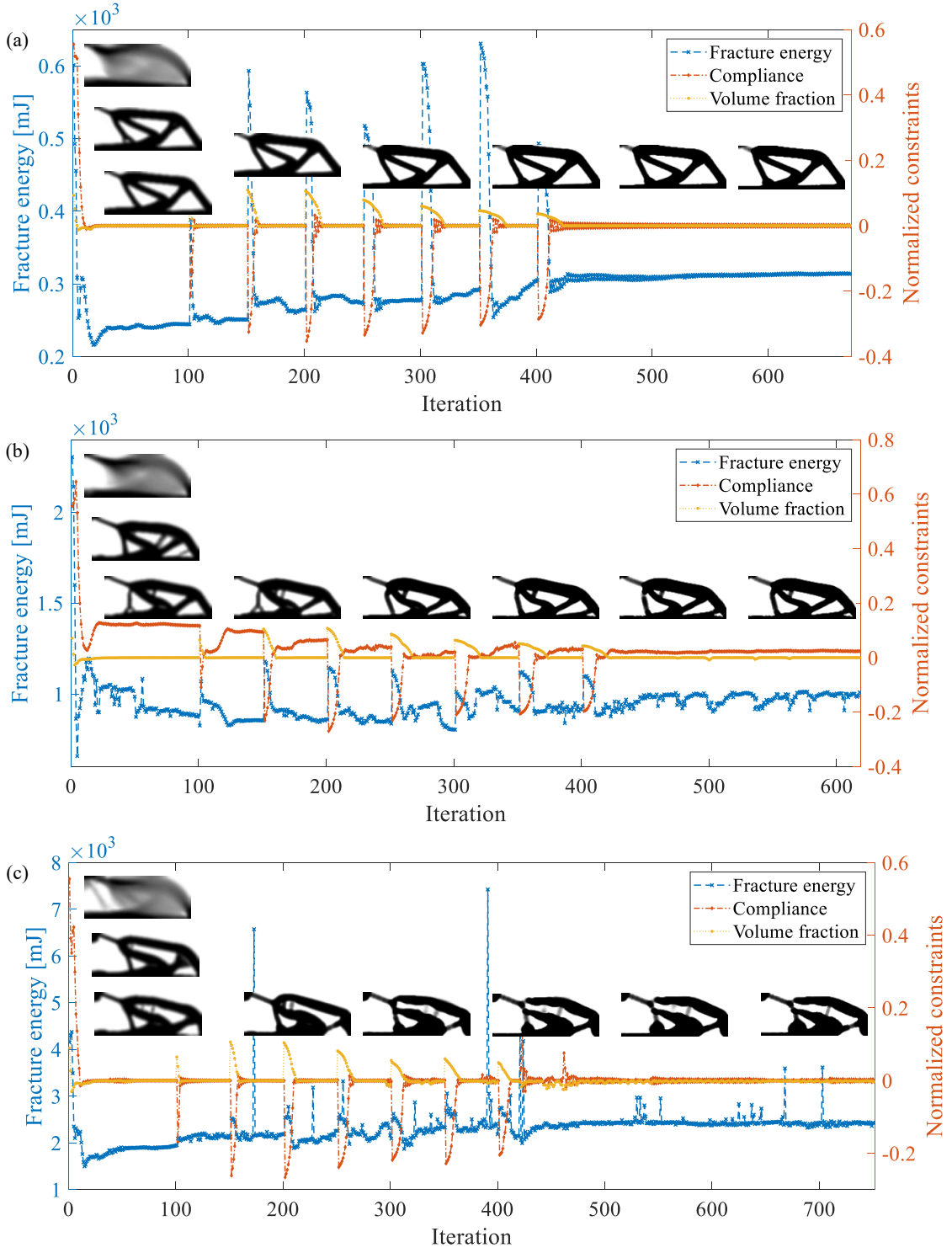

Fig. 5.13 Iteration process of the topology optimization for $t_{\max} = 100\ \mu s$ for different lading rates: (a) $v_0 = 20$ m/s; (b) $v_0 = 40$ m/s; (c) $v_0 = 60$ m/s.

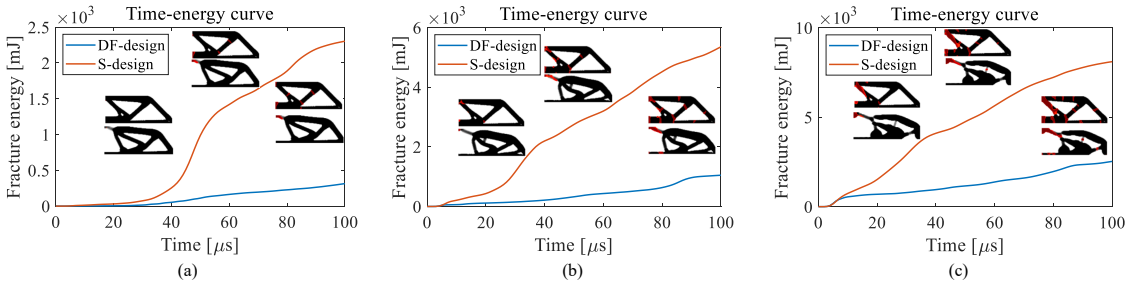

Fig. 5.14 Comparison of time-energy curves for S- and DF-designs for $t_{\max} = 100\mu s$ at different loading rates: (a) $v_0 = 20$ m/s; (b) $v_0 = 40$ m/s; $v_0 = 60$ m/s.

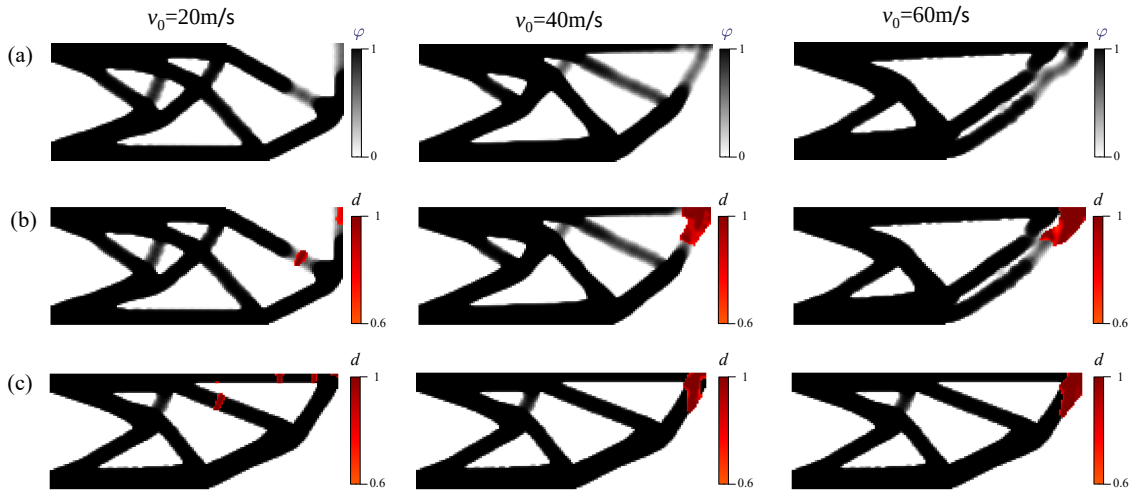

Fig. 5.15 Topological designs for the cantilever beam and corresponding final fracture patterns for different loading rates: (a) DF-design: final topology; (b) DF-design: final crack pattern; (c) S-design: final crack patterns.

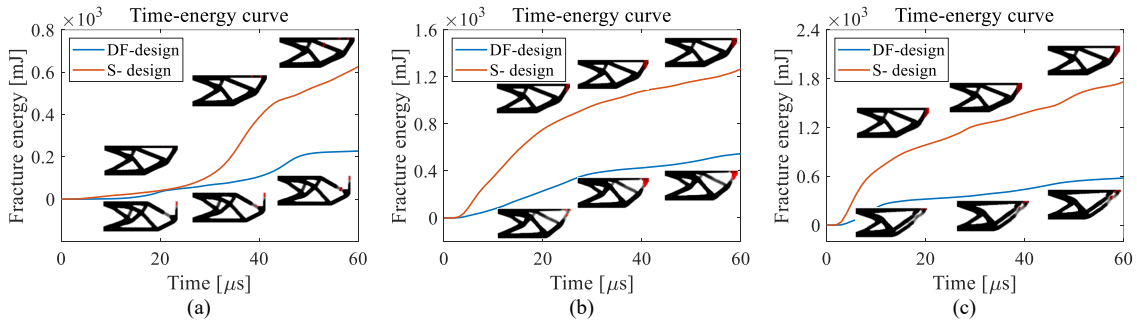

Fig. 5.16 Comparison of time-energy curves for S- and DF-designs at different loading rates: (a) $v_0 = 20$ m/s; (b) $v_0 = 40$ m/s; $v_0 = 60$ m/s.

Table 5.5 Comparison on the fracture energy of DF- and S-design for the cantilever beam at the final time for different loading rates.

Loading rate (m/s)	S-design	DF-design	Fracture energy reduction
20	638.56	227.20	64.4%
40	1289.30	546.75	57.6%
60	1788.05	578.54	67.6%

Fig. 5.15(b) shows the crack pattern at $t_{\max} = 60$ μs. Fig. 5.15(c) depicts the final crack pattern of the S- design for comparison. It is worth noting that there remain some gray elements in the DF- designs. This issue is a classical one found by several other authors in dynamic topology optimization. For example, it is discussed as a key issue in [351] and found in other works such as in [424, 439]. As the main objective of this paper is to present the new topology optimization algorithm with fracture minimization objective, fully addressing this problem is reported to later studies. Fig. 5.16 depicts the fracture energy evolution of the DF- and S- designs in a period of time [0-60 μs]. Table 5.5 provides the comparison of fracture energy for different loading rates of the DF- and S- designs at the final time. Again, the DF-designs show large reductions of the fracture energy. Further investigations, including comparisons with stress-based linear topology optimization, could be conducted in future studies.

Fig. 5.17 depicts the iterative processes of the topology optimizations for different loading rates. A good convergence is obtained and all the constraints are reached. The computational time for the case $v_0 = 20$m/s is 12.7 h for 624 iterations.

As a final remark, we can note that in most studied examples, the cracks are rather diffuse damage zones. In the present phase field framework, the cracks width depends on the mesh density. To maintain reasonable computational costs, we used meshes which do not allow very fine descriptions of cracks. However, it has been shown in many other studies (see e.g. [147]) that the phase field method is fully convergent with respect to the mesh density, even

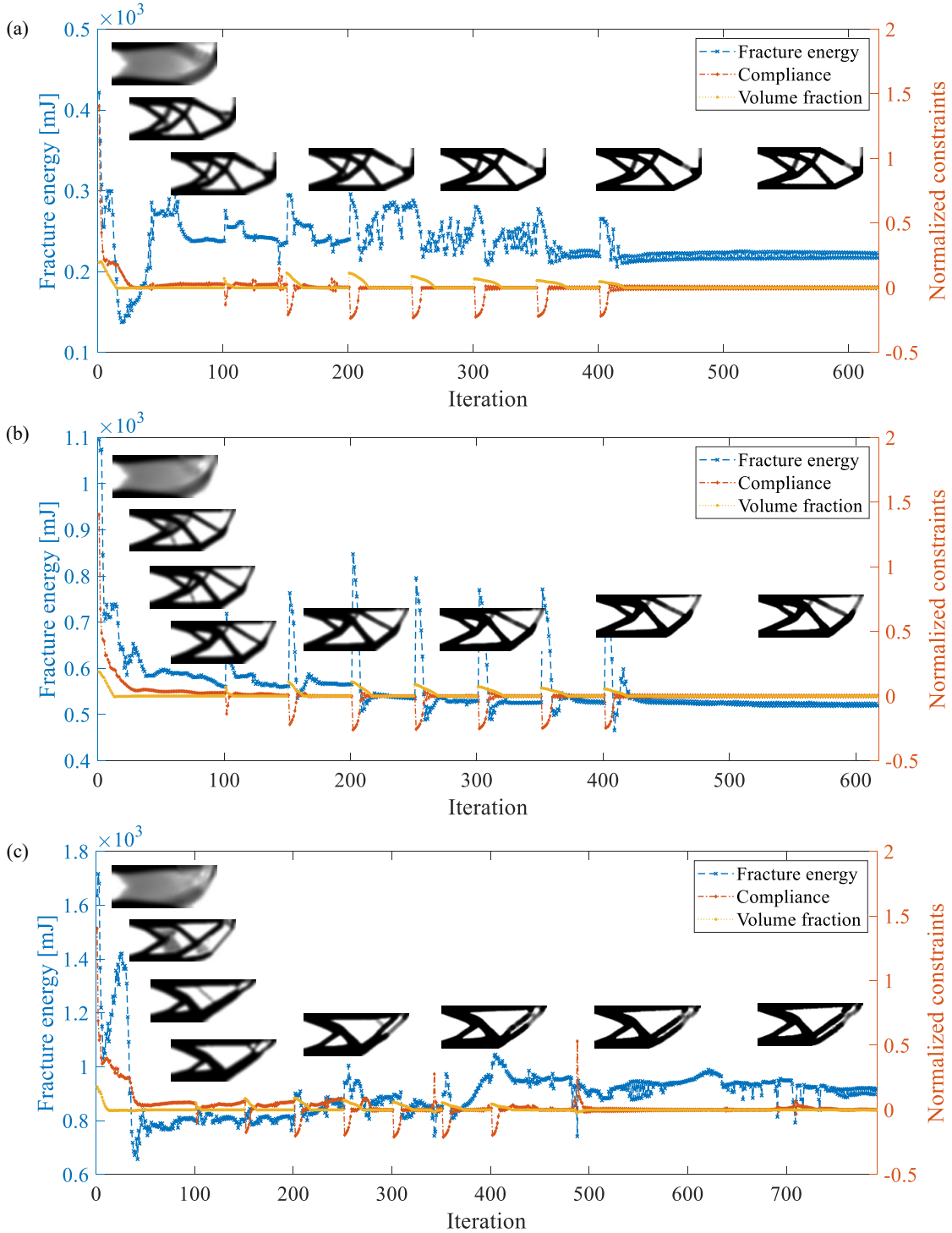

Fig. 5.17 Iteration process of the topology optimization of cantilever beam for different lading rates: (a) $v_0 = 20$ m/s; (b) $v_0 = 40$ m/s; (c) $v_0 = 60$ m/s.

in the dynamic case. Then, finer crack descriptions can be obtained if faster computational ressources are available.

5.6 Conclusion

A SIMP topology optimization framework for maximizing the dynamic fracture resistance has been proposed. Several contributions have been introduced. The dynamic phase field method for fracture has been combined with SIMP topology optimization. Then, a topology optimization minimizing the fracture energy as an objective function under constraints of material volume and verification of local equilibrium equations has been originally proposed. Semi-analytical expressions of sensitivities in this context have been derived, and their accuracy using numerical finite difference approximations has been validated. The algorithm involves solving at each iteration first a static problem to evaluate the compliance and then a full dynamic fracture problem from initiation to crack propagation, during a given period of time, then taking into account the whole loading history. A staggered scheme with convergence iterations has been used to solve the dynamic phase field problem thus authorizing larger time steps. Numerical examples on structural problems subjected to impacts for different loading velocities have been investigated. The examples show that the present dynamic analysis allows reducing the fracture energy as compared to the designs obtained from static classical topology optimization analysis.

Chapter 6

Topology optimization for the impact fracture resistance of quasi-brittle structures

6.1 Introduction

In this Chapter, we investigate an approach that combines the phase field method and TO for the impact fracture resistance of brittle structures. Unlike the previous chapter, the external work with respect to the impact loads is defined as the objective function and maximized for enhancing the structural impact fracture resistance. Using the advantages of the phase field method, the dynamic fracture behavior is considered for the first time in the TO of structures subjected to impact loads. We derive a semi-analytical sensitivity analysis formulation and validate it by comparing with the numerical central difference method. We illustrate the effectiveness and potential of the proposed approach through several numerical examples for impact resistant designs.

6.2 Topology optimization formulations

6.2.1 Material interpolation scheme

We use the SIMP model [30, 26] for TO in this chapter. By assuming a pseudo-density $\varphi \in [0,1]$, the material properties can be interpolated according to:

$$\begin{aligned} E(\varphi) &= [E_{\min} + (1 - E_{\min})\,\varphi^{p_E}]\,E_0, \\ \rho(\varphi) &= [\rho_{\min} + (1 - \rho_{\min})\,\varphi^{p_\rho}]\,\rho_0, \\ \mathscr{G}_c(\varphi) &= \left[G_{c,\min} + \left(1 - \mathscr{G}_{c,\min}\right)\varphi^{p_{\mathscr{G}}}\right]\mathscr{G}_{c,0}, \end{aligned} \tag{6.1}$$

in which E_0, ρ_0 and $\mathscr{G}_{c,0}$ denote three different material properties, the Young's modulus, density and critical energy release rate, respectively; $E_{\min}$, $\rho_{\min}$ and $\mathscr{G}_{c,\min}$ are the artificial lower limits to avoid numerical singularity in zero-pseudo density zone. Above, p denotes the penalty factors, of which the subscript indicates the corresponding material properties. The definition of the SIMP parameters are provided in Table 6.1. Note that the penalty factor of critical energy release rate is gradually increased from 1 to 2 by introducing a threshold ξ. When the iteration number n reaches the threshold value ξ, $p_{\mathscr{G}} = 2$ is employed. In this paper, $\xi = 50$ is adopted.

Table 6.1 Material interpolation parameters.

Interpolated material properties	Penalty factor	Artificial lower limit
Young's modulus, E	3	10^{-6}
Density, ρ	1	10^{-6}
Critical energy release rate, $\mathscr{G}_c$	$1 + \min\left[1, \frac{1}{\xi}(n-1)\right]$	10^{-2}

6.2.2 Optimization problem

Maximize the structural impact resistance where the impact velocity is prescribed is equivalent to maximize the external work required for a load in a limited time or until the failure. The problem is similar to [403, 210] in a quasi-static context. However, here the kinetic energy is considered. By using the trapezoidal rule, we have following discrete approximating of the external work:

$$J = \frac{1}{2}\sum_{n=1}^{N_s}\left(\boldsymbol{F}_u^n + \boldsymbol{F}_u^{n-1}\right)^T \Delta \boldsymbol{u}^n, \tag{6.2}$$

where n indexes the loading step and N_s is the maximal loading step number; $\boldsymbol{F}_u^n$ denotes the equivalent external force, which satisfies Eq. (5.29) at each time step; $\Delta\boldsymbol{u}^n = \boldsymbol{u}^n - \boldsymbol{u}^{n-1}$ denotes the incremental displacement.

Using the advantages of the phase field method, the entire quasi-brittle fracture process of the structure in dynamics can be described without re-meshing and the corresponding internal energy with respect to the external work can be estimated. The TO problem for maximizing the external work is formulated as:

$$\begin{aligned} \max_{\boldsymbol{\varphi}\in[0,1]} &: J(\boldsymbol{\varphi}), \\ \text{s. t.} &: C - C_0 \leq 0, \\ &: V - \chi V_0 \leq 0. \end{aligned} \tag{6.3}$$

In Eq. (6.3), the external work is maximized under the constraints of structural static compliance and total volume fraction. The static compliance can be evaluated by $C = \boldsymbol{F}_s \cdot \boldsymbol{u}_s$, in which $\boldsymbol{F}_s$ and $\boldsymbol{u}_s$ denote a testing static external force and the corresponding displacement response, respectively, before the phase field simulation is performed; C_0 denotes the optimization constraint on the static compliance. The compliance constraint is adopted for avoiding a *weak design* [351, 449]. $V = \sum_{e=1}^{N_e} V_e \varphi_e$ denotes the structural volume (area in 2D), $V_0 = \sum_{e=1}^{N_e} V_e$ represents the total volume of the design domain and χ denotes the target volume constraint fraction.

6.2.3 Sensitivity analysis

In this section, the sensitivity of external work is derived by means of the adjoint method [194, 61]. By introducing two Lagrange multipliers, $\boldsymbol{\alpha}^n$ and $\boldsymbol{\beta}^n$, the external work shown in Eq. (6.2) can be rewritten as the following form without modifying the original value as:

$$J = \frac{1}{2}\sum_{n=1}^{N_\mathrm{s}} \left\{ \left(\boldsymbol{F}_u^n + \boldsymbol{F}_u^{n-1}\right)^T \Delta\boldsymbol{u}^n + \left(\boldsymbol{\alpha}^n\right)^T \boldsymbol{R}_u^n + \left(\boldsymbol{\beta}^n\right)^T \boldsymbol{R}_u^{n-1} \right\}. \tag{6.4}$$

Following [403, 210], all degrees of freedom (DOF) are segmented into essential (index E: associated with Dirichlet boundary conditions) and free (index F: remaining DOF) entries. For a vector $\mathbf{V}$ and a matrix $\mathbf{M}$, we have:

$$\mathbf{V} \sim \begin{bmatrix} \mathbf{V}_\mathrm{E} \\ \mathbf{V}_\mathrm{F} \end{bmatrix} \quad \text{and} \quad \mathbf{M} \sim \begin{bmatrix} \mathbf{M}_\mathrm{EE} & \mathbf{M}_\mathrm{EF} \\ \mathbf{M}_\mathrm{FE} & \mathbf{M}_\mathrm{FF} \end{bmatrix}, \tag{6.5}$$

Then, the residual of the displacement problem at n-th loading step can be expressed by

$$\boldsymbol{R}_u^n = \begin{bmatrix} \boldsymbol{M}_{\mathrm{EE}} & \boldsymbol{M}_{\mathrm{EF}} \\ \boldsymbol{M}_{\mathrm{FE}} & \boldsymbol{M}_{\mathrm{FF}} \end{bmatrix} \begin{bmatrix} \ddot{\boldsymbol{u}}_{\mathrm{E}}^n \\ \ddot{\boldsymbol{u}}_{\mathrm{F}}^n \end{bmatrix} + \begin{bmatrix} \boldsymbol{K}_{u,\mathrm{EE}}^n & \boldsymbol{K}_{u,\mathrm{EF}}^n \\ \boldsymbol{K}_{u,\mathrm{FE}}^n & \boldsymbol{K}_{u,\mathrm{FF}}^n \end{bmatrix} \begin{bmatrix} \boldsymbol{u}_{\mathrm{E}}^n \\ \boldsymbol{u}_{\mathrm{F}}^n \end{bmatrix} - \begin{bmatrix} \boldsymbol{F}_{u,\mathrm{E}}^n \\ \boldsymbol{0} \end{bmatrix}. \tag{6.6}$$

Using the property that the Lagrange multipliers are independent to the design variables, we obtain the expanded form of the partial derivative of J with respect to φ_e, according to:

$$\begin{aligned} \frac{\partial J}{\partial \varphi_e} = \frac{1}{2}\sum_{n=1}^{N_{\mathrm{s}}} \Bigg\{ & (\Delta \boldsymbol{u}^n)^T \left(\frac{\partial \boldsymbol{F}_u^n}{\partial \varphi_e} + \frac{\partial \boldsymbol{F}_u^{n-1}}{\partial \varphi_e} \right) + \left(\boldsymbol{F}_u^n + \boldsymbol{F}_u^{n-1} \right)^T \frac{\partial \Delta \boldsymbol{u}^n}{\partial \varphi_e} \\ & + (\boldsymbol{\alpha}^n)^T \left(\frac{\partial \boldsymbol{K}_u^n}{\partial \varphi_e} \boldsymbol{u}^n + \boldsymbol{K}_u^n \frac{\partial \boldsymbol{u}^n}{\partial \varphi_e} + \frac{\partial \boldsymbol{M}}{\partial \varphi_e} \ddot{\boldsymbol{u}}^n + \boldsymbol{M} \frac{\partial \ddot{\boldsymbol{u}}^n}{\partial \varphi_e} - \frac{\partial \boldsymbol{F}_u^n}{\partial \varphi_e} \right) \\ & + \left(\boldsymbol{\beta}^n \right)^T \left(\frac{\partial \boldsymbol{K}_u^{n-1}}{\partial \varphi_e} \boldsymbol{u}^{n-1} + \boldsymbol{K}_u^{n-1} \frac{\partial \boldsymbol{u}^{n-1}}{\partial \varphi_e} + \frac{\partial \boldsymbol{M}}{\partial \varphi_e} \ddot{\boldsymbol{u}}^{n-1} + \boldsymbol{M} \frac{\partial \ddot{\boldsymbol{u}}^{n-1}}{\partial \varphi_e} - \frac{\partial \boldsymbol{F}_u^{n-1}}{\partial \varphi_e} \right) \Bigg\}, \end{aligned} \tag{6.7}$$

in which both $\frac{\partial \boldsymbol{u}}{\partial \varphi_e}$ and $\frac{\partial \ddot{\boldsymbol{u}}}{\partial \varphi_e}$ are involved. By using the chain rule, these two unknown derivations can be unified, as:

$$\frac{\partial \ddot{\boldsymbol{u}}^n}{\partial \varphi_e} = \frac{\partial \ddot{\boldsymbol{u}}^n}{\partial \boldsymbol{u}^n} \frac{\partial \boldsymbol{u}^n}{\partial \varphi_e}, \tag{6.8}$$

where $\frac{\partial \ddot{\boldsymbol{u}}^n}{\partial \boldsymbol{u}^n}$ can be obtained from the Newmark's scheme as:

$$\frac{\partial \ddot{\boldsymbol{u}}^n}{\partial \boldsymbol{u}^n} = \frac{4}{\Delta t^2}. \tag{6.9}$$

Substituting Eqs. (6.8) and (6.9) into Eq. (6.7) and combining the similar terms, we have:

$$\begin{aligned} \frac{\partial J}{\partial \varphi_e} = \frac{1}{2}\sum_{n=1}^{N_{\mathrm{s}}} \Bigg\{ & (\boldsymbol{\alpha}^n)^T \left(\frac{\partial \boldsymbol{K}_u^n}{\partial \varphi_e} \boldsymbol{u}^n + \frac{\partial \boldsymbol{M}}{\partial \varphi_e} \ddot{\boldsymbol{u}}^n \right) + \left(\boldsymbol{\beta}^n \right)^T \left(\frac{\partial \boldsymbol{K}_u^{n-1}}{\partial \varphi_e} \boldsymbol{u}^{n-1} + \frac{\partial \boldsymbol{M}}{\partial \varphi_e} \ddot{\boldsymbol{u}}^{n-1} \right) \\ & + \left(\boldsymbol{F}_u^n + \boldsymbol{F}_u^{n-1} \right)^T \frac{\partial \Delta \boldsymbol{u}^n}{\partial \varphi_e} + (\Delta \boldsymbol{u}^n - \boldsymbol{\alpha}^n)^T \frac{\partial \boldsymbol{F}_u^n}{\partial \varphi_e} + (\boldsymbol{\alpha}^n)^T \left(\boldsymbol{K}_u^n + \frac{4}{\Delta t^2} \boldsymbol{M} \right) \frac{\partial \boldsymbol{u}^n}{\partial \varphi_e} \\ & + \left(\Delta \boldsymbol{u}^n - \boldsymbol{\beta}^n \right)^T \frac{\partial \boldsymbol{F}_u^{n-1}}{\partial \varphi_e} + \left(\boldsymbol{\beta}^n \right)^T \left(\boldsymbol{K}_u^{n-1} + \frac{4}{\Delta t^2} \boldsymbol{M} \right) \frac{\partial \boldsymbol{u}^{n-1}}{\partial \varphi_e} \Bigg\}. \end{aligned} \tag{6.10}$$

It is noted that we use the Dirichlet boundary condition, which results in:

$$\frac{\partial \Delta \boldsymbol{u}^n}{\partial \varphi_e} = \begin{bmatrix} \boldsymbol{0} \\ \frac{\partial \Delta \boldsymbol{u}_{\mathrm{F}}^n}{\partial \varphi_e} \end{bmatrix}, \quad \frac{\partial \boldsymbol{u}^n}{\partial \varphi_e} = \begin{bmatrix} \boldsymbol{0} \\ \frac{\partial \boldsymbol{u}_{\mathrm{F}}^n}{\partial \varphi_e}, \end{bmatrix}, \tag{6.11}$$

and

$$\boldsymbol{F}_u^n = \begin{bmatrix} \boldsymbol{F}_{u,\mathrm{E}}^n \\ \mathbf{0} \end{bmatrix}, \quad \frac{\partial \boldsymbol{F}_u^n}{\partial \varphi_e} = \begin{bmatrix} \frac{\partial \boldsymbol{F}_{u,\mathrm{E}}^n}{\partial \varphi_e} \\ \mathbf{0}, \end{bmatrix}, \tag{6.12}$$

resulting into:

$$\left(\boldsymbol{F}_u^n + \boldsymbol{F}_u^{n-1}\right)^T \frac{\partial \Delta \boldsymbol{u}^n}{\partial \varphi_e} = \begin{bmatrix} \boldsymbol{F}_{u,\mathrm{E}}^n + \boldsymbol{F}_{u,\mathrm{E}}^{n-1} \\ \mathbf{0} \end{bmatrix}^T \begin{bmatrix} \mathbf{0} \\ \frac{\partial \Delta \boldsymbol{u}_{\mathrm{F}}^n}{\partial \varphi_e} \end{bmatrix} = \mathbf{0}. \tag{6.13}$$

The parts with unknown derivatives $\frac{\partial \boldsymbol{F}_u^n}{\partial \varphi_e}$ and $\frac{\partial \boldsymbol{F}_u^{n-1}}{\partial \varphi_e}$ in Eq. (6.10) can be vanished by defining:

$$\boldsymbol{\alpha}_{\mathrm{E}}^n = \Delta \boldsymbol{u}_{\mathrm{E}}^n \quad \text{and} \quad \boldsymbol{\beta}_{\mathrm{E}}^n = \Delta \boldsymbol{u}_{\mathrm{E}}^n. \tag{6.14}$$

Substituting Eqs. (6.11)-(6.14) into Eq. (6.10), after some calculations, we obtain:

$$\begin{aligned} \frac{\partial J}{\partial \varphi_e} = \frac{1}{2} \sum_{n=1}^{N_\mathrm{s}} \Bigg\{ & \left(\boldsymbol{\alpha}^n\right)^T \left(\frac{\partial \boldsymbol{K}_u^n}{\partial \varphi_e} \boldsymbol{u}^n + \frac{\partial \boldsymbol{M}}{\partial \varphi_e} \ddot{\boldsymbol{u}}^n \right) + \left(\boldsymbol{\beta}^n\right)^T \left(\frac{\partial \boldsymbol{K}_u^{n-1}}{\partial \varphi_e} \boldsymbol{u}^{n-1} + \frac{\partial \boldsymbol{M}}{\partial \varphi_e} \ddot{\boldsymbol{u}}^{n-1} \right) \\ & + \left[\left(\boldsymbol{\alpha}_{\mathrm{E}}^n\right)^T \left(\boldsymbol{K}_{u,\mathrm{EF}}^n + \frac{4}{\Delta t^2} \boldsymbol{M}_{\mathrm{EF}} \right) + \left(\boldsymbol{\alpha}_{\mathrm{F}}^n\right)^T \left(\boldsymbol{K}_{u,\mathrm{FF}}^n + \frac{4}{\Delta t^2} \boldsymbol{M}_{\mathrm{FF}} \right) \right] \frac{\partial \boldsymbol{u}_{\mathrm{F}}^n}{\partial \varphi_e} \\ & + \left[\left(\boldsymbol{\beta}_{\mathrm{E}}^n\right)^T \left(\boldsymbol{K}_{u,\mathrm{EF}}^{n-1} + \frac{4}{\Delta t^2} \boldsymbol{M}_{\mathrm{EF}} \right) + \left(\boldsymbol{\beta}_{\mathrm{F}}^n\right)^T \left(\boldsymbol{K}_{u,\mathrm{FF}}^{n-1} + \frac{4}{\Delta t^2} \boldsymbol{M}_{\mathrm{FF}} \right) \right] \frac{\partial \boldsymbol{u}_{\mathrm{F}}^{n-1}}{\partial \varphi_e} \Bigg\}. \end{aligned} \tag{6.15}$$

To vanish the items with $\frac{\partial \boldsymbol{u}_{\mathrm{F}}^n}{\partial \varphi_e}$ and $\frac{\partial \boldsymbol{u}_{\mathrm{F}}^{n-1}}{\partial \varphi_e}$, the following problems must be solved:

$$\left(\boldsymbol{K}_{u,\mathrm{EF}}^n + \frac{4}{\Delta t^2} \boldsymbol{M}_{\mathrm{EF}} \right) \left(\boldsymbol{\alpha}_{\mathrm{E}}^n\right) + \left(\boldsymbol{K}_{u,\mathrm{FF}}^n + \frac{4}{\Delta t^2} \boldsymbol{M}_{\mathrm{FF}} \right) \left(\boldsymbol{\alpha}_{\mathrm{F}}^n\right) = \mathbf{0}, \tag{6.16}$$

and

$$\left(\boldsymbol{K}_{u,\mathrm{EF}}^{n-1} + \frac{4}{\Delta t^2} \boldsymbol{M}_{\mathrm{EF}} \right) \left(\boldsymbol{\beta}_{\mathrm{E}}^n\right) + \left(\boldsymbol{K}_{u,\mathrm{FF}}^{n-1} + \frac{4}{\Delta t^2} \boldsymbol{M}_{\mathrm{FF}} \right) \left(\boldsymbol{\beta}_{\mathrm{F}}^n\right) = \mathbf{0}, \tag{6.17}$$

from which, the remaining part of Lagrange multipliers can be solved in associated with Eq. (6.14).

The sensitivity of the external work can be finally expressed by:

$$\boxed{\frac{\partial J}{\partial \varphi_e} = \frac{1}{2} \sum_{n=1}^{N_\mathrm{s}} \left\{ \left(\boldsymbol{\alpha}^n\right)^T \left(\frac{\partial \boldsymbol{K}_u^n}{\partial \varphi_e} \boldsymbol{u}^n + \frac{\partial \boldsymbol{M}}{\partial \varphi_e} \ddot{\boldsymbol{u}}^n \right) + \left(\boldsymbol{\beta}^n\right)^T \left(\frac{\partial \boldsymbol{K}_u^{n-1}}{\partial \varphi_e} \boldsymbol{u}^{n-1} + \frac{\partial \boldsymbol{M}}{\partial \varphi_e} \ddot{\boldsymbol{u}}^{n-1} \right) \right\},} \tag{6.18}$$

in which the Lagrange multipliers are already known and only the derivations of stiffness and mass matrices with respect to φ_e remains to be determined, as:

$$\frac{\partial \boldsymbol{K}_u^n}{\partial \varphi_e} = \int_\Omega (\boldsymbol{B}^u)^T \frac{\partial \mathbf{C}_n}{\partial \varphi_e} \boldsymbol{B}^u \, \mathrm{d}\Omega \quad \text{and} \quad \frac{\partial \boldsymbol{M}}{\partial \varphi_e} = \int_\Omega \frac{\partial \rho}{\partial \varphi_e} (\boldsymbol{N}^u)^T \boldsymbol{N}^u \mathrm{d}\Omega, \tag{6.19}$$

where $\frac{\partial \rho}{\partial \varphi_e}$ is time-independent, and can be directly computed from the material interpolation scheme for density; $\frac{\partial \mathbf{C}_n}{\partial \varphi_e}$ can be derived from Chapter 5 in a matrix form as:

$$\frac{\partial \mathbf{C}_n}{\partial \varphi_e} = \left((1-d^n)^2 + k\right) \left(\frac{\partial \lambda}{\partial \varphi_e} \mathscr{R}_n^+ [\mathbf{1}] [\mathbf{1}] + 2 \frac{\partial \mu}{\partial \varphi_e} \boldsymbol{P}_n^+ \right) + \left(\frac{\partial \lambda}{\partial \varphi_e} \mathscr{R}_n^- [\mathbf{1}] [\mathbf{1}] + 2 \frac{\partial \mu}{\partial \varphi_e} \boldsymbol{P}_n^- \right), \tag{6.20}$$

in which $\boldsymbol{P}_n^\pm$ are the matrix form of the fourth-order tensor $\mathbb{P}_n^\pm$; $\frac{\partial \lambda}{\partial \varphi_e}$ and $\frac{\partial \mu}{\partial \varphi_e}$ can be derived from the definition of Lamé coefficients shown in Chapter 5 by using the material interpolation scheme for the Young's modulus.

The optimization techniques described in Chapter 5 are employed. We should note that the maximal value of η is defined as 32 in this Chapter.

6.3 Numerical examples

In this section, the topology of three typical types of structures are designed for enhancing impact resistance. The structural response subjected to impact loading is solved by using the dynamic phase field method, implying that the dynamic fracture process of the structures is taken into account. Fig. 6.1 depicts the imposed velocity on the structures, from which the loading velocity increases sharply from 0 to v_0 in a short time t_0 and then remains constant until the time reaches the maximal value $t_{\max}$. The brittle material property is assumed and taken from the Kalthoff-Winkler experiment [180] as summarized in Table 6.2.

Table 6.2 Material parameters.

Material properties	Symbol	Value	Unit
Young's modulus	E_0	1.9×10^5	MPa
Poisson's ratio	ν	0.3	-
Density	ρ_0	8×10^{-9}	ton/mm^3
Critical energy release rate	$\mathscr{G}_{c,0}$	22.17	N/mm

Before implementing TO, we first validate the accuracy of the derived sensitivity analysis on a simple cantilever beam structure. Fig. 6.2 depicts a short cantilever beam, which is a

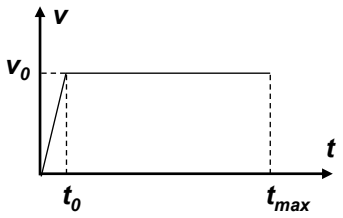

Fig. 6.1 Illustration of the imposed velocity.

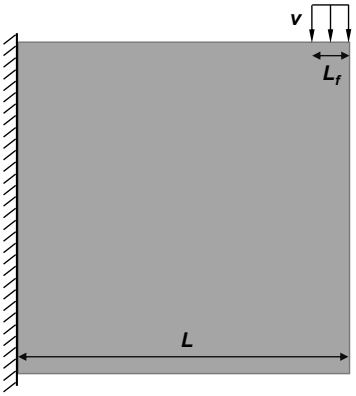

Fig. 6.2 The geometry and boundary condition of the short cantilever for sensitivity validation.

Table 6.3 Numerical parameters for validation of sensitivity analysis.

φ	$\Delta\varphi_e$	ℓ	v_0	τ^n	t_0	$t_{\max}$	tol
0.5	10^{-6}	1 mm	40m/s	1 μs	2 μs	80 μs	10^{-5}

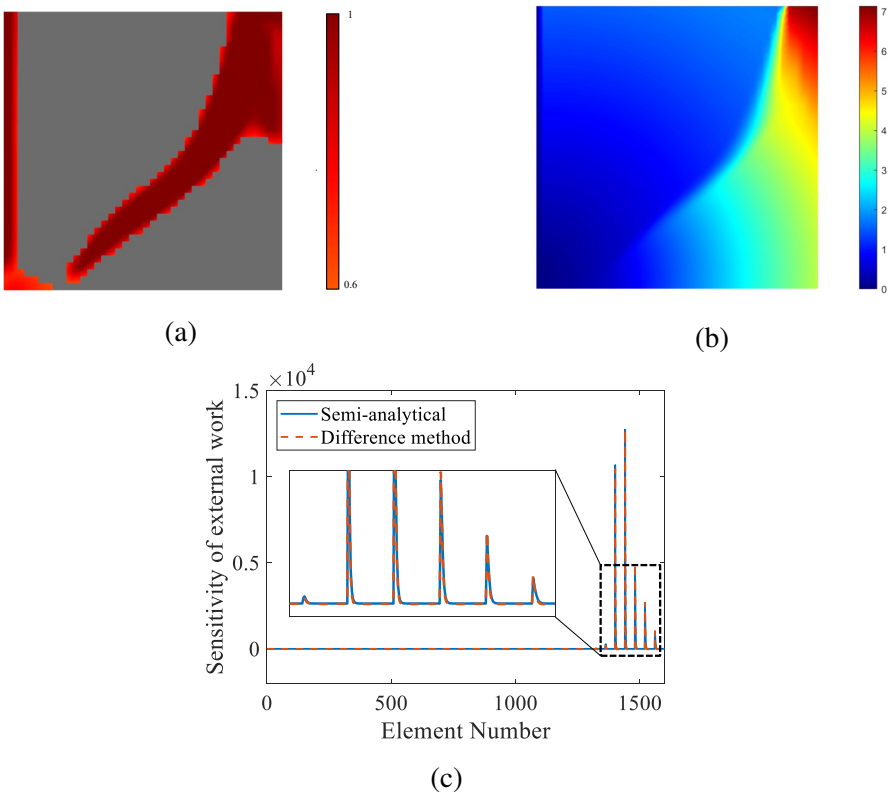

Fig. 6.3 Validation of sensitivity analysis: (a) fracture pattern at $t_{\max} = 80\ \mu$s; (b) magnitude of the displacement at $t_{\max} = 80\ \mu$s; (c) comparison of the sensitivity results.

square structure with a side length of $L = 40$mm. The left end of the structure is clamped. The upper right of the structure is imposed by the prescribed velocity and the length of the loading surface is $L_f = 4$mm. The central difference method is employed for providing a reference solution to our results. The central difference method can be concluded by:

$$\frac{\partial f(\boldsymbol{\varphi})}{\partial \varphi_e} \approx \frac{f(\varphi_1, ..., \varphi_e + \Delta\varphi_e, ..., \varphi_{N_e}) - f(\varphi_1, ..., \varphi_e - \Delta\varphi_e, ..., \varphi_{N_e})}{2\Delta\varphi_e}, \tag{6.21}$$

where $\Delta\varphi_e$ is a pseudo-density perturbation parameter. For the sake of computational cost, the structure is discretized by a 40×40 four-node quadrilateral finite element mesh. The numerical parameters for the sensitivity validation are summarized in Table 6.3.

Fig. 6.3a depicts the fracture pattern of the structure at time $t_{\max} = 80\ \mu$s. For the sake of clarity, only the phase field values with $d > 0.6$ are shown. Fig. 6.3b depicts the magnitude of the corresponding displacement response at the final time. It can be seen that the displacement response is severely affected by the occurrence of brittle dynamic fracture. Under the impact, the deformation and fracture of the structure occur at the same time, so there is almost no displacement response in the area separated by the crack. Fig. 6.3c shows a

comparison of the elemental sensitivities obtained by our semi-analytical sensitivity analysis and the difference method. We can see that both reference and proposed semi-analytical expression agree well.

6.3.1 Carrier plate

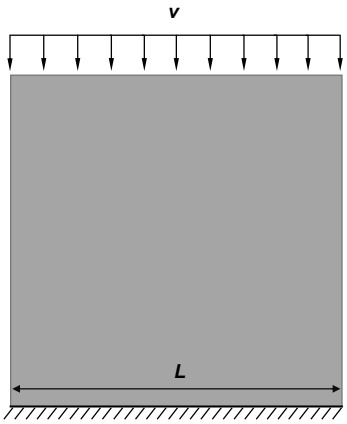

Fig. 6.4 The geometry and boundary condition of the carrier plate

In this example, we optimize a square carrier plate for maximal impact resistance. Fig. 6.4 depicts the geometry and boundary condition of the carrier plate. The square plate has a side length of $L = 100$mm, which is discretized with a 100×100 four-node quadrilateral finite element mesh. The bottom of the structure is fixed and the top of the structure is imposed by a impact load. The impact velocity in this example is $v = 20$m/s, and three different maximal loading time, $t_{\max} = 20\mu$s, 40μs and 60μs, are investigated. The compliance constraint for this example is defined by $C_0 = 40$N·mm with respect to a testing static external force $F_s = -10$N. The volume fraction constraint is $\chi = 0.3$. The filter radius is $r_{\min} = 3$mm. For the dynamic phase field simulation, we define $\ell = 2$mm, $\Delta t = 1\mu$s, $t_0 = 2\mu$s and $tol = 10^{-5}$.

Fig. 6.5(a) depicts the topological designs with respect to different loading time. Depending on the loading time, we get different designs, from which we can see that most of the materials tend to be distributed near loading area for sustaining more external works. Their static load carrying capacity are ensured by bar connections between the loaded and fixed areas. Fig. 6.5(b) shows the final crack patterns of these designs. It is observed that the areas where the designs fractured are also different. Fig. 6.6 shows the corresponding iterative process of the topological designs. It shows good convergence for both objective function and constraints.

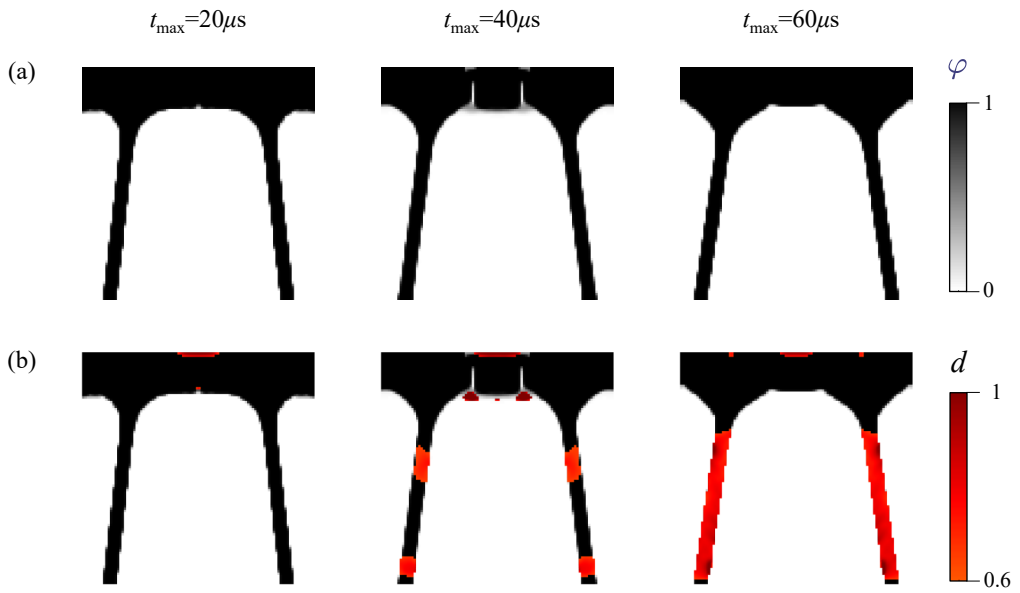

Fig. 6.5 (a) Topological designs with respect to different loading time; (b) Final crack patterns corresponding to the designs.

6.3.2 Half MBB-beam

In this example, we investigate a half-MBB beam for maximal impact resistance via topology optimization. Fig. 6.7 depicts the geometry and boundary condition of the half-MBB beam. The structure is of a length $L = 150$mm and height $H = 60$mm, and it is discretized by a 150 four-node quadrilateral finite element mesh. The left side of the structure is constrained in the x-direction and the right bottom corner is supported in the y-direction. An impact load is applied to the upper left corner of the structure with a width of $l_f = 4$mm. Two different impact velocities, $v_0 = 20$m/s and $v_0 = 60$m/s, are respectively considered. The maximal loading time is $t_{\max} = 50\mu$s. The compliance constraint for this structure is defined by $C_0 = 250$N·mm with respect to a test force $F_s = 100$N. The volume fraction constraint of this example is $\chi = 0.5$. The filter radius is $r_{\min} = 3$mm. The maximal iteration of the TO is limited to 60 steps. For the dynamic phase field simulation, we define $\ell = 2$mm, $\Delta t = 1\mu$s, $t_0 = 2\mu$s and $tol = 10^{-5}$.

Fig. 6.8(a) depicts the topological designs with respect different loading rate. It can be observed that the proposed TO method gives different topological designs corresponding to different loading rates, respectively. For better impact resistance, the materials of both designs tends to be distributed near the loading area. Fig 6.8(b) shows the final crack pattern of the corresponding designs, which exhibits a diversity of the dynamic fracture under different

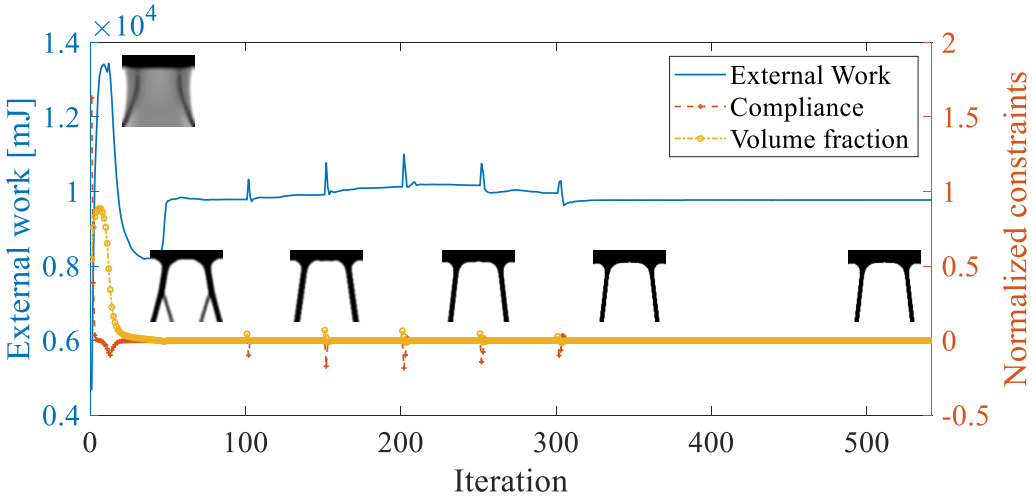

(a) $t_{\max} = 20\mu s$

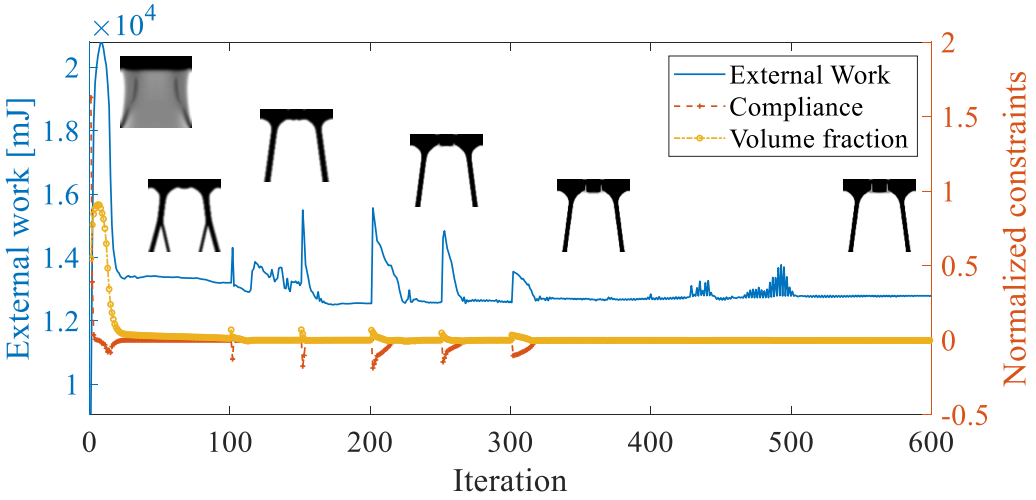

(b) $t_{\max} = 40\mu s$

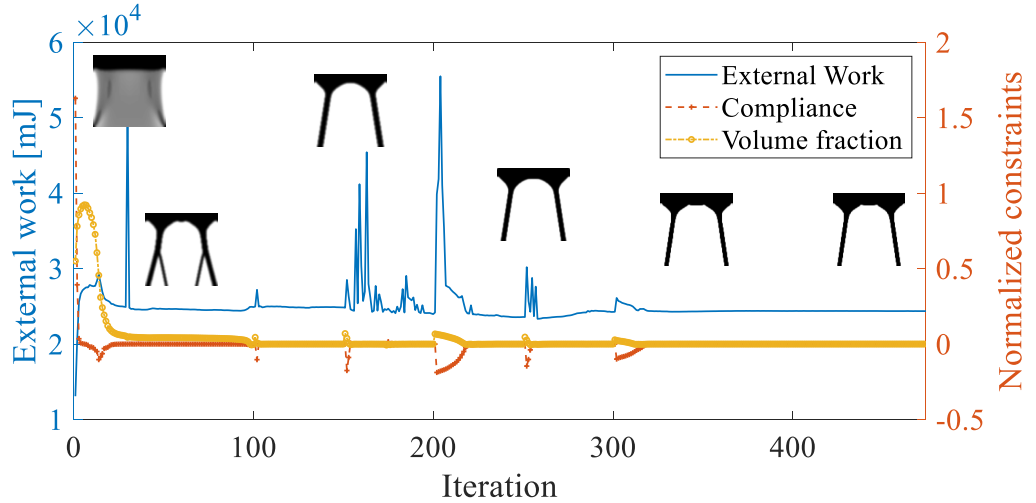

(c) $t_{\max} = 60\mu s$

Fig. 6.6 Iterative process of the topology optimizations.

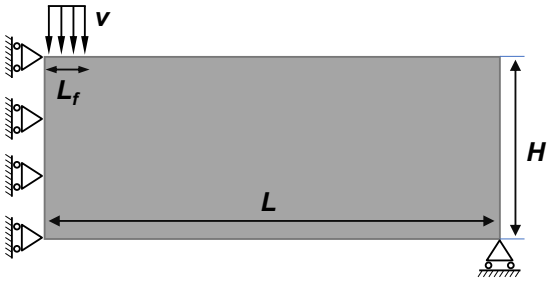

Fig. 6.7 The geometry and boundary condition of the half-MBB beam

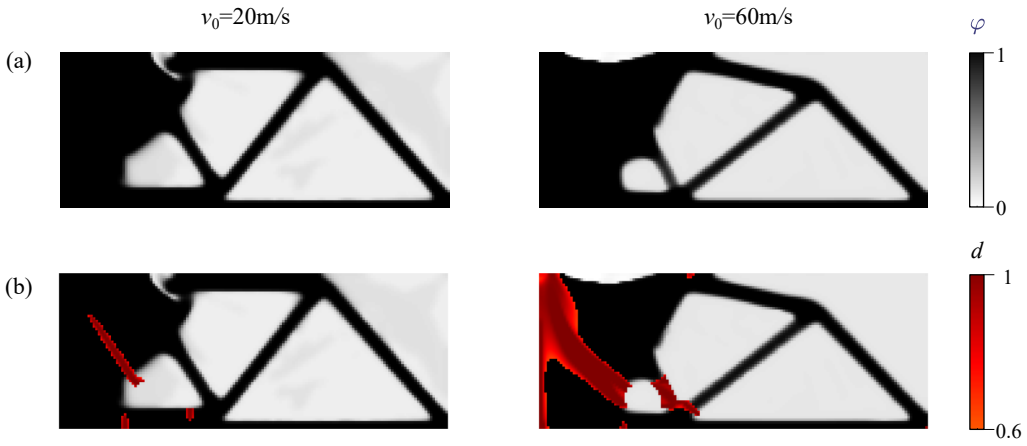

Fig. 6.8 (a) Topological designs with respect to different loading rate; (b) Final crack patterns corresponding to the designs.

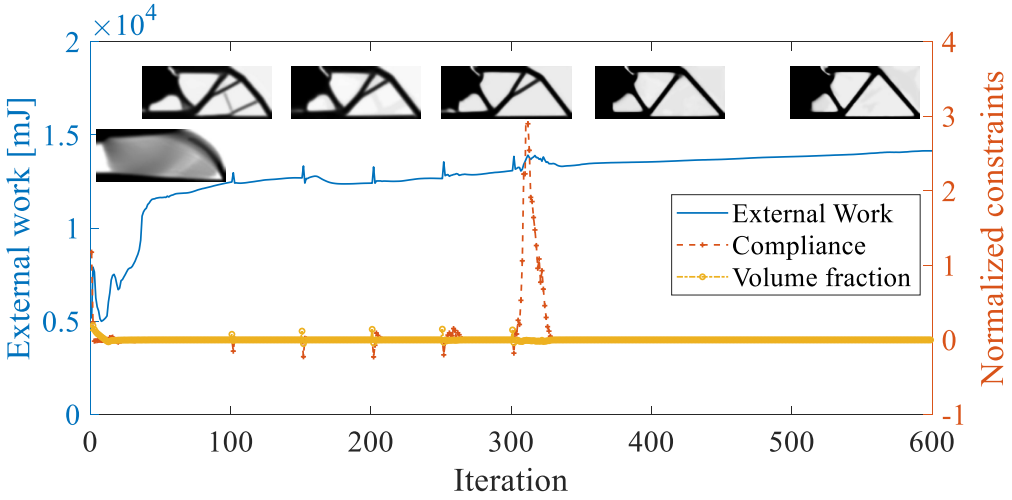

(a) $v_0 = 20$m/s

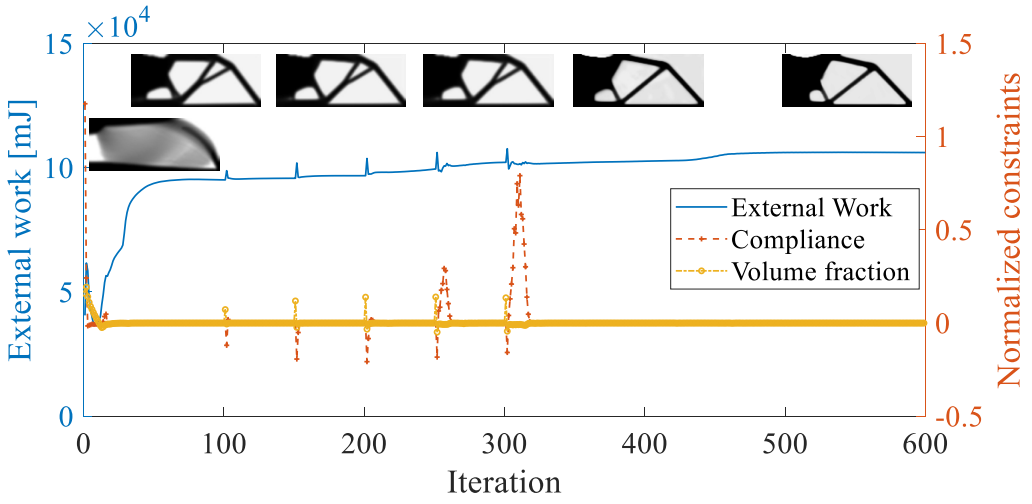

(b) $v_0 = 60$m/s

Fig. 6.9 Iterative process of the topology optimizations

loading rates. Fig. 6.9 shows the iterative process of the topological designs, from which good convergences are observed.

(a) (b) (c)

Fig. 6.10 Reference designs of the half-MBB beam: (a) S-design; (b) D-design for $v_0 = 20$m/s; (b) D-design for $v_0 = 60$m/s.

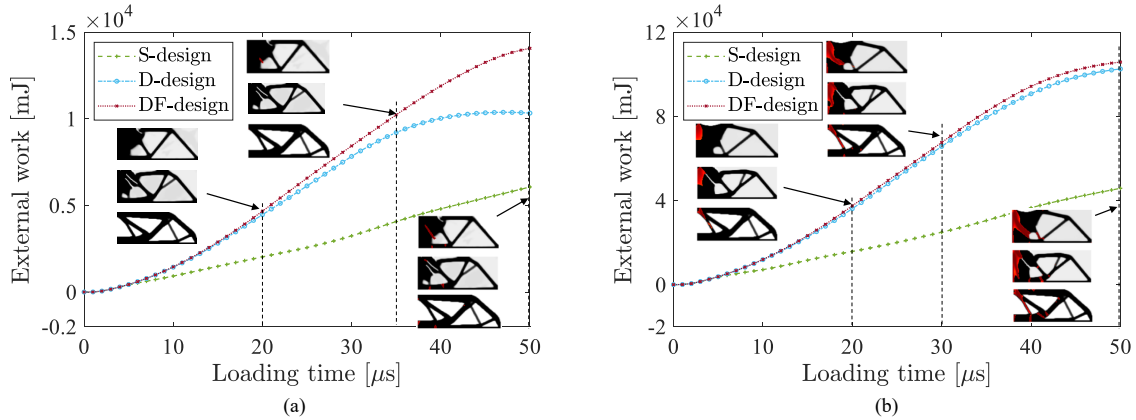

Fig. 6.11 Comparison of the external work.

To further illustrate the advantage the DF-design, three different reference designs of the half-MBB beam, as shown in Fig. 6.10, are compared with our designs. Fig. 6.10(a) shows the S-design for minimal structural compliance, while Fig. 6.10(b) and (c) are the D-designs for maximal external work without dynamic fracture consideration with respect to $v_0 = 20$m/s and $v_0 = 60$m/s, respectively. Fig. 6.11 shows the time-energy curves of these reference design and our DF-designs within prescribed loading time, all results taking into account dynamic fracture effects. From Fig. 6.11(a), in which the loading rate is $v_0 = 20$m/s, the DF-design exhibits a much larger external work required to reach the prescribed boundary displacements than the D- and S- designs. It indicates that DF-design has a better impact resistance. When it comes to a much higher loading rate $v_0 = 60$m/s, as which is shown in Fig. 6.11(b), the DF-design remains a considerable advantage over the S-design, but only a slight advantage over the D-design. We suppose that this is due to dynamic effects at such high loading rates. Tables 6.4 and 6.5 provide the comparison of the external work values at $t = 50\mu$s corresponding to the curves shown in Fig. 6.11(a) and (b), from which the advantage of the DF-design is clearly illustrated.

Table 6.4 Comparison on the required external work for DF-, D- and S- designs at $t = 50\mu$s under the loading rate $v_0 = 20$ m/s

Design method	External work (mJ)	Difference (compared to DF-design)
DF-design	1.42×10^4	-
D-design	1.03×10^4	-27.5%
S-design	0.62×10^4	-56.3%

Table 6.5 Comparison on the required external work for DF-, D- and S- designs at $t = 50\mu$s under the loading rate $v_0 = 60$ m/s

Design method	External work (mJ)	Difference (compared to DF-design)
DF-design	10.61×10^4	-
D-design	10.29×10^4	-3.0%
S-design	4.65×10^4	-56.2%

6.3.3 Cantilever beam

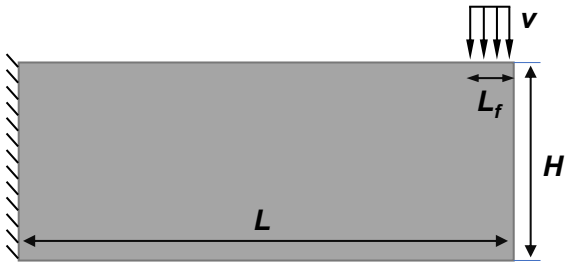

Fig. 6.12 The geometry and boundary condition of the long cantilever beam

In this example, we investigate a cantilever beam for the impact resistance topology optimization. Fig. 6.12 depicts the geometry and boundary condition of the long cantilever beam, of which the length and height are $L = 150$mm and $H = 60$mm, respectively. The left side of the structure is fixed and the right top surface with length $L_f = 4$mm is loaded by a prescribed loading rate. Two different loading rates are respectively considered, which are $v_0 = 40$m/s and $v_0 = 60$m/s. The maximal loading time of this example is $t_{\max} = 40\mu$s. The structure is discretized by a 150×60 four-node quadrilateral finite element mesh. The compliance constraint for this example is $C_0 = 180$N·mm with respect to a test force vector $\boldsymbol{F}_s = -100$N. The volume fraction constraint is $\chi = 0.5$. The filter radius is $r_{\min} = 3$mm. The parameters of the dynamic phase field method are $\ell = 2$mm, $\Delta t = 1\mu$s, $t_0 = 2\mu$s and $tol = 10^{-5}$.

Fig. 6.13(a) depicts the topological designs corresponding to $v_0 = 40$m/s and $v_0 = 60$m/s respectively. We can see that although the designs are somewhat different, the materials

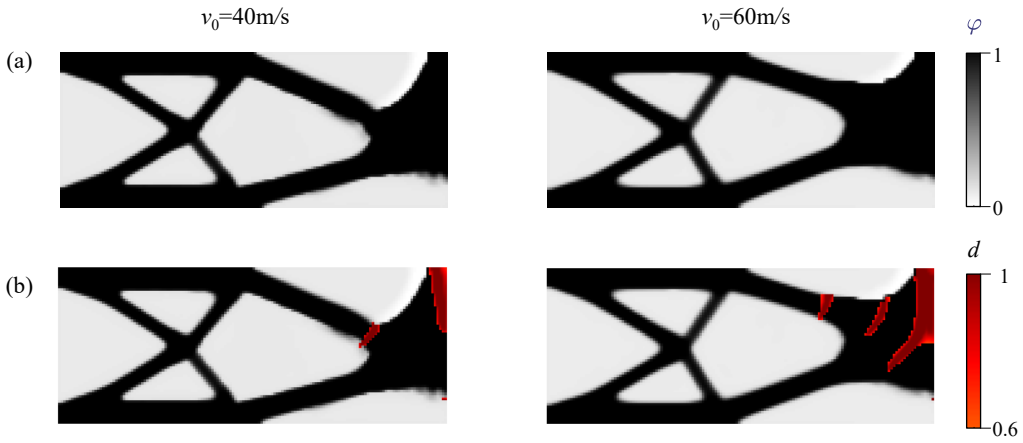

Fig. 6.13 (a) Topological designs with respect to different loading rate; (b) Final crack patterns corresponding to the designs.

are arranged close to the loading area. Fig. 6.13(b) depicts their final crack patterns, from which we can observe the difference and the structure subject to higher loading rate exhibits apparent dynamic cracking behavior. Fig. 6.14 shows the iterative process of these two topological designs, which illustrate the good convergence of the TOs.

Fig. 6.15 gives three reference designs of the long cantilever beam. They are one static compliance minimization design (S-design) and two dynamic external work maximization designs for different loading rates with out fracture consideration (D-design). Similarly, these designs are compared to the DF-designs within the dynamic phase field. Fig. 6.16(a) and (b) show the time-energy curves of these designs corresponding to the two prescribed loading rates $v_0 = 40$m/s and $v_0 = 60$m/s, respectively. We can observe that the DF-designs remain big advantage to the S-designs and have slight superiority to the D-designs. For comparison purpose, Tables 6.6 and 6.7 provide the cumulative required external work at the final time, from which the external work are compared in terms of values. Once again, the DF-designs lead to better impact resistance.

Table 6.6 Comparison on the required external work for DF-, D- and S- designs at $t = 40\mu$s under the loading rate $v_0 = 40$ m/s

Design method	External work (mJ)	Difference (compared to DF-design)
DF-design	1.90×10^4	-
D-design	1.83×10^4	-3.7%
S-design	0.82×10^4	-56.8%

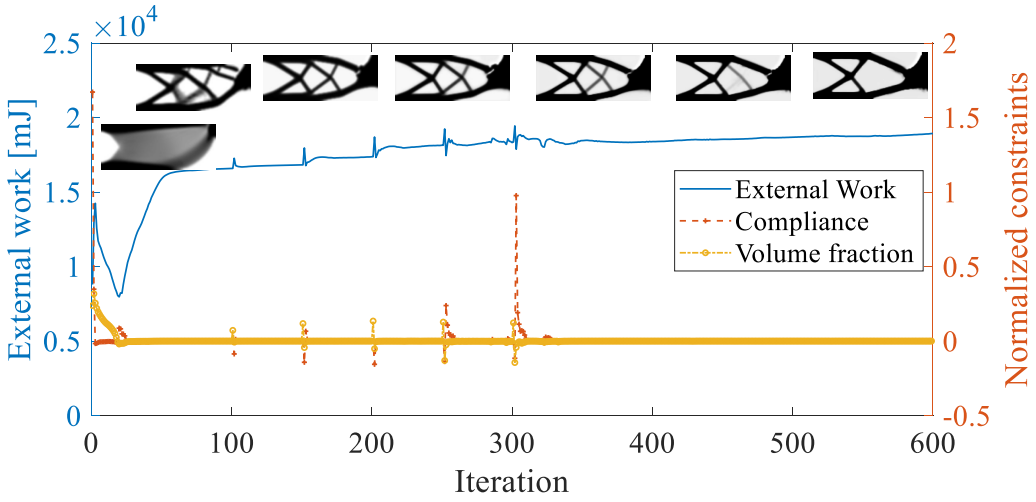

(a) $v_0 = 20$m/s

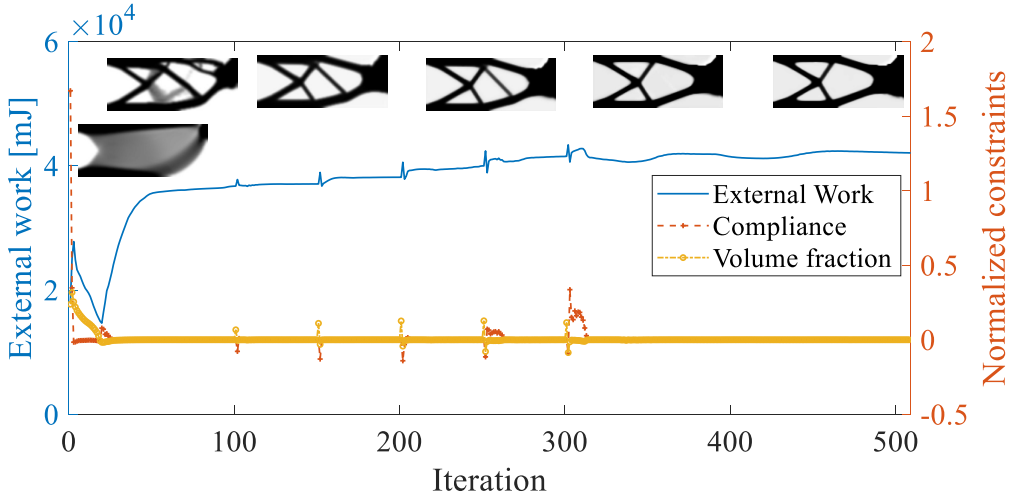

(b) $v_0 = 60$m/s

Fig. 6.14 Iterative process of the topology optimizations

(a) (b) (c)

Fig. 6.15 Reference designs of the long cantilever beam: (a) S-design; (b) D-design for $v_0 = 40$m/s; (b) D-design for $v_0 = 60$m/s.

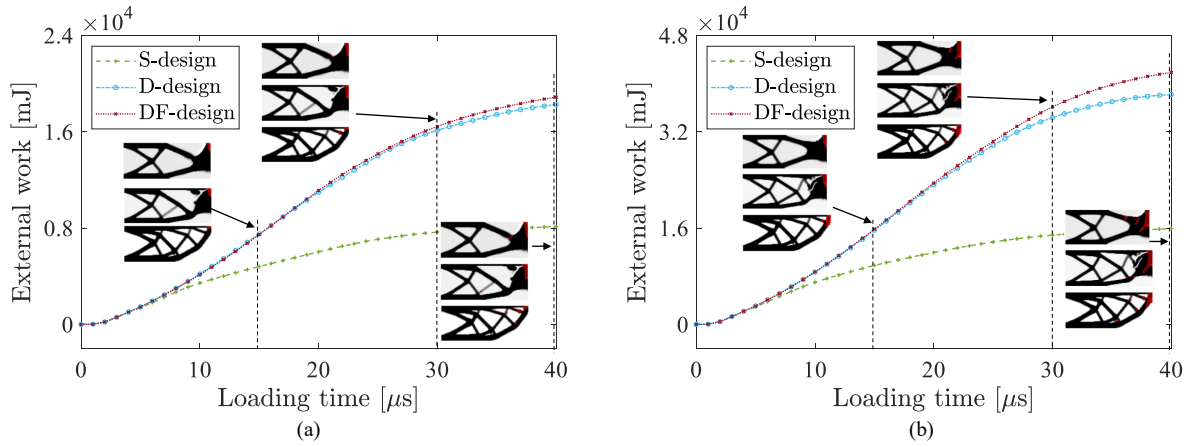

Fig. 6.16 Comparison of the external work.

Table 6.7 Comparison on the required external work for DF-, D- and S- designs at $t = 40\mu$s under the loading rate $v_0 = 60$ m/s

Design method	External work (mJ)	Difference (compared to DF-design)
DF-design	4.21×10^4	-
D-design	3.83×10^4	-9.0%
S-design	1.60×10^4	-62.0%

6.4 Conclusions

In this chapter, we extended the proposed topology optimization framework with considering dynamic fracture to maximize the external work of impact loads. From another perspective, the fracture-resistant structures were designed by topology optimization. Again, semi-analytical sensitivity analysis expressions were formulated for external work in the dynamic context. Then, several numerical examples were presented to illustrate the potential of this method.

The main contributions of this chapter can be summarized as follows:

- Fracture-resistant structures were designed by topology optimization for maximizing the external work of impact loads.
- Efficient semi-analytical sensitivity analysis expressions were provided and validated.
- Structural topological design for impact loading bearing capacity, while considering the fracture of the structure, was studied for the first time.
- It is an extension of our previous work [403, 210], where the quasi-static problem is extended to the dynamic.

Chapter 7

Conclusions and perspectives

7.1 General conclusions

In this thesis, we investigated topology optimization methods in the dynamic contexts with emphasis on: (a) developing a BESO-based topology optimization method for the frequency response problem; (b) developing robust topology optimization methods in the frequency-domain dynamics for both probabilistic and non-probabilistic uncertainties; (c) developing a dynamic fracture involved topology optimization framework for the design of impact loaded structures. The detailed contributions of this thesis are summarized as follows.

In Chapter 2, we proposed a normalization strategy for the BESO-based topology optimization method to improve its stability and convergence. We then firstly applied it to the frequency response problem, which was difficult to the conventional BESO method. We have discussed the reasons why conventional BESO has difficulties to achieve frequency response optimization, and how the proposed normalization strategy-based BESO (NBESO) method can circumvent this problem. More importantly, the NBESO method can be regarded as an extension of the conventional BESO method with better stability and convergence, and can handle problems that are difficult for the conventional BESO method, such as the stress problems [119, 118] and fracture-resistant designs [211].

In Chapter 3, we investigated the robust topology optimization for probabilistic uncertainty. Although there has been a lot of research on this topic in the topology optimization community, especially in the last decade, our contributions to this topic are clear: (a) we were nearly the first to study topology optimization with uncertainty in a dynamic context; (b) we employed a hybrid interval random model to describe the probabilistic uncertainty with imprecise quantities, such as interval model based expectation and standard deviation; (c) an improved hybrid perturbation (IHPA) method was developed for predicting the performance of structures under uncertainty at very low computational costs; (d) we extended the proposed

robust topology optimization method to dynamics for design of various types of structures, including the design of isotropic structures, laminated composite plates and multi-scale composite structures.

In Chapter 4, we introduced a recently emerged interval field model for non-probabilistic uncertainty with spatial dependence into topology optimization in dynamics. We proposed an interval-field based perturbation analysis (IFPA) method for evaluating the *worst case* of the single material structures under uncertainty associated with material properties and loading, and its efficiency and accuracy were validated. Based on the robust topology optimization framework, the sensitivity analysis was derived. Considering that epistemic uncertainty with spatial dependence had been studied recently, this part of the work was one of the first to contribute to topology optimization.

In Chapter 5, we developed a framework to encompass dynamic fractures in topology optimization. We combined the fracture phase field method with topology optimization. A path-independent method was presented, by which the computational costs and complexity of the problem were greatly reduced. We derived a semi-analytical expression of sensitivities in this context, whose accuracy was also validated. We suggested a fracture energy as the objective function for optimization and performed topology optimizations in this framework. We have demonstrated with a few numerical examples that the proposed method allows for reduction of fracture energy.

In Chapter 6, we extended the context of the previous chapter by applying it to the design of structures resistant to impact fracture. We optimized the structure for maximal external work with respect to the impact loads. Similarly, a semi-analytical expression of sensitivity was derived for the external work. The potential of this method was finally illustrated by several numerical examples.

In general, this thesis contributed to topology optimization in structural dynamics, investigated the problems in both frequency-domain and time-domain, and covered vibration and impacting problems. The work was carried out based on both BESO method and SIMP method, and we focused on the improvement of BESO method. Uncertainties in both probabilistic and non-probabilistic forms were considered in this context. Finally, we considered the dynamic fracture problem in topology optimization, which constitutes a breakthrough in this area.

7.2 Perspectives

We believe that this thesis work opens several perspectives, detailed as follows:

From Chapter 2, the proposed NBESO method was implemented for the frequency response problem that is characterized by a strong localization. Further research could be conducted for other typical problems characterized by this feature, for instance, topology optimization for stress-constrained problem in dynamics, which to the best of our knowledge has been rarely studied.

From Chapter 3, we developed an IHPA method, by which the structural performances can be quickly evaluated. However, we should also note that in the IHPA method, the first-order Taylor expansion was twice performed with neglecting the higher-order terms. Such processing is not problematic for dealing with the problems we presented. However, for some problems with large-scale uncertainties, this loss of precision may cause inaccurate predictions. Therefore, in follow-up works, we would suggest developing alternative solutions to refine this method and make it more applicable while balancing accuracy and efficiency.

From Chapter 4, a recently emerged interval field model was introduced for topology optimization. Since the research on interval fields is still in the early stage, the model used has the problem of overfitting. We have found through practice that when the value of the truncation number is too large, the value that should be obtained may not be achieved through the interval field model. To this end, we have developed a novel B-spline based interval field decomposition method in [150] to explicitly construct the interval field, in which the problem of overfitting can be avoided. We should note that the proposed IFPA method is still valid for that case.

From Chapters 5 and 6, we have conducted the proposed method for the topology optimization of classical and challenging complex single material structures. In the later studies, it would be interesting to apply this approach to the design of various types of structures, like the two-phase composite structures, periodic lattice structures and biological shell-infill structures. Besides, we could constrain the maximal value of the phase field, as in the case of the stress-constrained topology optimization problem, and then make a comparative study on these two methods in enhancing the structural strength. As a final remark, we could extend phase field method to dynamics in a context of various behaviors (e.g. quasi-brittle, elastoplastic) and include them in our topology optimization research.

References

[1] Aage, N., Poulsen, T. H., Gersborg-Hansen, A., and Sigmund, O. (2008). Topology optimization of large scale stokes flow problems. *Structural and Multidisciplinary Optimization*, 35(2):175–180.

[2] Akl, W., El-Sabbagh, A., Al-Mitani, K., and Baz, A. (2009). Topology optimization of a plate coupled with acoustic cavity. *International Journal of Solids and Structures*, 46(10):2060–2074.

[3] Allaire, G., Jouve, F., and Toader, A.-M. (2002). A level-set method for shape optimization. *Comptes Rendus Mathematique*, 334(12):1125–1130.

[4] Allaire, G., Jouve, F., and Toader, A.-M. (2004). Structural optimization using sensitivity analysis and a level-set method. *Journal of computational physics*, 194(1):363–393.

[5] Ambati, M., Gerasimov, T., and De Lorenzis, L. (2015). A review on phase-field models of brittle fracture and a new fast hybrid formulation. *Computational Mechanics*, 55(2):383–405.

[6] Amir, O. (2013). A topology optimization procedure for reinforced concrete structures. *Computers and Structures*, 114-115:46–58.

[7] Amir, O. and Sigmund, O. (2013). Reinforcement layout design for concrete structures based on continuum damage and truss topology optimization. *Structural and Multidisciplinary Optimization*, 47(2):157–174.

[8] Amir, O., Sigmund, O., Lazarov, B. S., and Schevenels, M. (2012). Efficient reanalysis techniques for robust topology optimization. *Computer Methods in Applied Mechanics and Engineering*, 245:217–231.

[9] Andkjær, J. and Sigmund, O. (2011). Topology optimized low-contrast all-dielectric optical cloak. *Applied Physics Letters*, 98(2):021112.

[10] Andreassen, E., Clausen, A., Schevenels, M., Lazarov, B. S., and Sigmund, O. (2011). Efficient topology optimization in MATLAB using 88 lines of code. *Structural and Multidisciplinary Optimization*, 43(1):1–16.

[11] Andreassen, E., Ferrari, F., Sigmund, O., and Diaz, A. R. (2018). Frequency response as a surrogate eigenvalue problem in topology optimization. *International Journal for Numerical Methods in Engineering*, 113(8):1214–1229.

[12] Ang, A. H.-S. and Tang, W. H. (1984). *Probability concepts in engineering planning and design, vol. 2: Decision, risk, and reliability.* John Wiley & Sons, Inc., New York, NY.

[13] Aoues, Y. and Chateauneuf, A. (2010). Benchmark study of numerical methods for reliability-based design optimization. *Structural and multidisciplinary optimization*, 41(2):277–294.

[14] Atkinson, K. and Han, W. (2009). *Numerical Solution of Fredholm Integral Equations of the Second Kind*, pages 473–549. Springer New York, New York, NY.

[15] Aulig, N., Nutwell, E., Menzel, S., and Detwiler, D. (2018). Preference-based topology optimization for vehicle concept design with concurrent static and crash load cases. *Structural and Multidisciplinary Optimization*, 57(1):251–266.

[16] Bai, S. and Kang, Z. (2021). Robust topology optimization for structures under bounded random loads and material uncertainties. *Computers & Structures*, 252:106569.

[17] Bai, Y., Zhou, H., Lei, F., and Lei, H. (2019). An improved numerically-stable equivalent static loads (esls) algorithm based on energy-scaling ratio for stiffness topology optimization under crash loads. *Structural and Multidisciplinary Optimization*, 59(1):117–130.

[18] Balamurugan, R., Ramakrishnan, C., and Singh, N. (2008). Performance evaluation of a two stage adaptive genetic algorithm (tsaga) in structural topology optimization. *Applied Soft Computing*, 8(4):1607–1624.

[19] Beer, M., Ferson, S., and Kreinovich, V. (2013). Imprecise probabilities in engineering analyses. *Mechanical systems and signal processing*, 37(1-2):4–29.

[20] Behrou, R. and Guest, J. K. (2017). Topology optimization for transient response of structures subjected to dynamic loads. In *18th AIAA/ISSMO multidisciplinary analysis and optimization conference*, page 3657.

[21] Belytschko, T. and Black, T. (1999a). Elastic crack growth in finite elements with minimal remeshing. *International journal for numerical methods in engineering*, 45(5):601–620.

[22] Belytschko, T. and Black, T. (1999b). Elastic crack growth in finite elements with minimal remeshing. *International Journal for Numerical Methods in Engineering*, 45:601–620.

[23] Ben-Haim, Y. (1994). A non-probabilistic concept of reliability. *Structural safety*, 14(4):227–245.

[24] Ben-Haim, Y. and Elishakoff, I. (1995). Discussion on: a non-probabilistic concept of reliability. *Structural Safety*, 17(3):195–199.

[25] Ben-Haim, Y. and Elishakoff, I. (2013). *Convex models of uncertainty in applied mechanics*. Elsevier.

[26] Bendsøe, M. P. (1989). Optimal shape design as a material distribution problem. *Structural optimization*, 1(4):193–202.

[27] Bendsøe, M. P. (1995). *Optimization of structural topology, shape, and material*. Springer Berlin Heidelberg, Berlin, Heidelberg.

[28] Bendsøe, M. P., Díaz, A., and Kikuchi, N. (1993). Topology and generalized layout optimization of elastic structures. In *Topology design of structures*, pages 159–205. Springer.

[29] Bendsøe, M. P. and Díaz, A. R. (1994). Optimization of material properties for improved frequency response. *Structural optimization*, 7(1):138–140.

[30] Bendsøe, M. P. and Sigmund, O. (1999). Material interpolation schemes in topology optimization. *Archive of applied mechanics*, 69(9):635–654.

[31] Bendsøe, M. P. and Sigmund, O. (2004). *Topology Optimization: Theory, Methods, and Applications*. Springer Berlin Heidelberg, Berlin, Heidelberg.

[32] Bendsoe, M. P. and Sigmund, O. (2013). *Topology optimization: theory, methods, and applications*. Springer Science & Business Media.

[33] Bendsøe, M. P. and Kikuchi, N. (1988). Generating optimal topologies in structural design using a homogenization method. *Computer Methods in Applied Mechanics and Engineering*, 71(2):197 – 224.

[34] Beyer, H.-G. and Sendhoff, B. (2007). Robust optimization–a comprehensive survey. *Computer methods in applied mechanics and engineering*, 196(33-34):3190–3218.

[35] Bird, G. (1981). Monte-carlo simulation in an engineering context. *Progress in Astronautics and Aeronautics*, 74:239–255.

[36] Birker, T. (1995). Generalized michell structures—exact least-weight truss layouts for combined stress and displacement constraints: Part ii—analytical solutions within a two-bar topology. *Structural optimization*, 9(3):214–219.

[37] Bleyer, J., Roux-Langlois, C., and Molinari, J.-F. (2017). Dynamic crack propagation with a variational phase-field model: limiting speed, crack branching and velocity-toughening mechanisms. *International Journal of Fracture*, 204(1):79–100.

[38] Bobby, S., Suksuwan, A., Spence, S. M., and Kareem, A. (2017). Reliability-based topology optimization of uncertain building systems subject to stochastic excitation. *Structural Safety*, 66:1–16.

[39] Borden, M. J., Verhoosel, C. V., Scott, M. A., Hughes, T. J., and Landis, C. M. (2012). A phase-field description of dynamic brittle fracture. *Computer Methods in Applied Mechanics and Engineering*, 217:77–95.

[40] Borel, P. I., Harpøth, A., Frandsen, L. H., Kristensen, M., Shi, P., Jensen, J. S., and Sigmund, O. (2004). Topology optimization and fabrication of photonic crystal structures. *Optics express*, 12(9):1996–2001.

[41] Borrvall, T. and Petersson, J. (2001). Topology optimization using regularized intermediate density control. *Computer Methods in Applied Mechanics and Engineering*, 190(37-38):4911–4928.

[42] Borrvall, T. and Petersson, J. (2003). Topology optimization of fluids in stokes flow. *International journal for numerical methods in fluids*, 41(1):77–107.

[43] Bourdin, B. (2001). Filters in topology optimization. *International journal for numerical methods in engineering*, 50(9):2143–2158.

[44] Bourdin, B., Francfort, G. A., and Marigo, J.-J. (2008). The variational approach to fracture. *Journal of elasticity*, 91(1-3):5–148.

[45] Brevault, L., Lacaze, S., Balesdent, M., and Missoum, S. (2016). Reliability Analysis in the Presence of Aleatory and Epistemic Uncertainties, Application to the Prediction of a Launch Vehicle Fallout Zone. *Journal of Mechanical Design*, 138(11). 111401.

[46] Bruggi, M. (2008). On an alternative approach to stress constraints relaxation in topology optimization. *Structural and multidisciplinary optimization*, 36(2):125–141.

[47] Bruggi, M. and Duysinx, P. (2012). Topology optimization for minimum weight with compliance and stress constraints. *Structural and Multidisciplinary Optimization*, 46(3):369–384.

[48] Bruns, T. (2005). A reevaluation of the simp method with filtering and an alternative formulation for solid–void topology optimization. *Structural and Multidisciplinary Optimization*, 30(6):428–436.

[49] Bruns, T. E. and Tortorelli, D. A. (2001). Topology optimization of non-linear elastic structures and compliant mechanisms. *Computer methods in applied mechanics and engineering*, 190(26-27):3443–3459.

[50] Bruns, T. E. and Tortorelli, D. A. (2003). An element removal and reintroduction strategy for the topology optimization of structures and compliant mechanisms. *International journal for numerical methods in engineering*, 57(10):1413–1430.

[51] Buhl, T., Pedersen, C. B., and Sigmund, O. (2000). Stiffness design of geometrically nonlinear structures using topology optimization. *Structural and Multidisciplinary Optimization*, 19(2):93–104.

[52] Burger, M., Hackl, B., and Ring, W. (2004). Incorporating topological derivatives into level set methods. *Journal of computational physics*, 194(1):344–362.

[53] Callens, R. R., Faes, M. G., and Moens, D. (2021). Local explicit interval fields for non-stationary uncertainty modelling in finite element models. *Computer Methods in Applied Mechanics and Engineering*, 379:113735.

[54] Challis, V. J., Roberts, A. P., and Wilkins, A. H. (2008). Fracture resistance via topology optimization. *Structural and Multidisciplinary Optimization*, 36(3):263–271.

[55] Chan, Y.-C., Shintani, K., and Chen, W. (2019). Robust topology optimization of multi-material lattice structures under material and load uncertainties. *Frontiers of Mechanical Engineering*, 14:141–152.

[56] Chandrasekhar, A. and Suresh, K. (2021). Tounn: topology optimization using neural networks. *Structural and Multidisciplinary Optimization*, 63(3):1135–1149.

[57] Chen, N., Yu, D., Xia, B., and Ma, Z. (2016). Topology optimization of structures with interval random parameters. *Computer Methods in Applied Mechanics and Engineering*, 307:300–315.

[58] Chen, S., Chen, W., and Lee, S. (2010a). Level set based robust shape and topology optimization under random field uncertainties. *Structural and Multidisciplinary Optimization*, 41(4):507–524.

[59] Chen, S., Gonella, S., Chen, W., and Liu, W. K. (2010b). A level set approach for optimal design of smart energy harvesters. *Computer Methods in Applied Mechanics and Engineering*, 199(37-40):2532–2543.

[60] Chi, H., Zhang, Y., Tang, T. L. E., Mirabella, L., Dalloro, L., Song, L., and Paulino, G. H. (2021). Universal machine learning for topology optimization. *Computer Methods in Applied Mechanics and Engineering*, 375:112739.

[61] Cho, S. and Jung, H.-S. (2003). Design sensitivity analysis and topology optimization of displacement–loaded non-linear structures. *Computer Methods in Applied Mechanics and Engineering*, 192(22):2539–2553.

[62] Choi, W. and Park, G. (2002). Structural optimization using equivalent static loads at all time intervals. *Computer Methods in Applied Mechanics and Engineering*, 191(19):2105–2122.

[63] Choi, W.-S. and Park, G. (1999). Transformation of dynamic loads into equivalent static loads based on modal analysis. *International Journal for Numerical Methods in Engineering*, 46(1):29–43.

[64] Chu, D. N., Xie, Y., Hira, A., and Steven, G. (1996). Evolutionary structural optimization for problems with stiffness constraints. *Finite elements in analysis and design*, 21(4):239–251.

[65] Csébfalvi, A. and Lógó, J. (2018). A critical analysis of expected-compliance model in volume-constrained robust topology optimization with normally distributed loading directions, using a minimax-compliance approach alternatively. *Advances in Engineering Software*, 120:107–115.

[66] Da, D. and Qian, X. (2020). Fracture resistance design through biomimicry and topology optimization. *Extreme Mechanics Letters*, 40:100890.

[67] Da, D. and Yvonnet, J. (2020). Topology optimization for maximizing the fracture resistance of periodic quasi-brittle composites structures. *Materials*, 13(15).

[68] Da, D., Yvonnet, J., Xia, L., and Li, G. (2018). Topology optimization of particle-matrix composites for optimal fracture resistance taking into account interfacial damage. *International Journal for Numerical Methods in Engineering*, 115(5):604–626.

[69] da Silva, G. A. and Beck, A. T. (2018). Reliability-based topology optimization of continuum structures subject to local stress constraints. *Structural and Multidisciplinary Optimization*, 57(6):2339–2355.

[70] da Silva, G. A., Cardoso, E. L., and Beck, A. T. (2020). Comparison of robust, reliability-based and non-probabilistic topology optimization under uncertain loads and stress constraints. *Probabilistic Engineering Mechanics*, 59:103039.

[71] Dahl, J., Jensen, J. S., and Sigmund, O. (2008). Topology optimization for transient wave propagation problems in one dimension. *Structural and Multidisciplinary Optimization*, 36(6):585–595.

[72] Dantan, J.-Y., Gayton, N., Qureshi, A. J., Lemaire, M., and Etienne, A. (2013). Tolerance analysis approach based on the classification of uncertainty (aleatory/epistemic). *Procedia CIRP*, 10:287–293.

[73] Davoudi, M. and Kim, C. (2019). Topology optimization for crashworthiness of thin-walled structures under axial crash considering nonlinear plastic buckling and locations of plastic hinges. *Engineering Optimization*, 51(5):775–795.

[74] De Gournay, F., Allaire, G., and Jouve, F. (2008). Shape and topology optimization of the robust compliance via the level set method. *ESAIM: Control, Optimisation and Calculus of Variations*, 14(1):43–70.

[75] Deaton, J. D. and Grandhi, R. V. (2014). A survey of structural and multidisciplinary continuum topology optimization: post 2000. *Structural and Multidisciplinary Optimization*, 49(1):1–38.

[76] Deaton, J. D. and Grandhi, R. V. (2016). Stress-based design of thermal structures via topology optimization. *Structural and Multidisciplinary Optimization*, 53(2):253–270.

[77] Delissen, A., van Keulen, F., and Langelaar, M. (2020). Efficient limitation of resonant peaks by topology optimization including modal truncation augmentation. *Structural and Multidisciplinary Optimization*, 61(6):2557–2575.

[78] Dempster, A. P. (2008). Upper and lower probabilities induced by a multivalued mapping. In *Classic works of the Dempster-Shafer theory of belief functions*, pages 57–72. Springer.

[79] Deng, C., Wang, Y., Qin, C., Fu, Y., and Lu, W. (2022). Self-directed online machine learning for topology optimization. *Nature Communications*, 13(1):1–14.

[80] Deng, J. and Chen, W. (2017). Concurrent topology optimization of multiscale structures with multiple porous materials under random field loading uncertainty. *Structural and Multidisciplinary Optimization*, 56:1–19.

[81] Deng, Y., Liu, Z., Zhang, P., Liu, Y., and Wu, Y. (2011). Topology optimization of unsteady incompressible navier–stokes flows. *Journal of Computational Physics*, 230(17):6688–6708.

[82] Díaaz, A. R. and Kikuchi, N. (1992). Solutions to shape and topology eigenvalue optimization problems using a homogenization method. *International Journal for Numerical Methods in Engineering*, 35(7):1487–1502.

[83] Dilgen, C. B., Dilgen, S. B., Fuhrman, D. R., Sigmund, O., and Lazarov, B. S. (2018a). Topology optimization of turbulent flows. *Computer Methods in Applied Mechanics and Engineering*, 331:363–393.

[84] Dilgen, S. B., Dilgen, C. B., Fuhrman, D. R., Sigmund, O., and Lazarov, B. S. (2018b). Density based topology optimization of turbulent flow heat transfer systems. *Structural and Multidisciplinary Optimization*, 57(5):1905–1918.

[85] Do, D. M., Gao, W., and Song, C. (2016). Stochastic finite element analysis of structures in the presence of multiple imprecise random field parameters. *Computer Methods in Applied Mechanics and Engineering*, 300:657–688.

[86] Doltsinis, I. and Kang, Z. (2004). Robust design of structures using optimization methods. *Computer methods in applied mechanics and engineering*, 193(23-26):2221–2237.

[87] Dong, H.-W., Su, X.-X., Wang, Y.-S., and Zhang, C. (2014). Topological optimization of two-dimensional phononic crystals based on the finite element method and genetic algorithm. *Structural and Multidisciplinary Optimization*, 50(4):593–604.

[88] Dong, H.-W., Zhao, S.-D., Wang, Y.-S., and Zhang, C. (2017). Topology optimization of anisotropic broadband double-negative elastic metamaterials. *Journal of the Mechanics and Physics of Solids*, 105:54–80.

[89] Du, J. and Olhoff, N. (2007a). Minimization of sound radiation from vibrating bimaterial structures using topology optimization. *Structural and Multidisciplinary Optimization*, 33(4):305–321.

[90] Du, J. and Olhoff, N. (2007b). Topological design of freely vibrating continuum structures for maximum values of simple and multiple eigenfrequencies and frequency gaps. *Structural and Multidisciplinary Optimization*, 34(2):91–110.

[91] Du, J. and Olhoff, N. (2010). Topological design of vibrating structures with respect to optimum sound pressure characteristics in a surrounding acoustic medium. *Structural and Multidisciplinary Optimization*, 42(1):43–54.

[92] Dubois, D. (2010). Representation, propagation, and decision issues in risk analysis under incomplete probabilistic information. *Risk Analysis: An International Journal*, 30(3):361–368.

[93] Duddeck, F., Hunkeler, S., Lozano, P., Wehrle, E., and Zeng, D. (2016). Topology optimization for crashworthiness of thin-walled structures under axial impact using hybrid cellular automata. *Structural and Multidisciplinary Optimization*, 54(3):415–428.

[94] Duddeck, F. and Volz, K. (2012). A new topology optimization approach for crashworthiness of passenger vehicles based on physically defined equivalent static loads. In *ICrash International Crashworthiness Conference, Milano, Italy*.

[95] Dühring, M. B., Jensen, J. S., and Sigmund, O. (2008). Acoustic design by topology optimization. *Journal of sound and vibration*, 317(3-5):557–575.

[96] Dunning, P. D. and Kim, H. A. (2013). Robust topology optimization: Minimization of expected and variance of compliance. *AIAA Journal*, 51(11):2656–2664.

[97] Dunning, P. D., Kim, H. A., and Mullineux, G. (2011). Introducing loading uncertainty in topology optimization. *AIAA journal*, 49(4):760–768.

[98] Duysinx, P. and Bendsøe, M. P. (1998). Topology optimization of continuum structures with local stress constraints. *International Journal for Numerical Methods in Engineering*, 43(8):1453–1478.

[99] Elesin, Y., Lazarov, B. S., Jensen, J. S., and Sigmund, O. (2014). Time domain topology optimization of 3d nanophotonic devices. *Photonics and Nanostructures-Fundamentals and Applications*, 12(1):23–33.

[100] Elishakoff, I. and Colombi, P. (1993). Combination of probabilistic and convex models of uncertainty when scarce knowledge is present on acoustic excitation parameters. *Computer methods in applied mechanics and engineering*, 104(2):187–209.

[101] Elishakoff, I. and Ohsaki, M. (2010). *Optimization and anti-optimization of structures under uncertainty*. World Scientific.

[102] Enevoldsen, I. and Sørensen, J. D. (1994). Reliability-based optimization in structural engineering. *Structural safety*, 15(3):169–196.

[103] Eschenauer, H. A. (1992). Multidisciplinary modeling and optimization in design processes. *Gesellschaft angewandte Mathematik und Mechanik Jahrestagung Goettingen West Germany Zeitschrift Flugwissenschaften*, 72(6):438.

[104] Eschenauer, H. A. and Olhoff, N. (2001). Topology optimization of continuum structures: a review. *Appl. Mech. Rev.*, 54(4):331–390.

[105] Faes, M. and Moens, D. (2017). Identification and quantification of spatial interval uncertainty in numerical models. *Computers & Structures*, 192:16–33.

[106] Fan, Z., Xia, L., Lai, W., Xia, Q., and Shi, T. (2019). Evolutionary topology optimization of continuum structures with stress constraints. *Structural and Multidisciplinary Optimization*, 59(2):647–658.

[107] Fang, J., Sun, G., Qiu, N., Kim, N. H., and Li, Q. (2017). On design optimization for structural crashworthiness and its state of the art. *Structural and Multidisciplinary Optimization*, 55(3):1091–1119.

[108] Ferrari, F., Lazarov, B. S., and Sigmund, O. (2018). Eigenvalue topology optimization via efficient multilevel solution of the frequency response. *International Journal for Numerical Methods in Engineering*, 115(7):872–892.

[109] Ferson, S., Kreinovich, V., Hajagos, J., Oberkampf, W., and Ginzburg, L. (2007). Experimental uncertainty estimation and statistics for data having interval uncertainty. *Sandia National Laboratories, Report SAND2007-0939*, 162.

[110] Forsberg, J. and Nilsson, L. (2007). Topology optimization in crashworthiness design. *Structural and Multidisciplinary Optimization*, 33(1):1–12.

[111] Fragiadakis, M. and Papadrakakis, M. (2008). Modeling, analysis and reliability of seismically excited structures: computational issues. *International journal of computational methods*, 5(04):483–511.

[112] Francfort, G. A. and Marigo, J.-J. (1998). Revisiting brittle fracture as an energy minimization problem. *Journal of the Mechanics and Physics of Solids*, 46(8):1319–1342.

[113] Freund, L. B. (1998). *Dynamic fracture mechanics*. Cambridge university press.

[114] Gan, N. and Wang, Q. (2021). Topology optimization of multiphase materials with dynamic and static characteristics by beso method. *Advances in Engineering Software*, 151:102928.

[115] Gao, J., Luo, Z., Xia, L., and Gao, L. (2019). Concurrent topology optimization of multiscale composite structures in matlab. *Structural and Multidisciplinary Optimization*, 60:2621–2651.

[116] Gao, T. and Zhang, W. (2010). Topology optimization involving thermo-elastic stress loads. *Structural and multidisciplinary optimization*, 42(5):725–738.

[117] Gao, W., Song, C., and Tin-Loi, F. (2010). Probabilistic interval analysis for structures with uncertainty. *Structural Safety*, 32(3):191–199.

[118] Garcez, G. L., Pavanello, R., and Picelli, R. (Accepted). Bi-directional evolutionary topology optimization based on stress minimization under design-dependent surface loads. *Engineering Optimization*.

[119] Garcez, G. L., Picelli, R., and Pavanello, R. (2021). Stress-based structural topology optimization for design-dependent self-weight loads problems using the beso method. *Engineering Optimization*, pages 1–17.

[120] Gea, H. C. and Luo, J. (2001). Topology optimization of structures with geometrical nonlinearities. *Computers & Structures*, 79(20-21):1977–1985.

[121] Geelen, R. J., Liu, Y., Hu, T., Tupek, M. R., and Dolbow, J. E. (2019). A phase-field formulation for dynamic cohesive fracture. *Computer Methods in Applied Mechanics and Engineering*, 348:680–711.

[122] Gersborg-Hansen, A., Sigmund, O., and Haber, R. B. (2005). Topology optimization of channel flow problems. *Structural and multidisciplinary optimization*, 30(3):181–192.

[123] Ghanem, R. (1999). The Nonlinear Gaussian Spectrum of Log-Normal Stochastic Processes and Variables. *Journal of Applied Mechanics*, 66(4):964–973.

[124] Ghanem, R. G. and Spanos, P. D. (1991). Spectral stochastic finite-element formulation for reliability analysis. *Journal of Engineering Mechanics*, 117(10):2351–2372.

[125] Ghanem, R. G. and Spanos, P. D. (2003). *Stochastic finite elements: a spectral approach*. Courier Corporation.

[126] Giraldo-Londoño, O., Aguiló, M. A., and Paulino, G. H. (2021). Local stress constraints in topology optimization of structures subjected to arbitrary dynamic loads: a stress aggregation-free approach. *Structural and Multidisciplinary Optimization*, 64(6):3287–3309.

[127] Giraldo-Londoño, O. and Paulino, G. H. (2021). Polydyna: a matlab implementation for topology optimization of structures subjected to dynamic loads. *Structural and Multidisciplinary Optimization*, 64(2):957–990.

[128] Guest, J. K., Asadpoure, A., and Ha, S.-H. (2011). Eliminating beta-continuation from heaviside projection and density filter algorithms. *Structural and Multidisciplinary Optimization*, 44(4):443–453.

[129] Guest, J. K. and Igusa, T. (2008). Structural optimization under uncertain loads and nodal locations. *Computer Methods in Applied Mechanics and Engineering*, 198(1):116–124.

[130] Guest, J. K., Prévost, J. H., and Belytschko, T. (2004). Achieving minimum length scale in topology optimization using nodal design variables and projection functions. *International Journal for Numerical Methods in Engineering*, 61(2):238–254.

[131] Guirguis, D. and Aly, M. F. (2016). A derivative-free level-set method for topology optimization. *Finite Elements in Analysis and Design*, 120:41–56.

[132] Guirguis, D., Melek, W. W., and Aly, M. F. (2018). High-resolution non-gradient topology optimization. *Journal of Computational Physics*, 372:107–125.

[133] Guo, K., Yang, Z., Yu, C.-H., and Buehler, M. J. (2021). Artificial intelligence and machine learning in design of mechanical materials. *Materials Horizons*, 8(4):1153–1172.

[134] Guo, X. and Cheng, G.-D. (2010). Recent development in structural design and optimization. *Acta Mechanica Sinica*, 26(6):807–823.

[135] Guo, X., Zhang, W., Zhang, J., and Yuan, J. (2016). Explicit structural topology optimization based on moving morphable components (mmc) with curved skeletons. *Computer methods in applied mechanics and engineering*, 310:711–748.

[136] Guo, X., Zhang, W., and Zhong, W. (2014). Doing topology optimization explicitly and geometrically—a new moving morphable components based framework. *Journal of Applied Mechanics*, 81(8).

[137] Guo, X., Zhao, X., Zhang, W., Yan, J., and Sun, G. (2015). Multi-scale robust design and optimization considering load uncertainties. *Computer Methods in Applied Mechanics and Engineering*, 283:994–1009.

[138] Haber, R., Bendøse, M., and Jog, C. (1996). Perimeter constrained topology optimization of continuum structures. In *IUTAM Symposium on Optimization of Mechanical Systems*, pages 113–120. Springer.

[139] Halkjær, S., Sigmund, O., and Jensen, J. S. (2005). Inverse design of phononic crystals by topology optimization. *Zeitschrift für Kristallographie-Crystalline Materials*, 220(9-10):895–905.

[140] Halkjær, S., Sigmund, O., and Jensen, J. S. (2006). Maximizing band gaps in plate structures. *Structural and Multidisciplinary Optimization*, 32(4):263–275.

[141] Hassani, B. (1996). A direct method to derive the boundary conditions of the homogenization equation for symmetric cells. *Communications in Numerical Methods in Engineering*, 12:185–196.

[142] Hassani, B. and Hinton, E. (1998). A review of homogenization and topology opimization ii—analytical and numerical solution of homogenization equations. *Computers & structures*, 69(6):719–738.

[143] He, Z., Jiang, H., Wu, Y., Li, E., Zhou, B., and Tang, Q. (2020). Robust topological design of actuator-coupled structures with hybrid uncertainties. *Acta Mechanica*, 231:1621–1638.

[144] He, Z., Wu, Y., and Li, E. (2018). Topology optimization of structure for dynamic properties considering hybrid uncertain parameters. *Structural and Multidisciplinary Optimization*, 57(2):625–638.

[145] Hegemier, G. and Prager, W. (1969). On michell trusses. *International Journal of Mechanical Sciences*, 11(2):209–215.

[146] Helton, J. C., Johnson, J., Oberkampf, W. L., and Storlie, C. B. (2007). A sampling-based computational strategy for the representation of epistemic uncertainty in model predictions with evidence theory. *Computer Methods in Applied Mechanics and Engineering*, 196(37-40):3980–3998.

[147] Hofacker, M. and Miehe, C. (2013). A phase field model of dynamic fracture: Robust field updates for the analysis of complex crack patterns. *International Journal for Numerical Methods in Engineering*, 93(3):276–301.

[148] Holmberg, E., Torstenfelt, B., and Klarbring, A. (2013). Stress constrained topology optimization. *Structural and Multidisciplinary Optimization*, 48(1):33–47.

[149] Hooijkamp, E. C. and Keulen, F. v. (2018). Topology optimization for linear thermomechanical transient problems: modal reduction and adjoint sensitivities. *International Journal for Numerical Methods in Engineering*, 113(8):1230–1257.

[150] Hu, H., Wu, Y., Batou, A., and Ouyang, H. (2021). B-spline based interval field decomposition method. *Under submission*.

[151] Huang, X. and Xie, M. (2010a). *Evolutionary topology optimization of continuum structures: methods and applications*. John Wiley & Sons.

[152] Huang, X. and Xie, Y. (2007). Convergent and mesh-independent solutions for the bi-directional evolutionary structural optimization method. *Finite Elements in Analysis and Design*, 43(14):1039–1049.

[153] Huang, X. and Xie, Y. (2008). Optimal design of periodic structures using evolutionary topology optimization. *Structural and Multidisciplinary Optimization*, 36(6):597–606.

[154] Huang, X. and Xie, Y. (2010b). Evolutionary topology optimization of continuum structures with an additional displacement constraint. *Structural and Multidisciplinary Optimization*, 40(1-6):409.

[155] Huang, X. and Xie, Y. M. (2009). Bi-directional evolutionary topology optimization of continuum structures with one or multiple materials. *Computational Mechanics*, 43(3):393.

[156] Huang, X., Zuo, Z., and Xie, Y. (2010a). Evolutionary topological optimization of vibrating continuum structures for natural frequencies. *Computers & structures*, 88(5-6):357–364.

[157] Huang, X., Zuo, Z., and Xie, Y. M. (2010b). Evolutionary topological optimization of vibrating continuum structures for natural frequencies. *Computers & Structures*, 88:357–364.

[158] Iga, A., Nishiwaki, S., Izui, K., and Yoshimura, M. (2009). Topology optimization for thermal conductors considering design-dependent effects, including heat conduction and convection. *International Journal of Heat and Mass Transfer*, 52(11-12):2721–2732.

[159] Jalalpour, M. and Tootkaboni, M. (2016). An efficient approach to reliability-based topology optimization for continua under material uncertainty. *Structural and Multidisciplinary Optimization*, 53(4):759–772.

[160] James, K. A. and Waisman, H. (2014). Failure mitigation in optimal topology design using a coupled nonlinear continuum damage model. *Computer methods in applied mechanics and engineering*, 268:614–631.

[161] Jang, H.-H., Lee, H., Lee, J., and Park, G. (2012). Dynamic response topology optimization in the time domain using equivalent static loads. *AIAA journal*, 50(1):226–234.

[162] Jaynes, E. T. (1957). Information theory and statistical mechanics. *Physical review*, 106(4):620.

[163] Jensen, J. S. (2007). Topology optimization of dynamics problems with padé approximants. *International journal for numerical methods in engineering*, 72(13):1605–1630.

[164] Jensen, J. S. and Pedersen, N. L. (2006). On maximal eigenfrequency separation in two-material structures: the 1d and 2d scalar cases. *Journal of Sound and Vibration*, 289(4-5):967–986.

[165] Jensen, J. S. and Sigmund, O. (2005). Topology optimization of photonic crystal structures: a high-bandwidth low-loss t-junction waveguide. *JOSA B*, 22(6):1191–1198.

[166] Jensen, J. S. and Sigmund, O. (2011). Topology optimization for nano-photonics. *Laser & Photonics Reviews*, 5(2):308–321.

[167] Jiang, C., Han, X., Liu, G., and Liu, G. (2008). A nonlinear interval number programming method for uncertain optimization problems. *European Journal of Operational Research*, 188(1):1–13.

[168] Jiang, C., Han, X., Lu, G., Liu, J., Zhang, Z., and Bai, Y. (2011a). Correlation analysis of non-probabilistic convex model and corresponding structural reliability technique. *Computer Methods in Applied Mechanics and Engineering*, 200(33-36):2528–2546.

[169] Jiang, C., Li, W., Han, X., Liu, L., and Le, P. (2011b). Structural reliability analysis based on random distributions with interval parameters. *Computers & Structures*, 89(23-24):2292–2302.

[170] Jiang, C., Ni, B., Han, X., and Tao, Y. (2014a). Non-probabilistic convex model process: A new method of time-variant uncertainty analysis and its application to structural dynamic reliability problems. *Computer Methods in Applied Mechanics and Engineering*, 268:656–676.

[171] Jiang, C., Ni, B., Liu, N., Han, X., and Liu, J. (2016). Interval process model and non-random vibration analysis. *Journal of Sound and Vibration*, 373:104–131.

[172] Jiang, C., Zhang, Q., Han, X., Liu, J., and Hu, D. (2015). Multidimensional parallelepiped model—a new type of non-probabilistic convex model for structural uncertainty analysis. *International Journal for Numerical Methods in Engineering*, 103(1):31–59.

[173] Jiang, C., Zhang, Q., Han, X., and Qian, Y. (2014b). A non-probabilistic structural reliability analysis method based on a multidimensional parallelepiped convex model. *Acta Mechanica*, 225(2):383–395.

[174] Jiang, C., Zheng, J., and Han, X. (2018). Probability-interval hybrid uncertainty analysis for structures with both aleatory and epistemic uncertainties: a review. *Structural and Multidisciplinary Optimization*, 57(6):2485–2502.

[175] Jiang, H., Wei, B., Zhou, E., Wu, Y., and Li, X. (2021). Robust topology optimization for thermoelastic hierarchical structures with hybrid uncertainty. *Journal of Thermal Stresses*, 44(12):1458–1478.

[176] Jog, C. (2002). Topology design of structures subjected to periodic loading. *Journal of Sound and Vibration*, 253(3):687–709.

[177] Jung, D. and Gea, H. C. (2004). Topology optimization of nonlinear structures. *Finite Elements in Analysis and Design*, 40(11):1417–1427.

[178] Jung, H.-S. and Cho, S. (2004). Reliability-based topology optimization of geometrically nonlinear structures with loading and material uncertainties. *Finite elements in analysis and design*, 41(3):311–331.

[179] Jung, J., Hyun, J., Goo, S., and Wang, S. (2015). An efficient design sensitivity analysis using element energies for topology optimization of a frequency response problem. *Computer Methods in Applied Mechanics and Engineering*, 296:196–210.

[180] Kalthoff, J. and Winkler, S. (1988). Failure mode transition at high rates of shear loading. *DGM Informationsgesellschaft mbH, Impact Loading and Dynamic Behavior of Materials*, 1:185–195.

[181] Kang, Z. and Liu, P. (2018). Reliability-based topology optimization against geometric imperfections with random threshold model. *International Journal for Numerical Methods in Engineering*, 115(1):99–116.

[182] Kang, Z., Liu, P., and Li, M. (2017). Topology optimization considering fracture mechanics behaviors at specified locations. *Structural and Multidisciplinary Optimization*, 55(5):1847–1864.

[183] Kang, Z. and Luo, Y. (2009). Non-probabilistic reliability-based topology optimization of geometrically nonlinear structures using convex models. *Computer Methods in Applied Mechanics and Engineering*, 198(41-44):3228–3238.

[184] Kang, Z. and Zhang, W. (2016). Construction and application of an ellipsoidal convex model using a semi-definite programming formulation from measured data. *Computer Methods in Applied Mechanics and Engineering*, 300:461–489.

[185] Kang, Z., Zhang, X., Jiang, S., and Cheng, G. (2012). On topology optimization of damping layer in shell structures under harmonic excitations. *Structural and Multidisciplinary Optimization*, 46(1):51–67.

[186] Kato, J. and Ramm, E. (2013). Multiphase layout optimization for fiber reinforced composites considering a damage model. *Engineering Structures*, 49:202–220.

[187] Kawamoto, A. (2009). Stabilization of geometrically nonlinear topology optimization by the levenberg–marquardt method. *Structural and Multidisciplinary Optimization*, 37(4):429–433.

[188] Kharmanda, G. and Olhoff, N. (2001). Reliability-based topology optimization. Institute of Mechanical Engineering, Aalborg University, Denmark.

[189] Kharmanda, G., Olhoff, N., Mohamed, A., and Lemaire, M. (2004). Reliability-based topology optimization. *Structural and Multidisciplinary Optimization*, 26(5):295–307.

[190] Kim, S. Y., Mechefske, C. K., and Kim, I. Y. (2013). Optimal damping layout in a shell structure using topology optimization. *Journal of Sound and Vibration*, 332(12):2873–2883.

[191] Kim, T. S. and Kim, Y. Y. (2000). Mac-based mode-tracking in structural topology optimization. *Computers & Structures*, 74(3):375–383.

[192] Kirsch, U. (1990). On the relationship between optimum structural topologies and geometries. *Structural optimization*, 2(1):39–45.

[193] Klarbring, A. and Strömberg, N. (2013). Topology optimization of hyperelastic bodies including non-zero prescribed displacements. *Structural and Multidisciplinary Optimization*, 47(1):37–48.

[194] Komkov, V., Choi, K. K., and Haug, E. J. (1986). *Design sensitivity analysis of structural systems*, volume 177. Academic press.

[195] Kristiansen, H., Poulios, K., and Aage, N. (2021). Topology optimization of structures in transient impacts with coulomb friction. *International Journal for Numerical Methods in Engineering*.

[196] Krog, L. A. and Olhoff, N. (1999). Optimum topology and reinforcement design of disk and plate structures with multiple stiffness and eigenfrequency objectives. *Computers & Structures*, 72(4-5):535–563.

[197] Kruse, R. and Meyer, K. D. (1988). Confidence intervals for the parameters of a linguistic random variable. In *Combining Fuzzy Imprecision with Probabilistic Uncertainty in Decision Making*, pages 113–123. Springer.

[198] Lau, G. K. and Du, H. (2005). Topology optimization of head suspension assemblies using modal participation factor for mode tracking. *Microsystem technologies*, 11(12):1243–1251.

[199] Lazarov, B. S., Schevenels, M., and Sigmund, O. (2012). Topology optimization with geometric uncertainties by perturbation techniques. *International Journal for Numerical Methods in Engineering*, 90(11):1321–1336.

[200] Le, C., Norato, J., Bruns, T., Ha, C., and Tortorelli, D. (2010). Stress-based topology optimization for continua. *Structural and Multidisciplinary Optimization*, 41(4):605–620.

[201] Lee, H.-A. and Park, G.-J. (2012). Topology Optimization for Structures With Nonlinear Behavior Using the Equivalent Static Loads Method. *Journal of Mechanical Design*, 134(3). 031004.

[202] Lee, H.-A. and Park, G.-J. (2015). Nonlinear dynamic response topology optimization using the equivalent static loads method. *Computer Methods in Applied Mechanics and Engineering*, 283:956–970.

[203] Lee, J. W. and Kim, Y. Y. (2009). Topology optimization of muffler internal partitions for improving acoustical attenuation performance. *International journal for numerical methods in engineering*, 80(4):455–477.

[204] Lei, X., Liu, C., Du, Z., Zhang, W., and Guo, X. (2019). Machine learning-driven real-time topology optimization under moving morphable component-based framework. *Journal of Applied Mechanics*, 86(1):011004.

[205] Li, E., He, Z., Hu, J., and Long, X. (2017a). Volumetric locking issue with uncertainty in the design of locally resonant acoustic metamaterials. *Computer Methods in Applied Mechanics and Engineering*, 324:128–148.

[206] Li, J., Ni, B., Jiang, C., and Fang, T. (2018). Dynamic response bound analysis for elastic beams under uncertain excitations. *Journal of Sound and Vibration*, 422:471–489.

[207] Li, L. and Khandelwal, K. (2017). Design of fracture resistant energy absorbing structures using elastoplastic topology optimization. *Structural and Multidisciplinary Optimization*, 56(6):1447–1475.

[208] Li, L., Zhang, G., and Khandelwal, K. (2017b). Topology optimization of energy absorbing structures with maximum damage constraint. *International Journal for Numerical Methods in Engineering*, 112(7):737–775.

[209] Li, M., Tang, W., and Yuan, M. (2014). Structural dynamic topology optimization based on dynamic reliability using equivalent static loads. *Structural and Multidisciplinary Optimization*, 49(1):121–129.

[210] Li, P., Wu, Y., and Yvonnet, J. (2021a). A simp-phase field topology optimization framework to maximize quasi-brittle fracture resistance of 2d and 3d composites. *Theoretical and Applied Fracture Mechanics*, 114:102919.

[211] Li, P., Yvonnet, J., and Wu, Y. (2022). Improved fracture resistance of 3d-printed elastoplastic structures with respect to their topology and orientation of deposited layers. *International Journal of Mechanical Sciences*, 220:107147.

[212] Li, Q., Sigmund, O., Jensen, J. S., and Aage, N. (2021b). Reduced-order methods for dynamic problems in topology optimization: A comparative study. *Computer Methods in Applied Mechanics and Engineering*, 387:114149.

[213] Li, Q., Steven, G., and Xie, Y. (1999). On equivalence between stress criterion and stiffness criterion in evolutionary structural optimization. *Structural optimization*, 18(1):67–73.

[214] Li, Q., Steven, G., and Xie, Y. (2001). A simple checkerboard suppression algorithm for evolutionary structural optimization. *Structural and Multidisciplinary Optimization*, 22(3):230–239.

[215] Li, Q., Steven, G. P., Xie, Y. M., and Querin, O. M. (2004). Evolutionary topology optimization for temperature reduction of heat conducting fields. *International Journal of Heat and Mass Transfer*, 47(23):5071–5083.

[216] Li, Q., Wu, Q., Liu, J., He, J., and Liu, S. (2021c). Topology optimization of vibrating structures with frequency band constraints. *Structural and Multidisciplinary Optimization*, 63(3):1203–1218.

[217] Li, W., Meng, F., Chen, Y., Li, Y. f., and Huang, X. (2019). Topology optimization of photonic and phononic crystals and metamaterials: a review. *Advanced Theory and Simulations*, 2(7):1900017.

[218] Lin, X., Li, E., He, Z., and Wu, Y. (2020). A novel method to study the phononic crystals with fluid–structure interaction and hybrid uncertainty. *Acta Mechanica*, 231(1):321–352.

[219] Lin, Z.-Q., Gea, H. C., and Liu, S.-T. (2011). Design of piezoelectric energy harvesting devices subjected to broadband random vibrations by applying topology optimization. *Acta Mechanica Sinica*, 27(5):730–737.

[220] Liu, B., Huang, X., Huang, C., Sun, G., Yan, X., and Li, G. (2017a). Topological design of structures under dynamic periodic loads. *Engineering Structures*, 142:128–136.

[221] Liu, B., Jiang, C., Li, G., and Huang, X. (2020). Topology optimization of structures considering local material uncertainties in additive manufacturing. *Computer Methods in Applied Mechanics and Engineering*, 360:112786.

[222] Liu, H., Zhang, W., and Gao, T. (2015). A comparative study of dynamic analysis methods for structural topology optimization under harmonic force excitations. *Structural and Multidisciplinary Optimization*, 51(6):1321–1333.

[223] Liu, J., Gaynor, A. T., Chen, S., Kang, Z., Suresh, K., Takezawa, A., Li, L., Kato, J., Tang, J., Wang, C. C., et al. (2018a). Current and future trends in topology optimization for additive manufacturing. *Structural and multidisciplinary optimization*, 57(6):2457–2483.

[224] Liu, J. and Gea, H. C. (2018). Robust topology optimization under multiple independent unknown-but-bounded loads. *Computer Methods in Applied Mechanics and Engineering*, 329:464–479.

[225] Liu, J., Wen, G., Qing, Q., Li, F., and Xie, Y. M. (2018b). Robust topology optimization for continuum structures with random loads. *Engineering Computations*.

[226] Liu, J., Wen, G., Qing, Q., and Xie, Y. M. (2017b). An efficient method for topology optimization of continuum structures in the presence of uncertainty in loading direction. *International Journal of Computational Methods*, 14(05):1750054.

[227] Liu, K., Paulino, G. H., and Gardoni, P. (2016a). Reliability-based topology optimization using a new method for sensitivity approximation-application to ground structures. *Structural and Multidisciplinary Optimization*, 54(3):553–571.

[228] Liu, P., Luo, Y., and Kang, Z. (2016b). Multi-material topology optimization considering interface behavior via xfem and level set method. *Computer methods in applied mechanics and engineering*, 308:113–133.

[229] Liu, Q., Chan, R., and Huang, X. (2016c). Concurrent topology optimization of macrostructures and material microstructures for natural frequency. *Materials & Design*, 106:380–390.

[230] Liu, Q., Ruan, D., and Huang, X. (2018c). Topology optimization of viscoelastic materials on damping and frequency of macrostructures. *Computer Methods in Applied Mechanics and Engineering*, 337:305 – 323.

[231] Logo, J., Ghaemi, M., and Rad, M. M. (2009). Optimal topologies in case of probabilistic loading: the influence of load correlation. *Mechanics based design of structures and machines*, 37(3):327–348.

[232] Long, X., Jiang, C., Han, X., and Gao, W. (2015). Stochastic response analysis of the scaled boundary finite element method and application to probabilistic fracture mechanics. *Computers & Structures*, 153:185–200.

[233] Luh, G.-C. and Chueh, C.-H. (2004). Multi-modal topological optimization of structure using immune algorithm. *Computer Methods in Applied Mechanics and Engineering*, 193(36-38):4035–4055.

[234] Luh, G.-C., Lin, C.-Y., and Lin, Y.-S. (2011). A binary particle swarm optimization for continuum structural topology optimization. *Applied Soft Computing*, 11(2):2833–2844.

[235] Luo, Y., Kang, Z., and Li, A. (2009a). Structural reliability assessment based on probability and convex set mixed model. *Computers & Structures*, 87(21-22):1408–1415.

[236] Luo, Y., Kang, Z., Luo, Z., and Li, A. (2009b). Continuum topology optimization with non-probabilistic reliability constraints based on multi-ellipsoid convex model. *Structural and Multidisciplinary Optimization*, 39(3):297–310.

[237] Luo, Y., Wang, M. Y., and Kang, Z. (2013). An enhanced aggregation method for topology optimization with local stress constraints. *Computer Methods in Applied Mechanics and Engineering*, 254:31–41.

[238] Luo, Y., Wang, M. Y., and Kang, Z. (2015). Topology optimization of geometrically nonlinear structures based on an additive hyperelasticity technique. *Computer methods in applied mechanics and engineering*, 286:422–441.

[239] Luo, Y., Zhan, J., Xing, J., and Kang, Z. (2019). Non-probabilistic uncertainty quantification and response analysis of structures with a bounded field model. *Computer Methods in Applied Mechanics and Engineering*, 347:663–678.

[240] Luo, Z. (2013). A short survey: Topological shape optimization of structures using level set methods. *Journal of Applied Mechanical Engineering*, 2(2):123.

[241] Ma, Z.-D., Cheng, H.-C., and Kikuchi, N. (1994). Structural design for obtaining desired eigenfrequencies by using the topology and shape optimization method. *Computing Systems in Engineering*, 5(1):77–89.

[242] Ma, Z.-D., Kikuchi, N., and Cheng, H.-C. (1995). Topological design for vibrating structures. *Computer methods in applied mechanics and engineering*, 121(1-4):259–280.

[243] Ma, Z.-D., Kikuchi, N., and Hagiwara, I. (1993). Structural topology and shape optimization for a frequency response problem. *Computational mechanics*, 13(3):157–174.

[244] Maeda, Y., Nishiwaki, S., Izui, K., Yoshimura, M., Matsui, K., and Terada, K. (2006). Structural topology optimization of vibrating structures with specified eigenfrequencies and eigenmode shapes. *International Journal for Numerical Methods in Engineering*, 67(5):597–628.

[245] Mandal, T. K., Nguyen, V. P., and Wu, J.-Y. (2020). Evaluation of variational phase-field models for dynamic brittle fracture. *Engineering Fracture Mechanics*, 235:107169.

[246] Manickarajah, D., Xie, Y., and Steven, G. (1998). An evolutionary method for optimization of plate buckling resistance. *Finite Elements in Analysis and Design*, 29(3-4):205–230.

[247] Martin, A. and Deierlein, G. G. (2020). Structural topology optimization of tall buildings for dynamic seismic excitation using modal decomposition. *Engineering Structures*, 216:110717.

[248] Massa, F., Tison, T., and Lallemand, B. (2006). A fuzzy procedure for the static design of imprecise structures. *Computer methods in applied mechanics and engineering*, 195(9-12):925–941.

[249] Maute, K. (2014). Topology optimization under uncertainty. In *Topology optimization in structural and continuum mechanics*, pages 457–471. Springer.

[250] Maute, K. and Frangopol, D. M. (2003). Reliability-based design of mems mechanisms by topology optimization. *Computers & Structures*, 81(8-11):813–824.

[251] Maxwell, J. (1895). *Scientific papers II*. Cambridge University Press.

[252] Mayer, R. R., Kikuchi, N., and Scott, R. A. (1996). Application of topological optimization techniques to structural crashworthiness. *International Journal for Numerical Methods in Engineering*, 39(8):1383–1403.

[253] McKeown, J. J. (1997). A note on the equivalence between maximum stiffness and maximum strength trusses. *Engineering Optimization*, 29(1-4):443–456.

[254] Meng, Z., Pang, Y., Pu, Y., and Wang, X. (2020). New hybrid reliability-based topology optimization method combining fuzzy and probabilistic models for handling epistemic and aleatory uncertainties. *Computer Methods in Applied Mechanics and Engineering*, 363:112886.

[255] Michell, A. G. M. (1904). Lviii. the limits of economy of material in frame-structures. *The London, Edinburgh, and Dublin Philosophical Magazine and Journal of Science*, 8(47):589–597.

[256] Miehe, C., Hofacker, M., and Welschinger, F. (2010a). A phase field model for rate-independent crack propagation: Robust algorithmic implementation based on operator splits. *Computer Methods in Applied Mechanics and Engineering*, 199(45-48):2765–2778.

[257] Miehe, C. and Lambrecht, M. (2001). Algorithms for computation of stresses and elasticity moduli in terms of Seth-Hill's family of generalized strain tensors. *Communications in Numerical Methods in Engineering*, 17(5):337–353.

[258] Miehe, C., Schänzel, L.-M., and Ulmer, H. (2015). Phase field modeling of fracture in multi-physics problems. part i. balance of crack surface and failure criteria for brittle crack propagation in thermo-elastic solids. *Computer Methods in Applied Mechanics and Engineering*, 294:449–485.

[259] Miehe, C., Welschinger, F., and Hofacker, M. (2010b). Thermodynamically consistent phase-field models of fracture: Variational principles and multi-field fe implementations. *International journal for numerical methods in engineering*, 83(10):1273–1311.

[260] Miller, O., Freund, L., and Needleman, A. (1999). Energy dissipation in dynamic fracture of brittle materials. *Modelling and Simulation in Materials Science and Engineering*, 7(4):573.

[261] Min, S., Kikuchi, N., Park, Y., Kim, S., and Chang, S. (1999). Optimal topology design of structures under dynamic loads. *Structural optimization*, 17(2):208–218.

[262] Mlejnek, H. (1992). Some aspects of the genesis of structures. *Structural optimization*, 5(1):64–69.

[263] Moens, D. and Hanss, M. (2011). Non-probabilistic finite element analysis for parametric uncertainty treatment in applied mechanics: Recent advances. *Finite Elements in Analysis and Design*, 47(1):4–16.

[264] Moens, D., Munck, M. D., Desmet, W., and Vandepitte, D. (2011). Numerical dynamic analysis of uncertain mechanical structures based on interval fields. In *IUTAM symposium on the vibration analysis of structures with uncertainties*, pages 71–83. Springer.

[265] Moens, D. and Vandepitte, D. (2005). A survey of non-probabilistic uncertainty treatment in finite element analysis. *Computer methods in applied mechanics and engineering*, 194(12-16):1527–1555.

[266] Moens, D. and Vandepitte, D. (2007). Interval sensitivity theory and its application to frequency response envelope analysis of uncertain structures. *Computer methods in applied mechanics and engineering*, 196(21-24):2486–2496.

[267] Moës, N., Dolbow, J., and Belytschko, T. (1999). A finite element method for crack growth without remeshing. *International journal for numerical methods in engineering*, 46(1):131–150.

[268] Mogami, K., Nishiwaki, S., Izui, K., Yoshimura, M., and Kogiso, N. (2006). Reliability-based structural optimization of frame structures for multiple failure criteria using topology optimization techniques. *Structural and Multidisciplinary Optimization*, 32(4):299–311.

[269] Möller, B., Graf, W., and Beer, M. (2000). Fuzzy structural analysis using α-level optimization. *Computational mechanics*, 26(6):547–565.

[270] Mozumder, C., Renaud, J. E., and Tovar, A. (2012). Topometry optimisation for crashworthiness design using hybrid cellular automata. *International journal of vehicle design*, 60(1/2):100–120.

[271] Muscolino, G. and Sofi, A. (2012). Stochastic analysis of structures with uncertain-but-bounded parameters via improved interval analysis. *Probabilistic Engineering Mechanics*, 28:152–163.

[272] Nakshatrala, P. and Tortorelli, D. (2015). Topology optimization for effective energy propagation in rate-independent elastoplastic material systems. *Computer methods in applied mechanics and engineering*, 295:305–326.

[273] Neves, M., Rodrigues, H., and Guedes, J. (1995). Generalized topology design of structures with a buckling load criterion. *Structural optimization*, 10(2):71–78.

[274] Nguyen, T. H., Song, J., and Paulino, G. H. (2011). Single-loop system reliability-based topology optimization considering statistical dependence between limit-states. *Structural and Multidisciplinary Optimization*, 44(5):593–611.

[275] Nguyen, T. T., Yvonnet, J., Bornert, M., and Chateau, C. (2016). Initiation and propagation of complex 3d networks of cracks in heterogeneous quasi-brittle materials: Direct comparison between in situ testing-microct experiments and phase field simulations. *Journal of the Mechanics and Physics of Solids*, 95:320–350.

[276] Nguyen, T.-T., Yvonnet, J., Waldmann, D., and He, Q.-C. (2020). Implementation of a new strain split to model unilateral contact within the phase field method. *International Journal for Numerical Methods in Engineering*, 121(21):4717–4733.

[277] Nguyen, T. T., Yvonnet, J., Zhu, Q. Z., Bornert, M., and Chateau, C. (2015). A phase field method to simulate crack nucleation and propagation in strongly heterogeneous materials from direct imaging of their microstructure. *Engineering Fracture Mechanics*, 139:18–39.

[278] Nguyen, V. P. and Wu, J.-Y. (2018). Modeling dynamic fracture of solids with a phase-field regularized cohesive zone model. *Computer Methods in Applied Mechanics and Engineering*, 340:1000–1022.

[279] Ni, B., Jiang, C., and Han, X. (2016). An improved multidimensional parallelepiped non-probabilistic model for structural uncertainty analysis. *Applied Mathematical Modelling*, 40(7-8):4727–4745.

[280] Ni, B. Y. and Jiang, C. (2020). Interval field model and interval finite element analysis. *Computer Methods in Applied Mechanics and Engineering*, 360.

[281] Ni, B. Y., Wu, P. G., Li, J. Y., and Jiang, C. (2020). A semi-analytical interval method for response bounds analysis of structures with spatially uncertain loads. *Finite Elements in Analysis and Design*, 182:103483.

[282] Niu, B., He, X., Shan, Y., and Yang, R. (2018). On objective functions of minimizing the vibration response of continuum structures subjected to external harmonic excitation. *Structural and Multidisciplinary Optimization*, 57(6):2291–2307.

[283] Noguchi, Y., Yamada, T., Izui, K., and Nishiwaki, S. (2018). Topology optimization for hyperbolic acoustic metamaterials using a high-frequency homogenization method. *Computer Methods in Applied Mechanics and Engineering*, 335:419–471.

[284] Noh, J. Y. and Yoon, G. H. (2012). Topology optimization of piezoelectric energy harvesting devices considering static and harmonic dynamic loads. *Advances in Engineering Software*, 53:45–60.

[285] Norato, J., Bell, B., and Tortorelli, D. A. (2015). A geometry projection method for continuum-based topology optimization with discrete elements. *Computer Methods in Applied Mechanics and Engineering*, 293:306–327.

[286] Ogawa, S. and Yamada, T. (2021). Topology optimization of dynamic problems based on finite deformation theory. *International Journal for Numerical Methods in Engineering*.

[287] Oh, S., Jung, Y., Kim, S., Lee, I., and Kang, N. (2019). Deep generative design: Integration of topology optimization and generative models. *Journal of Mechanical Design*, 141(11).

[288] Olesen, L. H., Okkels, F., and Bruus, H. (2006). A high-level programming-language implementation of topology optimization applied to steady-state navier–stokes flow. *International Journal for Numerical Methods in Engineering*, 65(7):975–1001.

[289] Olhoff, N., Bendsøe, M. P., and Rasmussen, J. (1991). On cad-integrated structural topology and design optimization. *Computer Methods in Applied Mechanics and Engineering*, 89(1-3):259–279.

[290] Olhoff, N. and Du, J. (2005). Topological design of continuum structures subjected to forced vibration. *Proceedings of 6th world congresses of structural and multidisciplinary optimization, Rio de Janeiro, Brazil*.

[291] Olhoff, N. and Du, J. (2009). *On Topological Design Optimization of Structures Against Vibration and Noise Emission*, pages 217–276. Springer Vienna, Vienna.

[292] Olhoff, N. and Du, J. (2016). Generalized incremental frequency method for topological designof continuum structures for minimum dynamic compliance subject to forced vibration at a prescribed low or high value of the excitation frequency. *Structural and Multidisciplinary Optimization*, 54(5):1113–1141.

[293] Olhoff, N. and Taylor, J. E. (1983). On Structural Optimization. *Journal of Applied Mechanics*, 50(4b):1139–1151.

[294] Ortmann, C. and Schumacher, A. (2013). Graph and heuristic based topology optimization of crash loaded structures. *Structural and Multidisciplinary Optimization*, 47(6):839–854.

[295] Osher, S. and Sethian, J. A. (1988). Fronts propagating with curvature-dependent speed: Algorithms based on hamilton-jacobi formulations. *Journal of computational physics*, 79(1):12–49.

[296] Papadimitriou, D. I. and Mourelatos, Z. P. (2018). Reliability-Based Topology Optimization Using Mean-Value Second-Order Saddlepoint Approximation. *Journal of Mechanical Design*, 140(3). 031403.

[297] Papadrakakis, M. and Papadopoulos, V. (1996). Robust and efficient methods for stochastic finite element analysis using monte carlo simulation. *Computer methods in applied mechanics and engineering*, 134(3-4):325–340.

[298] Papadrakakis, M., Papadopoulos, V., and Lagaros, N. D. (1996). Structural reliability analyis of elastic-plastic structures using neural networks and monte carlo simulation. *Computer methods in applied mechanics and engineering*, 136(1-2):145–163.

[299] Pedersen, C. B. (2003). Topology optimization for crashworthiness of frame structures. *International journal of crashworthiness*, 8(1):29–39.

[300] Pedersen, C. B. (2004). Crashworthiness design of transient frame structures using topology optimization. *Computer methods in applied mechanics and engineering*, 193(6-8):653–678.

[301] Pedersen, C. B., Buhl, T., and Sigmund, O. (2001). Topology synthesis of large-displacement compliant mechanisms. *International Journal for numerical methods in engineering*, 50(12):2683–2705.

[302] Pedersen, N. L. (2000). Maximization of eigenvalues using topology optimization. *Structural and multidisciplinary optimization*, 20(1):2–11.

[303] Petersson, J. and Sigmund, O. (1998). Slope constrained topology optimization. *International Journal for Numerical Methods in Engineering*, 41(8):1417–1434.

[304] Pham, K., Amor, H., Marigo, J.-J., and Maurini, C. (2011). Gradient damage models and their use to approximate brittle fracture. *International Journal of Damage Mechanics*, 20(4):618–652.

[305] Picelli, R., Vicente, W., Pavanello, R., and Xie, Y. (2015). Evolutionary topology optimization for natural frequency maximization problems considering acoustic–structure interaction. *Finite Elements in Analysis and Design*, 106:56–64.

[306] Qiu, Z. and Elishakoff, I. (1998). Antioptimization of structures with large uncertain-but-non-random parameters via interval analysis. *Computer methods in applied mechanics and engineering*, 152(3-4):361–372.

[307] Qiu, Z., Yang, D., and Elishakoff, I. (2008). Probabilistic interval reliability of structural systems. *International Journal of Solids and Structures*, 45(10):2850–2860.

[308] Querin, O., Steven, G., and Xie, Y. (2000a). Evolutionary structural optimisation using an additive algorithm. *Finite elements in Analysis and Design*, 34(3-4):291–308.

[309] Querin, O., Young, V., Steven, G., and Xie, Y. (2000b). Computational efficiency and validation of bi-directional evolutionary structural optimisation. *Computer methods in applied mechanics and engineering*, 189(2):559–573.

[310] Querin, O. M., Steven, G. P., and Xie, Y. M. (1998). Evolutionary structural optimisation (eso) using a bidirectional algorithm. *Engineering computations*, 15(8):1031–1048.

[311] Raghu, P., Rajagopal, A., Jalan, S., and Reddy, J. (2021). Modeling of brittle fracture in thick plates subjected to transient dynamic loads using a hybrid phase field model. *Meccanica*, 56(6):1269–1286.

[312] Raponi, E., Bujny, M., Olhofer, M., Aulig, N., Boria, S., and Duddeck, F. (2019). Kriging-assisted topology optimization of crash structures. *Computer Methods in Applied Mechanics and Engineering*, 348:730–752.

[313] Reddy, J. N. (2003). *Mechanics of laminated composite plates and shells: theory and analysis*. CRC press.

[314] Ren, H., Zhuang, X., Anitescu, C., and Rabczuk, T. (2019). An explicit phase field method for brittle dynamic fracture. *Computers & Structures*, 217:45–56.

[315] Richardson, J. N., Coelho, R. F., and Adriaenssens, S. (2015). Robust topology optimization of truss structures with random loading and material properties: A multiobjective perspective. *Computers & Structures*, 154:41–47.

[316] Rong, J., Xie, Y., Yang, X., and Liang, Q. (2000). Topology optimization of structures under dynamic response constraints. *Journal of Sound and Vibration*, 234(2):177–189.

[317] Rozvany, G. and Birker, T. (1995). Generalized michell structures—exact least-weight truss layouts for combined stress and displacement constraints: Part i—general theory for plane trusses. *Structural optimization*, 9(3):178–188.

[318] Rozvany, G. and Gollub, W. (1990). Michell layouts for various combinations of line supports—i. *International journal of mechanical sciences*, 32(12):1021–1043.

[319] Rozvany, G., Gollub, W., and Zhou, M. (1997). Exact michell layouts for various combinations of line supports—part ii. *Structural optimization*, 14(2):138–149.

[320] Rozvany, G. and Querin, O. (2002a). Theoretical foundations of sequential element rejections and admissions (sera) methods and their computational implementation in topology optimization. In *9th AIAA/ISSMO symposium on multidisciplinary analysis and optimization*, page 5521.

[321] Rozvany, G., Querin, O., and Logo, J. (2004). Sequential element rejection and admission (sera) method: Application to multiconstraint problems. In *10th AIAA/ISSMO Multidisciplinary Analysis and Optimization Conference*, page 4523.

[322] Rozvany, G. I. (1996). Some shortcomings in michell's truss theory. *Structural optimization*, 12(4):244–250.

[323] Rozvany, G. I. (2009). A critical review of established methods of structural topology optimization. *Structural and multidisciplinary optimization*, 37(3):217–237.

[324] Rozvany, G. I. and Querin, O. M. (2001). Present limitations and possible improvements of sera (sequential element rejections and admissions) methods in topology optimization. *Proceedings of WCSMO*, 4.

[325] Rozvany, G. I. and Querin, O. M. (2002b). Combining eso with rigorous optimality criteria. *International journal of vehicle design*, 28(4):294–299.

[326] Rozvany, G. I., Zhou, M., and Birker, T. (1992). Generalized shape optimization without homogenization. *Structural optimization*, 4(3-4):250–252.

[327] Rozvany, G. I. N., Bendsøe, M. P., and Kirsch, U. (1995). Layout Optimization of Structures. *Applied Mechanics Reviews*, 48(2):41–119.

[328] Rupp, C. J., Evgrafov, A., Maute, K., and Dunn, M. L. (2009). Design of piezoelectric energy harvesting systems: a topology optimization approach based on multilayer plates and shells. *Journal of Intelligent Material Systems and Structures*, 20(16):1923–1939.

[329] Russ, J. B. and Waisman, H. (2019). Topology optimization for brittle fracture resistance. *Computer Methods in Applied Mechanics and Engineering*, 347:238–263.

[330] Russ, J. B. and Waisman, H. (2020). A novel topology optimization formulation for enhancing fracture resistance with a single quasi-brittle material. *International Journal for Numerical Methods in Engineering*, 121(13):2827–2856.

[331] Russ, J. B. and Waisman, H. (2021). A novel elastoplastic topology optimization formulation for enhanced failure resistance via local ductile failure constraints and linear buckling analysis. *Computer Methods in Applied Mechanics and Engineering*, 373:113478.

[332] Sato, Y., Izui, K., Yamada, T., Nishiwaki, S., Ito, M., and Kogiso, N. (2019). Reliability-based topology optimization under shape uncertainty modeled in eulerian description. *Structural and multidisciplinary optimization*, 59(1):75–91.

[333] Schevenels, M., Lazarov, B. S., and Sigmund, O. (2011). Robust topology optimization accounting for spatially varying manufacturing errors. *Computer Methods in Applied Mechanics and Engineering*, 200(49-52):3613–3627.

[334] Sherif, K., Witteveen, W., Puchner, K., and Irschik, H. (2010). Efficient topology optimization of large dynamic finite element systems using fatigue. *Aiaa Journal*, 48(7):1339–1347.

[335] Shobeiri, V. (2020). Bidirectional evolutionary structural optimization for nonlinear structures under dynamic loads. *International Journal for Numerical Methods in Engineering*, 121(5):888–903.

[336] Shu, L., Wang, M. Y., Fang, Z., Ma, Z., and Wei, P. (2011). Level set based structural topology optimization for minimizing frequency response. *Journal of Sound and Vibration*, 330(24):5820–5834.

[337] Sigmund, O. (1995). Tailoring materials with prescribed elastic properties. *Mechanics of Materials*, 20:351–368.

[338] Sigmund, O. (1997). On the design of compliant mechanisms using topology optimization. *Journal of Structural Mechanics*, 25(4):493–524.

[339] Sigmund, O. (2001a). A 99 line topology optimization code written in matlab. *Structural and multidisciplinary optimization*, 21(2):120–127.

[340] Sigmund, O. (2001b). Design of multiphysics actuators using topology optimization–part ii: Two-material structures. *Computer methods in applied mechanics and engineering*, 190(49-50):6605–6627.

[341] Sigmund, O. (2007). Morphology-based black and white filters for topology optimization. *Structural and Multidisciplinary Optimization*, 33(4):401–424.

[342] Sigmund, O. (2009). Manufacturing tolerant topology optimization. *Acta Mechanica Sinica*, 25(2):227–239.

[343] Sigmund, O. (2011). On the usefulness of non-gradient approaches in topology optimization. *Structural and Multidisciplinary Optimization*, 43(5):589–596.

[344] Sigmund, O. and Maute, K. (2012). Sensitivity filtering from a continuum mechanics perspective. *Structural and Multidisciplinary Optimization*, 46(4):471–475.

[345] Sigmund, O. and Maute, K. (2013). Topology optimization approaches. *Structural and Multidisciplinary Optimization*, 48(6):1031–1055.

[346] Sigmund, O. and Petersson, J. (1998). Numerical instabilities in topology optimization: a survey on procedures dealing with checkerboards, mesh-dependencies and local minima. *Structural optimization*, 16(1):68–75.

[347] Sigmund, O. and Søndergaard Jensen, J. (2003). Systematic design of phononic band–gap materials and structures by topology optimization. *Philosophical Transactions of the Royal Society of London. Series A: Mathematical, Physical and Engineering Sciences*, 361(1806):1001–1019.

[348] Sigmund, O. and Torquato, S. (1997). Design of materials with extreme thermal expansion using a three-phase topology optimization method. *Journal of the Mechanics and Physics of Solids*, 45(6):1037–1067.

[349] Silva, E. C. N. and Kikuchi, N. (1999). Design of piezoelectric transducers using topology optimization. *Smart Materials and Structures*, 8(3):350.

[350] Silva, M., Tortorelli, D. A., Norato, J. A., Ha, C., and Bae, H.-R. (2010). Component and system reliability-based topology optimization using a single-loop method. *Structural and Multidisciplinary Optimization*, 41(1):87–106.

[351] Silva, O. M., Neves, M. M., and Lenzi, A. (2019). A critical analysis of using the dynamic compliance as objective function in topology optimization of one-material structures considering steady-state forced vibration problems. *Journal of Sound and Vibration*, 444:1–20.

[352] Silva, O. M., Neves, M. M., and Lenzi, A. (2020). On the use of active and reactive input power in topology optimization of one-material structures considering steady-state forced vibration problems. *Journal of Sound and Vibration*, 464:114989.

[353] Sofi, A. (2015). Structural response variability under spatially dependent uncertainty: stochastic versus interval model. *Probabilistic Engineering Mechanics*, 42:78–86.

[354] Soize, C. (2001). Maximum entropy approach for modeling random uncertainties in transient elastodynamics. *The Journal of the Acoustical Society of America*, 109(5):1979–1996.

[355] Sosnovik, I. and Oseledets, I. (2019). Neural networks for topology optimization. *Russian Journal of Numerical Analysis and Mathematical Modelling*, 34(4):215–223.

[356] Soto, C. (2004). Structural topology optimization for crashworthiness. *International journal of crashworthiness*, 9(3):277–283.

[357] Stefanou, G. (2009). The stochastic finite element method: past, present and future. *Computer methods in applied mechanics and engineering*, 198(9-12):1031–1051.

[358] Stolpe, M. and Svanberg, K. (2001). An alternative interpolation scheme for minimum compliance topology optimization. *Structural and Multidisciplinary Optimization*, 22(2):116–124.

[359] Sun, J., Tian, Q., Hu, H., and Pedersen, N. L. (2019). Topology optimization for eigenfrequencies of a rotating thin plate via moving morphable components. *Journal of Sound and Vibration*, 448:83–107.

[360] Svanberg, K. (1987). The method of moving asymptotes—a new method for structural optimization. *International journal for numerical methods in engineering*, 24(2):359–373.

[361] Takezawa, A., Daifuku, M., Nakano, Y., Nakagawa, K., Yamamoto, T., and Kitamura, M. (2016). Topology optimization of damping material for reducing resonance response based on complex dynamic compliance. *Journal of Sound and Vibration*, 365:230–243.

[362] Takezawa, A., Yoon, G. H., Jeong, S. H., Kobashi, M., and Kitamura, M. (2014). Structural topology optimization with strength and heat conduction constraints. *Computer Methods in Applied Mechanics and Engineering*, 276:341–361.

[363] Talischi, C., Paulino, G. H., Pereira, A., and Menezes, I. F. (2012). Polytop: a matlab implementation of a general topology optimization framework using unstructured polygonal finite element meshes. *Structural and Multidisciplinary Optimization*, 45(3):329–357.

[364] Tcherniak, D. (2002). Topology optimization of resonating structures using simp method. *International Journal for Numerical Methods in Engineering*, 54(11):1605–1622.

[365] Thore, C.-J., Holmberg, E., and Klarbring, A. (2017). A general framework for robust topology optimization under load-uncertainty including stress constraints. *Computer Methods in Applied Mechanics and Engineering*, 319:1–18.

[366] Tian, F., Tang, X., Xu, T., Yang, J., and Li, L. (2019). A hybrid adaptive finite element phase-field method for quasi-static and dynamic brittle fracture. *International Journal for Numerical Methods in Engineering*, 120(9):1108–1125.

[367] Tootkaboni, M., Asadpoure, A., and Guest, J. K. (2012). Topology optimization of continuum structures under uncertainty–a polynomial chaos approach. *Computer Methods in Applied Mechanics and Engineering*, 201:263–275.

[368] Torii, A. J. (2019). Robust compliance-based topology optimization: A discussion on physical consistency. *Computer Methods in Applied Mechanics and Engineering*, 352:110–136.

[369] Tortorelli, D. A. and Michaleris, P. (1994). Design sensitivity analysis: overview and review. *Inverse problems in Engineering*, 1(1):71–105.

[370] Tsui, K.-L. (1992). An overview of taguchi method and newly developed statistical methods for robust design. *Iie Transactions*, 24(5):44–57.

[371] Tsuji, Y., Hirayama, K., Nomura, T., Sato, K., and Nishiwaki, S. (2006). Design of optical circuit devices based on topology optimization. *IEEE Photonics Technology Letters*, 18(7):850–852.

[372] Tu, J., Choi, K. K., and Park, Y. H. (1999). A New Study on Reliability-Based Design Optimization. *Journal of Mechanical Design*, 121(4):557–564.

[373] Utkin, L. V. (2004). An uncertainty model of structural reliability with imprecise parameters of probability distributions. *ZAMM-Journal of Applied Mathematics and Mechanics/Zeitschrift für Angewandte Mathematik und Mechanik: Applied Mathematics and Mechanics*, 84(10-11):688–699.

[374] Van Dijk, N. P., Maute, K., Langelaar, M., and Van Keulen, F. (2013). Level-set methods for structural topology optimization: a review. *Structural and Multidisciplinary Optimization*, 48(3):437–472.

[375] van Mierlo, C., Faes, M. G., and Moens, D. (2021). Inhomogeneous interval fields based on scaled inverse distance weighting interpolation. *Computer Methods in Applied Mechanics and Engineering*, 373:113542.

[376] Van Trees, H. L. (2004). *Detection, estimation, and modulation theory, part I: detection, estimation, and linear modulation theory*. John Wiley & Sons.

[377] Verbart, A., Langelaar, M., and Keulen, F. v. (2017). A unified aggregation and relaxation approach for stress-constrained topology optimization. *Structural and Multidisciplinary Optimization*, 55(2):663–679.

[378] Vicente, W., Zuo, Z., Pavanello, R., Calixto, T., Picelli, R., and Xie, Y. (2016). Concurrent topology optimization for minimizing frequency responses of two-level hierarchical structures. *Computer Methods in Applied Mechanics and Engineering*, 301:116–136.

[379] Wadbro, E. and Berggren, M. (2006). Topology optimization of an acoustic horn. *Computer methods in applied mechanics and engineering*, 196(1-3):420–436.

[380] Wang, C. and Matthies, H. G. (2020a). A comparative study of two interval-random models for hybrid uncertainty propagation analysis. *Mechanical Systems and Signal Processing*, 136:106531.

[381] Wang, C. and Matthies, H. G. (2020b). A modified parallelepiped model for non-probabilistic uncertainty quantification and propagation analysis. *Computer Methods in Applied Mechanics and Engineering*, 369:113209.

[382] Wang, C. and Matthies, H. G. (2020c). Random model with fuzzy distribution parameters for hybrid uncertainty propagation in engineering systems. *Computer Methods in Applied Mechanics and Engineering*, 359:112673.

[383] Wang, L., Cai, Y.-R., and Liu, D. (2018). Multiscale reliability-based topology optimization methodology for truss-like microstructures with unknown-but-bounded uncertainties. *Computer Methods in Applied Mechanics and Engineering*, 339:358–388.

[384] Wang, L., Liu, D., Yang, Y., Wang, X., and Qiu, Z. (2017). A novel method of non-probabilistic reliability-based topology optimization corresponding to continuum structures with unknown but bounded uncertainties. *Computer Methods in Applied Mechanics and Engineering*, 326:573–595.

[385] Wang, L., Ni, B., Wang, X., and Li, Z. (2021). Reliability-based topology optimization for heterogeneous composite structures under interval and convex mixed uncertainties. *Applied Mathematical Modelling*, 99:628–652.

[386] Wang, L., Wang, X., and Xia, Y. (2014). Hybrid reliability analysis of structures with multi-source uncertainties. *Acta Mechanica*, 225(2):413–430.

[387] Wang, L., Zhao, X., and Liu, D. (2022). Size-controlled cross-scale robust topology optimization based on adaptive subinterval dimension-wise method considering interval uncertainties. *Engineering with Computers*, pages 1–18.

[388] Wang, M. Y. and Wang, X. (2004). "color" level sets: a multi-phase method for structural topology optimization with multiple materials. *Computer Methods in Applied Mechanics and Engineering*, 193(6-8):469–496.

[389] Wang, M. Y., Wang, X., and Guo, D. (2003). A level set method for structural topology optimization. *Computer methods in applied mechanics and engineering*, 192(1-2):227–246.

[390] Wang, S. Y. and Tai, K. (2005). Structural topology design optimization using genetic algorithms with a bit-array representation. *Computer methods in applied mechanics and engineering*, 194(36-38):3749–3770.

[391] Wang, Y. and Kang, Z. (2018). A velocity field level set method for shape and topology optimization. *International Journal for Numerical Methods in Engineering*, 115(11):1315–1336.

[392] Wang, Y., Luo, Z., Kang, Z., and Zhang, N. (2015). A multi-material level set-based topology and shape optimization method. *Computer Methods in Applied Mechanics and Engineering*, 283:1570–1586.

[393] Wei, P. and Wang, M. Y. (2009). Piecewise constant level set method for structural topology optimization. *International Journal for Numerical Methods in Engineering*, 78(4):379–402.

[394] Wu, C., Fang, J., Zhou, S., Zhang, Z., Sun, G., Steven, G. P., and Li, Q. (2020a). Level-set topology optimization for maximizing fracture resistance of brittle materials using phase-field fracture model. *International Journal for Numerical Methods in Engineering*, 121(13):2929–2945.

[395] Wu, D. and Gao, W. (2017). Hybrid uncertain static analysis with random and interval fields. *Computer Methods in Applied Mechanics and Engineering*, 315:222–246.

[396] Wu, J., Gao, J., Luo, Z., and Brown, T. (2016). Robust topology optimization for structures under interval uncertainty. *Adv. Eng. Softw.*, 99:36–48.

[397] Wu, J., Luo, Z., Li, H., and Zhang, N. (2017). Level-set topology optimization for mechanical metamaterials under hybrid uncertainties. *Computer Methods in Applied Mechanics and Engineering*, 319:414–441.

[398] Wu, Y., Li, E., He, Z. C., Lin, X. Y., and Jiang, H. X. (2020b). Robust concurrent topology optimization of structure and its composite material considering uncertainty with imprecise probability. *Computer Methods in Applied Mechanics and Engineering*, 364:112927.

[399] Wu, Y., Mi, D., Zhang, L.-Z., and Cheng, A.-G. (2020c). Robust topological design of laminated composite plate under interval random hybrid uncertainties. *International Journal of Materials and Product Technology*, 61(2-4):160–184.

[400] Wu, Y., Yvonnet, J., Li, P., and He, Z.-C. (2022). Topology optimization for enhanced dynamic fracture resistance of structures. *Computer Methods in Applied Mechanics and Engineering*, 394:114846.

[401] Xia, B. and Yu, D. (2014). An interval random perturbation method for structural-acoustic system with hybrid uncertain parameters. *International Journal for Numerical Methods in Engineering*, 97(3):181–206.

[402] Xia, B., Yu, D., and Liu, J. (2013). Hybrid uncertain analysis of acoustic field with interval random parameters. *Computer Methods in Applied Mechanics and Engineering*, 256:56–69.

[403] Xia, L., Da, D., and Yvonnet, J. (2018a). Topology optimization for maximizing the fracture resistance of quasi-brittle composites. *Computer Methods in Applied Mechanics and Engineering*, 332:234–254.

[404] Xia, L., Xia, Q., Huang, X., and Xie, Y. M. (2018b). Bi-directional evolutionary structural optimization on advanced structures and materials: a comprehensive review. *Archives of Computational Methods in Engineering*, 25(2):437–478.

[405] Xia, L., Zhang, L., Xia, Q., and Shi, T. (2018c). Stress-based topology optimization using bi-directional evolutionary structural optimization method. *Computer Methods in Applied Mechanics and Engineering*, 333:356–370.

[406] Xia, Q., Shi, T., and Wang, M. Y. (2011). A level set based shape and topology optimization method for maximizing the simple or repeated first eigenvalue of structure vibration. *Structural and Multidisciplinary Optimization*, 43(4):473–485.

[407] Xie, Y. and Steven, G. (1996). Evolutionary structural optimization for dynamic problems. *Computers & Structures*, 58(6):1067–1073.

[408] Xie, Y. M. and Steven, G. P. (1993). A simple evolutionary procedure for structural optimization. *Computers & structures*, 49(5):885–896.

[409] Xie, Y. M. and Steven, G. P. (1997). Basic evolutionary structural optimization. In *Evolutionary structural optimization*, pages 12–29. Springer.

[410] Xu, B., Han, Y., and Zhao, L. (2020). Bi-directional evolutionary topology optimization of geometrically nonlinear continuum structures with stress constraints. *Applied Mathematical Modelling*, 80:771–791.

[411] Xu, B., Huang, X., and Xie, Y. (2016). Two-scale dynamic optimal design of composite structures in the time domain using equivalent static loads. *Composite Structures*, 142:335–345.

[412] Xu, M., Wang, S., and Xie, X. (2019). Level set-based isogeometric topology optimization for maximizing fundamental eigenfrequency. *Frontiers of Mechanical Engineering*, 14(2):222–234.

[413] Xu, S., Cai, Y., and Cheng, G. (2010). Volume preserving nonlinear density filter based on heaviside functions. *Structural and Multidisciplinary Optimization*, 41(4):495–505.

[414] Yan, K., Cheng, G. D., and Wang, B. P. (2018). Topology optimization of damping layers in shell structures subject to impact loads for minimum residual vibration. *Journal of Sound and Vibration*, 431:226–247.

[415] Yan, K. and Wang, B. P. (2020). Two new indices for structural optimization of free vibration suppression. *Structural and Multidisciplinary Optimization*, 61(5):2057–2075.

[416] Yan, X., Huang, X., Zha, Y., and Xie, Y. (2014). Concurrent topology optimization of structures and their composite microstructures. *Computers & Structures*, 133:103–110.

[417] Yang, D., Liu, H., Zhang, W., and Li, S. (2018). Stress-constrained topology optimization based on maximum stress measures. *Computers & Structures*, 198:23–39.

[418] Yang, X. and Li, Y. (2014). Structural topology optimization on dynamic compliance at resonance frequency in thermal environments. *Structural and Multidisciplinary Optimization*, 49(1):81–91.

[419] Yang, X., Xie, Y., Steven, G., and Querin, O. (1999a). Bidirectional evolutionary method for stiffness optimization. *AIAA journal*, 37(11):1483–1488.

[420] Yang, X., Xie, Y., Steven, G., and Querin, O. (1999b). Topology optimization for frequencies using an evolutionary method. *Journal of Structural Engineering*, 125(12):1432–1438.

[421] Yi, G. and Youn, B. D. (2016). A comprehensive survey on topology optimization of phononic crystals. *Structural and Multidisciplinary Optimization*, 54(5):1315–1344.

[422] Yin, H., Yu, D., and Xia, B. (2018). Reliability-based topology optimization for structures using fuzzy set model. *Computer Methods in Applied Mechanics and Engineering*, 333:197–217.

[423] Yoon, G. H. (2010a). Maximizing the fundamental eigenfrequency of geometrically nonlinear structures by topology optimization based on element connectivity parameterization. *Computers & structures*, 88(1-2):120–133.

[424] Yoon, G. H. (2010b). Structural topology optimization for frequency response problem using model reduction schemes. *Computer Methods in Applied Mechanics and Engineering*, 199(25-28):1744–1763.

[425] Yoon, G. H. and Kim, Y. Y. (2007). Topology optimization of material-nonlinear continuum structures by the element connectivity parameterization. *International journal for numerical methods in engineering*, 69(10):2196–2218.

[426] Yu, Y., Hur, T., Jung, J., and Jang, I. G. (2019). Deep learning for determining a near-optimal topological design without any iteration. *Structural and Multidisciplinary Optimization*, 59(3):787–799.

[427] Yvonnet, J. (2019). *Computational Homogenization of Heterogeneous Materials with Finite Elements*. Springer International Publishing, Cham.

[428] Zadeh, L. A. (1978). Fuzzy sets as a basis for a theory of possibility. *Fuzzy sets and systems*, 1(1):3–28.

[429] Zadeh, L. A. (1984). Review of a mathematical theory of evidence. *AI magazine*, 5(3):81–81.

[430] Zeng, D. and Duddeck, F. (2017). Improved hybrid cellular automata for crashworthiness optimization of thin-walled structures. *Structural and Multidisciplinary Optimization*, 56(1):101–115.

[431] Zhan, J., Luo, Y., Zhang, X., and Kang, Z. (2020). A general assessment index for non-probabilistic reliability of structures with bounded field and parametric uncertainties. *Computer Methods in Applied Mechanics and Engineering*, 366:113046.

[432] Zhang, H., Mullen, R. L., and Muhanna, R. L. (2010). Interval monte carlo methods for structural reliability. *Structural Safety*, 32(3):183–190.

[433] Zhang, W., Zhao, L., Gao, T., and Cai, S. (2017). Topology optimization with closed b-splines and boolean operations. *Computer Methods in Applied Mechanics and Engineering*, 315:652–670.

[434] Zhang, X. and Kang, Z. (2014). Dynamic topology optimization of piezoelectric structures with active control for reducing transient response. *Computer Methods in Applied Mechanics and Engineering*, 281:200–219.

[435] Zhang, X., Kang, Z., and Zhang, W. (2016a). Robust topology optimization for dynamic compliance minimization under uncertain harmonic excitations with inhomogeneous eigenvalue analysis. *Structural and Multidisciplinary Optimization*, 54(6):1469–1484.

[436] Zhang, Z., Chen, J., Li, E., Li, W., Swain, M., and Li, Q. (2016b). Topological design of all-ceramic dental bridges for enhancing fracture resistance. *International journal for numerical methods in biomedical engineering*, 32(6):e02749.

[437] Zhang, Z., Li, Y., Zhou, W., Chen, X., Yao, W., and Zhao, Y. (2021). Tonr: An exploration for a novel way combining neural network with topology optimization. *Computer Methods in Applied Mechanics and Engineering*, 386:114083.

[438] Zhao, J. and Wang, C. (2014). Robust structural topology optimization under random field loading uncertainty. *Structural and Multidisciplinary Optimization*, 50(3):517–522.

[439] Zhao, J. and Wang, C. (2017). Topology optimization for minimizing the maximum dynamic response in the time domain using aggregation functional method. *Computers & Structures*, 190:41–60.

[440] Zhao, J., Yoon, H., and Youn, B. D. (2019a). Concurrent topology optimization with uniform microstructure for minimizing dynamic response in the time domain. *Computers & Structures*, 222:98–117.

[441] Zhao, J., Yoon, H., and Youn, B. D. (2019b). An efficient concurrent topology optimization approach for frequency response problems. *Computer Methods in Applied Mechanics and Engineering*, 347:700–734.

[442] Zhao, J., Yoon, H., and Youn, B. D. (2020). An adaptive hybrid expansion method (ahem) for efficient structural topology optimization under harmonic excitation. *Structural and Multidisciplinary Optimization*, 61(3):895–921.

[443] Zhao, Q., Chen, X., Ma, Z., and Lin, Y. (2016). A comparison of deterministic, reliability-based topology optimization under uncertainties. *Acta Mechanica Solida Sinica*, 29(1):31–45.

[444] Zhao, Q., Zhang, H., Zhang, T., Hua, Q., Yuan, L., and Wang, W. (2019c). An efficient strategy for non-probabilistic reliability-based multi-material topology optimization with evidence theory. *Acta Mechanica Solida Sinica*, 32(6):803–821.

[445] Zheng, J., Luo, Z., Jiang, C., and Gao, J. (2019). Robust topology optimization for concurrent design of dynamic structures under hybrid uncertainties. *Mechanical Systems and Signal Processing*, 120:540–559.

[446] Zheng, J., Luo, Z., Jiang, C., Ni, B., and Wu, J. (2018a). Non-probabilistic reliability-based topology optimization with multidimensional parallelepiped convex model. *Structural and Multidisciplinary Optimization*, 57(6):2205–2221.

[447] Zheng, J., Luo, Z., Li, H., and Jiang, C. (2018b). Robust topology optimization for cellular composites with hybrid uncertainties. *International Journal for Numerical Methods in Engineering*, 115:695–713.

[448] Zheng, Y., Da, D., Li, H., Xiao, M., and Gao, L. (2020). Robust topology optimization for multi-material structures under interval uncertainty. *Applied Mathematical Modelling*, 78:627–647.

[449] Zhou, E., Wu, Y., Lin, X., Li, Q., and Xiang, Y. (2021a). A normalization strategy for beso-based structural optimization and its application to frequency response suppression. *Acta Mechanica*, 232(4):1307–1327.

[450] Zhou, H. (2010). Topology Optimization of Compliant Mechanisms Using Hybrid Discretization Model. *Journal of Mechanical Design*, 132(11). 111003.

[451] Zhou, M. and Rozvany, G. (1991). The coc algorithm, part ii: Topological, geometrical and generalized shape optimization. *Computer methods in applied mechanics and engineering*, 89(1-3):309–336.

[452] Zhou, M. and Rozvany, G. (2001). On the validity of eso type methods in topology optimization. *Structural and Multidisciplinary Optimization*, 21(1):80–83.

[453] Zhou, P., Peng, Y., and Du, J. (2021b). Topology optimization of bi-material structures with frequency-domain objectives using time-domain simulation and sensitivity analysis. *Structural and Multidisciplinary Optimization*, 63(2):575–593.

[454] Zhou, Y., Zhang, W., Zhu, J., and Xu, Z. (2016). Feature-driven topology optimization method with signed distance function. *Computer Methods in Applied Mechanics and Engineering*, 310:1–32.

[455] Zhu, J., Zhang, W., and Qiu, K. (2007). Bi-directional evolutionary topology optimization using element replaceable method. *Computational Mechanics*, 40(1):97–109.

[456] Zhu, J.-H., Liu, T., Zhang, W.-H., Wang, Y.-L., and Wang, J.-T. (2021). Concurrent optimization of sandwich structures lattice core and viscoelastic layers for suppressing resonance response. *Structural and Multidisciplinary Optimization*, 64(4):1801–1824.

[457] Zhu, J.-H., Zhang, W.-H., and Xia, L. (2016). Topology optimization in aircraft and aerospace structures design. *Archives of Computational Methods in Engineering*, 23(4):595–622.

[458] Zhu, Y., Wang, Y., Zhang, X., and Kang, Z. (2022). A new form of forbidden frequency band constraint for dynamic topology optimization. *Structural and Multidisciplinary Optimization*, 65(4):1–16.

[459] Zuo, W. and Saitou, K. (2017). Multi-material topology optimization using ordered simp interpolation. *Structural and Multidisciplinary Optimization*, 55(2):477–491.

[460] Zuo, Z., Xie, Y., and Huang, X. (2009). Combining genetic algorithms with beso for topology optimization. *Structural and multidisciplinary optimization*, 38(5):511–523.